Numerical Simulation of Performance and Solar-to-Fuel Conversion Efficiency for Photoelectrochemical Devices

Thesis by

Yikai Chen

In Partial Fulfillment of the Requirements for

the degree of

Doctor of Philosophy

CALIFORNIA INSTITUTE OF TECHNOLOGY

Pasadena, California

2021

(Defended on June 1st, 2021)

Yikai Chen
ORCID: 0000-0002-2955-9671

ACKNOWLEDGEMENTS

First, I would like to thank my advisor, Prof. Nathan Lewis, for his passion, dedication, and mentorship throughout my entire graduate study. I would also like to thank Dr. Chengxiang Xiang (CX) for his generous advice and plenty of comments he gave on my projects.

Kimberly M. Papadantonakis and Bruce S. Brunschwig, I sincerely appreciate all the help and support you have provided.

Special gratitude towards Melany L. Hunt, Austin J. Minnich, and Harry B. Gray for serving on my thesis committee.

Many thanks to Sophia Haussener, who introduced COMSOL to me in the very beginning of my career and gave me lots of encouragement.

Rui Liu, Teddy Huang, Ke Sun, thanks a lot for all the help on the electrochemistry side. Shu Hu, thank you for helping me better understand the semiconductor theories. I was so lucky to be able to collaborate with all of you.

Barbara Miralles and Holly L. Golcher, thank you for all the help and support on the administrative side.

Xinghao Zhou, Jingjing Jiang, Sisir Yalamanchili, Kathleen M. Kennedy, Paul Nunez, Stefan T. Omelchenko, Pai Buabthong, Katherine Z. Rinaldi, Ethan Simonoff, Kathryn R. Hamann, Weilai Yu, Jacqueline A. Dowling, Ellen Yan, and all the people in the Lewis group, it was such a great pleasure to work with you. Thank you for all the moments we've shared, all the shared dreams, wishes and laughter, and above all, for your friendship. Each precious second will be treasured in my heart forever.

Finally, I would like to thank my parents for their unconditional love and support. My husband, Jing Li, throughout the ups and downs of life, you never left my side; thank you for being my rock. Aiden, my dear baby, thank you for always being my delightful cheerleader. I love you all!

ABSTRACT

The Industrial Revolution was energized by coal, petroleum, and natural gas. It is clear that fossil fuels, which drive steam and electrical engines, made possible a monumental increase in the amount of productive energy available to humans. But in the meantime, the constant burning of fossil fuels has changed the natural greenhouse, intensified global warming, deteriorated air quality, and eventually caused irreversible environmental damage on our planet. Renewable energy especially solar energy offers a desirable approach toward meeting our growing energy needs while largely reducing fossil fuel burning. The major problems in terms of harvesting energy directly from sunlight turn out to be low energy concentration and intermittency. Building solar-fuel generators, which stores solar energy in chemical bonds, similar to photosynthesis in nature, provides a possible solution to these two problems. Carbon-free chemicals, such as hydrogen gas, which are produced by solar-driven water-splitting, or carbon-neutral chemicals, such as methane and ethylene, which are produced by solar-driven CO_2 reduction, are all promising clean fuels for solar storage.

This thesis is focused on studying the performance and solar to fuel conversion efficiency of existing and hypothetical test-bed photoelectrochemical prototypes using multi-physics modeling and simulation to lay a foundation for future implementation and scale-up of the integrated, solar-driven systems. For water-splitting systems, a sensitivity analysis has been made to assess the relative importance of improvements in electrocatalysts, light absorbers, and system geometry on the efficiency of solar-to-hydrogen generators. Besides, an integrated photoelectrolysis system sustained by water vapor is designed and modeled. Under concentrated sunlight, the performance of the photoelectrochemical system with 10× solar concentrators was simulated and the impact of hydrogen bubbles that are generated inside the cathodic chamber on the performance of the photoelectrolysis system was evaluated. For CO_2 reduction systems, operational constraints and strategies for systems to effect the sustainable, solar-driven reduction of atmospheric CO_2 were investigated. The spatial and light-intensity dependence of product distributions in an integrated photoelectrochemical CO_2 reduction system was modeled and simulated. Finally, the

performance a flow-through gas diffusion electrode for electrochemical reduction of CO or CO_2 was evaluated.

This thesis can be divided into three parts. The first part discusses the importance of solar energy. The second part includes Chapter II, Chapter III, Chapter IV, and Chapter V, which deals with solar-driven water-splitting cells, and the third part includes Chapter VI, Chapter VII, and Chapter VIII, which deals with solar-driven CO_2 reduction cells.

PUBLISHED CONTENT AND CONTRIBUTIONS

1) K. Walczak et al. “Modeling, Simulation, and Fabrication of a Fully Integrated, Acid-stable, Scalable Solar-Driven Water-Splitting System”. In: ChemSusChem, Volume 8, Issue 3, pp. 544-551.
   DOI: 10.1002/cssc.201402896.
   Y.C. participated in all the numerical calculation for the PEC performance and in writing the manuscript.

2) Y. Chen et al. “A sensitivity analysis to assess the relative importance of improvements in electrocatalysts, light absorbers, and system geometry on the efficiency of solar-fuels generators”. In: Energy Environ. Sci., 2015, 8, 876-886.
   DOI: 10.1039/C4EE02314E.
   Y.C. participated in all the modeling, calculation, results analysis, and writing the manuscript.

3) C. Xiang and Y. Chen et al. “Modeling an integrated photoelectrolysis system sustained by water vapor”. In: Energy Environ. Sci., 2013, 6, 3713-3721
   DOI: 10.1039/C3EE42143K.
   Y.C. participated in all the modeling, calculation, results analysis, and writing the manuscript.

4) Y. Chen et al. “Modeling the Performance of an Integrated Photoelectrolysis System with 10x Solar Concentrators”. In: 2014 J. Electrochem. Soc. 161 F1101
   DOI: 10.1149/2.0751410jes.
   Y.C. participated in all the model build-up, numerical simulation, results analysis, and writing the manuscript.

5) Y. Chen et al. “A quantitative analysis of the efficiency of solar-driven water-splitting device designs based on tandem photoabsorbers patterned with islands of metallic electrocatalysts”. In: Energy Environ. Sci., 2015, 8, 1736-1747.
   DOI: 10.1039/C5EE00311C.
   Y.C. participated in all the MATLAB coding, data reading, and numerical and experimental results comparison and analysis, as well as writing the manuscript.

6) Y. Chen et al. “Operational constraints and strategies for systems to effect the sustainable, solar-driven reduction of atmospheric CO_2”. In: Energy Environ. Sci., 2015, 8, 3363-3674.
   DOI: 10.1039/C4EE02908B.
   Y.C. participated in all the model build-up, numerical simulation, results analysis, and writing the manuscript.

7) Y. Chen et al. “Modeling and Simulation of the Spatial and Light-Intensity Dependence of Product Distributions in an Integrated Photoelectrochemical CO_2 Reduction System”. In: ACS Energy Lett., 2016, 1, 1, 273-280.

DOI: 10.1021/acsenergylett.6b00134.
Y.C. participated in all the model build-up, numerical simulation, results analysis, and writing the manuscript.

8) Y. Chen et al. “Modeling the Performance of A Flow-Through Gas Diffusion Electrode for Electrochemical Reduction of CO or CO_2”. In: 2020 J. Electrochem. Soc. 167 114503
DOI: 10.1149/1945-7111/ab987a.
Y.C. participated in all the model build-up, numerical simulation, results analysis, and writing the manuscript.

TABLE OF CONTENTS

LIST OF ILLUSTRATIONS

LIST OF TABLES

Chapter I

INTRODUCTION

1.1 The importance of solar energy

1.1.1 Global warming and CO_2 emission

For 2.5 million years the earth's climate has fluctuated cycling from ice ages to warmer periods, but since the pre-industrial period, due to human activities, primarily fossil fuel burning, the planet's temperature has risen unusually fast, about 1 degree Celsius, a number that is currently increasing by 0.2 degrees Celsius per decade, as shown in Figure 1.1.

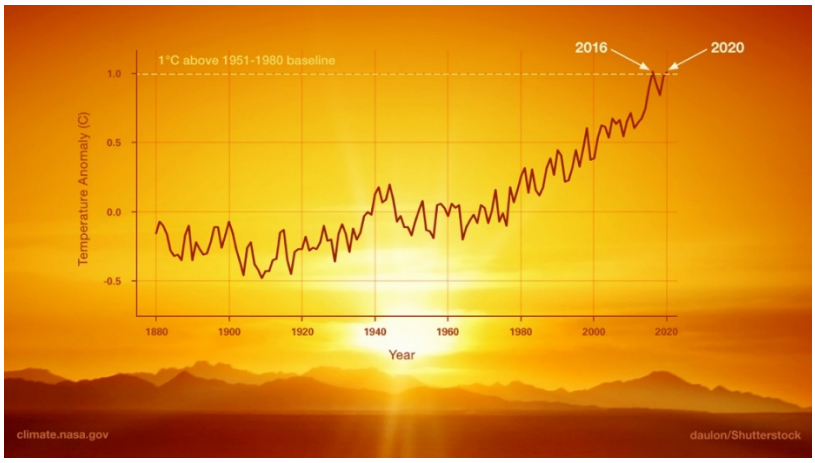

Figure 1.1: The change in global surface temperature relative to 1951-1980 average temperatures, with the year 2020 tying with 2016 for warmest on record (Source: NASA Goddard Institute for Space Studies). Credit: NASA/JPL-Caltech

Ever since the industrial revolution began, factories, power plants as well as cars have burned fossil fuels such as oil and coal, which leads to the release of huge amount of carbon dioxide and other gases into the atmosphere. These gases trap heat near the earth through a naturally occurring process, the greenhouse effect. The greenhouse effect begins with the sun and the energy it radiates to the earth. The earth and the atmosphere absorb some of this

energy while the rest is radiated back to the space. Naturally occurring gases in the atmosphere trap some of this energy, reflect it back and warm the earth. Scientists believe that the greenhouse effect is being intensified by the extra greenhouse gases that humans have released. Evidence for global warming includes a recent string of very warm years. As NASA Goddard Institute for Space Studies (GISS) points out, the last seven years have been the warmest seven years on record, typifying the ongoing and dramatic warming trend. Meanwhile, the anthropogenic greenhouse gas (GHG) emissions have increased year by year. Readings in Figure 1.2 show that GHG emissions go up from 27 $GtCO_2$-eq/yr in 1970 to 49 $GtCO_2$-eq/yr in 2010, with 1.3%/yr increase rate from 1970 to 2000, and 2.2%/yr increase rate from 2000 to 2010. Out of all the GHG emissions increase from 1970 to 2010, 78% came from CO_2 emissions from fossil fuel combustion and industrial processes.

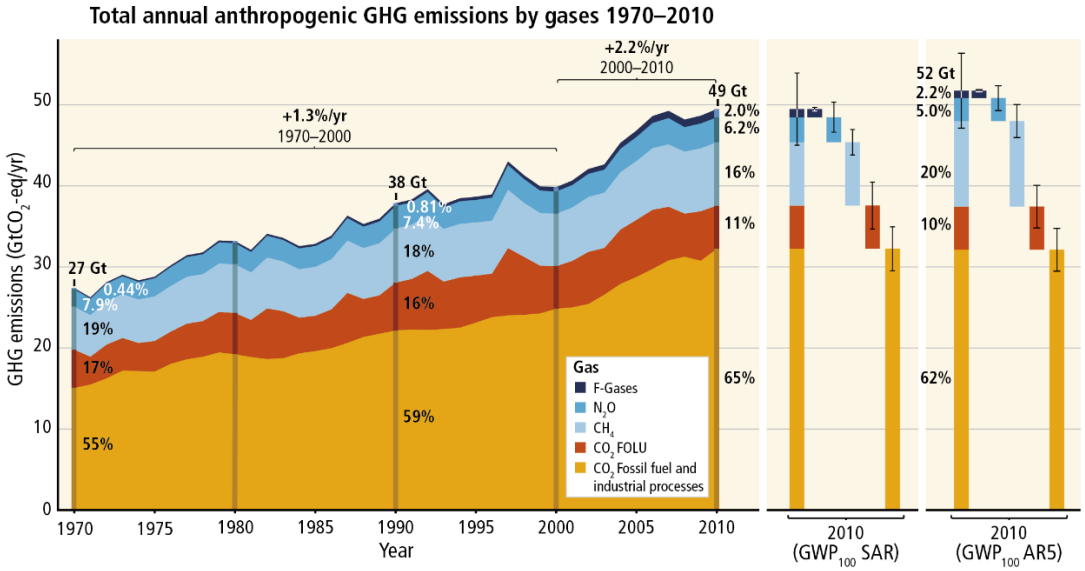

Figure 1.2: Total annual anthropogenic greenhouse gas (GHG) emissions (gigatonne of CO_2-equivalent per year, $GtCO_2$-eq/yr) for the period 1970 to 2010 by gases: CO_2 from fossil fuel combustion and industrial processes; CO_2 from Forestry and Other Land Use (FOLU); methane (CH_4); nitrous oxide (N_2O); uorinated gases covered under the Kyoto Protocol (F-gases). Right hand side shows 2010 emissions, using alternatively CO_2 - equivalent emission weightings based on IPCC Second Assessment Report (SAR) and AR5 values. (Reprinted with permission from ref[1].)

As a result, the GHG concentrations in the atmosphere have increased rapidly. It turns out that atmospheric concentrations of GHGs are at levels that are unprecedented in at least 800,000 years. As Figure 1.3 indicates, concentrations of carbon dioxide, methane and nitrous oxide have all shown large increases since 1750 (40%, 150% and 20%, respectively). CO_2 concentrations are increasing at the fastest observed decadal rate of change (2.0 ± 0.1 ppm/yr) for 2002– 2011. After almost one decade of stable CH_4 concentrations since the late 1990s, atmospheric measurements have shown renewed increases since 2007. N_2O concentrations have steadily increased at a rate of 0.73 ± 0.03 ppb/yr over the last three decades.

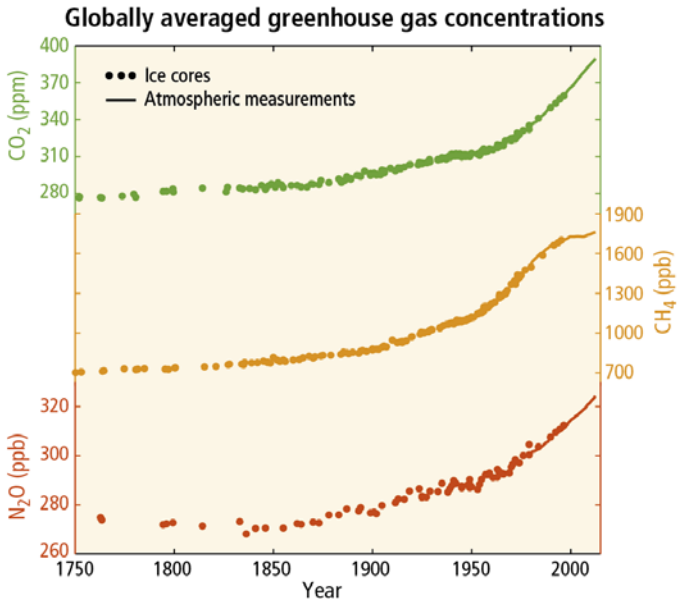

Figure 1.3: Atmospheric concentrations of the greenhouse gases carbon dioxide (CO_2, green), methane (CH_4, orange) and nitrous oxide (N_2O, red) determined from ice core data (dots) and from direct atmospheric measurements (lines). (Reprinted with permission from ref [1].)

The ocean has absorbed between 20% and 30% of total anthropogenic carbon dioxide emissions in recent decades (7.2 to 10.8 billion metric tons per year)[2]. As a result of more carbon dioxide emissions into the atmosphere, since the beginning of the Industrial Revolution, the acidity of surface ocean waters has increased by about 30%.[2] Nevertheless,

due to global warming, Arctic sea ice is shrinking. According to NASA studies the extent of Arctic sea ice has declined about 10% in the last 30 years. Global sea level rose about 20 centimeters in the last century. The rate in the last two decades, however, is nearly double that of the last century and accelerating slightly every year. If the global surface temperature keeps increasing at the current pace, it is estimated to go up by 5.6 degrees Celsius by the end of the century. Climate models predict more subtle changes based on this assumption. Weather patterns will change and make hurricanes more frequent, severe droughts will become more common in warm areas and eventually more species will be unable to adapt to the changing conditions and face extinction.

1.1.2 Fossil fuels burning and air pollution

Aside from the greenhouse gases, fossil fuel burning also generates SO_2 and nitrogen containing chemicals, which will form fine particulate matter (<2.5 μm), usually named as $PM_{2.5}$, after a series of atmospheric chemistry reactions:

$$SO_2 + H_2O = H_2SO_3$$
$$H_2SO_3 + O_2(O_3) = H_2SO_4$$
$$H_2SO_4 + NH_3 = NH_4HSO_4$$
$$H_2SO_4 + 2NH_3 = (NH_4)_2SO_4$$
$$HNO_3 + NH_3 = NH_4NO_3$$

Figure 1.4 shows $PM_{2.5}$ level remains very high in a broad swath stretching from the Saharan Desert in Northern Africa to Eastern Asia. Compared with maps of population density, it suggests that more than 80% people in the world are currently breathing polluted air with $PM_{2.5}$ concentration higher than 10 $\mu g/m^3$, which is the guideline value World Health Organization (WHO) has recommended to achieve for $PM_{2.5}$ annual mean concentration.

$PM_{2.5}$ can cause a variety of health problems, which will possibly lead to irregular heartbeat, aggravated asthma, decreased lung function and increased respiratory symptoms. Meanwhile $PM_{2.5}$ are believed to be the main cause of reduced visibility in the United States. Depending on their chemical composition, the impact of $PM_{2.5}$ on the environment may

include depleting the nutrients in soil, damaging sensitive forest and farm crops and making lakes and streams acidic. Therefore, it is very urgent that strong actions need to be taken to curb the deteriorating trend of air pollution.

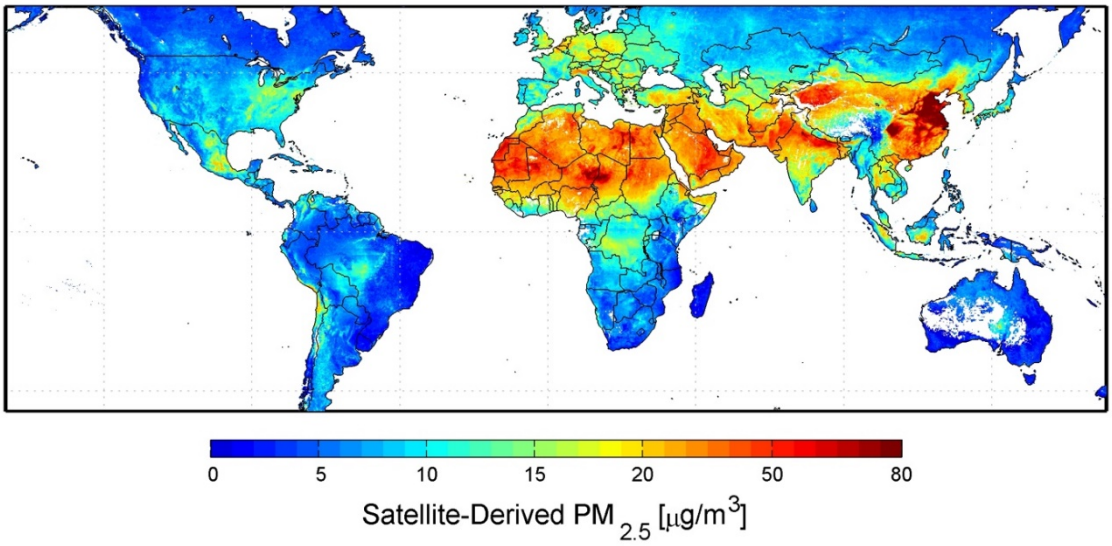

Figure 1.4: Global satellite-derived map of $PM_{2.5}$ averaged over 2001 to 2006. Credit: Dalhousie University, Aaron van Donkelaar

1.1.3 Renewable energy

Figure 1.5 indicates that in 2019, the total energy consumed by U.S. only reaches 92.94 quadrillion Btu. Fossil fuels (petroleum, natural gas and coal) burning has the major share of 79%, which, as discussed in the previous sections, has made non-negligible damage to the environment. In order to decrease the greenhouse gases emission and meet the energy demand at the same time, renewable energy is the solution. Renewable energy has a variety of sources, the most popular ones are: solar, wind, hydro, tidal, geothermal and biomass. Solar energy is the most abundant clean energy on the earth. As Table 1.1 shows, the power supplied by the sun reaches 36,000 TW, which is four orders of magnitude higher than the power supplied by hydro, geothermal and biomass, two orders of magnitude higher than the power supplied by wind, and three orders of magnitude higher than the world consumption

rate. Therefore, energy harvested directly from sunlight offers a desirable approach toward fulfilling, with minimal environmental impact, the need for clean energy.

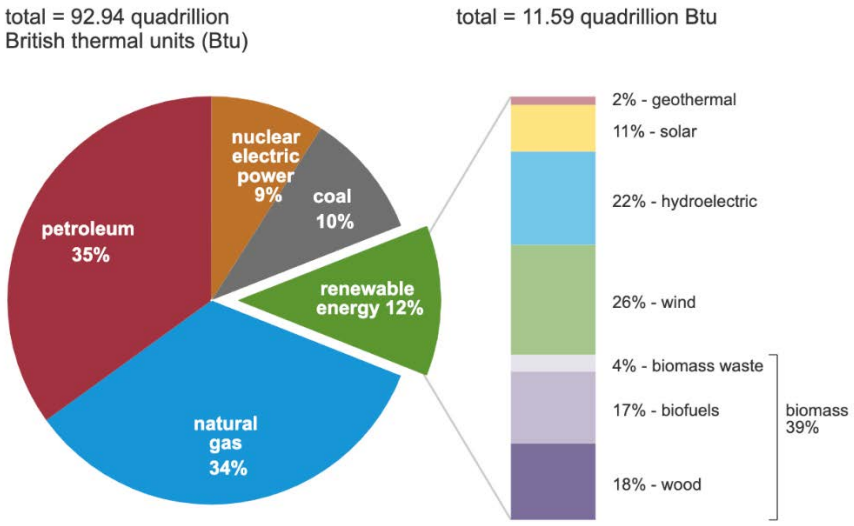

Figure 1.5: U.S. primary energy consumption by energy source, 2019 (Source: U.S. Energy Information Administration, Monthly Energy Review, Table 1.3 and 10.1, April 2020)

Renewable energy	Power supply or consumption (TW or TWy/y)
Solar reaching on land	36,000
Hydro	3-4
Geothermal	0.2-3
Wind	75-130
Biomass	2-6
World consumption	18.3

Table 1.1: Comparison of power supply of various types of renewable energy, and world energy consumption in 2014. (Data from source ref [3,4])

However, in order to fully utilize solar energy for the global energy demand, several important goals need to be met. First, the energy conversion system must have high efficiency. Second, the solar-fuel generators must be cost-effective in order to grow to multi-terawatt scale. Next, the system must be able to provide a stable, constant energy flux. Due to the daily and seasonal variability in renewable energy sources such as sunlight, energy harvested from the sun needs to be efficiently converted into chemical fuel that can be stored, transported, and used upon demand. Finally but most importantly, the whole system must meet all the safety standards.

1.2 Solar-to-fuel conversion system

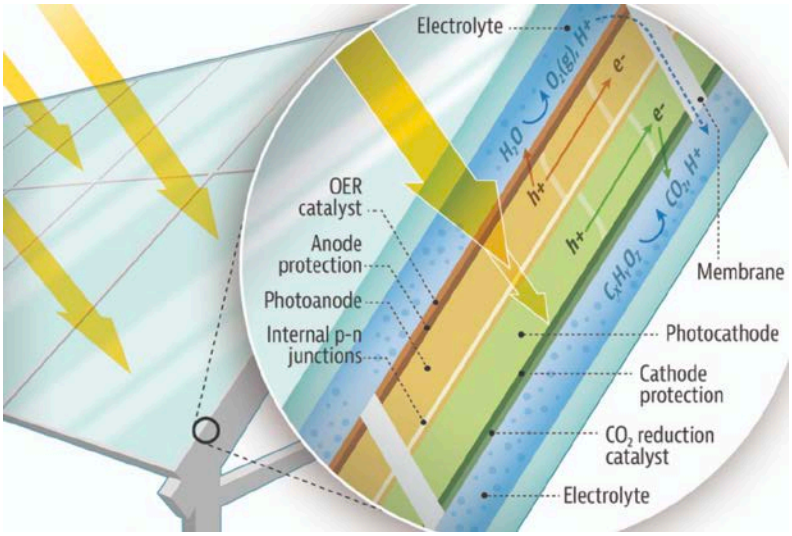

Figure 1.6: Schematic illustration for an integrated photoelectrochemical device. Credit: Reused with permission from JCAP/Caltech

Interest in the development of solar-fuel generators began with the pioneering research of Fujishima and Honda in the early 1970s.[5,6] As Figure 1.6 shows, the primary components of a solar-fuel generator include photoabsorbers, electrocatalysts, membrane separators, electrolytes, and the supporting structures. The photoabsorbers capture and convert the

incident photons into energetic electrons and holes, to provide the voltage and current for the fuel-forming reactions. The electrocatalysts lower the kinetic overpotentials and effect the efficiency, stability and selectivity of the fuel-forming reactions. The membrane separators prevent product crossover, both to avoid deleterious product recombination and explosive/flammable product mixtures, and provides a facile ion transport pathway. The electrolytes facilitate ion transport between the cathode and anode compartments. The supporting structure includes a mechanism for gathering light (e.g., window, lens arrays), input and output ports (e.g., input feedstocks, water/vapor and effluent products), structural elements, and serve as a temporary storage space for products.

Most laboratory research has focused on studying and optimizing intrinsic material properties of photoelectrochemical assemblies in a half-cell configuration,[7-15] in which the reactant/product transport is optimized by external stirring and in which any resistive losses due to solution transport in the cell are compensated by an external voltage bias. Over the last four decades, a variety of unassisted water-splitting demonstrations have been reported, though reports of robust product separation and collection are rare.[16-25] As shown in Figure 1.7 and Figure 1.8, a collaborative work done by Joint Center Artificial Photosynthesis (JCAP) has constructed a prototype, that can lead to a deployable and scalable solar fuels generation system and includes not only the light absorbers, electrocatalyts, membrane separator, and electrolyte components, but also a chassis to synergistically integrate the these components while maintaining their optimal geometric layout and safe operation.

This thesis is focused on further studying the performance and solar to fuel conversion efficiency of existing and hypothetical test-bed photoelectrochemical prototypes using multi-physics modeling and simulation to lay a foundation for future implementation and scale-up of the integrated, solar-driven systems. My entire work can be broken into two parts: the first part includes Chapter II, Chapter III, Chapter IV and Chapter V, which deals with solar-driven water-splitting cell, the second part includes Chapter VI, Chapter VII and Chapter VIII, which deals with solar-driven CO_2 reduction cell.

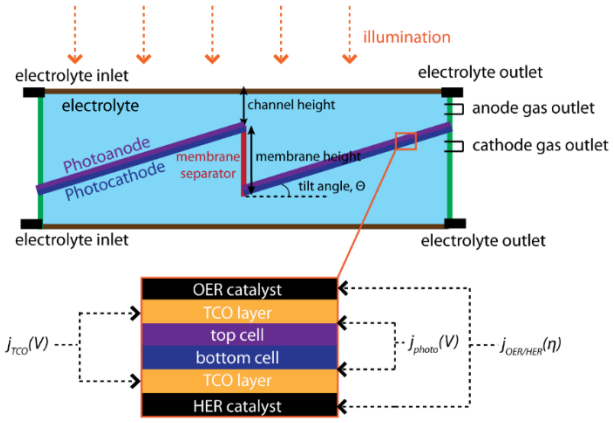

Figure 1.7: Schematic illustration of the device construct of the louvered design solar-hydrogen device.

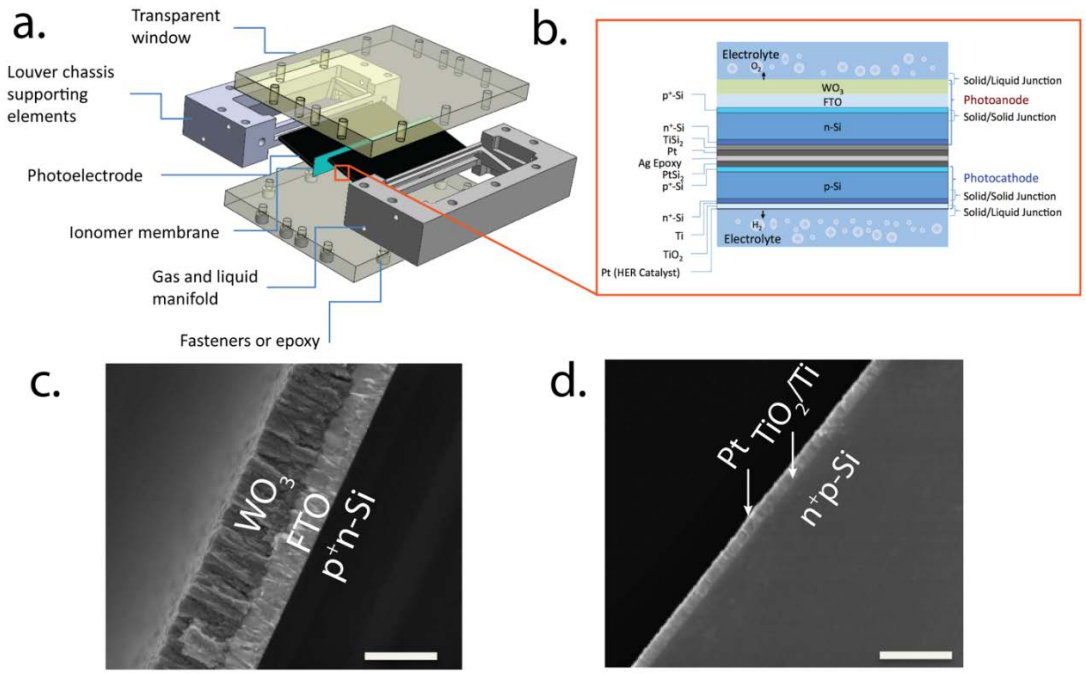

Figure 1.8: (a) The exploded view of the CAD model for the louvered design. (b) A cross-sectional schematic of the monolithically integrated photoelectrode assembly. (c) and (d) Cross-sectional scanning electron micrographs of the photoanode assembly (WO_3/FTO/p^+n-Si) and photocathode assembly (Pt/TiO_2/Ti/n^+p-Si), respectively. The inset scale bar is 1 μm.

1.2.1 Solar-driven water-splitting cell

1.2.1.1 Sensitivity analysis

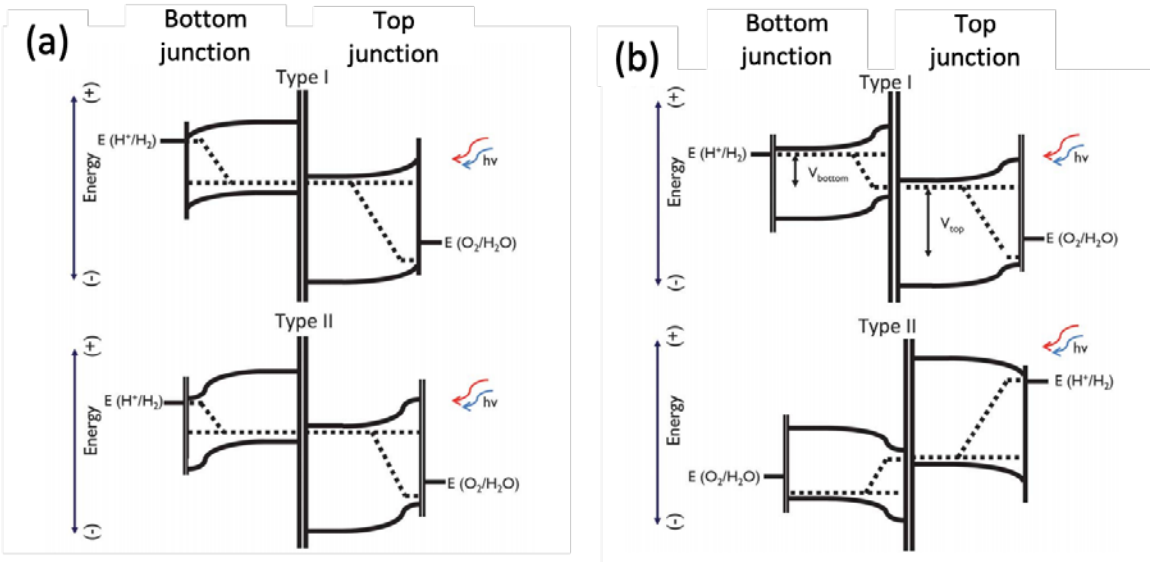

Figure 1.9: Schematic energy band diagrams of an integrated photoelectrochemical (PEC) system under 1 Sun illumination for (a) the photocathode + photoanode PEC system, and (b) the tandem light absorber + electrocatalyst PEC system. Types I and II illustrate the semiconductor–liquid junctions and buried junctions, respectively.

An integrated solar-driven water-splitting cell generally has two configurations, photocathode + photoanode PEC and tandem absorber + electrocatalysts PEC. Figure 1.9a shows the energy band diagram for the first configuration, where a photoanode and a photocathode are connected back-to-back with an Ohmic contact. The photogenerated minority-carrier electrons drift and diffuse to the photocathode-electrolyte interface and reduce H^+ to H_2, while the photogenerated minority-carrier holes drift and diffuse to the photoanode-electrolyte interface and oxidize water to O_2. In the meantime, the majority-carriers (holes in photocathode and electrons in photoanode) recombine at the Ohmic contact. Both the semiconductor-liquid junction, which is formed at the photoelectrode-electrolyte interface, as seen in Type I, and the 'buried' junction, which is formed inside the photoelectrode, as seen in Type II, can be served as the asymmetrical barrier to effectively

separate the photogenerated carriers in this configuration. The energy band diagram for the second configuration is indicated in Figure 1.9b. This model consists a tandem two-junction light absorber and HER/OER catalysts that are in electrical connection to the electron/hole collectors of the light absorber. For this configuration, both junctions can be 'buried', as seen in Type I, or one of the junctions can be at the photoelectrode-electrolyte interface, as seen in Type II.

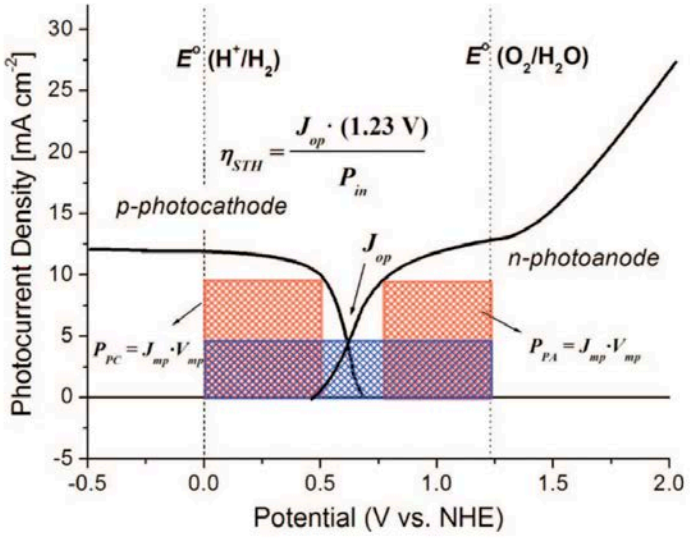

Figure 1.10: Overlaid current density-potential behavior for a p-type photocathode and an n-type photoanode, with overall efficiency projected by the power generated $P_{STH} = J_{op}$ (1.23 V) by the cell for splitting water.

The overall solar-to-hydrogen conversion efficiency (STH) of the water-splitting system is calculated through

$$\eta_{STH} = \frac{1.23(V) \cdot J_{op}(mA\ cm^{-2})}{P_{in}\ (mW\ cm^{-2})}, \qquad \text{(Eq. 1.1)}$$

where J_{op} stands for the operating photocurrent density and P_{in} represents the total incident solar irradiance. By independently characterizing photoanodes and photocathodes, the expected performance of an integrated system can be directly calculated. J_{op} can be obtained by overlapping the individually calculated J-V data for each photoanode/photocathode, as

shown in Figure 1.10, in which the red shaded area illustrates the maximal power generated for each component of the cell while the blue shaded area illustrates the power generated at the operating current density.

Solar to hydrogen conversion efficiency of such a system depends on the performance and materials properties of all the individual components as well as the design of the system. Significant research efforts are being devoted to improving the performance of all of the system components, yet some improvements will result in larger gains in the overall system efficiency than others. In Chapter II, a sensitivity analysis of the solar-to-hydrogen conversion efficiency with respect to the materials properties of light absorbers, electrocatalysts, and the geometric design parameters, for a series of specific but generic designs for solar-fuels generators, has been described. The analysis has revealed the relative importance of reductions in the overpotentials of electrocatalysts, of improvements in the materials properties of light absorbers, and of optimization in the system geometry for various types of solar-fuels generators, while considering operation at a range of temperatures as well as under a variety of illumination intensities including up to 10-fold optical concentration. Such a sensitivity analysis provides a quantitative framework within which to assess the gains in system performance that can be attained as a result of improving, relative to the current state-of-the-art, the performance of different components of the system, and provides a useful framework for setting a forward R&D agenda for such systems.

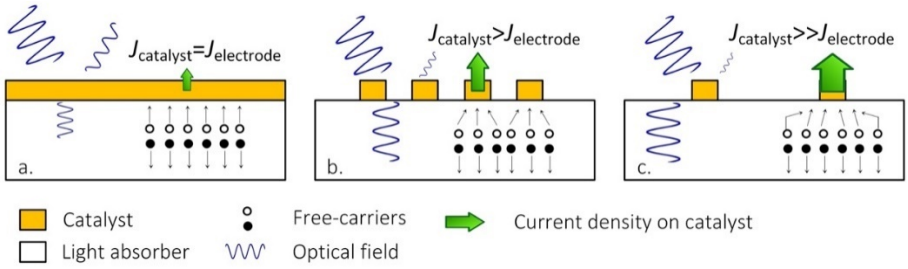

Figure 1.11: Schematic illustration of the trade-offs between optical obscuration and concentrated operational current densities at the catalyst surface for photoabsorbers (a), coated with continuous electrocatalyst films; (b) coated with patterned electrocatalyst films with high filling fractions, and (c) coated with patterned electrocatalyst films with low filling fractions.

Furthermore, efficient photoelectrochemical water splitting requires the use of electrocatalysts that reduce the kinetic barriers to the reduction and oxidation half-reactions. However, the electrocatalysts can absorb or reflect light, and thus can limit the overall solar-to-hydrogen conversion efficiency. One strategy for reducing the optical obscuration that results from the presence of the electrocatalyst layer is to produce a patterned catalyst film that results in a low geometric filling fraction of the metal catalyst on the surface of the light absorbers, as seen in Figure 1.11, but reducing the filling fraction also increases the kinetic overpotentials required for the desired reactions. The trade-off between the optical obscuration and kinetic overpotentials of electrocatalyst films patterned onto the surface of tandem light-absorber structures in model photoelectrosynthetic water-splitting systems was investigated using a 0-dimensional load-line analysis and experimental measurements. The electrocatalytic performance of the catalyst at high current densities, normalized to the electrocatalyst surface area, is an important factor in the dependence of the optimal solar-to-hydrogen (STH) conversion efficiency, $\eta_{STH,opt}$, on the filling fraction (f_c) of the patterned catalysts, because even under conditions that produce minority-carrier current densities of $\sim$10 mA cm^{-2} at the solid/liquid interface, the current density at catalyst-bearing sites can be >1–2 A cm^{-2} in low filling-fraction films. The maximum STH conversion efficiency, $\eta_{STH,opt}$, using a hypothetical electrocatalyst that was optically transparent but which nevertheless exhibited a current-density *versus* potential behavior that is characteristic of the most active Pt films measured experimentally regardless of their optical obscuration, was calculated as 26.7%. By comparison, the maximum $\eta_{STH,opt}$ of 24.9% for real patterned Pt electrocatalyst films closely approached this ideal-case limit. Hence, patterned electrocatalysts with very low filling fractions can provide a potentially promising path to the realization of efficient large-scale photoelectrolysis systems while minimizing the use of scarce noble metals.

1.2.1.2 Liquid electrolyte vs. water-vapor

An integrated solar-driven water-splitting cell has the potential for large-scale solar energy conversion and storage. The design principles and operational details of the cell depend on

the system input feedstock. Most studies use the liquid electrolyte as a feedstock, where strong acid and strong base are typically employed to reduce the resistive loss in the system. The use of water vapor or pure water as the feedstock has several potential advantages, which can benefit large-scale implementation of a photoelectrolysis system. In Chapter III, some unique challenges are addressed and the design criteria for such a system is studied by a multi-physics numerical model that accounts for charge and species conservation, electron and ion transport, and electrochemical processes.

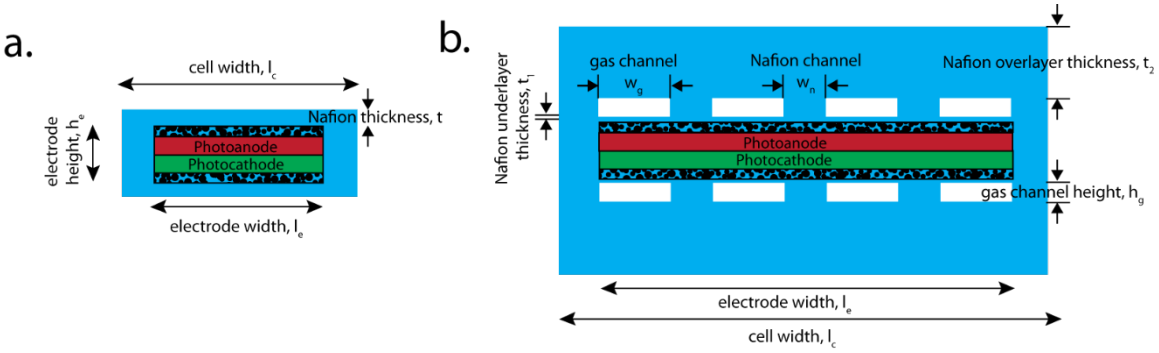

Figure 1.12: Schematic illustrations of two cell designs for a photoelectrolysis device sustained by a water vapor feed. Both designs contain a photocathode (red), a photoanode (green), electrocatalyst layers (dotted) and Nafion film (blue) used as a representative solid polymer electrolyte material. In Design A, the electrode width, electrode height, cell width and Nafion thickness are labeled as l_e, h_e, l_c and t, respectively. In Design B, the gas channel width, gas channel height, Nafion channel width, Nafion underlayer thickness and Nafion overlayer thickness are labeled as w_g, h_g, w_n, t_1, and t_2, respectively.

Two designs (Figure 1.13) for an integrated photoelectrolysis system sustained by water vapor have been investigated using a multi-physics numerical model that accounts for charge and species conservation, electron and ion transport, and electrochemical processes. Both designs leverage the use of a proton-exchange membrane that provides conductive pathways for reactant/product transport and prevents product crossover. The resistive losses, product gas transport, and gas crossovers as a function of the geometric parameters of the two designs have been evaluated systematically. In these designs, minimization of

pathways in the membrane that can support the diffusive transport of product gases from the catalyst to the gas-collecting chamber was required to prevent supersaturation of hydrogen or oxygen gases at the Nafion/catalyst interface. Due to the small, thin membrane layer that was required, a small electrode width (< 300 μm) was also required to produce low resistive losses in the system. Alternatively, incorporation of a structured membrane that balances the gas transport and ionic transport allows the maximum electrode width to be increased to dimensions as large as a few millimeters. Diffusive gas transport between the cathode and anode was the dominant source for crossover of the product gases under such circumstances. The critical dimension of the electrode required to produce acceptably low rates of product crossover was also investigated through the numerical modeling and device simulations.

1.2.1.3 Photoelectrochemical system at 10 Sun

For the purpose of large-scale, distributed solar-to-fuel applications, cell designs that utilize a low-multiple concentrating solar collector, such as a 10× concentrator, are of particular interest. These designs can have high operating current densities without requiring active solar tracking or temperature-regulation systems.[26,27] In Chapter IV, two designs for an integrated photoelectrolysis system that uses a 10× concentrating solar collector have been investigated in detail. The system performance was evaluated using a multi-physics model that accounted for the properties of the tandem photoabsorbers, mass transport, and the electrocatalytic performance of the oxygen-evolution and hydrogen-evolution reactions (OER and HER, respectively). The solar-to-hydrogen (STH) conversion efficiencies and the ohmic losses associated with proton transport in the solution electrolyte and through the membrane of the photoelectrolysis system were evaluated systematically as a function of the cell dimensions, the operating temperatures, the bandgap combinations of the tandem cell, and the performance of both the photoabsorbers and electrocatalysts. Relative to designs of optimized systems that would operate without a solar concentrator, the optimized 10× solar concentrator designs possessed larger ohmic losses and exhibited less uniformity in the distribution of the current density along the width of the photoelectrode.

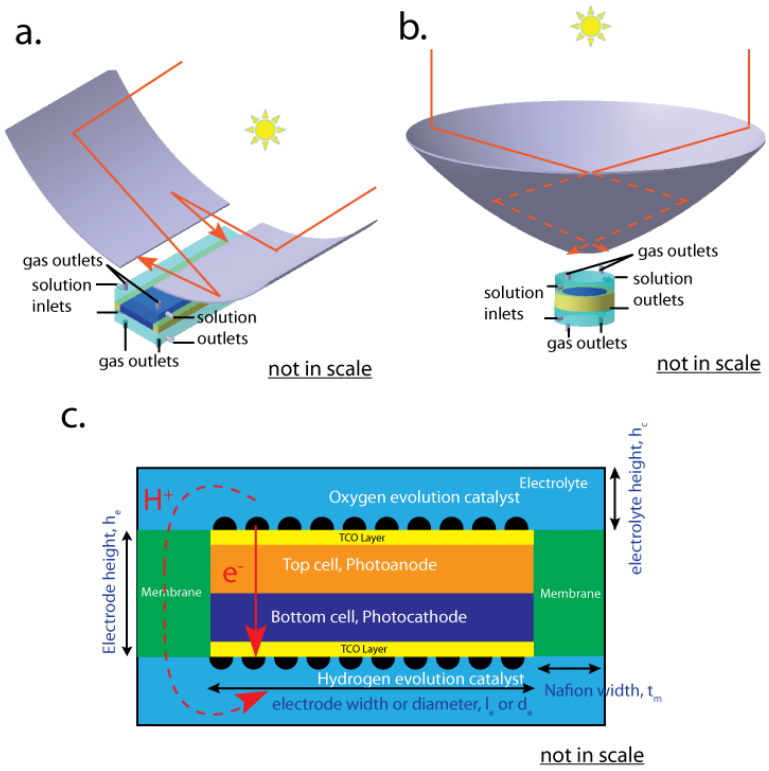

Figure 1.13: Schematic illustrations of two designs for a 10× concentrator photoelectrolysis system: a) a two-dimensional "trough" design and b) a three-dimensional "bubble wrap" design. Both designs contain a solar concentrator (grey) and an integrated photoelectrolysis assembly. The orange lines schematically indicate selected ray traces of the light path that concentrates the sunlight. c) Cross-sectional illustration of an integrated photoelectrolysis system, which includes a photoanode (orange), a photocathode (purple), TCO layers (yellow), oxygen-evolution catalysts (top black hemispheres), hydrogen-evolution catalysts (bottom black hemispheres), Nafion films (green) and solution electrolyte (blue). The electronically conductive pathways occur from the oxygen-evolution catalysts through the TCO, the top cell, the bottom cell, and the second TCO, to the hydrogen-evolution catalysts (solid arrow). The main ionically conductive pathways (dashed arrows), that produce the predominant ohmic drop in the system, occur laterally from the oxygen-evolution catalysts (that are the site of proton production during current flow) in the top electrolyte to and through the surrounding membrane, and laterally in the bottom electrolyte to the hydrogen-evolution catalysts (that are the sites of proton consumption during current flow).

To minimize resistive losses while maximizing the solar-to-hydrogen conversion efficiency, η_{STH}, both of the designs, a two-dimensional "trough" design (Figure 1.13a) and a three-dimensional "bubble wrap" design (Figure 1.13b), required that the electrode width or diameter, respectively, was no larger than a few millimeters. As the size of the electrodes increased beyond this limiting dimension, the η_{STH} became more sensitive to the performance of the photoabsorbers and catalysts. At a fixed electrode dimension, increases in the operating temperature reduced the efficiency of cells with smaller electrodes, due to degradation in the performance of the photoabsorber with increasing temperature. In contrast, cells with larger electrode dimensions showed increases in efficiency as the temperature increased, due to increases in the rates of electrocatalysis and due to enhanced mass transport. The simulations indicted that cells that contained 10% photoabsorber area, and minimal amounts of Nafion or other permselective membranes (i.e. areal coverages and volumetric fractions of only a few percent of the cell), with the remaining area comprised of a suitable, low-cost inert, non-porous material (flexible polymers, inert inorganic materials, etc.) should be able to produce high values of η_{STH}, with η_{STH} = 29.8% for an optimized design with a bandgap combination of 1.6 eV/0.9 eV in a tandem photoabsorber system at 350 K.

1.2.1.4 Bubble effect on the performance of gas evolution electrodes

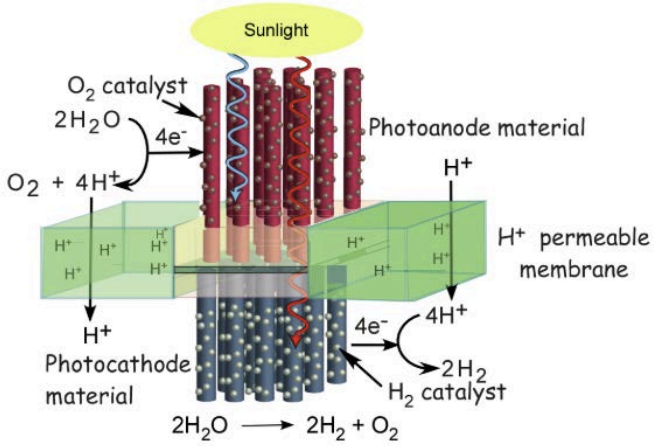

Figure 1.14: Schematic illustration of an integrated photoelectrochemical water-splitting system with microwire arrays. Credit: Reused with permission from JCAP/Caltech

In an integrated photoelectrochemical water-splitting system, hydrogen and oxygen are continuously being produced in the cathodic and anodic chamber, respectively, as seen in Figure 1.14. Gas evolution is vital to the system performance, especially under high current densities. Chapter V presents a numerical approach to explore the impact of gas evolution on the planar electrodes as well as microwire arrays. Such an impact can mainly be broken into three parts: local reversible hydrogen electrode potential shift, hyperpolarization, and the increase of electrolyte solution resistance. Local reversible hydrogen electrode potential shift plays the most important role here, it takes up more than 40% of the total potential drop between the cathode and reference electrode, following correction for cell resistance. Microwire array structure will help reduce the impact of bubbles on the solution conductance, but its influence on the local reversible hydrogen electrode potential shift varies locally on the electrode surface.

1.2.2 Solar-driven CO_2 reduction system

1.2.2.1 Operational constraints and strategies

Development of a sustainable, solar-driven CO_2 reduction system is still in the proof-of-concept stage, and faces significant challenges both in fundamental materials discovery and engineering designs of cell and system architectures. Despite the lack of active, selective and stable electrocatalysts for the CO_2 reduction reaction (CO_2RR), it is important to understand the operational constraints and attainable system efficiencies based on the CO_2 mass transport properties from the atmosphere towards the electrode surface for atmospheric cell operation. In Chapter VI, two strategies that could significantly enhance the CO_2 transport and increase the steady-state limiting current density at p_{CO2} = 400 ppm have been described. Additionally, the transport limitations of CO_2 from the tropopause down to the cathode surface, through five different regions with five different length scales (from tens of nanometers to tens of kilometers) have also been analytically evaluated, in order to understand the transport limitations of the CO_2RR for a system that might eventually be deployed at global scale.

$CO_2 + H_2O \underset{k_{1-}}{\overset{k_{1+}}{\rightleftharpoons}} H^+ + HCO_3^-$	k_{1+}=0.037 s^{-1} k_{1-}=7.83x10^4 M^{-1} s^{-1}
$CO_2 + OH^- \underset{k_{2-}}{\overset{k_{2+}}{\rightleftharpoons}} HCO_3^-$	k_{2+}=2.23x10^3 M^{-1} s^{-1} k_{2-}=4.85x10^{-5} s^{-1}
$HCO_3^- \underset{k_{3-}}{\overset{k_{3+}}{\rightleftharpoons}} H^+ + CO_3^{2-}$	k_{3+}=2.5 s^{-1} k_{3-}=5x10^{-10} M^{-1} s^{-1}
$HCO_3^- + OH^- \underset{k_{4-}}{\overset{k_{4+}}{\rightleftharpoons}} H_2O + CO_3^{2-}$	k_{4+}=6x10^9 M^{-1} s^{-1} k_{4-}=1.2 s^{-1}

Table 1.2: The chemical reactions occurring inside the bicarbonate solution and their corresponding forward and backward rate constants.

The operational constraints for a 6-electron/6-proton CO_2 reduction system, as shown in Table 1.2, that operates at the concentration of CO_2 in the current atmosphere (p_{CO_2} = 400 ppm) have been evaluated on a variety of scale lengths that span from laboratory scale to global scale. Due to the low concentration of CO_2 in the atmosphere, limitations due to mass transport of CO_2 from the tropopause have been evaluated through five different regions, each with different characteristic length scales: the troposphere; the atmospheric boundary layer (ABL); the canopy layer; a membrane layer; and an aqueous electrolyte layer. The resulting CO_2 conductance, and associated physical transport limitations, will set the ultimate limit on the efficiency and areal requirements of a sustainable solar-driven CO_2 reduction system regardless of the activity or selectivity of catalysts for reduction of CO_2 at the molecular level. At the electrolyte/electrode interface, the steady-state limiting current density and the concomitant voltage loss associated with the CO_2 concentration overpotential in a one-dimensional solar-driven CO_2 reduction cell have been assessed quantitatively using a mathematical model that accounts for diffusion, migration and convective transport, as well as for bulk electrochemical reactions in the electrolyte. At p_{CO2} = 400 ppm, the low diffusion coefficient combined with the low solubility of CO_2 in aqueous solutions constrains the steady-state limiting current density to <0.1 mA cm^{-2} in a typical electrochemical cell with

natural convection and employing electrolytes with a range of pH values. Hence, in such a system, the CO_2 capture area must be 100- to 1000-fold larger than the solar photon collection area to enable a >10% efficient solar-driven CO_2 reduction system (based on the solar collection area). This flux limitation is consistent with estimates of oceanic CO_2 uptake fluxes that have been developed in conjunction with carbon-cycle analyses for use in coupled atmosphere/ocean general circulation models. Two strategies to improve the feasibility of obtaining efficient and sustainable CO_2 transport to a cathode surface at p_{CO_2} = 400 ppm are described and modeled quantitatively. The first strategy employs yet unknown catalysts, analogous to carbonic anhydrases, that dramatically accelerate the chemically enhanced CO_2 transport in the aqueous electrolyte layer by enhancing the acid–base reactions in a bicarbonate buffer system. The rapid interconversion from bicarbonate to CO_2 in the presence of such catalysts near the cathode surface would in principle yield significant increases in the steady-state limiting current density and allow for >10% solar-fuel operation at the cell level. The second strategy employs a thin-layer cell architecture to improve the diffusive transport of CO_2 by use of an ultrathin polymeric membrane electrolyte. Rapid equilibration of CO_2 at the gas/electrolyte interface, and significantly enhanced diffusive fluxes of CO_2 in electrolytes, are required to increase the steady-state limiting current density of such a system. This latter approach however only is feasible for gaseous products, because liquid products would coat the electrode and therefore thicken the hydrodynamic boundary layer and accordingly reduce the diffusive CO_2 flux to the electrode surface. Regardless of whether the limitations due to mass transport to the electrode surface are overcome on the laboratory scale, at global scales the ultimate CO_2 flux limitations will be dictated by mass transport considerations related to transport of atmospheric CO_2 to the boundary plane of the solar-driven reactor system. The transport of CO_2 across the troposphere/ABL interface, the ABL/canopy layer interface, and the canopy layer/electrolyte interface have therefore been assessed, to provide upper bounds on the ultimate limits for the solar-to-fuel (STF) conversion efficiency for systems that are intended to effect the reduction of atmospheric CO_2 in a sustainable fashion at global scale.

1.2.2.2 Spatial and light intensity dependence of product distributions in an integrated PEC CO_2 reduction cell

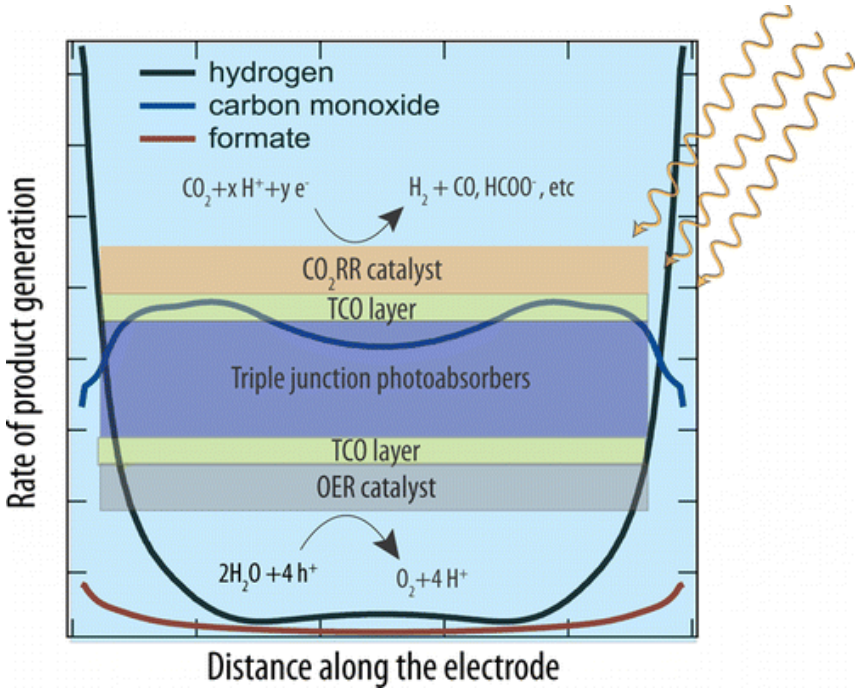

Figure 1.15: Schematic illustration of an integrated PEC CO_2 reduction cell.

It is noted that in a full photoelectrochemical CO_2 reduction cell, product distribution varies along the electrode surface, as seen in Figure 1.15. Chapter VII will discuss this scenario in detail.

A multi-physics model that accounts for the performance of the electrocatalysts and light absorbers, as well as for the transport properties of the electrolyte and dissolved CO_2, was used to evaluate the spatial distribution of the CO_2 reduction products in the cell. The product distribution variation along the electrode surface was evaluated for two exemplary catalysts, metallic Ag and Cu, respectively. The product distribution was additionally compared that obtained in a three-electrode experiment under potentiostatic conditions in which the working electrode comprised a nearly equipotential surface. The maximum power point of the light absorbers determined the optimal current density of the overall reaction, J_{total}, but

this operating condition did not generally result in an optimized partial current density for the CO_2 reduction reaction (CO_2RR), J_{CO2}. Hence, in a tandem photoconversion device, the band-gap combinations that produced an optimum J_{CO2} were substantially different than the band-gap combinations that produced an optimum J_{total}. Even in a 1-dimensional, face-to-face cell architecture, in which the cathode was nearly an equipotential surface under a specific illumination intensity, the relative percentage of CO_2RR products produced by the exemplary electrocatalysts varied substantially as the illumination intensity was varied. In an integrated, 2-dimensional PEC cell architecture, the product distribution varied along the width of the electrode, due to spatially non-uniform transport losses in conjunction with the dependence of the faradaic efficiency on electrode potential. The integrated partial current density for the CO_2RR was thus a function of the illumination intensity as well as the geometric dimensions of the cell. To achieve the same product selectivity as in a potentiostatic, "half-cell" configuration, the electrocatalyst must retain its selectivity over a range of cathode potentials in an integrated, 2-dimensional PEC cell architecture, and this range is dependent on the transport losses and current-voltage relation of the light absorbers, the geometric parameters of the cell, the illumination intensity, and the behavior of the electrocatalysts for the oxygen-evolution reaction (OER).

1.2.2.3 Planar electrode vs. GDE

Electrochemical CO_2 or CO reduction,as listed in Table 1.3, is often performed in aqueous electrolytes, such as bicarbonate or carbonate solutions. The low solubility of CO_2 and CO in aqueous solutions, in conjunction with the values of the liquid-phase diffusion coefficients of CO_2 and CO, consequently constrains the attainable current densities for CO_2 or CO reduction. One approach to increasing the operating current density of the electrode is to substantially reduce the thickness of the boundary layer.[28] Gas-diffusion electrodes (GDEs) provide an opportunity to effectively reduce the boundary-layer thickness to hundreds of nanometers.

$H_2O \underset{k_{1b}}{\overset{k_{1f}}{\rightleftarrows}} H^+ + OH^-$	$k_{1f} = 10^8\ s^{-1}$ $k_{1b} = 10^{19}\ M^{-1}\ s^{-1}$
$H_3PO_4 \underset{k_{2b}}{\overset{k_{2f}}{\rightleftarrows}} H_2PO_4^- + H^+$	$k_{2f} = 10^7\ s^{-1}$ $k_{2b} = 1.32\text{x}10^9\ M^{-1}\ s^{-1}$
$H_2PO_4^- \underset{k_{3b}}{\overset{k_{3f}}{\rightleftarrows}} HPO_4^{2-} + H^+$	$k_{3f} = 10^7\ s^{-1}$ $k_{3b} = 1.62\text{x}10^{14}\ M^{-1}\ s^{-1}$
$HPO_4^{2-} \underset{k_{4b}}{\overset{k_{4f}}{\rightleftarrows}} PO_4^{3-} + H^+$	$k_{4f} = 10^7\ s^{-1}$ $k_{4b} = 4.68\text{x}10^{19}\ M^{-1}\ s^{-1}$
$CO_2 + H_2O \underset{k_{5f}}{\overset{k_{5b}}{\rightleftarrows}} H^+ + HCO_3^-$	$k_{5f} = 0.036\ s^{-1}$ $k_{5b} = 7.83\text{x}10^4\ M^{-1}\ s^{-1}$
$CO_2 + OH^- \underset{k_{6b}}{\overset{k_{6f}}{\rightleftarrows}} HCO_3^-$	$k_{6f} = 2.23\text{x}10^3\ M^{-1}\ s^{-1}$ $k_{6b} = 4.85\text{x}10^{-5}\ s^{-1}$
$HCO_3^- \underset{k_{7b}}{\overset{k_{7f}}{\rightleftarrows}} H^+ + CO_3^{2-}$	$k_{7f} = 2.5\ s^{-1}$ $k_{7b} = 5\text{x}10^{10}\ M^{-1}\ s^{-1}$
$HCO_3^- + OH^- \underset{k_{8b}}{\overset{k_{8f}}{\rightleftarrows}} H_2O + CO_3^{2-}$	$k_{8f} = 6\text{x}10^9\ M^{-1}\ s^{-1}$ $k_{8b} = 1.2\ s^{-1}$

Table 1.3: The chemical reactions occurring inside the bicarbonate with phosphate buffer solution and their corresponding forward and backward rate constants.

A flow-through gas diffusion electrode (GDE) consisting of agglomerate catalysts for CO or CO_2 reduction, gas channels for reactants, aqueous electrolytes for ionic transport, and metallic current collectors is shown in Figure 1.16. The geometric partial current densities and Faradaic Efficiencies (FE) for CH_4, C_2H_4 and H_2 generation in GDEs is much higher, compared to the behavior of analogous aqueous-based planar electrodes. The pH-dependent kinetics for CH_4 and C_2H_4 generation can represent the intrinsic catalytic characteristics for the agglomerate catalyst. It is indicated that relative to planar electrodes for either CO reduction (COR) or CO_2 reduction (CO_2R), substantial increases in electrochemical reduction rates and Faradaic efficiencies are expected when flow-through GDEs are used.

For CO_2 reduction, substantial loss of CO_2 via chemical reaction with the locally alkaline electrolyte was observed due to the increased pH in operating GDEs. Further details will be discussed in Chapter VIII.

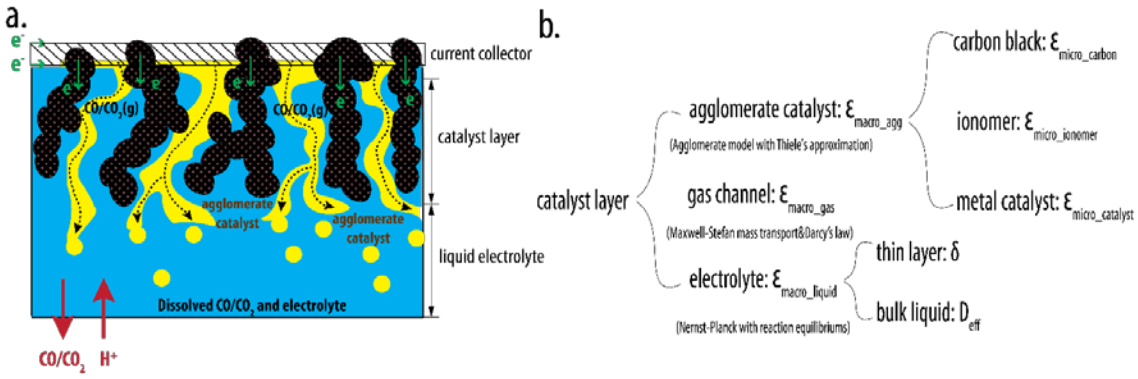

Figure 1.16: (a) A schematic illustration of a flow through gas diffusion electrode (GDE). (b) A schematic illustration of the catalyst layer containing an agglomerate catalyst, gas channel, and aqueous electrolyte.

REFERENCES:

1. R. K. Pachauri and L. A. Meyer. *Climate Change 2014: Synthesis Report. Contribution of Working Groups I, II and III to the Fifth Assessment Report of the Intergovernmental Panel on Climate Change.* Report. 2015.

2. https://climate.nasa.gov/evidence/

3. P. Murphy. *Solar Update, in Solar Heating and Cooling Programme.* Report. International Energy Agency: USA, 2009.

4. P. Murphy. *Solar Update, in Solar Heating and Cooling Programme.* Report. International Energy Agency: USA, 2015.

5. M. G. Walter, E. L. Warren, J. R. McKone, S. W. Boettcher, Q. X. Mi, E. A. Santori, N. S. Lewis *Chem. Rev.* **2010**, 110, 6446-6473.

6. N. S. Lewis, D. G. Nocera *P Natl Acad Sci USA*. **2007**, 104, 20142-20142.

7. S. W. Boettcher, J. M. Spurgeon, M. C. Putnam, E. L. Warren, D. B. Turner-Evans, M. D. Kelzenberg, J. R. Maiolo, H. A. Atwater, N. S. Lewis *Science*. **2010**, 327, 185-187.

8. K. Keis, E. Magnusson, H. Lindstrom, S. E. Lindquist, A. Hagfeldt *Sol Energ Mat Sol C*. **2002**, 73, 51-58.

9. G. M. Wang, H. Y. Wang, Y. C. Ling, Y. C. Tang, X. Y. Yang, R. C. Fitzmorris, C. C. Wang, J. Z. Zhang, Y. Li *Nano Lett.* **2011**, 11, 3026-3033.

10. A. Paracchino, V. Laporte, K. Sivula, M. Gratzel, E. Thimsen *Nat Mater*. **2011**, 10, 456-461.

11. A. B. Murphy, P. R. F. Barnes, L. K. Randeniya, I. C. Plumb, I. E. Grey, M. D. Horne, J. A. Glasscock *Int J Hydrogen Energ*. **2006**, 31, 1999-2017.

12. K. Sivula, R. Zboril, F. Le Formal, R. Robert, A. Weidenkaff, J. Tucek, J. Frydrych, M. Gratzel *J Am Chem Soc*. **2010**, 132, 7436-7444.

13. D. K. Zhong, J. W. Sun, H. Inumaru, D. R. Gamelin *J Am Chem Soc*. **2009**, 131, 6086-+.

14. Q. X. Mi, A. Zhanaidarova, B. S. Brunschwig, H. B. Gray, N. S. Lewis *Energ. Environ. Sci.* **2012**, 5, 5694-5700.

15. J. M. Spurgeon, J. M. Velazquez, M. T. McDowell *Phys. Chem. Chem. Phys.* **2014**, 16, 3623-3631.

16. O. Khaselev, J. A. Turner *Science*. **1998**, 280, 425-427.

17. S. Y. Reece, J. A. Hamel, K. Sung, T. D. Jarvi, A. J. Esswein, J. J. H. Pijpers, D. G. Nocera *Science*. **2011**, 334, 645-648.

18. R. E. Rocheleau, E. L. Miller, A. Misra *Energ Fuel*. **1998**, 12, 3-10.

19. K. Fujii, S. Nakamura, M. Sugiyama, K. Watanabe, B. Bagheri, Y. Nakano *Int. J. Hydrogen Energy*. **2013**, 38, 14424-14432.

20. S. Licht, B. Wang, S. Mukerji, T. Soga, M. Umeno, H. Tributsch *J. Phys. Chem. B*. **2000**, 104, 8920-8924.

21. N. A. Kelly, T. L. Gibson *Int. J. Hydrogen Energy*. **2006**, 31, 1658-1673.

22. B. Seger, T. Pedersen, A. B. Laursen, P. C. K. Vesborg, O. Hansen, I. Chorkendorff *J. Am. Chem. Soc.* **2013**, 135, 1057-1064.

23. F. F. Abdi, L. H. Han, A. H. M. Smets, M. Zeman, B. Dam, R. van de Krol *Nat Commun*. **2013**, 4.

24. F. Zhu, J. Hu, I. Matulionis, T. Deutsch, N. Gaillard, A. Kunrath, E. Miller, A. Madan *Philos Mag*. **2009**, 89, 2723-2739.

25. E. S. Smotkin, S. Cerveramarch, A. J. Bard, A. Campion, M. A. Fox, T. Mallouk, S. E. Webber *J Phys Chem-Us*. **1987**, 91, 6-8.

26. R. Winston, J. C. Miñano and P. G. Benitez, *Nonimaging optics*, Academic Press, 2005.

27. J. J. O'Gallagher, *Synthesis Lectures on Energy and the Environment: Technology, Science, and Society*, 2008, **2**, 1-120.

28. A. J. Bard and L. R. Faulkner, *Electrochemical Methods: Fundamentals and Applications, 2nd Edition*, 2000.

Chapter II

A SENSITIVITY ANALYSIS TO ASSESS THE RELATIVE IMPORTANCE OF IMPROVEMENTS IN ELECTROCATALYSTS, LIGHT ABSORBERS, AND SYSTEM GEOMETRY ON THE EFFECIENCY OF SOLAR -FUELS GENERATORS

2.1 Introduction

Most concepts for a solar-fuels generators include components for light absorption and charge separation, electrocatalysts for one or both of the half-reactions involved in the production of fuels from H_2O or from H_2O and CO_2, and a membrane or other physical separation barrier to ensure separation of the products.[1-3] All of these envisioned system components are the basis for active areas of research, with the goal of improving the activity, stability, and mutual compatibility of the various components for use in a fully operational, efficient, robust, intrinsically safe, scalable, demonstration of a solar-fuels generator.[1-11]

In the discipline of systems engineering, a sensitivity analysis is a routine, critical tool to identify the main levers, i.e. the components of the system for which improvements in performance will have the most impact on improving the performance of the system as a whole.[12] In general, a sensitivity analysis can only beneficially be performed when a system design is in hand, because the architecture of the system will play a significant, if not dominant, role in the outcome, and will determine the inputs and outputs of the system-based sensitivity analysis. For example, different sensitivity analyses would be needed to ascertain the key levers in optimizing the flight speed or flight time of a jet-powered, fixed-wing aircraft relative to optimizing the speed or flight time of a helicopter.

This chapter is based on results in: Yikai Chen, Shu Hu, Chengxiang Xiang and Nathan S. Lewis, Energy Environ. Sci., 2015, 8, 876-886 – Published by The Royal Society of Chemistry.

The theoretical, and practically realizable, efficiencies of a solar-driven water-splitting device based on theoretical materials properties, or on current state-of-the-art materials and components, have not been presented in the literature for a specific system design concept in hand.[13, 14 15] Recently, several generic systems-level concepts for solar-fuels generators have been presented[16-20] in sufficiently specific detail to enable a meaningful sensitivity analysis to identify the key levers that will produce the largest performance improvements within the overall design space of the systems of interest. The state-of-the-art performance values of many classes of electrocatalysts for key reactions of interest, including the hydrogen-evolution reaction (HER), the oxygen-evolution reaction (OER), and possible CO_2-reduction reactions (CO_2RR), have also recently been compiled and documented.[11, 21, 22] Additionally, the state-of-the-art performance of individual light absorbers, as well as the performance of combinations of light absorbers for use in tandem structures, have been recently reviewed.[1] Extensive modeling and simulation efforts, using validated multi-physics modeling approaches, have also been performed recently on a variety of system geometries and for a variety of operating temperatures, illumination intensities, and optical concentration factors.[16-20]

We report herein a "one factor at a time" sensitivity analysis[23-25] for several types of generic designs of solar-fuels generators. In this study, the sensitivity of the efficiency of the generation of solar fuels to the properties of the various system components was evaluated as a function of the total overpotential of the electrocatalysts for a variety of light absorbers having a range of band gaps and having varying materials quality. An additional sensitivity analysis has been performed to determine the key levers for improving the efficiency of solar-fuels generation over a range of operating temperatures and under concentrated illumination. The sensitivity analysis clearly shows the extent to which improvements, relative to the state-of-the-art, in the overpotential of the electrocatalysts, in the system geometry and design, in the properties of the light absorbers, and in the properties of the membranes will provide gains in overall attainable system efficiency. In this respect, the sensitivity analysis serves to survey the possible system design space and

highlights areas that will have the largest impact on improving the performance of the system as a whole.

2.2 Modeling

2.2.1 Device designs

The generic design of the solar-driven water-splitting device investigated herein contained a photoabsorber component, electrocatalyst layers for the OER and for the HER, a membrane separator, and liquid electrolytes. The generic design includes several specific cell constructs. The detailed geometric parameters of these cell constructs have been described previously.[16-18, 20] The photoabsorber component contained a tandem-junction photoelectrochemical cell, in which 100% of the incident solar photon flux arrives at the photoabsorber surface in either an unconcentrated, planar design or in a concentrated design coupled with a 10x optical solar concentrator. The optical obscuration due to the liquid electrolyte, electrocatalyst layers, and membrane separators were neglected in the calculation. The OER and HER electrocatalyst layers were located directly on the top and the bottom of the anode and cathode sides of the photoabsorber component, respectively, in which the geometric surface area of the HER catalyst and OER catalyst were identical and were bounded to the geometric area of the tandem photoabsorber. The membrane separator was employed to provide the required ion-transport pathways between the cathode and anode compartments as well as to provide effective barriers to the crossover of products. The liquid electrolyte contained strong acid or strong base (e.g., 1 M H_2SO_4(aq) or 1 M KOH(aq)), which produced negligible pH gradients at the surfaces of the electrocatalysts under operating conditions. The transport of ions through the membrane and in the liquid electrolyte was the source of any additional resistive losses in the device.

Although other solar-fuel generators, e.g., CO_2-reduction reactors, contain some components in common with the solar-driven water-splitting device described above, the specific cell designs and operational constraints of a CO_2-reduction reactor could vary significantly from those of a water-splitting reactor, due to different system-level constraints.

Moreover, depending on the specific reduction products, the thermodynamic potentials for other fuel-forming reactions can vary significantly from those of water splitting. Thus, the modeling and simulation results and associated sensitivity analysis described herein are only explicitly directed towards, and applicable, to solar-driven water-splitting systems of the general design classes evaluated herein.

2.2.2 Solar-to-hydrogen (STH) conversion efficiency

The operating current density, J_{op}, of an integrated set of light absorbers arranged in a tandem configuration was calculated by the following equation:

$$V_{op}(J_{op}) = \boldsymbol{\phi_0} + \eta_{OER}(J_{op}) + \left|\eta_{HER}(J_{op})\right| + R_{eff}\ (J_{op}) \quad \text{(Eq. 2.1)}$$

where $V_{op}(J_{op})$ is the current-voltage relationship of the tandem photoabsorbers, $\boldsymbol{\phi_0}$ is the thermodynamic potential for the water-splitting reaction, R_{eff} is the effective transport resistance in the membrane separator and the liquid electrolyte, and $\eta_{OER}(J_{op})$ and $\eta_{HER}(J_{op})$ are the overpotentials for the OER and HER, respectively.

The STH conversion efficiency, η_{STH}, is defined as:

$$\Phi_{STH} = \frac{1.23\ (V) \times J_{op}\ (mA\ cm^{-2})}{S\ (mW\ cm^{-2})} \quad \text{(Eq. 2.2)}$$

with J_{op} the operating photocurrent density (mA cm^{-2}) and S the total incident solar irradiance (mW cm^{-2}).

2.2.3 Shockley-Queisser limit for light absorbers

The ideal limiting case, i.e. the Shockley-Queisser (S-Q) limit, in which the current-voltage relationship for a tandem photoabsorber is determined by use of a detailed-balance calculation, is obtained when the current density at the operating photovoltage is equal to the sum of the incident solar radiation (J_{ph}) and the thermal radiation (J_{th}) minus the radiative emission (J_{rad}):[26]

$$J = J_{ph} + J_{th} - J_{rad} \quad \text{(Eq. 2.3)}$$

J_{ph}, J_{th} and J_{rad} were determined by:[26]

$$J_{ph} = C \times e \int_{\mathbf{E}_g}^{\infty} \mathrm{d}\hbar\omega\ \frac{\Lambda}{\mathrm{d}\hbar\omega}, \quad \text{(Eq. 2.4)}$$

$$J_{rad} = \frac{e(n_{top}^2+n_{bottom}^2)}{4\,\pi^2 c^2}\int_{\mathbf{E}_g/\hbar}^{\infty} \omega^2 \exp\left(\frac{eV-\hbar\omega}{kT}\right)\mathrm{d}\omega \ , \qquad \text{(Eq. 2.5)}$$

$$\text{and } J_{th} = \frac{e(n_{top}^2+n_{bottom}^2)}{4\,\pi^2 c^2}\int_{\mathbf{E}_g/\hbar}^{\infty} \omega^2 \exp\left(-\frac{\hbar\omega}{kT}\right)\mathrm{d}\omega \ . \qquad \text{(Eq. 2.6)}$$

where e is the unsigned charge on an electron, Λ is the wavelength-dependent solar flux in the Air Mass (AM)1.5 solar spectrum, $\hbar$ is an abbreviation for $h/2\pi$ with h being Planck's constant, ω is the frequency of the incident light, n_{top} and n_{bottom} are the refractive indices of the top and the bottom of the tandem absorber, T and V are the operating temperature and the operating voltage, respectively, and $\mathbf{E}_g$ is the band gap of the top or bottom light absorber, as indicated by the appropriate subscript.

Several approaches have been proposed to effectively utilize even highly optically absorbing electrocatalysts in solar fuels generators, including deposition of catalysts on the back side of the structure to reflect light back into the absorbers, deposition of catalysts along the surfaces or at the bases of microwire arrays to reflect light into the internal volume of the light-absorber structure, or deposition of catalysts in pre-determined islands on planar photoelectrode structures to minimize obscuration.[27-31] Any optical obscuration by the electrocatalysts would lower all of the efficiencies calculated herein by approximately the ratio of transmitted light to the light reflected outside of the specific light-absorber structure of concern. A more specific analysis of the variation of efficiency with light intensity has been performed separately for several specific system geometries.[17]

The numerical relationship between the current density and voltage obtained from the Shockley-Queisser model was fitted using the ideal diode relationship:

$$J = J_{ph} - J_0\left[\exp\left(\frac{eV}{\gamma kT}\right) - 1\right] \qquad \text{(Eq. 2.7)}$$

where J_0 is the reverse saturation current density and γ is the diode ideality factor. In the sensitivity analysis, the value of J_{ph} was not changed for a given light absorber, because J_{ph} is given by the relationship between the wavelength-dependent absorption behavior of the semiconductor and the spectral irradiance of incident sunlight, as expressed by eq (2.4-2.6).

In contrast, the value of J_o was increased by as much as 21 orders of magnitude from the Shockley-Queisser limit, to account for a range of materials properties of the light absorbers of interest. This variation in J_o produced lower open-circuit voltages for a given light absorber at a given value of J_{ph}, with the relationship between J_o and V_{oc} given explicitly by eq (2.7).

2.2.4 Behavior of electrocatalysts, membrane separator and solution electrolyte

The current density, $i_{OER/HER}$ as a function of the overpotential, η, for the OER and HER can be described by the Butler-Volmer equation:[32]

$$i_{OER/HER} = i_{0,OER/HER}[\exp(\frac{\alpha_{a,OER/HER}F}{RT}) - \exp(-\frac{\alpha_{c,OER/HER}F\eta}{RT})] \quad \text{(Eq. 2.8)}$$

where $i_{0,OER/HER}$ is the exchange-current density for OER or HER, respectively, and $\alpha_{a,OER/HER}$ and $\alpha_{c,OER/HER}$ are the anodic and cathodic transfer coefficients for the OER or the HER, respectively. Note that use of the Butler-Volmer equation to describe the overpotential of the electrocatalysts as a function of current density produces a different overvoltage at each current density in the operational system, as opposed to assuming a fixed voltage drop for a given set of light absorbers independent of whether the system is operating at open-circuit (no current passed), at the light-limited current density, at the maximum power point of the system, or with additional ohmic resistance drops due to the cell design.

The exchange-current density for the OER or the HER is dependent on temperature, and was calculated using:

$$i_{0,T,OER/HER} = i_{0,T_{ref},OER/HER}\exp(\frac{E_{a,OER/HER}}{RT_{ref}})\exp(-\frac{E_{a,OER/HER}}{RT}), \quad \text{(Eq. 2.9)}$$

where $E_{a.OER/HER}$ is the activation energy for the OER or HER, respectively, $i_{0,T_{ref},OER/HER}$ is the exchange-current density for the OER or HER, respectively, at the reference temperature. $E_{a,OER/HER}$ was set to 42560 J mol^{-1} and 28900 J mol^{-1} for iridium oxide and platinum catalysts, respectively, in 1 M H_2SO_4(aq).[33]

The behavior of each electrocatalyst and of each anodic/cathodic electrocatalyst system was described by reference to a figure-of-merit, $\eta_{overpotential}^{10\ mA\ cm^{-2}}$, which specified the overpotential required by that electrocatalyst (or electrocatalyst system) on an otherwise ideally nonpolarizeable electrode (or anode and cathode combination) to provide a current density of 10 mA cm^{-2}. This figure-of-merit allowed for a concise description of the relevant Butler-Volmer properties of the electrocatalysts according to eq (2.8) and (2.9).

The temperature dependence of the effective transport resistance, R_{eff}, was defined as:

$$R_{eff,T} = \frac{R_{eff,ref}}{(1+\alpha[T-T_{ref}])}, \qquad \text{(Eq. 2.10)}$$

where the reference temperature, T_{ref}, is 300 K and the coefficient α was taken to be 0.019 K^{-1}, by fitting the experimental data for 1.0 M sulfuric acid.[34]

Based on eq (2.1–2.10), a zero-dimensional (0-D) analysis of the STH conversion efficiency was obtained, in which the tandem photoabsorbers, electrocatalysts, liquid electrolyte and membrane separators were coupled in series and the optical absorption, photo-carrier transport and ionic transport were coupled in parallel. The electrode surfaces were assumed to be isopotential surfaces, and the spatial inhomogeneity of the current-density distribution along the electrodes was approximated by the use of a 0-D effective transport resistance. Note that while the 0-D load-line analysis captures the key performance characteristics of an integrated photoelectrolysis system, the detailed device construct and geometrical parameters, and their influence on the current density and potential distribution in an actual three-dimensional operating system, are not elucidated in such an analysis.

The 0-D current-voltage model could also be employed to evaluate η_{STH} for a system constructed using a discrete photovoltaic device connected in series to a discrete

electrolyzer (PV+electrolyzer), in which the efficiencies of the photovoltaic device and of the electrolyzer were optimized independently. A comparison between the dependence on temperature and illumination intensity dependence of η_{STH} for an integrated photoelectrochemical system and for a stand-alone PV+electrolyzer system has been described previously.[17] The low resistive loss due to a lower operating current density in the integrated system, or "distributed internal electrolyzer", especially at low illumination intensities, and the enhanced kinetics and transport at elevated temperatures in the integrated designs are the main reason that an integrated system outperformed a stand-alone PV+electrolyzer system under the conditions evaluated in that work.

2.3 Results and discussion

2.3.1 State-of-the-art component properties

a) Electrocatalysts

The polarization behavior for the overall water-splitting process is dependent on the combined interfacial kinetics of the HER for the OER catalysts.[32] A reduction in the overpotential for the HER and/or for the OER has been one of the major research goals of electrocatalyst development.[21] Some of the most active electrocatalysts reported to date operate in aqueous alkaline media, including Ni-Mo alloys for the HER (overpotential of 75 mV at 10 mA cm^{-2} with a Tafel slope of 40 mV/dec) and (Fe-Ni)O_x alloys for the OER (overpotential of 280 mV at 10 mA cm^{-2} with a Tafel slope of 40 mV/dec).[35, 36] In acidic aqueous solutions, the state-of-the-art electrocatalysts for HER and OER contain noble metals and metal oxides, such as Pt and RuO_2, which operate at 55 mV and 270 mV overpotential at 10 mA cm^{-2} for the HER and OER, respectively[5, 37], although recent work with transition-metal phosphides has shown overpotentials for the HER that approach that of Pt.[38-40] Recent benchmarking work[21] has shown that in aqueous alkaline solutions, many active non-noble metal electrocatalysts for the OER exhibit mutually similar overpotentials, of between 350 mV and 430 mV, at an operating current density of 10 mA cm^{-2}. In addition, under acidic conditions, no reported active OER electrocatalyst is stable under anodic operational conditions except for IrO_x.[21]

The total kinetic overpotential, $\eta_{overpotential}^{10\ mA\ cm^{-2}}$, used to characterize the behavior of the electrocatalysts was the sum of the overpotentials for OER and HER at 10 mA cm^{-2}, and was dependent on the exchange-current density and the Tafel slopes for the OER and HER, all of which were varied systematically in this analysis. For example, the current-voltage relationship for the HER was fixed, and the exchange-current density for the OER, $i_{0,\,OER}$, was varied from 1.1×10^{-2} mA cm^{-2} to 1.1×10^{-46} mA cm^{-2}. This procedure resulted in total electrocatalyst overpotentials ranging from 194 mV to 1965 mV at the current density of 10 mA cm^{-2}. The total overpotential at 10 mA cm^{-2} of current density was a concise, useful figure-of-merit used herein to differentiate between, and identify, the various different electrocatalyst combinations, but the actual operating current densities of each tandem absorber/electrocatalyst combination in the operating system of interest were calculated individually for each system using the load-line analysis of Eq (1). Because the total overpotential is the important system-level quantity, the procedure used herein to designate and vary the behavior of the electrocatalysts was general for variation in either the exchange-current density of the OER or the HER, or both.

b) Light Absorbers

For light absorbers, a tandem structure can produce significantly higher solar energy-conversion efficiencies than a single-junction system. The optimal solar-to-hydrogen conversion efficiency is highly dependent on the combination of band gaps of the tandem light absorbers.[14, 19] For instance, under 1 Sun illumination with an Air Mass (AM) 1.5 solar spectrum, the optimal top/bottom semiconductor band-gap combination is 1.65 eV/0.95 eV, which could yield, at the detailed-balance limit, a solar-to-hydrogen conversion efficiency of 31.1% in a system using Pt and RuO_x electrocatalysts and an optimized system design that minimizes the solution resistance (0.1 ohm cm^{-2}).[19]

However, the discovery of stable and high-performing light-absorber materials that are comprised of earth-abundant elements and that have a band gap of ~ 1.6–1.8 eV has proven challenging. The reported energy-conversion efficiency and current-voltage performance of state-of-the-art light-absorber materials for the top cell, i.e., $BiVO_4$, FeO_x, and WO_3, are

far below the S-Q limit. Additionally, the band gaps of these materials are far from the ideal band gap for the top cell of a system. For instance, state-of-the art WO_3 prepared by electrodeposition or sputtering exhibits a solar energy-conversion efficiency of $\leq 1.3\%$ in contact with 1 M H_2SO_4(aq).[41, 42] The misalignment between the conduction band of the WO_3 and the Nernstian potential for the OER, as well as charge-carrier recombination at the surface and in the bulk, result in an open-circuit voltage, 650 mV, that is low considering the large band gap of WO_3 (2.6 –2.7 eV).[41, 42]

c) System Design Space

The detailed geometry of the cell construct, as well as the choice of the solution electrolyte, also can have a significant impact on the overall solar-to-hydrogen system efficiency.[18] Targeted geometric parameters for various types of cells, including a vapor-feed solar-driven water-splitting system and a 10x solar concentrator-assisted water-splitting system, have been explored in detail.[16, 20] The resistive loss, concentration overpotential and effects of electrodialysis of different electrolytes, including strong base/acid and buffered solutions has also been investigated.[43] When an optimal cell configuration and strongly acidic or alkaline electrolytes are employed, the average resistive loss in the membrane separator and solution electrolyte can be limited to less than 100 mV at an operational current density of 10 mA cm^{-2}.[17, 18] In this work, the effective transport resistance was set to 10 ohm cm^{-2}, which resulted in 100 mV potential loss at 10 mA cm^{-2}. These resistive losses were accounted for in the calculation of η_{STH} in this study, along with the kinetic overpotential losses due to the water-splitting reaction. The voltage losses were fixed relative to the band gap regardless of the actual system operating conditions,[14, 44] but instead, as given by eqs (1)-(10), the voltage losses were explicitly a function of the operating voltage and current, in conjunction with the current-dependent ohmic-based voltage losses and kinetically based electrocatalyst overpotential losses, in the specific system being evaluated.

The sensitivity analysis investigated herein is applicable to several specific device designs, including a “closed-sandwich” design where the photocathode and photoanode are

assembled back-to-back,[18] an "open-sandwich" design with suitable spectral-splitting in which the photocathode and photoanode are assembled side-by-side,[18] a one-dimensional "trough" design and two-dimensional "bubble-wrap" design for the photoelectrochemical cells coupled to solar concentrators,[16] and a membrane-enclosed, vapor-feed design.[20] The analysis is not applicable to device designs in which the geometric area of the electrolyzing components is significantly different from that of the light absorbers.

d) Membranes/Separators

Depending on the specific device designs, the permeability and conductivity of the membrane separator could impact the overall η_{STH} of the device. Ion transport through the separator is necessary and results in a resistive loss in the system. Nevertheless, many highly conductive polymers, e.g., Nafion (10 S m^{-1}), exhibit minimal resistive loss at 10 mA cm^{-2} in optimized device geometries.[17, 18] Another primary function of a membrane separator is to block the diffusive and convective crossovers for the product gases. In certain microstructured cell designs, η_{STH} is highly dependent on the permeability of the membrane materials.[45] Through use of a thick membrane separator (50 μm to 100 μm) and/or with an optimized cell geometry, the efficiency loss due to product crossover can be negligible.[17, 18, 45]

2.3.2 Optimal STH conversion efficiency at different total overpotentials

In the "one factor at a time" sensitivity analysis performed herein, the performance that can be obtained for various families of tandem light absorbers has been investigated in detail, with the families of tandem light absorbers designated either by operation at the S-Q limit or by containing various levels of defects that will degrade the photovoltage by increasing the J_o of the absorbers away from the S–Q limit. In this process, for a given set of electrocatalysts (denoted by their total overpotential at 10 mA cm^{-2} of current density, $\eta_{overpotential}^{10\ mA\ cm^{-2}}$, as a concise figure-of-merit descriptor, but not constrained to operate at 10 mA cm^{-2} in the actual system of interest), the band gaps of the tandem light absorbers were varied to ascertain the optimally performing tandem light-absorber combination for a given set of OER and HER electrocatalysts.

Hence, for a given set of electrocatalysts, the analysis identified the maximum system efficiency, $\eta_{STH,opt}$, that could be obtained through use of the set of light absorbers that were identified as optimal with those specific electrocatalysts. In addition, for that same specific set of electrocatalysts, the optimization process was repeated, and a separate tandem-absorber combination was identified to give the optimum system efficiency, but with the light absorbers having their photovoltage degraded by a specified amount from the S-Q limit, as described by an increased exchange- current density (and consequently decreased photopotential at constant charge-carrier injection level) for this separate set of tandem light absorbers. Thus, a different set of tandem light absorbers produced optimal system efficiencies for each specified combination of electrocatalysts and for each family of light absorbers (as quantified by the increase in J_o of the light absorbers relative to the S-Q limit).

Note that this process produces a fundamentally different outcome, and answers a fundamentally different question, than evaluating the degradation in efficiency of a specific set of tandem light absorbers as a function of increases in the overpotentials of the electrocatalysts. In the latter approach, the optimum band-gap combination for a tandem structure is identified in the absence of any system losses, and then the decrease in efficiency is evaluated in response to increases in assumed voltage losses in the system.[14, 44] In such a situation, modest increases in the electrocatalyst overpotential can produce large decreases in the resulting system efficiency, especially when the tandem structure is designed to barely provide sufficient photovoltage to drive the electrocatalysts at near the light-limited current density during operation at optimal performance. In practice, such higher overpotential catalysts would instead optimally be utilized in conjunction with light absorbers that themselves had higher band gaps, to yield higher system efficiencies by allowing for operation at or near the light-limited current density with the specific set of electrocatalysts of interest. The optimized efficiency, $\eta_{STH,opt}$, of the latter system would be lower than that of the former system, due to the a slight decrease in the light-limited current density arising from the required increase in band gaps of the newly optimized tandem light absorbers, but the optimized efficiency would not be nearly as low as the

efficiency of a system in which the tandem-absorber band gaps were fixed in the design and implementation phases and thus did not drive the electrocatalysts being used in that system at the highest possible current densities during system operation.

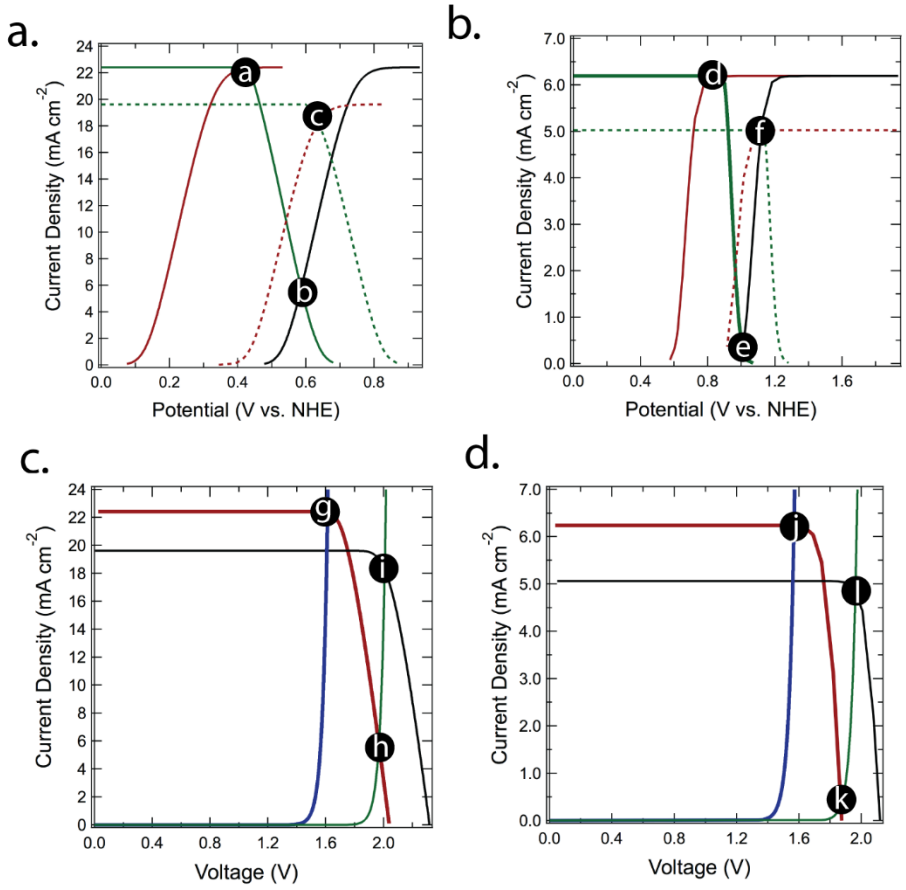

Figure 2.1. Analysis of the operating current density of solar-driven water-splitting cells using a photocathode+photoanode analysis (1a, b) and a tandem photoabsorber+overall loading curve analysis (1c, d). The photoabsorbers performed at S-Q limit in a) and c) and performed at the reverse saturation current density of 10^{21} J_0 in b) and d).

The process used herein is specifically illustrated in Figure 2.1a-d. Using the electrocatalytic performance of the state-of-the-art electrocatalysts as described by the B-

V relation (for an electrocatalyst system described concisely by the figure-of-merit having a value of $\eta_{overpotential}^{10\ mA\ cm^{-2}}$=355 mV), the band-gap combination of the tandem photoabsorbers was optimized and yielded $\eta_{STH,opt}$ at the S-Q limit for absorbers having a tandem band-gap combination of 1.7 eV/1.0 eV. In this "photocathode+photoanode" optimization process, for each combination of light absorbers and electrocatalysts, a load-line analysis based on two half-cell current-voltage characteristics was used, and the intersection point described the operating current of the full cell derived from these two half-cells. The green curves in Figure 2.1a represent the resulting current-voltage relation of the photocathode and the photoanode, in which the operating current density produced $\eta_{STH,opt} = \eta_{STH,\ a} = 27.5\%$.

The electrocatalytic performance of the HER catalyst was then fixed, and the overpotential of the OER catalyst was increased by decreasing the exchange-current density ($\eta_{overpotential}^{10\ mA\ cm^{-2}}$=757 mV). As shown in black in Figure 2.1a, the new operating point that resulted from this increase in catalyst overpotential produced a very large decrease in system efficiency, to $\eta_{STH,\ b} = 7.1\%$. However, for this new set of electrocatalysts, the original tandem light-absorber structure no longer provides the band-gap combination that provides the highest possible system efficiency. When the band gaps of the tandem system were reoptimized in response to the increased overpotential of this new electrocatalyst system, with the constraint that the absorbers were still performing at the S-Q limit, the half-cell behavior in Figure 2.1a in blue was obtained, and the resultant operating point yielded $\eta_{STH,opt} = \eta_{STH,\ c} = 22.4\%$. The light-limited current density of these new tandem absorbers is lower than the light-limited current density of the absorbers that were used to obtain the curves in green (and yield operating points a or b) in Figure 2.1, because the band gaps of the new optimally performing system were increased (and thus J_{ph} decreased for a given illumination intensity and spectral distribution from the sun) relative to the band gaps of the original system (in a and b). However, the system efficiency with the specified electrocatalysts is much higher for the newly optimized system, because the increased band gaps provide a sufficient increase in photovoltage to overcome the increased catalyst overpotentials, and therefore allow system operation at point c, near the

light-limited current density of the newly optimized tandem light absorber combination, with band gaps of 1.8 eV/1.2 eV. Reoptimization of the band gaps of the tandem structure therefore allowed the design of a system with a much higher system efficiency for these degraded electrocatalysts than the system efficiency obtained by fixing the properties of the tandem structure based on negligible system losses, and then absorbing the entirety of any real system voltage losses directly in the form of decreases to the resulting system efficiency.

In a subsequent step, the overall optimum system efficiency $\eta_{STH,opt}$ was recalculated for each specific electrocatalyst system of interest, but with the constraint that the light absorbers were degraded in performance from the S-Q limit by a specified increase in J_o. For example, for the original electrocatalyst behavior corresponding to the blue half-cell curves in Figure 2.1a, the green curves in Figure 2.1b described the half-cell characteristics of the tandem structure in which J_o was increased by 10^{21} relative to the values of J_o obtained from the S-Q limit. For this specific combination of electrocatalysts, the optimal system efficiency was very low, corresponding to $\eta_{STH,opt} = \eta_{STH,d} = 7.7\%$. Due to the low photovoltage of the degraded light absorbers relative to the values of their band gaps, the optimal system efficiency for this set of electrocatalyst properties required a very significant increase in the band gap of the absorbers, to values of 2.5 eV/1.9 eV, to drive the electrocatalysts and thus produced low overall optimal system efficiencies. For these tandem light-absorber systems, the same increase in electrocatalyst overpotential as that represented in Figure 2.2a produced operating point e in Figure 2.2b, with a corresponding decrease in efficiency to $\eta_{STH,e} = 0.4\%$. Reoptimization of the band gaps, however, produced a system having significantly higher efficiencies, as represented by the intersection of the red and the green curves in Figure 2.1b at operating point f ($\eta_{STH,op} = \eta_{STH,f} = 6.0\%$).

A different approach, the “tandem photoabsorber + overall loading curve” configuration (2.1c, d), was also employed to obtain the η_{STH} of the system, which yielded the identical results to the half-cell load-line analysis depicted in Figures 2.1a,b. In Figure 2.1c and

2.1d, the blue and the green curves represent the overall water-splitting loading curves with $\eta_{overpotential}^{10\ mA\ cm^{-2}}$= 355 mV and $\eta_{overpotential}^{10\ mA\ cm^{-2}}$=757 mV, respectively. The red curve represents the current-voltage characteristic of the tandem photoabsorbers, in which the band-gap combination was optimized (1.7 eV/1.0 eV) for the blue loading curve. The resulting $\eta_{STH,opt} = \eta_{STH,\,g}$ was 27.5%, which corresponds to the operating current density at point g. The $\eta_{STH,\,h}$ decreased to 7.1%, which corresponds to the operating point h, when the activity of the electrocatalysts decreased (blue loading curve) without the reoptimization of the band-gap combination. When the band-gap combination was optimized (1.8 eV/1.2 eV) for the green loading curve, the resulting $\eta_{STH,opt} = \eta_{STH,\,i}$ was increased to 22.4%, which corresponds to the operating point i. The same trend was observed in Figure 2.2d, in which the quality of the tandem photoabsorber was varied by changing the reverse-saturation current density to 10^{21} J_0 ($\eta_{STH,\,j}$=7.7%, $\eta_{STH,\,k}$=0.4% and $\eta_{STH,\,l}$=6.0%).

Figure 2.2a plots $\eta_{STH,opt}$ for the system design space of interest, incorporating the optimized tandem-cell arrangement, as a function of the behavior of various different combinations of electrocatalysts. As described above, at each value of the total overpotential, the entire suite of band-gap combinations for the tandem cell was explored to identify the combination that produced the optimum efficiency, $\eta_{STH,opt}$, at the specified total system overpotential. In this process, the band gap of the top light absorber was varied from 1.3 eV to 3.0 eV, and band gap of the bottom light absorber ranged between 0.6 eV and 2.0 eV.

The numerical current-voltage characteristic of the light absorbers in the tandem cell under the Shockley-Queisser (S-Q) limit (blue curve) was obtained using the ideal photodiode relationship. As shown in the top-most data set plotted in Figure 2.2a, for light absorbers operating at the detailed-balance limit, the slope of $\eta_{STH,opt}$ as a function of the total overpotential, $\frac{\Delta\eta_{STH,opt}}{\Delta\eta_{overpotential}^{10\ mA\ cm^{-2}}}$, was ~ 0.01 % mV^{-1}. Hence, at 10 mA cm^{-2} of operating

current density, decreases in the total overpotential by 100 mV, from 400 mV to 300 mV, would result in 1 percentage-point change in $\eta_{STH,opt}$.

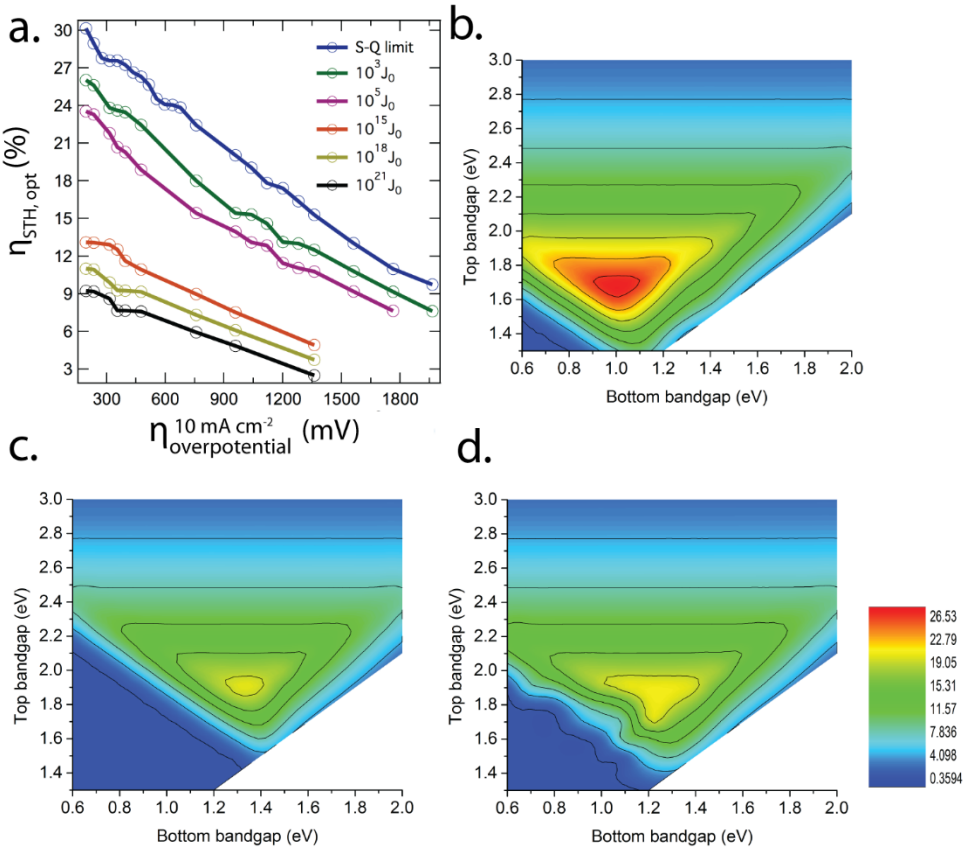

Figure 2.2. a) Optimal STH conversion efficiency, $\eta_{STH,opt}$, at all band-gap combinations as a function of the electrocatalyst characteristics described by the total electrocatalytic overpotential at 10 mA cm^{-2} for hydrogen-evolution reaction (HER) and the oxygen-evolution reaction (OER). The actual operating current densities for each system were obtained using a load-line analysis, as described in Figure 2.1. The reverse-saturation current densities for the photoabsorbers were swept from the Shockley-Queisser (S-Q) limit, J_0, to 10^{21} J_0. b) $\eta_{STH,opt}$ as a function of the top and bottom band-gap combinations when the reverse-saturation current density and the total overpotential at 10 mA cm^{-2} were set to J_0 and 355 mV and c) J_0 and 959 mV and d) 10^5 J_0 and 355 mV, respectively.

State-of-the-art electrocatalysts in alkaline solution, such as Ni-Mo alloy for the HER and $NiFeO_x$ mixed-metal oxides for OER, exhibit 75 mV and 280 mV overpotential, respectively, at operating current densities of 10 mA cm^{-2}. The calculation that corresponds to this particular catalyst system at detailed-balance limit is shown in Figure 2.2 b, where $\eta_{STH,opt,}$ is 27.5% at the band-gap combination of 1.7 eV/1.0 eV. Improving the existing catalyst system by decreasing the overpotential for the OER by 100 mV at a current density of 10 mA cm^{-2}, which would represent very significant progress in electrocatalyst development, would result in a potential possible efficiency improvement of 1 percentage point in $\eta_{STH,opt}$ for the full system.

The reverse-saturation current density of the ideal photodiode at the detailed-balance limit, J_0, was then increased from J_0 to 10^{21} J_0, while the light-limited photocurrent density was maintained constant. This procedure was used to account for a very substantial degradation in the properties of the light absorbers relative to operation at the theoretical detailed-balance limit. The resulting open-circuit voltages were decreased significantly due to the increase of the reverse-saturation current densities. In fact, during this process, J_0 was increased to a value such that overall system efficiencies could not exceed 5% even with essentially zero overpotential and solution-resistance losses combined. For all values of J_0, the slope of $\eta_{STH,opt}$ as a function of the total overpotential, $\frac{\Delta\eta_{STH,opt}}{\Delta\eta^{10\ mA\ cm^{-2}}_{overpotential}}$, was approximately 0.01 % mV^{-1}.

As the total overpotential increased or as the reverse-saturation current density increased, the light-absorber combination that produced $\eta_{STH,opt}$ had higher band-gap values than the base case. Figure 2.2c and 2.2d show $\eta_{STH,opt}$ for all band-gap combinations when the total overpotential was 959 mV at the detailed-balance limit and the total overpotential was 355 mV with the reverse-saturation current density set to $10^5 J_0$, respectively. The corresponding optimal band-gap combination was 2.0 eV/ 1.2 eV in Figure 2.2c and was 1.9 eV/1.2 eV in Figure 2.2d.

Although the state-of-the-art electrocatalysts in alkaline solution exhibit a total overpotential of ~ 350 mV at 10 mA cm^{-2}, in acidic conditions, a paucity of stable earth-abundant electrocatalysts for OER have been reported, and thus development of an earth-abundant OER catalyst that is stable in acid would be a significant improvement upon the state-of-the-art.[21] Moreover, when the cathodic reaction involves the CO_2-reduction reaction, large overpotentials, typically over 1 V, are observed.[46] In these less-developed materials systems, improvements in the catalytic performance would result in significant enhancement of $\eta_{STH,opt}$.

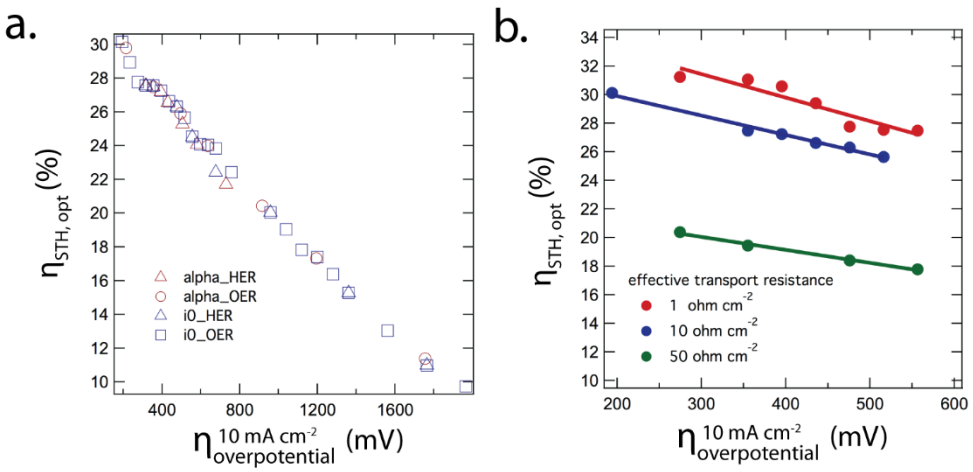

Figure 2.3. a) $\eta_{STH,opt}$ at all band-gap combinations as a function of the total electrocatalyst overpotential at 10 mA cm^{-2} when the exchange-current density for HER or OER, or the transfer coefficient for the HER or OER, was parametrically varied. The actual operating current densities for each system were obtained using a load-line analysis, as described in Figure 2.1. b) $\eta_{STH,opt}$ at all band-gap combinations as a function of the total electrocatalyst overpotential at 10 mA cm^{-2} (but with the actual operating current densities for each system were obtained using a load-line analysis, as described in Figure 2.1) when the effective transport resistance in the solution electrolyte and membrane separators was set to 1 ohm cm^{-2} (red), 10 ohm cm^{-2} (blue) and 50 ohm cm^{-2} (green).

Note that while the general trend, $\frac{\Delta\eta_{STH,opt}}{\Delta\eta_{overpotential}} \approx 0.01\%\ mV^{-1}$ shown in Figure 2.1 and 2.3 resulted in a marginal change of $\eta_{STH,opt}$ in response to the catalyst performance, significant change in the *relative* STH conversion efficiency could occur in low efficiency cells. For instance, when the OER overpotential at 10 mA cm^{-2} was reduced from 400 mV to 200 mV, which would represent significant advancement in catalyst development, in a cell employing tandem photoabsorbers that operate close to S-Q limit, the $\eta_{STH,opt}$ would increase from ~27.5% to 29.5% (by a factor of <10% relative). Alternatively, the same decrease in OER overpotential would make a much larger relative difference in the optimal system efficiency for poorly performing, degraded light absorbers, and could for example increase $\eta_{STH,opt}$ by a factor of 1.5 (i.e by 50% relative), from $\eta_{STH,opt}$ = 2% to $\eta_{STH,opt}$ = 3%. However, clearly one cannot convert an inefficient optimal system design into an efficient optimized system design by decreasing the OER overpotential by 100 mV from state-of-the-art values at the present time. Hence the sensitivity analysis clearly indicates that improvements in the light absorbers are both necessary and sufficient to enable highly increased efficiencies for optimized solar-driven water-splitting systems.

2.3.3 General trend of the sensitivity behavior

For electrocatalysts that follow the Butler-Volmer (B-V) relationship, the kinetic overpotential for the HER as well as for the OER not only depends on the exchange-current density but also on the transfer coefficient.[32] Figure 2.3a shows $\eta_{STH,opt}$ at the detailed-balance limit as a function of the total overpotential at 10 mA cm^{-2}, in which the transfer coefficient for HER and OER, or in which the exchange-current density for the HER and OER, were parametrically varied. The transfer coefficients for the HER and OER were varied so that the Tafel slopes for the corresponding reactions changed from 20 mV dec^{-1} to 240 mV dec^{-1}. The exchange-current density for HER was varied from 1.4 mA cm^{-2} to 1.4×10^{-36} mA cm^{-2} and the exchange-current density for the OER was varied from 1.1×10^{-2} mA cm^{-2} to 1.1×10^{-41} mA cm^{-2}. At all band-gap combinations, $\eta_{STH,opt}$ exhibited little

dependence on the four specific parameter variations, and $\eta_{STH,opt}$ exhibited a quasi-linear relationship with the total overpotential at 10 mA cm^{-2}. Thus, the total overpotential at a current density of 10 mA cm^{-2} is a globally useful figure-of-merit for evaluating the efficiency of the full water-splitting system in these generic system designs.

The three-dimensional transport-resistance distribution is highly dependent on the detailed design and geometric parameters of the cell as well as the ion-transport properties of the solution electrolyte. In this work, a 0-dimensional approximation was used to obtain an effective transport resistance. Figure 2.3b shows $\eta_{STH,opt}$ as a function of the total overpotential at 10 mA cm^{-2} when the effective transport resistance was set to 1 ohm cm^{-2}, 10 ohm cm^{-2} or 50 ohm cm^{-2}, respectively. Although $\eta_{STH,opt}$ showed a strong dependence on the detailed geometric parameters of the device, the slope, $\frac{\Delta\eta_{STH,opt}}{\Delta\eta^{10\ mA\ cm^{-2}}_{overpotential}}$, exhibited little dependence on the effective transport resistance. The red curve represented the optimal STH conversion efficiency with a smaller effective transport resistance. As a result, the overall efficiency was higher than the values displayed in Figure 2.2 but in no case did the value exceed the S-Q limit.

2.3.4 Operational temperature and illumination conditions

Figures 2.4a and 2.4b depict the sensitivity of $\eta_{STH,opt}$ as a function of the operational temperature and the incident illumination concentration, respectively. The value of $\eta_{STH,opt}$ exhibited a weak dependence on the operational temperature in the range of T = 300 K to 360 K. At the detailed-balance limit, $\eta_{STH,opt}$ decreased from 27.5% to 26.3% when the operating temperature increased from 300 K to 360 K. The weak temperature dependence resulted from two competing effects: degradation of the performance of the light absorbers and enhancement of the electrocatalytic and ion-transport rates at elevated temperatures. As the operational temperature increased, the radiative recombination in the light absorbers increased according to Eq. (5), which resulted in a decrease in the performance of the light

absorbers. However, as the operational temperature increased, the total overpotential for electrocatalysis and the transport resistance according to Eq. (9) and Eq. (10) also decreased.

The value of $\eta_{STH,opt}$ exhibited a significant dependence on the optical concentration factor of the incident solar illumination. As the optical concentration increased, the resulting higher operational current density resulted in an increase in the kinetic overpotentials needed to drive the HER and OER at the required interfacial flux. As a result, $\eta_{STH,opt}$ at the detailed-balance limit decreased from 30.1% to 25.1% when the optical concentration increased from 1 Sun (100 mW cm^{-2}) to 20 Sun (2000 mW cm^{-2}).

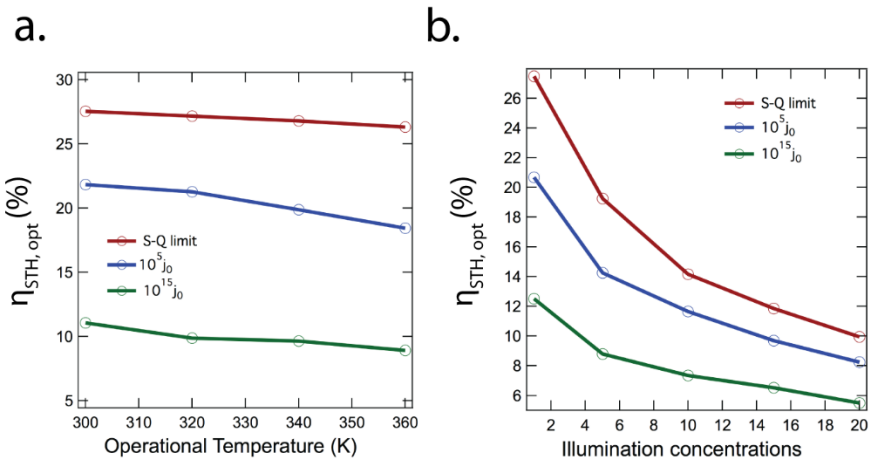

Figure 2.4. a) $\eta_{STH,opt}$ at all band-gap combinations as a function of the operational temperature for the integrated system, b) $\eta_{STH,opt}$ at all band-gap combinations as a function of the illumination-concentration factor for the integrated system. Three photoabsobers having reverse-saturation current densities either at the S-Q limit (red) (J_o), $10^5 J_0$ (blue) or $10^{15} J_0$ (green) were calculated.

2.4 Conclusions

The sensitivity analysis yielded a general trend for the behavior of $\eta_{STH,opt}$ as a function of the total overpotential for HER and OER at 10 mA cm^{-2}, regardless of the quality of the light absorbers. In response to a change in catalyst properties, the band-gap combinations of the tandem photoabsorber were varied to then achieve the optimal STH conversion efficiency at the specified total overpotential. As the total overpotential increased, the optimal band-gap combinations shifted to higher band-gap values to accommodate the additional voltage requirements. Hence, a relatively small decrease in the optimal STH efficiency was observed, and a reduction in the overpotential at 10 mA cm^{-2} by 100 mV from values for present state-of-the-art electrocatalysts resulted in ~1percentage-point improvement of the optimally attainable STH conversion efficiency. The sensitivity factor, $\frac{\Delta\eta_{STH,opt}}{\Delta\eta_{overpotential}^{10\ mA\ cm^{-2}}}$, , in general exhibited a very weak dependence on the detailed kinetic parameters of the HER and OER or on effective transport resistance of the membrane separator and the solution electrolyte. Leveraging the enhanced electrocatalysis and solution transport at elevated temperatures in the integrated system, the optimal STH conversion efficiency also exhibited a very weak dependence on the operational temperature. Using state-of-the-art catalyst systems, the optimal STH conversion efficiency showed a strong dependence on the optical concentration factor.

REFRENCE:

1. M. G. Walter, E. L. Warren, J. R. McKone, S. W. Boettcher, Q. X. Mi, E. A. Santori and N. S. Lewis, *Chem. Rev.*, 2010, 110, 6446-6473.
2. N. S. Lewis and D. G. Nocera, *P Natl Acad Sci USA*, 2007, 104, 20142-20142.
3. T. R. Cook, D. K. Dogutan, S. Y. Reece, Y. Surendranath, T. S. Teets and D. G. Nocera, *Chem. Rev.*, 2010, 110, 6474-6502.
4. J. R. McKone, N. S. Lewis and H. B. Gray, *Chemistry of Materials*, 2014, 26, 407-414.

5. C. C. L. McCrory, S. Jung, J. C. Peters and T. F. Jaramillo, *J. Am. Chem. Soc.*, 2013, DOI: 10.1021/ja407115p.
6. J. Suntivich, K. J. May, H. A. Gasteiger, J. B. Goodenough and Y. Shao-Horn, *Science*, 2011, 334, 1383-1385.
7. Q. X. Mi, Y. Ping, Y. Li, B. F. Cao, B. S. Brunschwig, P. G. Khalifah, G. A. Galli, H. B. Gray and N. S. Lewis, *J. Am. Chem. Soc.*, 2012, 134, 18318-18324.
8. M. Long, W. M. Cai, J. Cai, B. X. Zhou, X. Y. Chai and Y. H. Wu, *J Phys Chem B*, 2006, 110, 20211-20216.
9. A. Kudo, K. Omori and H. Kato, *J. Am. Chem. Soc.*, 1999, 121, 11459-11467.
10. A. Kay, I. Cesar and M. Gratzel, *J. Am. Chem. Soc.*, 2006, 128, 15714-15721.
11. B. Kumar, M. Llorente, J. Froehlich, T. Dang, A. Sathrum and C. P. Kubiak, *Annu Rev Phys Chem*, 2012, 63, 541-+.
12. A. Saltelli, M. Ratto, T. Andres, F. Campolongo, J. Cariboni, D. Gatelli, M. Saisana and S. Tarantola, *Global Sensitivity Analysis: The Primer*, John Wiley & Sons, 2008.
13. L. C. Seitz, Z. B. Chen, A. J. Forman, B. A. Pinaud, J. D. Benck and T. F. Jaramillo, *Chemsuschem*, 2014, 7, 1372-1385.
14. J. R. Bolton, S. J. Strickler and J. S. Connolly, *Nature*, 1985, 316, 495-500.
15. H. Doscher, J. Geisz, T. Deutsch and J. A. Turner, *Energy Environ. Sci.*, 2014,7, 2951-2956.
16. Y. K. Chen, C. X. Xiang, S. Hu and N. S. Lewis, *J. Electrochem. Soc.* 2014, 161, 10, F1101-F1110.
17. S. Haussener, S. Hu, C. Xiang, A. Z. Weber and N. Lewis, *Energy Environ. Sci.*, 2013, 6, 3605-3618.
18. S. Haussener, C. X. Xiang, J. M. Spurgeon, S. Ardo, N. S. Lewis and A. Z. Weber, *Energy Environ. Sci.*, 2012, 5, 9922-9935.
19. S. Hu, C. X. Xiang, S. Haussener, A. D. Berger and N. S. Lewis, *Energy Environ. Sci.*, 2013, 6, 2984-2993.
20. C. Xiang, Y. Chen and N. S. Lewis, *Energy Environ. Sci.*, 2013, 6, 3713-3721.

21. C. C. L. McCrory, S. H. Jung, J. C. Peters and T. F. Jaramillo, *J. Am. Chem. Soc.*, 2013, 135, 16977-16987.
22. J. L. Qiao, Y. Y. Liu, F. Hong and J. J. Zhang, *Chem Soc Rev*, 2014, 43, 631-675.
23. R. Bailis, M. Ezzati and D. M. Kammen, *Science*, 2005, 308, 98-103.
24. J. E. Campbell, G. R. Carmichael, T. Chai, M. Mena-Carrasco, Y. Tang, D. R. Blake, N. J. Blake, S. A. Vay, G. J. Collatz, I. Baker, J. A. Berry, S. A. Montzka, C. Sweeney, J. L. Schnoor and C. O. Stanier, *Science*, 2008, 322, 1085-1088.
25. J. M. Murphy, D. M. H. Sexton, D. N. Barnett, G. S. Jones, M. J. Webb and D. A. Stainforth, *Nature*, 2004, 430, 768-772.
26. W. Shockley and H. J. Queisser, *J Appl Phys*, 1961, 32, 510.
27. E. L. Warren, J. R. McKone, H. A. Atwater, H. B. Gray and N. S. Lewis, *Energy Environ. Sci.*, 2012, 5, 9653-9661.
28. M. D. Kelzenberg, D. B. Turner-Evans, M. C. Putnam, S. W. Boettcher, R. M. Briggs, J. Y. Baek, N. S. Lewis and H. A. Atwater, *Energy Environ. Sci.*, 2011, 4, 866-871.
29. M. C. Putnam, S. W. Boettcher, M. D. Kelzenberg, D. B. Turner-Evans, J. M. Spurgeon, E. L. Warren, R. M. Briggs, N. S. Lewis and H. A. Atwater, *Energy Environ. Sci.*, 2010, 3, 1037-1041.
30. S. W. Boettcher, E. L. Warren, M. C. Putnam, E. A. Santori, D. Turner-Evans, M. D. Kelzenberg, M. G. Walter, J. R. McKone, B. S. Brunschwig, H. A. Atwater and N. S. Lewis, *J. Am. Chem. Soc.*, 2011, 133, 1216-1219.
31. S. Hu, M. R. Shaner, J. A. Beardslee, M. Lichterman, B. S. Brunschwig and N. S. Lewis, *Science*, 2014, 344, 1005-1009.
32. A. J. Bard and L. R. Faulkner, *Electrochemical Methods, Fundamentals and Applications*, Wiley, 2nd edition edn., 2000.
33. K. Kinoshita, *Electrochemical Oxygen Technology. 1992*, New York: Wiley.
34. H. E. Darling, *Journal of Chemical & Engineering Data*, 1964, 9, 421-426.
35. D. E. Brown, M. N. Mahmood, A. K. Turner, S. M. Hall and P. O. Fogarty, *Int J Hydrogen Energ*, 1982, 7, 405-410.

36. J. Landon, E. Demeter, N. Inoglu, C. Keturakis, I. E. Wachs, R. Vasic, A. I. Frenkel and J. R. Kitchin, *Acs Catal*, 2012, 2, 1793-1801.

37. S. Trasatti, *J Electroanal Chem*, 1972, 39, 163.

38. J. McEnaney, J. Crompton, J. Callejas, E. Popczun, A. Biacchi, N. S. Lewis and R. Sc*haak, Chem. Mater., 2014,* 26 (16), pp 4826–4831.

39. *J. McEnaney, J. Crompton, E. Popczun, J. Callejas, R. C., N. S. Lewis and R. E. Schaak, Chem. Commun., 2014,* 50, 11026.

40. J. Callejas, J. McEnaney, C. Read, J. Crompton, A. Biacchi, E. Popczun, T. Gordon, N. S. Lewis and R. Schaak, *Journal of the American Chemical Society, Submitted,* 2014.

41. Q. X. Mi, A. Zhanaidarova, B. S. Brunschwig, H. B. Gray and N. S. Lewis, *Energy Environ. Sci.*, 2012, 5, 5694-5700.

42. J. M. Spurgeon, J. M. Velazquez and M. T. McDowell, *Phys Chem Chem Phys*, 2014, 16, 3623-3631.

43. M. R. Singh, C. Xiang and N. S. Lewis, *manuscript in preparation,* 2014.

44. M. C. Hanna and A. J. Nozik, *J. Appl. Phys*, 2006, 100.

45. A. Berger, R. A. Segalman and J. Newman, *Energy Environ. Sci.*, 2014, 7, 1468-1476.

46. Y. Hori, H. Wakebe, T. Tsukamoto and O. Koga, *Electrochim Acta*, 1994, 39, 1833-1839.

Chapter III

MODELING AN INTEGRATED PHOTOELECTROLYSIS SYSTEM SUSTAINED BY WATER VAPOR

3.1 Introduction

An integrated photoelectrolysis system in which light absorbers, electrocatalysts and membrane separators are integrated together efficiently, scalably and robustly is an interesting option for solar energy conversion and storage applications.[1-3] The fundamental properties, design principles, and operational details of the individual components in such an integrated system have been recently evaluated in detail.[4-11] To facilitate operation at high current densities (> 1 A cm^{-2} at 80-90 ^{o}C) and thus optimize the balance of systems cost,[12, 13] electrolytes based on the use of liquid water as a feed are employed exclusively in electrolyzers. However, an integrated solar-driven water-splitting system can in principle use gaseous water vapor as the feed stock, because the water vapor content of humid air is generally sufficient to provide the needed water flux under many circumstances to support the solar-generated photon flux, and corresponding product flux, that will be produced by a light-limited current density of 10-20 mA cm^{-2} typically obtained under unconcentrated sunlight.[14, 15]

The use of water vapor as the system input feedstock has several potential advantages as compared to a traditional device that contains a liquid electrolyte. A water vapor device would mitigate deleterious effects associated with bubble formation during operation,

---

This chapter is based on results in: Chengxiang Xiang, Yikai Chen and Nathan S. Lewis, Energy Environ. Sci., 2013, 6, 3713-3721 – Published by The Royal Society of Chemistry.

including blocking of active electrocatalytic sites, scattering or reflection of incident illumination away from the light absorbers, etc.[14, 16-19] The thermodynamic potential for the water-splitting reaction is also more favorable for gaseous water than for liquid water, because the electrolysis of liquid water ($E^0[H_2O(l)]$=1.229 V) requires an additional ~44 mV as compared to the electrolysis of water vapor ($E^0[H_2O(g)]$=1.185 V).[20]

The use of $H_2O(g)$ as a feed to an integrated photoelectrolysis system presents, however, some unique challenges with respect to ionic transport and product gas transport. The membrane is most likely to be in direct physical contact with the electrocatalysts, with the opposite side of the electrocatalyst being a solid piece of photoabsorber. To prevent delamination of the membrane at the interface, the hydrogen or oxygen produced at the electrocatalyst/membrane interface would therefore have to diffuse through the membrane without formation of bubbles. Spurgeon, et. al[21] performed a proof-of-concept study on a water electrolysis system sustained by water vapor by operating a commercially available, membrane-based fuel cell unit in reverse, with the reaction driving force provided by an external power supply. Electrically driven water-electrolysis systems generally utilize a membrane-electrode-assembly to optimize the electrical, proton and gas transport. However, in an integrated photoelectrolysis system, the introduction of a light-capturing element, the photoabsorber, will significantly alter the optimal design parameters of the system. Haussener, et. al.,[6, 7] have presented optimal design parameters and materials properties for two characteristic photoelectrochemical devices, both of which operate in 1 M H_2SO_4(aq). However, the engineering-design aspects that are related to the transport phenomena have yet to be investigated for a system based on a $H_2O(g)$ feed.

In this work, two characteristic cell designs that use a proton exchange membrane and that exhibit low resistive loss (< 100 mV), facile gas transport, and minimal gas crossover while in operation (10 mA cm^{-2}) have been evaluated in detail. The first cell design uses a thin, membrane enclosed, micro-scale photoabsorber (critical dimension < 300 μm) and represents an approach in which the ionic pathway between the cathode and the anode, and the diffusive pathway for the gas transport in membrane from the catalyst to the gas-

collecting chamber, are both minimized. The second cell design features a structured membrane enclosed by mm-scale photoabsorbers, and represents a situation in which the ionic pathways and gas transport are optimized separately, by adjusting the proton transport channel and the gas transport channel in the system. Simulations of product crossover in micro-sized electrodes have also been performed, and these results indicate that the use of a proton-exchange membrane, such as Nafion, inherently minimizes the product crossover in such systems.

3.2 Modeling

3.2.1 Governing equations

The ionic transport in a proton-exchange membrane, e.g., Nafion, is governed by Ohm's law:

$$i_l = \sigma_l \nabla \phi_l, \qquad \text{(Eq. 3.1)}$$

where σ_l is the electrolyte conductivity, ϕ_l is the electrolyte potential and i_l is the ionic current. Assuming dilute-solution theory, in which the interactions among the solutes are not rigorously considered, the electrolyte conductivity can be derived from the Nernst–Planck equation, yielding:[22]

$$\sigma_l = \frac{F^2}{RT} \sum_i z_i^2 D_i c_i, \qquad \text{(Eq. 3.2)}$$

where c_i is the concentration of species i, D_i is the diffusion coefficient of species i, z_i is the charge number of the ionic species, and F is Faraday's constant.

The kinetics of electrocatalysis at the electrode/membrane interface are governed by the Butler-Volmer equations applied to the oxygen-evolution reaction (OER) and to the hydrogen-evolution reaction (HER):[20]

$$i_{R,OER/HER} = i_{0,OER/HER}[\exp(\frac{\alpha_{a,OER/HER} F \eta}{RT}) - \exp(-\frac{\alpha_{c,OER/HER} F \eta}{RT})], \qquad \text{(Eq. 3.3)}$$

where $i_{0,OER}$ and $i_{0,HER}$ are the respective exchange-current densities, $\alpha_{a,OER}$ and $\alpha_{a,HER}$ are the transfer coefficients for the OER and HER, respectively, and η is the overpotential, which is defined as

$$\eta = \phi_s - \phi_l - \phi_0 , \qquad \text{(Eq. 3.4)}$$

where ϕ_s and ϕ_l are the electric and electrolyte potential at the electrode-electrolyte interface, respectively, and ϕ_0 is the equilibrium potential. The value of ϕ_0 was set to ϕ_0 = 0.0 V for the cathode and to 1.185 V for the anode. The conservation of charge and the continuity of current density were also employed at the electrode/membrane interface.[22]

The transport of gaseous products in Nafion is also governed by the Nernst–Planck equation. Assuming a zero velocity field, the governing equation reduces to Fick's second law at steady state:

$$0 = D_i \nabla^2 C_i , \qquad \text{(Eq. 3.5)}$$

where C_i is the concentration and D_i the diffusion coefficient of dissolved hydrogen or oxygen in Nafion.

3.2.2 Cell designs

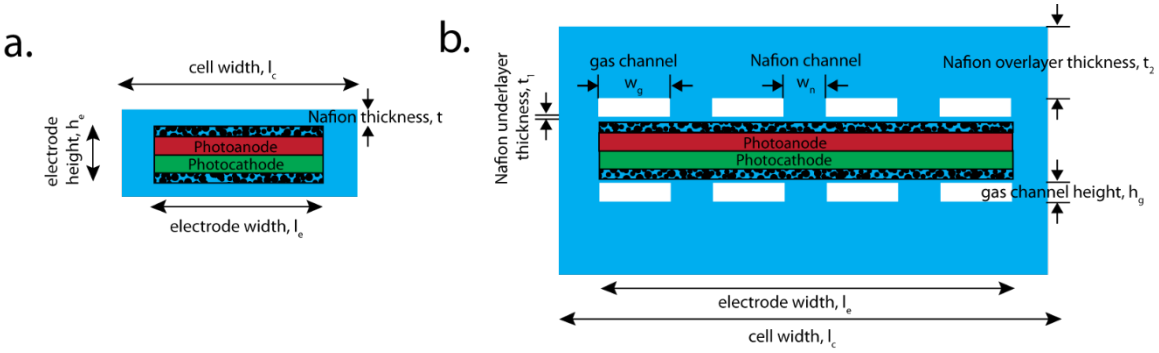

Figure 3.1. Schematic illustrations of two cell designs for a photoelectrolysis device sustained by a water vapor feed. Both designs contain a photocathode (red), a photoanode (green), electrocatalyst layers (dotted) and Nafion film (blue) used as a representative solid polymer electrolyte material. In Design A, the electrode width, electrode height, cell width and Nafion thickness are labeled as l_e, h_e, l_c and t, respectively. In Design B, the gas channel width, gas channel height, Nafion channel width, Nafion underlayer thickness and Nafion overlayer thickness are labeled as w_g, h_g, w_n, t_1, and t_2, respectively.

Figure 3.1 shows schematic illustrations of the two cell designs that were evaluated for performance during operation while fed by water vapor. Both designs are illustrated in 2-D cross sections, with the out-of-the-plane dimension assumed to be infinite. In Design A (Fig. 3.1a), the photoelectrolysis assembly contained a photocathode, a photoanode and electrocatalysts, all embedded in a proton-exchange membrane (e.g., Nafion). The fill fraction, defined as the ratio between the light-capturing geometric area and the total area of the cell, was determined by the ratio between the electrode width, l_e and the cell width, l_c. The Nafion film supports ionic transport between the anode and the cathode, and also supports product gas transport from the electrocatalysts to the gas-collecting chamber (not indicated). In Design B (Fig. 3.2b), the photoelectrolysis assembly was embedded in a structured Nafion film, with gas channels and Nafion channels introduced into the cell. Thin Nafion underlayers (0.5 μm) that were coated on top of the catalyst layers provided facile gas transport to the gas channels. The Nafion channels in between the gas channels provided low resistance pathways for ionic transport between the cathode and anode. Thick Nafion overlayers were further employed as required to meet specified design considerations, and served to decrease the resistive losses in the cell.

3.2.3 Modeling parameters

Table 3.1 presents the basic parameters used in the model. In the simulation of the resistive losses, symmetry boundary conditions for the current densities were used for the vertical walls of both designs. Insulating boundary conditions were applied at the upper and bottom bounds of the Nafion film. A Neumann (or second-type) boundary condition of the current flux (10 mA cm^{-2}) was applied at the electrode surface. The ionic conductivity of the Nafion film was set to 10 S m^{-1} in the subdomain settings. The electrochemical reactions for both designs were modeled as a surface reaction that occurred between the Nafion and the catalytic layer.

In the gas transport simulation, for Design A, a 1-D analytical calculation based on Fick's first law was used to determine the maximum sustainable flux at a given Nafion thickness, with the hydrogen (oxygen) concentrations at the Nafion/catalyst interface and the Nafion/vapor interface set to 0.78 mM (1.23 mM) and 0 mM (0 mM), respectively. For

Design B, symmetry boundary conditions for the H_2 or O_2 fluxes were used for the vertical walls. Insulating boundary conditions were applied at the upper and lower bounds of the Nafion film. Neumann (or second-type) boundary conditions of the gas fluxes (equivalent to 10 mA cm^{-2}) were applied at the electrode surface. The Dirichlet (or first-type) boundary condition was applied at the perimeters of the gas channels, where the concentrations of dissolved hydrogen was set to 0 mM, 0.2 mM, 0.4 mM or 0.6 mM for different sweep gas fluxes in the gas channel. The diffusion coefficient of the dissolved hydrogen and oxygen in the Nafion was set to 1.3×10^{-5} cm^2 s^{-1} and 6.1×10^{-6} cm^2 s^{-1}, respectively.

Electrochemical kinetics	OER exchange current density, $i_{R,OER}$	0.014 mA cm^{-2}
	OER anodic transfer coefficient, $\alpha_{a,OER}$	1.0
	OER cathodic transfer coefficient, $\alpha_{c,OER}$	0.1
	HER exchange current density, $i_{R,HER}$	1 mA cm^{-2}
	HER anodic transfer coefficient, $\alpha_{a,HER}$	2.57
	HER cathodic transfer coefficient, $\alpha_{c,HER}$	2.57
Nafion	Diffusivity H_2, D_{H_2}	1.3×10^{-5} cm^2 s^{-1}
	Diffusivity O_2, D_{O_2}	6.1×10^{-6} cm^2 s^{-1}
	Conductivity, σ_l	100 mS cm^{-1}
Operating conditions	Temperature, T	298 K
	Photocurrent density, i_{pc}	10 mA cm^{-2}

	Saturation concentration H_2, $c_{H_2,sat}$	0.78 mM
	Saturation concentration O_2, $c_{O_2,sat}$	1.23 mM

Table 3.1: Basic parameters used in the model.

In the crossover simulation, insulating boundary conditions were applied at the upper and bottom bounds of the Nafion film. The Dirichlet (or first-type) boundary condition was used at the electrode, where the concentration of the dissolved hydrogen was set to the solubility limit (0.78 mM at room temperature). The concentration of dissolved hydrogen was set to zero at the cathode and the anode, respectively, to evaluate the situation for the maximum diffusive crossover condition.

Free triangular discretization and a standard solver in the Comsol multi-physics package were used in the modeling. For Design A, the maximum and minimum mesh element size were set to 10 μm and 0.1 μm, respectively, and the maximum mesh element growth rate and the resolution of curvature were fixed to 1.2 and 0.25, respectively. For Design B, the maximum and minimum mesh element size were set to 100 μm and 1 μm, respectively, and the maximum mesh element growth rate and the resolution of curvature were set at 1.3 and 0.3, respectively. A relative tolerance of the corresponding variable of 0.001 was applied as the convergence criterion for both designs.

3.3 Results

3.3.1 Design A

3.3.1.1 Product gas transport (1-d transport)

In Design A, the oxygen and hydrogen transport from the Nafion/catalyst interface to the gas-collecting chamber can be treated as a 1-D diffusive gas transport process. Figure

3.2 shows the maximum current density that can be sustained in a 1-D planar geometry without supersaturation of hydrogen or oxygen at the Nafion/catalyst interface, as a function of the thickness of the Nafion film. For the cell to operate at 10 mA cm^{-2} without supersaturation at the Nafion/catalyst interface, the Nafion thickness can not exceed 1.9 μm for the photocathode side and 2.9 μm for the photoanode side. To ensure sufficient gas transport in the system, the thickness of the Nafion film in Design A was therefore set to 1.9 μm in all subsequent simulations.

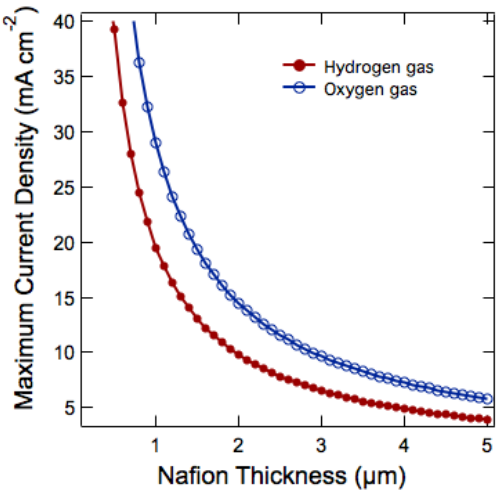

Figure 3.2. Maximum sustainable current density, as a function of the Nafion thickness, allowed to avoid supersaturation of oxygen (blue) or hydrogen (red) at the Nafion/catalyst interface in Design A.

3.3.1.2 Resistive losses

In Design A, the conductive pathways in the thin layer Nafion film (~ 2 μm) are significantly more confined than a liquid-electrolyte based design, for which the electrolyte height is typically on the order of several millimeters.[6] Figure 3.3 shows the resistive loss as a function of the normalized lateral position on the photoelectrode, for six electrode widths. A large variation in the resistance drops was observed across the electrode, due to longer ion transport pathways between the mid-point of the photocathode to the mid-point

to the photoanode and shorter pathways between the edge points, especially in geometries that had large electrode widths.

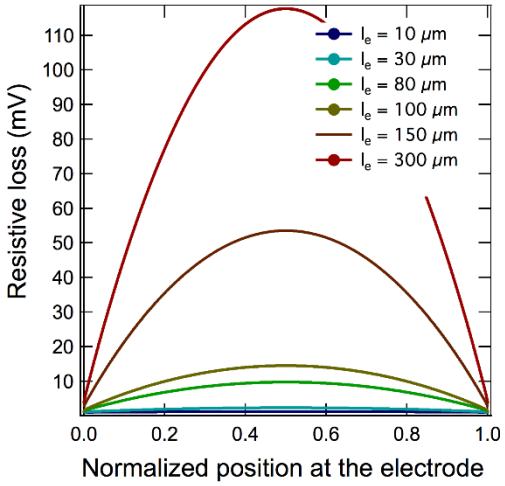

Figure 3.3. Resistive loss as a function of normalized position along the electrode for six different electrode widths in Design A.

Figure 3.4 shows the maximum resistive drops along the photoelectrodes as a function of the electrode width. Three electrode heights of the photoelectrode, 1 μm (Fig. 3.4a), 10 μm (Fig. 3.4b) and 100 μm (Fig. 3.4c), were simulated, to account for different types of photoabsorber materials. For each electrode height, three different fill fractions, $ff = l_e/l_c$, 0.5, 0.9 and 0.98 were also simulated, where l_e is the PV electrode width and l_c is the cell width. In all cases, the resistive loss increased as a function of the electrode width, due to increased length of the ionic pathways in the thin Nafion layer. When the electrode height was set to 1 μm, the resistive loss as a function of the electrode width exhibited little dependence on the fill fraction of the design. In contrast, as the electrode height increased, the resistive loss exhibited a stronger dependence on the fill fraction of the design. To minimize the resistive losses to < 100 mV, the electrode width should not exceed ~ 300 μm even with a 1 μm electrode height.

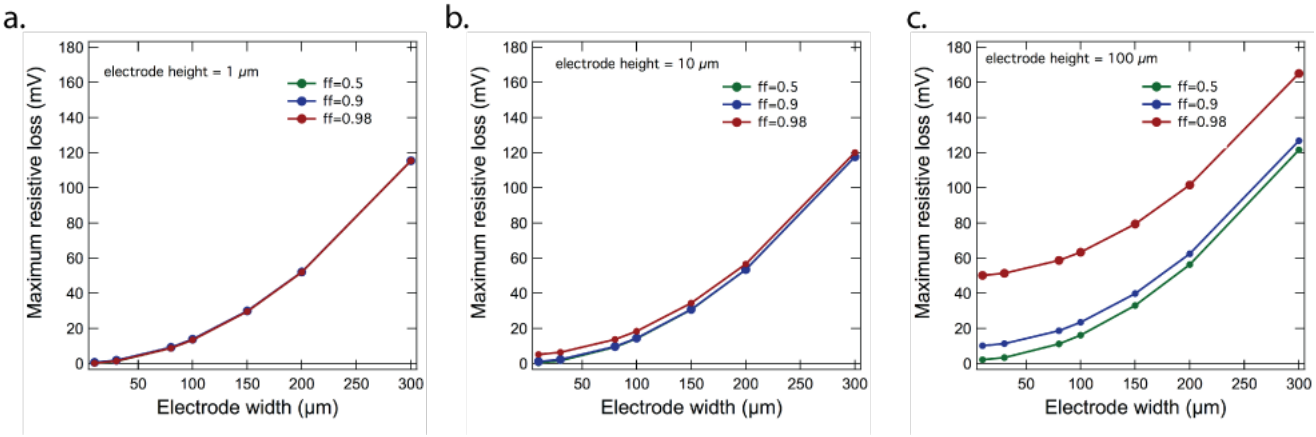

Figure 3.4. Maximum resistive loss as a function of the electrode width for three different electrode heights, 1 μm (a), 10 μm (b) and 100 μm (c), in Design A. Three fill fractions, 0.5 (green), 0.9 (blue) and 0.98 (red) were simulated for each electrode width.

3.3.2 Design B

3.3.2.1 Product gas transport (2-d)

In Design B, the structured Nafion film provides a balance between the ionic conductivity and gas transport of the products. Because 10 mA cm^{-2} of photocurrent density was generated uniformly along the photoelectrode, the regions directly beneath the Nafion channel would have the longest diffusive pathways. As the width of the Nafion channel decreases, gas transport improves due to the decreased length of pathways for the transport of the product gases. However, a decrease in the Nafion channel width will concomitantly hinder the ion transport and therefore increase the resistive losses in the cell.

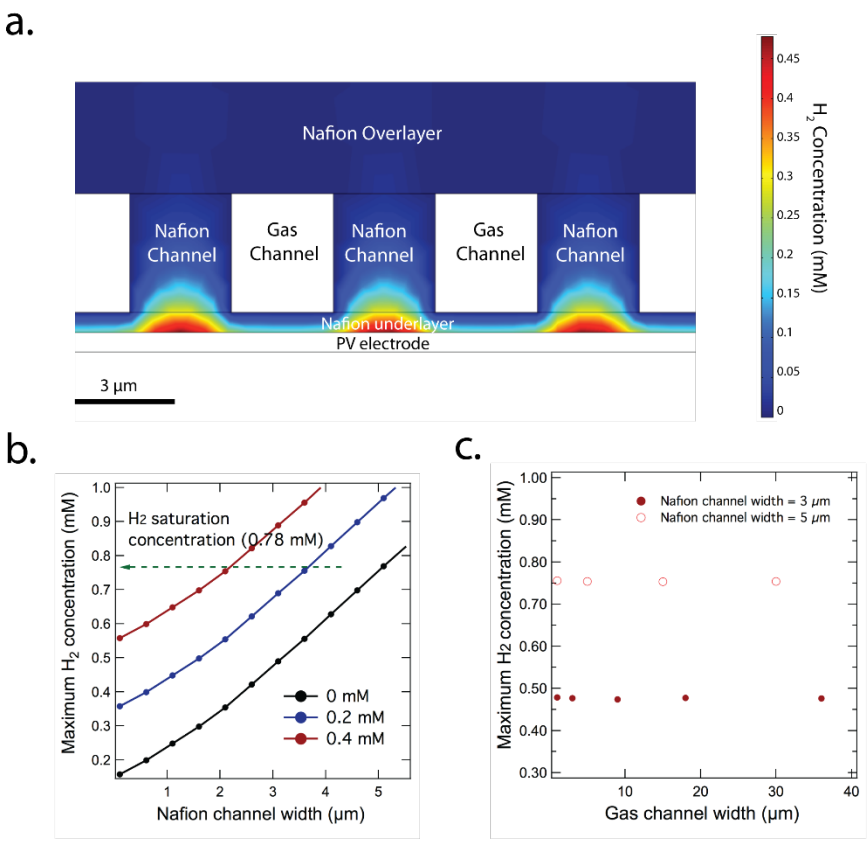

Figure 3.5. (a) The hydrogen concentration profile in Design B, where the electrode width, electrode height, Nafion channel width, gas channel width, gas channel height, Nafion underlayer thickness, Nafion overlayer thickness were set to 2.34 mm , 10 μm, 3 μm, 3 μm, 3 μm, 0.5 μm, and 200 μm, respectively. (b) The maximum hydrogen concentration as a function of the Nafion channel width, where the gas channel width was set to 5 μm and the hydrogen concentration at the perimeter of the gas channel was set to 0 mM (black), 0.20 mM (blue) or 0.40 mM (red). (c) The maximum hydrogen concentration as a function of the gas channel width, where the Nafion channel width was set to 3 μm (solid dot) and 5 μm (hollow dot), respectively.

Figure 3.5a depicts the hydrogen concentration profile in Design B with 10 mA cm^{-2} of photocurrent density generated uniformly at the photoelectrode/Nafion underlayer interface. The simulations indicated that the hydrogen concentration reached its highest

value at the mid-point of the Nafion channel along the photoelectrode. In this particular geometry, the highest hydrogen concentration was 0.47 mM, which is still below the saturation concentration of hydrogen in a film of Nafion (0.78 mM).

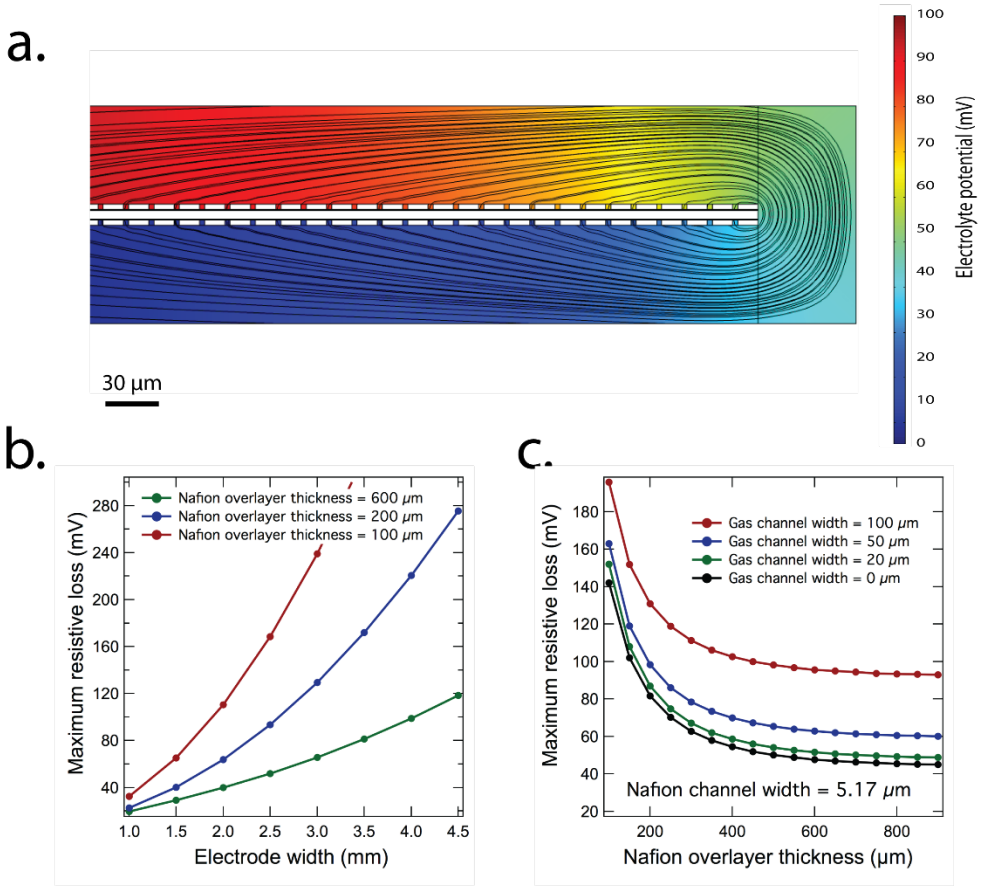

Figure 3.6 (a). The electrolyte potential profile in Design B, with the electrode width, electrode height, Nafion channel width, gas channel width, gas channel height, Nafion underlayer thickness, Nafion overlayer thickness were set to 2.34 mm, 10 µm, 5.17 µm, 20 µm , 5.17 µm, 0.5 µm and 150 µm, respectively. (b) The maximum resistive loss a function of the electrode width for three Nafion overlayer thickness, 100 µm (red), 200 µm (blue) and 600 µm (green). (c) The maximum resistive loss as a function of the Nafion overlayer thickness for four different gas channel widths. The electrode width and the Nafion channel height were set to 2.4 mm and 5.17 µm, respectively.

Figure 3.5b shows the maximum hydrogen concentration, which occurred in the mid-point of the Nafion film, as a function of the Nafion channel width, where the gas channel width was set to 50 μm and the hydrogen concentration at the perimeter of the gas channel was set to 0 mM (black), 0.20 mM (blue) or 0.40 mM (red). Figure 3.5c shows the maximum hydrogen concentration as a function of the gas channel width for two Nafion channel widths. The maximum hydrogen concentration showed a quasi-linear dependence on the width of the Nafion film, and exhibited no dependence on the width of the gas channel. The simulation results provided an upper bound (5.17 μm, 3.70 μm and 2.13 μm for the hydrogen concentration of 0 mM, 0.20 mM and 0.40 mM, respectively, at the perimeter of the gas channel) for the width of the Nafion channel needed to avoid supersaturation at the Nafion/catalyst interface. Thus, for effective hydrogen transport, a higher sweep gas flux in the gas channel is preferable to achieve a low hydrogen concentration at the perimeter of the gas channels. For a 1 m x 1 m system fed by water vapor, a sweep gas flux of 0.040 mol s^{-1} is required to achieve a 0.010 mM concentration of hydrogen at the perimeter of the gas channel.

3.3.2.2 Resistive losses

In Design B, the ionic pathways consist of three segments connected in series: the Nafion underlayer, the Nafion channel and the Nafion overlayer. The structured Nafion film maximizes the electrode width while maintaining low resistive losses (< 100 mV). Figure 3.6a shows the electrolyte potential profile in Design B, with the detailed cell geometry provided in the figure caption. As indicated by the trajectory of current density lines in black (Fig. 3.6a), the Nafion channels served as conductive bridges between the Nafion underlayer and the Nafion overlayer. In this particular geometry, the maximum resistive loss was 108 mV.

Figure 3.6b shows the maximum resistive loss as a function of the electrode width for three different Nafion overlayer thicknesses, when the gas channel width was set to zero.

Figure 3.6b provided an upper bound for the electrode width in Design B, where the conductive pathway between the cathode and anode was optimized. In these limiting cases (Fig. 3.6b), for a resistive drop of < 100 mV, the electrode width can not exceed 1.7 mm, 2.6 mm and 4.0 mm, respectively, when the Nafion overlayer thickness was set to 100 μm, 200 μm, and 600 μm, respectively.

The best limiting scenario for resistive losses simulated in Figure 3.6b did not provide sufficient product gas transport. To prevent supersaturation of product gases at the Nafion/catalyst interfaces, a Nafion channel with a width of < 5.17 μm (Fig. 3.5b) is required. Figure 3.6c shows the maximum resistive loss as a function of the Nafion overlayer thickness, when the electrode width and the Nafion channel width were set to 2.34 mm and 5.17 μm, respectively. The maximum resistive loss decreased as the Nafion overlayer thickness increased, and the resistive loss plateaued at a Nafion thickness of ~800 μm. The black curve shows the limiting case scenario in which the gas channel width was set to zero, and served to provide a lower bound for the resistive loss in this particular electrode width (2.34 mm) for Design B. The resistive loss also showed a strong dependence on the gas channel width. By choosing a smaller gas channel width (20 μm), the resistive loss (green curve) approached the limiting case scenario (black curve). As showin in Figure 3.6c, the gas channel width can not exceed 100 μm to maintain a low (< 100 mV) resistive loss for this particular electrode width (2.34 mm**).** Additional simulations were also performed with the Nafion channel width less than 5.17 μm, which is the upper-bound value that can support the required gas transport. When the Nafion channel width was decreased from 5 μm to 1 μm, the maximum resistive loss showed a weak dependence (< 10 mV variation) on the Nafion channel width. As shown in Figure 3.6c, as long as the electrode width does not exceed the upper-bound value, various combinations of the Nafion overlayer thickness and the gas channel width can be employed to achieve low resistive losses in Design B.

3.3.3 Gas crossover

Figure 3.7 shows the percentage of gas crossover due to diffusive transport between the cathode and anode as a function of the electrode width, for three different electrode heights. The gas crossover increased as the width of the electrode decreased. To avoid a gas mixture that contained > 4% H_2 in air (the flammability limit), the electrode width must exceed 45.5 µm or 20.2 µm, for an electrode height of 1 µm or 10 µm, respectively. For the 100 µm electrode height, the diffusive gas crossover would not exceed 4% H_2 in air. The convective gas crossovers were therefore inherently minimized in both designs by the use of the Nafion. Due to the small permeability of the Nafion film, ~10^{-18} m^2, the convective crossover was negligible in all the designs, even under significant pressure differential, e.g., 1 atm.

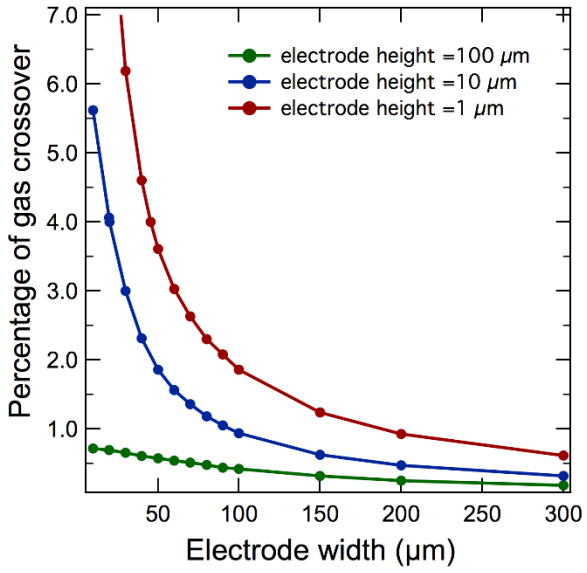

Figure 3.7. Percentage of gas crossover as a function of the electrode width when the electrode height was set to 1 µm (red), 10 µm (blue) and 100 µm (green).

3.4 Discussion

3.4.1 Effect of a lateral conductive layer

A lateral conductive layer has often been proposed and utilized to redistribute the current density and facilitate the ionic transport in the system, by focusing the current density at the edge of a PV-based electrode.[6] In such a system, the majority of the products, hydrogen and oxygen, are generated near the edge of the electrode, and the gases can readily bubble away in a liquid- electrolyte based system. However, use of such a design in a vapor feed system would result in product gases generated underneath the Nafion film, and transported by diffusion of dissolved gas in the membrane. When the current density increases rapidly at the edge of the electrode, the Nafion thickness therefore has to be reduced significantly to accommodate this gas transport. The resulting non-uniform Nafion coating further complicates the resistive losses and electrocatalysis in the system. For example, in Design B, when the electrode width was set to 2.34 mm (Fig. 3.6), the hydrogen concentration at the electrode edge exceeded the saturation concentration by several orders of magnitude, regardless of any combination of other geometric parameters that were discussed in the previous section. Similarly, in Design A, when the Nafion thickness was set to 1.9 μm, the hydrogen concentration exceeded the saturation concentration at the electrode edge in all cases simulated in Fig. 3.4. When the Nafion thickness was reduced uniformly to accommodate the high hydrogen flux at the electrode edge, the current density is further focused at the electrode edge, which will result in supersaturation of the gases. For an electrode width > 100 μm, no converged solution for a uniform thickness Nafion film was found thata could accommodate gas transport at the edges of the electrodes. For an electrode width of < 100 μm, at a constant Nafion thickness the maximum resistive loss was comparable (< 0.15 mV variation) with or without the lateral conductive layer present.

3.4.2 Comparison to a liquid water divice

An integrated photoelectrolysis system that does not have a liquid aqueous electrolyte but that nevertheless is sustained by a liquid water feed has similar design constraints to the systems evaluated herein based on a water vapor feed. However, the use of liquid water as the feedstock has two adverse effects on the system performance: i) a slightly higher (~ 44 mV) thermodynamic potential for the water-splitting reaction as compared to a vapor-fed device, ii) formation of bubbles at the Nafion/water interface. Moreover, an integrated system based on a liquid water feed or that contains a liquid aqueous electrolyte generally requires a relatively high-purity water solution to minimize contamination or corrosion of functional components (photoabsorbers, electrocatalysts, etc), whereas in a device fed by water vapor, a low purity water solution could be used as the source of the water vapor. Of course, the transport properties of a Nafion film can vary significantly in contact with different water sources, and such variations will alter somewhat the precise values of the optimum design parameters relative to those presented herein.

3.4.3 Comparison to an electrically connected PV and MEA design

A solar-driven water-splitting system sustained by a water vapor feed can also be realized by electrically connecting a PV unit to a membrane-electrode assembly (MEA). The MEA would then essentially operate as a fuel cell in reverse, in which the water vapor is the feedstock for the cathode and anode, and the photovoltage provided by the PV serves as the driving force for the electrolysis reaction. Detailed comparisons between an integrated photoelectrolysis device and a discrete PV+MEA system, for different band gap combinations of photoabsorbers[8] and various cell operating environments (irradiation and temperature), have been recently presented.[7] The integrated photoelectrolysis system leverages enhanced kinetics and transport at elevated temperatures, and therefore would outperform a discrete PV unit connected electrically to a discrete electrolysis system.[7] Moreover, an integrated photoelectrolysis system permits the use of a semiconductor/electrolyte junction, in which a single photoabsorber material serves as the

photocathode or anode in contact with electrolyte solution, in contrast to a standalone PV+MEA system in which a “buried” junction is required.

3.5 Conclusions

Detailed geometric parameters in two cell designs were investigated in this study for a photoelectrolysis system sustained by a water vapor feed. In Design A, the thickness of the Nafion film cannot exceed 1.9 μm to accommodate the product gas transport, and the width of the photoelectrode cannot exceed ~ 300 μm, to hold the resistive losses in the system to acceptable levels. In Design B, the maximum electrode width can be significantly increased, to ~ 4.5 mm by employing a structured Nafion film, for which the width of the Nafion channel cannot exceed 5.17 μm to accommodate the the required transport of the product gases. To prevent significant diffusive gas crossover (4%) for micro-sized electrodes, the width of the electrode has to exceed 45.5 μm or 20.2 μm, respectively for electrode heights of 1 μm or 10 μm, respectively. A lateral conductive layer, typically employed to lower the resistive loss in a photoelectrolysis system based on a liquid electrolyte, is unfavorable in a water vapor device, due to enhanced current densities at the electrode edges that cause supersaturation of product gases in the system.

REFERENCES:

1. Lewis, N. S., Toward cost-effective solar energy use. *Science* **2007,** 315, (5813), 798-801.

2. Lewis, N. S.; Nocera, D. G., Powering the planet: Chemical challenges in solar energy utilization. *Proceedings of the National Academy of Sciences of the United States of America* **2007,** 104, (50), 20142-20142.

3. Walter, M. G.; Warren, E. L.; McKone, J. R.; Boettcher, S. W.; Mi, Q. X.; Santori, E. A.; Lewis, N. S., Solar Water Splitting Cells. *Chemical Reviews* **2010,** 110, (11), 6446-6473.

4. Xiang, C. X.; Kimball, G. M.; Grimm, R. L.; Brunschwig, B. S.; Atwater, H. A.; Lewis, N. S., 820 mV open-circuit voltages from Cu_2O/CH_3CN junctions. *Energy & Environmental Science* **2011,** 4, (4), 1311-1318.

5. Xiang, C. X.; Meng, A. C.; Lewis, N. S., Evaluation and optimization of mass transport of redox species in silicon microwire-array photoelectrodes. *Proceedings of the National Academy of Sciences of the United States of America* **2012,** 109, (39), 15622-15627.

6. Haussener, S.; Xiang, C. X.; Spurgeon, J. M.; Ardo, S.; Lewis, N. S.; Weber, A. Z., Modeling, simulation, and design criteria for photoelectrochemical water-splitting systems. *Energy & Environmental Science* **2012,** 5, (12), 9922-9935.

7. Haussener, S.; Hu, S.; Xiang, C.; Weber, A. Z.; Lewis, N., Simulations of the irradiation and temperature dependence of the efficiency of tandem photoelectrochemical water-splitting systems. *Energy & Environmental Science* **2013**.

8. Hu, S.; Xiang, C.; Haussener, S.; Berger, A. D.; Lewis, N. S., An analysis of the optimal band gaps of light absorbers in integrated tandem photoelectrochemical water-splitting systems. *Energy & Environmental Science* **2013**.

9. Reece, S. Y.; Hamel, J. A.; Sung, K.; Jarvi, T. D.; Esswein, A. J.; Pijpers, J. J. H.; Nocera, D. G., Wireless Solar Water Splitting Using Silicon-Based Semiconductors and Earth-Abundant Catalysts. *Science* **2011,** 334, (6056), 645-648.

10. Suntivich, J.; May, K. J.; Gasteiger, H. A.; Goodenough, J. B.; Shao-Horn, Y., A Perovskite Oxide Optimized for Oxygen Evolution Catalysis from Molecular Orbital Principles. *Science* **2011,** 334, (6061), 1383-1385.

11. Boettcher, S. W.; Warren, E. L.; Putnam, M. C.; Santori, E. A.; Turner-Evans, D.; Kelzenberg, M. D.; Walter, M. G.; McKone, J. R.; Brunschwig, B. S.; Atwater, H. A.; Lewis, N. S., Photoelectrochemical Hydrogen Evolution Using Si Microwire Arrays. *Journal of the American Chemical Society* **2011,** 133, (5), 1216-1219.

12. Zhang, Y. J.; Wang, C.; Wan, N. F.; Liu, Z. X.; Mao, Z. Q., Study on a novel manufacturing process of membrane electrode assemblies for solid polymer electrolyte water electrolysis. *Electrochemistry Communications* **2007,** 9, (4), 667-670.

13. Grigoriev, S. A.; Porembsky, V. I.; Fateev, V. N., Pure hydrogen production by PEM electrolysis for hydrogen energy. *International Journal of Hydrogen Energy* **2006,** 31, (2), 171-175.

14. Khaselev, O.; Turner, J. A., A monolithic photovoltaic-photoelectrochemical device for hydrogen production via water splitting. *Science* **1998,** 280, (5362), 425-427.

15. Licht, S.; Wang, B.; Mukerji, S.; Soga, T.; Umeno, M.; Tributsch, H., Efficient solar water splitting, exemplified by RuO_2-catalyzed AlGaAs/Si photoelectrolysis. *Journal of Physical Chemistry B* **2000,** 104, (38), 8920-8924.

16. Philippe, M.; Jerome, H.; Sebastien, B.; Gerard, P., Modelling and calculation of the current density distribution evolution at vertical gas-evolving electrodes. *Electrochimica Acta* **2005,** 51, (6), 1140-1156.

17. Eigeldinger, J.; Vogt, H., The bubble coverage of gas-evolving electrodes in a flowing electrolyte. *Electrochimica Acta* **2000,** 45, (27), 4449-4456.

18. Janssen, L. J. J.; Vanstralen, S. J. D., Bubble Behavior on and Mass-Transfer to an Oxygen-Evolving Transparent Nickel Electrode in Alkaline-Solution. *Electrochimica Acta* **1981,** 26, (8), 1011-1022.

19. Bryson, A. W.; Hofman, D. L., A Population Balance Approach to the Study of Bubble Behavior at Gas-Evolving Electrodes. *Journal of Applied Electrochemistry* **1989,** 19, (1), 116-119.

20. Bard, A. J.; Faulkner, L. R., *Electrochemical Methods, Fundamentals and Applications.* 2nd edition ed.; Wiley: 2000.

21. Spurgeon, J. M.; Lewis, N. S., Proton exchange membrane electrolysis sustained by water vapor. *Energy & Environmental Science* **2011,** 4, (8), 2993-2998.

22. Newman, J.; Thomas-Alyea, K., *Electrochemical Systems*. Wiley & Sons: 2004.

Chapter IV

MODELING THE PERFORMANCE OF AN INTEGRATED PHOTOELECTROLYSIS SYSTEM WITH 10X SOLAR CONCENTRATORS

4.1 Introduction

Artificial photosynthesis could provide a promising route to large-scale solar energy conversion and storage[1-4]. Recent techno-economic studies have evaluated various designs for integrated photoelectrolysis systems, including a very promising system that makes use of concentrated illumination.[5,6] A discrete III-V photovoltaic cell connected electrically in series with a discrete polymer-electrolyte membrane (PEM) electrolyzer has demonstrated a solar-to-hydrogen (STH) conversion efficiency of 18% under 500 Suns[7]. Although concentrated photovoltaics (CPV) typically incorporate multi-stage optical systems to achieve high optical concentration (~ 400 Suns to 1200 Suns),[8-10] integrated photoelectrochemical systems for large scale, distributed solar-to-fuel applications are most likely operate efficiently and scalably at lower solar concentration factors (5 – 100) due to limitations associated with electrocatalytic overpotential losses, ohmic losses, and mass transport restrictions associated with high current densities in a system operating under very concentrated sunlight. Notably, systems that utilize a low-multiple concentrating solar collector, such as a 10× concentrator, requires little or no active solar tracking or temperature-regulation systems.[11-13] The conceptual designs of coupling low concentrator solar collectors with a photoelectrochemical cell were developed by a few researchers.[14,15] A principal advantage of a sunlight-concentrating design for a solar-to-fuels generator is the potential

---

This chapter is based on results in: Yikai Chen *et al* 2014 J. Electrochem. Soc. 161 F1101 – Published by The Electrochemical Society.

reduction of the usage per unit area of photoabsorber materials, which could result in a significant reduction in the system cost.[5,6] Although extensive modeling and simulation efforts have been completed for solar fuel generator system designs without solar concentrators, including various operating conditions and using different types of input feed-stocks including liquid electrolytes[16-18] and water vapor feeds[19], the design criteria and constraints for an integrated system that exploits concentrating solar collectors have not yet been evaluated.

The high-intensity illumination, and the expected elevated operating temperatures in a light-concentrating photoelectrolysis system, could have significant impacts on the performance of the individual components of the system, and thus on the efficiency of the system as a whole. Increases in the illumination intensity would increase the photocurrent density and would concomitantly improve the open-circuit voltage and the fill factor of the current-voltage characteristic of the photoabsorber materials.[20] The increased current density would also, however, result in an increase in the ohmic losses of the cell, as well as produce an increase to the overpotentials required to drive the oxygen-evolution reaction (OER) and the hydrogen-evolution reaction (HER).[21] Increases in the operating temperatures would introduce similar trade-offs to the system design, because the increased temperature would degrade the performance of the semiconducting light absorbers while improving both the mass transport in the electrolyte and the performance of the HER and OER catalysts. As a result, the overall system efficiency as a function of the cell geometry, the illumination intensity, and the operating temperature depends upon the working principles for each component as well as upon the detailed mathematical relationships between the components. Previously reported results from the modeling of integrated photoelectrolysis system designs without solar concentrators have shown that the geometric parameters of the cell dominate the cell performance. Specifically, the width of the photoelectrode must be less than a few centimeters to minimize the ohmic losses from the ionic transport in the electrolyte and membrane.[17,22] At the higher operating current density produced by concentrated sunlight, the details of the cell geometry are likely to play an even more important role. Although a smaller cell will typically reduce the efficiency losses due to mass transport in the electrolyte,

the assembly and integration of absorber materials and other system components could be easier with macroscopic, rather than microscopic, components. Thus, an optimal design would likely maximize the photoelectrode width while minimizing any efficiency losses due to mass transport limitations and ohmic losses.

In this work, two types of integrated photoelectrolysis systems that use a concentrated light source have been investigated: a two-dimensional "trough" design and a three-dimensional "bubble wrap" design. The concentration of the illumination was chosen to be ten-fold relative to natural sunlight. The solar-to-hydrogen (STH) conversion efficiency for the systems, and the ohmic loss as a function of the cell geometry, operating temperatures, and catalyst performance were evaluated systematically using a fully coupled model for the system as a whole. We have also evaluated the requirements for the size and placement of a proton-exchange membrane, such as Nafion, to minimize the usage of this material, as well as of analogous high-performance polymers, as the permselective gas-blocking component of the system.

4.2 Modeling

Cell designs

Figure 4.1 presents schematically the two cell designs that were modeled in this work. Both designs include a 10× solar concentrator and an integrated photoelectrolysis assembly. The detailed configuration and construction of the solar concentrator is beyond the scope of this work, but two-dimensional or three-dimensional Fresnel lens, compound parabolic concentrators (CPC), or dielectric totally internally reflecting concentrators could be employed to achieve the 10× solar concentration specified in the designs. For example, with ten-fold concentration, efficient light collection up to 7.5 hours/day can be achieved by compound parabolic concentrators only with occasional tilt adjustments.[23] The two-dimensional "trough" design (Fig.4.1a) contains a photoelectrode having a width, l_e, with l_e constrained to be 10% of the total cell width, l_c, consistent with 10x concentrating optics. The photoelectrode was taken to be infinitely long in the out-of-plane direction. The three-

dimensional “bubble wrap” design (Fig. 4.1b) consists of a disk photoelectrode with a diameter, d_e, that was constrained to be 32% of the cell diameter, d_c, again consistent with 10x concentrating optics. Both designs contained Nafion films and insulating plastics to prevent product crossover and for structural support. The Nafion films also provided the required pathways for ionic conduction between the photocathode and photoanode chambers. The detailed construct of the integrated photoelectrochemical cell is shown in Figure 4.1c. The photoanode and photocathode are each assumed to be coated by a protective transparent conductive oxide (TCO) layer, to aid in uniformity of the current density distribution and minimize the ohmic losses in the system. Oxygen-evolution catalysts were coated on top of the TCO in the photocathode, whereas hydrogen-evolution catalysts were coated on the bottom of the TCO in the photoanode.

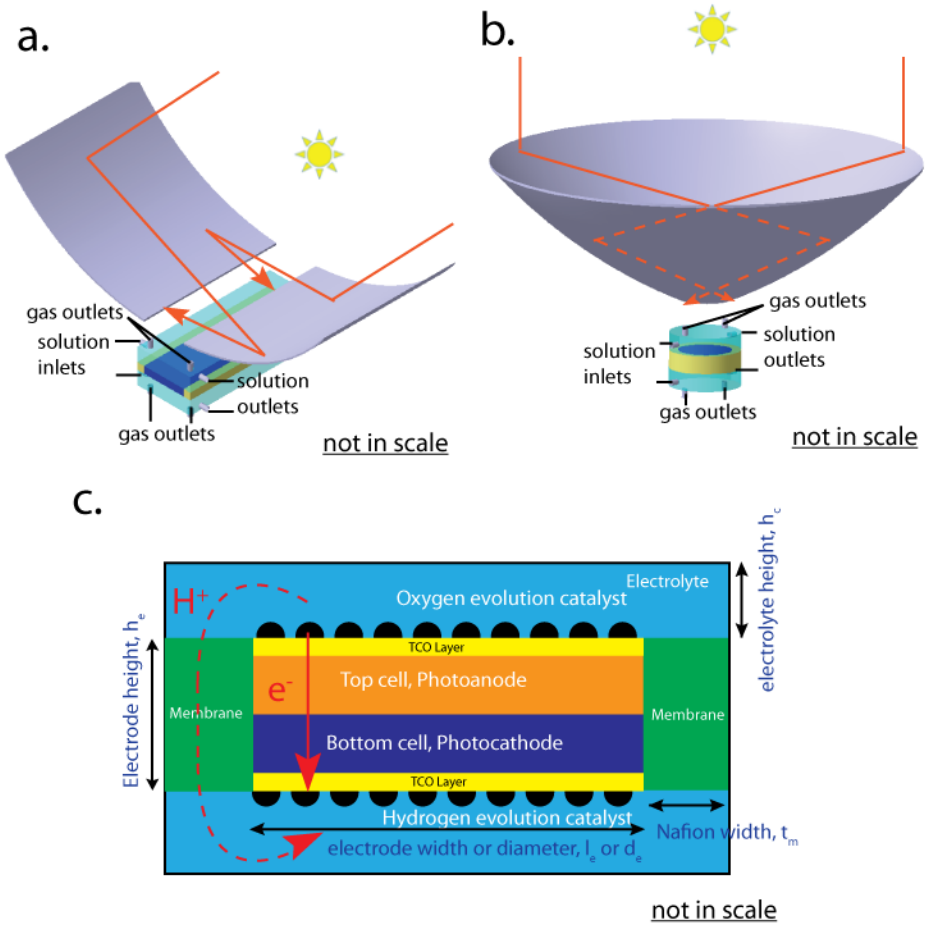

Figure 4.1. Schematic illustrations of two designs for a 10× concentrator photoelectrolysis system: a) a two-dimensional "trough" design and b) a three-dimensional "bubble wrap" design. Both designs contain a solar concentrator (grey) and an integrated photoelectrolysis assembly. The orange lines schematically indicate selected ray traces of the light path that concentrates the sunlight. c) Cross-sectional illustration of an integrated photoelectrolysis system, which includes a photoanode (orange), a photocathode (purple), TCO layers (yellow), oxygen-evolution catalysts (top black hemispheres), hydrogen-evolution catalysts (bottom black hemispheres), Nafion films (green) and solution electrolyte (blue). The electronically conductive pathways occur from the oxygen-evolution catalysts through the TCO, the top cell, the bottom cell, and the second TCO, to the hydrogen-evolution catalysts (solid arrow). The main ionically conductive pathways (dashed arrows), that produce the predominant ohmic drop in the system, occur laterally from the oxygen-evolution catalysts (that are the site of proton production during current flow) in the top electrolyte to and through the surrounding membrane, and laterally in the bottom electrolyte to the hydrogen-evolution catalysts (that are the sites of proton consumption during current flow). The electrode width, electrode diameter, electrode height, electrolyte height and Nafion width were represented by l_e, d_e, h_e, h_c, t_m, respectively.

Table 4.1 presents the basic input parameters used in the model. The system performance was evaluated for two pairs of OER and HER catalysts in 1.0 M H_2SO_4. The "No. 1" catalyst system assumed electrocatalytic properties typical of iridium oxide for the OER and platinum for the HER in acidic conditions, while the "No. 2" catalyst system assumed twice the OER and HER overpotentials exhibited by the "No. 1" catalyst system to produce a current density of 100 mA cm^{-2} for the anodic and cathodic processes respectively, based on the geometric area of a planar electrode.

	Operating temperature	
	300 K	350 K

Electrochemical kinetics	OER exchange current density, $i_{0,OER}$	0.0014 A m^{-2}	0.015 A m^{-2}
	OER anodic transfer coefficient, $\alpha_{a,OER}$	1.0 (No. 1 catalyst) 0.5 (No. 2 catalyst)	1.0
	OER cathodic transfer coefficient, $\alpha_{c,OER}$	0.1	
	HER exchange current density, $i_{0,HER}$	10 A m^{-2}	52 A m^{-2}
	HER anodic transfer coefficient, $\alpha_{a,HER}$	2.57 (No. 1 catalyst system) 1.27 (No. 2 catalyst system)	2.57
	HER cathodic transfer coefficient, $\alpha_{c,HER}$	2.57 (No. 1 catalyst system) 1.27 (No. 2 catalyst system)	2.57
	Electrolysis, ϕ_0	1.229 V	1.179 V
TCO	Conductivity, σ_{el}	10^5 S m^{-1}	$1.2x10^5$ S m^{-1}
Nafion	Conductivity, σ_m	10 S m^{-1}	11.2 S m^{-1}
Electrolyte	Conductivity, σ_l	40 S m^{-1}	78 S m^{-1}
Light absorbers	Top cell band gap, $\mathbf{E}_{g1}$	1.7 eV	
	Bottom cell band gap, $\mathbf{E}_{g2}$	1.1 eV	

Table 4.1: Basic parameters used in the model.

Equations describing transport and kinetics

The ion transport in the electrolyte and in the proton-exchange membrane, as well as the transport of electrons and holes in the TCO coatings, were modeled using Ohm's law:

$$j_{\mathrm{el,TCO,mem}} = -\sigma_{el,\mathrm{TCO,mem}} \nabla \phi_{\mathrm{el,TCO,mem}}, \quad \text{(Eq. 4.1)}$$

where $\sigma_{el,TCO,mem}$ is the conductivity of the electrolyte, TCO or the membrane (Nafion), respectively, $\nabla \phi_{\mathrm{el,TCO,mem}}$ is corresponding potential drop and $j_{\mathrm{el,TCO,mem}}$ is the corresponding current density.

The kinetics of electrocatalysis at the TCO and at the electrolyte interface for the OER and HER were modeled using the Butler-Volmer equation:

$$j_{R,OER/HER} = j_{0,OER/HER}[\exp(\frac{\alpha_{a,OER/HER} F \eta}{RT}) - \exp(-\frac{\alpha_{c,OER/HER} F \eta}{RT})], \quad \text{(Eq. 4.2)}$$

where $j_{\mathrm{R},OER/HER}$ is the current density for the OER or HER at the electrode/electrolyte interface, $j_{0,OER/HER}$ is the exchange-current density for the OER or HER, respectively, $\alpha_{a,OER/HER}$ and $\alpha_{c,OER/HER}$ are the corresponding anodic and cathodic transfer coefficients, respectively, F is Faraday's constant, R is the ideal gas constant, and η is the overpotential for the reaction, which is defined as

$$\eta = \phi_s - \phi_l - \phi_0, \quad \text{(Eq. 4.3)}$$

where ϕ_s and ϕ_l are the electric and electrolyte potentials at the interface, respectively, and ϕ_0 is the equilibrium potential for the reaction. Conservation of charge and continuity of current density were enforced at both the cathodic and anodic interfaces.

Photoelectrode and temperature dependence

The photoelectrode was modeled as two semiconducting light absorbers connected in series. One absorber had a band gap of 1.7 eV and was located directly on top of the other absorber, which had a band gap of 1.1 eV. Without solar concentration, such a tandem cell can provide sufficient photovoltage at light-limited current densities to allow the use of earth-abundant catalyst materials in a photoelectrolysis system.[18] The STH conversion

efficiency as a function of different band gap combinations with realistic cell geometries was also calculated in this study. The photovoltage of the tandem photoelectrode at a given operating current density, *J*, was determined by adding the photovoltages of the serially connected top and bottom half-cells, i.e.:

$$V_{tandem}(J) = V_{top}(J) + V_{bottom}(J). \quad \text{(Eq. 4.4)}$$

The relationship between the current density and voltage of the top and bottom half-cells was determined using a detailed-balance calculation, in which the current density of each half-cell was set equal to the sum of the current density produced by the incident solar radiation (J_{ph}) and the thermal radiation (J_{th}), minus the current density from radiative emission (J_{rad}):

$$J = J_{ph} + J_{th} - J_{rad}. \quad \text{(Eq. 4.5)}$$

The analytical expressions for J_{ph}, J_{th} and J_{rad} are well described in literature.[24,25] The operating current density of each half-cell was then calculated numerically at a given photovoltage. 100% of the above-band-gap solar flux was assumed to be absorbed and converted to photocurrent, so the photocurrent density was given by:

$$J_{ph} = C \times e \int_{\mathbf{E}_g}^{\infty} \mathrm{d}\hbar\omega \ \frac{\Lambda}{\mathrm{d}\hbar\omega}, \quad \text{(Eq. 4.6)}$$

where *C* is the concentration factor, e is the unsigned charge on an electron, $\mathbf{E}_g$ is the band gap of the photoabsorber, Λ is the wavelength-dependent solar flux in the Air Mass (AM)1.5 solar spectrum, *ħ* is an abbreviation for $h/2\pi$ with *h* being Planck's constant, and □ is the frequency of the incident light.

The radiative-emission currents were calculated from the relationship:

$$J_{rad} = \frac{e(n_{top}^2 + n_{bottom}^2)}{4\pi^2 c^2} \int_{\mathbf{E}_g/\hbar}^{\infty} \omega^2 \exp\left(\frac{eV - \hbar\omega}{kT}\right) \mathrm{d}\omega \ , \quad \text{(Eq. 4.7)}$$

where n_{top} and n_{bottom} are the refractive indices of the media on the top and at the bottom of the cell, respectively, *V* is the operating voltage, *T* is the absolute temperature, *k* is Boltzmann's constant, and *c* is the speed of light. The thermal radiation currents as a function of *T* were given by:

$$J_{th} = \frac{e(n_{top}^2 + n_{bottom}^2)}{4\pi^2 c^2} \int_{\mathbf{E}_g/\hbar}^{\infty} \omega^2 \exp\left(-\frac{\hbar\omega}{kT}\right) \mathrm{d}\omega \ . \quad \text{(Eq. 4.8)}$$

The numerical relationship between the current-density and voltage that was obtained from the detailed-balance calculation was then fitted using Eq. 4.9 for an ideal diode coupled with an effective series resistance:

$$J = J_{ph} - J_0 \left\{ \exp\left[\frac{e(V + JR_s)}{kT} \right] - 1 \right\}. \qquad \text{(Eq. 4.9)}$$

where J_0 is saturation current density in the dark, V is the applied photovoltage, and R_s is the effective series resistance. The fitted value for J was then used as the boundary condition at the photoelectrode-TCO interface. The effective series resistance was varied to approximate various situations in which the solar cell operated either at the detailed-balance limit or under non-ideal operating conditions in which the fill factor varied from 0.65 to 0.90.

Temperature-dependent conductivity of the electrolyte and membrane

The conductivity of the electrolyte as a function of the operating temperature was defined by:

$$\sigma_{l,T} = \sigma_{l,ref}(1 + \alpha[T - T_{ref}]), \qquad \text{(Eq. 4.10)}$$

where the reference temperature, T_{ref}, was 300 K and the coefficient α was 0.019 K^{-1}, which was fitted using experimental data for 1 M sulfuric acid.[26]

The temperature-dependent conductivity of the Nafion and the TCO layer was calculated by:

$$\sigma_{mem/TCO,T} = \sigma_{mem/TCO,T_{ref}} \exp\left(\frac{E_{a,mem/TCO}}{RT_{ref}}\right) \exp\left(-\frac{E_{a,mem/TCO}}{RT}\right), \qquad \text{(Eq. 4.11)}$$

where $\sigma_{mem/TCO,T_{ref}}$ is the Nafion/TCO conductivity at the reference temperature (300 K), $E_{a,mem/TCO}$ is the activation energy for Nafion (set to 2000 J mol^{-1})[27,28] and for TCO (set to 3185 J mol^{-1})[29], respectively . The exchange-current density for the OER and HER, respectively, in the Butler-Volmer equation was defined using the activation energy $E_{a.OER/HER}$:[30]

$$j_{0,\mathrm{T},OER/HER} = j_{0,\mathrm{T}_{ref},OER/HER} \exp(\frac{E_{a.OER/HER}}{RT_{ref}}) \exp(-\frac{E_{a.OER/HER}}{RT}) \ , \quad \text{(Eq. 4.12)}$$

where $j_{0,\mathrm{T}_{ref},OER/HER}$ is the exchange current density for the OER or HER at the reference temperature, and $E_{a,OER/HER}$ was assumed to be 42560 J mol^{-1} and 28900 J mol^{-1} [31,32] for iridium oxide[33] and platinum[24, 25] catalysts, respectively, in 1 M H_2SO_4(aq).

Boundary conditions

Boundary conditions that preserved the symmetry of the current density at the vertical walls were employed for both the trough and bubble wrap designs. Insulating boundary conditions were used at the upper and bottom bounds of the electrolyte domains. The current flux entering the TCO layers was calculated from the photovoltage using Eq. 4.9. The electrochemical reactions for both designs were modeled as surface reactions occurring at the interface of the solution and the TCO layer. The ionic conductivities of the Nafion film and of 1 M H_2SO_4 that were used in the modeling are listed in Table 1. For the crossover calculation, the Dirichlet (or first-type) boundary condition was employed at the interfaces of the electrolyte and the TCO layers. The hydrogen (oxygen) concentrations at the cathode (anode) were set to 0.78 mM (0 mM) and 0 mM (1.23 mM), respectively. Insulating boundary conditions for the product gas flux were also applied at the upper and bottom bounds of the solution domains.

Free triangular discretization and a standard solver in the Comsol multi-physics package were used in the modeling. For both designs, the maximum and minimum mesh-element sizes were set to 10 μm and 0.5 μm, respectively. The maximum mesh-element growth rate and the resolution of curvature were set at 1.3 and 0.3, respectively. A relative tolerance of the corresponding variable of 0.001 was applied as the convergence criterion for both designs.

Operating principles of device efficiency

The instantaneous STH conversion efficiency of an integrated photoelectrolysis device, η_{STH}, was defined as:

$$\eta_{STH} = \frac{J \cdot \phi_0}{P} \eta_F \eta_{pc}, \quad \text{(Eq. 4.14)}$$

where J is the current density output from the device, ϕ_0 is the equilibrium potential of the electrochemical reaction, P is the input power of the solar energy, η_F is the Faradaic efficiency of the electrode reaction, and η_{pc} is the product-collection efficiency. η_F was set to unity in the model, while η_{pc} was defined by the following equation:

$$\eta_{pc} = \frac{\int_{A_{a/c}} j dA - \int_{A_{sep}} nFN_{fuel} dA}{\int_{A_{a/c}} j dA}, \quad \text{(Eq. 4.15)}$$

where j is the current density at the interfaces between the catalysts and the solution, the net reaction current, N_{fuel}, represents the current lost due to diffusive crossover of hydrogen from the cathode to the anode chamber, n is number of electrons transferred (2 for the HER and 4 for the OER), $A_{a/c}$ and A_{sep} are the electrode area and the Nafion area that separates the anodic and cathodic chambers, respectively.

To obtain a simple 0-dimensional analytical picture of the cell performance for diagnostic purposes, and therefore to aid in understanding the efficiency of the entire system at the individual-component level, the current-voltage characteristics of the cell, and the polarization curve for the water-splitting reaction, were typically overlaid to determine the operating current density.

Comparison to photovoltaic cell in series with an electrolyzer

The STH efficiency of a stand-alone photovoltaic cell connected electrically in series with a discrete electrolyzer (PV + electrolyzer) was defined as,

$$\eta_{STH} = \eta_{PV} \cdot \eta_{electrolyzer} \cdot \eta_{DC-DC-converter}, \quad \text{(Eq. 4.16)}$$

where η_{PV} is the solar-to-electricity conversion efficiency of the photovoltaic cell, $\eta_{electrolyzer}$ is the electricity-to-hydrogen conversion efficiency of the electrolyzer and $\eta_{DC-DC-converter}$ is the efficiency of a DC-to-DC converter. The efficiency of the electrolyzer used for this comparison was the value optimized at a current density of ~1 A cm^{-2} and within the temperature range from 70 ºC to 80 ºC, representive of the performance characteristics of state-of-the-art commercially available electrolyzers.[34-37] In this study, an electrolyzer efficiency of 73.0% and a DC-to-DC converter efficiency of 85% (representative of values for converters that need to perform dynamic maximum power point tracking on the input DC power from the PV array as well as independent tracking on the output DC power that is supplied to the electrolyzer to insure maximum electrolyzer efficiency) were used in the calculation. The efficiency of the PV was chosen to be the detailed balance limit, for the same tandem photoabsorber system with the same band gap combination.

4.3 Results

4.3.1 Spatially non-uniform current density and catalytic overpotentials

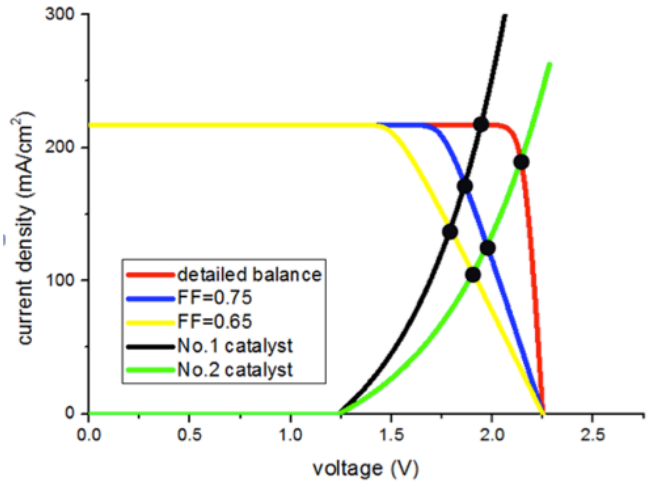

Figure 4.2 0-dimensional calculations of the operating current densities determined by the crossing points between the water-splitting polarization curves and the current density-voltage characteristics for tandem photoelectrode materials with three different fill factors

and two sets of catalysts. The detailed photovoltaic parameters and electrochemical parameters are listed in Table 4.1.

Figure 4.2 illustrates the results from a 0-dimensional analytical calculation of the performance of solar cells with three fill factors: detailed balance, 0.75, and 0.65, and the accompanying polarization behavior for the two modeled catalyst systems. The operating temperature for the cells was 300 K. The overall cell efficiency, which is determined by the operating current density at the crossing point, clearly depended strongly upon the combination of the current-voltage characteristics and the polarization behavior. However, the over-simplified 0-dimensional model can not adequately describe the non-uniform distribution of current at the photoelectrode and the resistive loss in the solution associated with specific geometries, both of which could have significant impacts on the cell efficiency.

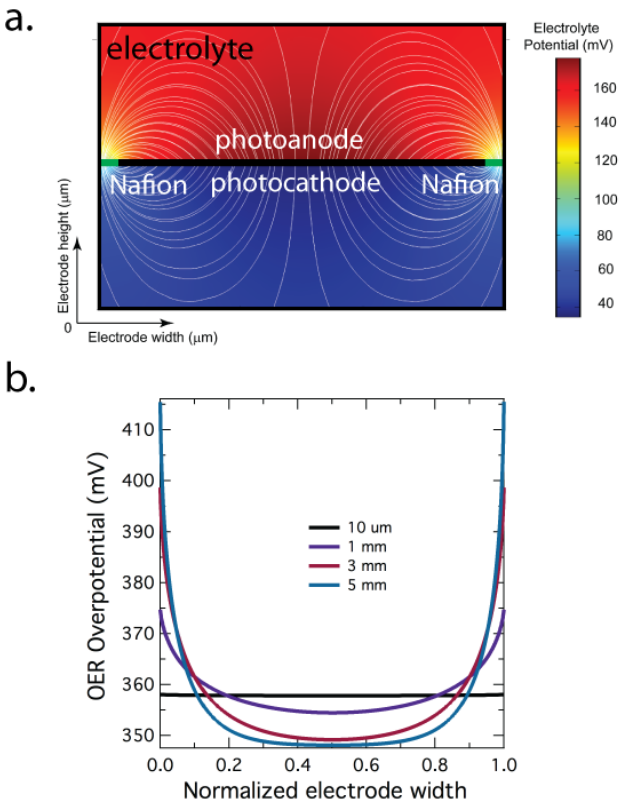

Figure 4.3. (a) Electrolyte potential-distribution profile for a “trough” design, with the electrode width, electrode height, solution height and Nafion coverage set to 3 mm, 10 μm,

5 mm and 1%, respectively. The black line represents the photocathode and photoanode assembly and the red lines represent the Nafion film. The streamline here represents the electrolyte current density. (b) The OER overpotential as a function of the normalized electrode width for a "trough" design with four electrode widths: 10 μm (black), 1 mm (red), 3 mm (green) and 5 mm (blue) under detailed-balance conditions at 350 K.

Figure 4.3a shows the potential profile within the electrolyte and the current-density distribution for a cross section of a "trough" cell. Due to the spatial distribution of the solution resistance, the overall polarization behavior at different locations along the electrode width varied significantly, especially for large electrode widths. Thus, even with the same current-voltage performance of the light absorber, the crossing point of the water-splitting polarization behavior and the photo-diode behavior, which determined the operating current density, varied along the electrode width. Consequently, the overpotentials for HER and OER along the electrode width also exhibited a strong position dependence. For example, Figure 4.3b shows the OER overpotential along the electrode for electrode widths of 10 μm, 1 mm, 3 mm and 5 mm, respectively. The distribution of the current density along the electrode width was highly non-uniform for this light-concentrating photoelectrolysis system. Compared to an unconcentrated system (data not shown), the OER overpotential difference between the mid-point and the two ends of the electrode increased from 6.5 mV to 49.4 mV (Figure 4.3b) and the maximum resistive loss increased from 17.2 mV to 143.1 mV (Figure 4.3a) with the same electrode width, electrode height and Nafion area (noted that the areal Nafion coverage for the un-concentrated system is 10 times larger than for the system that utilizes solar concentration).

4.3.2 STH Conversion Efficiency

The performance as a function of three important system-related geometric parameters: the electrode width or diameter; the electrode height; and the areal Nafion coverage of the entire cell, was evaluated systematically for both types of cell designs. The solution height was set to 5 mm (from the electrode to the upper or lower bound of the cell) so that the cell performance had a very weak dependence on the solution height.(17) The detailed current

density versus voltage characteristic of the tandem photoabsorbers was expected to have a significant impact on the overall value of η_{STH}. Figure 4.4 shows η_{STH} for the trough (a) and the bubble wrap (b) designs as a function of the electrode width, the electrode height and the Nafion coverage, for light absorbers operating at fill factors of 0.65 (i), 0.75 (ii), and for the detailed-balance limit (iii), respectively, at 350 K. In both designs, η_{STH} increased monotonically as the electrode width and height decreased, and as the Nafion coverage increased. The value of η_{STH} also increased as the fill factor of the tandem light absorbers increased from 0.65 to 0.885 (detailed-balance condition) in all cases. While the two designs showed similar efficiency trends, the efficiency of the bubble-wrap design was slightly higher than that of the trough design, when the electrode width of the trough design was equal to the electrode diameter in the bubble-wrap design. This difference occurred due to enhanced radial transport in the electrolyte in the latter design. For small electrode dimensions, the cell efficiencies exhibited a weak dependence on the Nafion coverage. For example, in the bubble-wrap design, increasing the Nafion coverage from 0.2% to 1% resulted in an increase in η_{STH} of a large electrode (d_e = 1 cm, h_e = 100 μm) from 11.7% to 25.0%, but for small electrode (d_e = 10 μm, h_e = 1 μm) η_{STH} remained unchanged at 25.5%. The value of η_{STH} reached a plateau as the Nafion coverage reached 1% of the entire cell width for both designs, which indicated that a large portion of the separator could be made of non-porous plastic without compromising the cell performance in either design. The decrease of the STH conversion efficiency due to the product gas crossover in both designs, even with smallest cell dimensions, was negligible (< 0.5%) due to the use of a membrane separator.

4.3.3 Ohmic losses associated with proton transport in the solution and in the membrane separator

An efficient solar-to-fuel generator requires low (< 100 mV) ohmic losses in the entire system.[17] The ohmic loss is however highly dependent on the cell geometry. As shown in Figure 4.1c, both electrons and ions must be transported at steady-state from the anode/OER interface to the cathode/HER interface. Hence, the electronically conductive

pathways occur from the oxygen-evolution catalysts through the TCO, the top cell, the bottom cell, and the second TCO, to the hydrogen-evolution catalysts. In contrast, the main ionically conductive pathways, that produce the predominant ohmic drop in the system, occur laterally from the oxygen-evolution catalysts (that are the site of proton production during current flow) in the top electrolyte to and through the surrounding membrane, and laterally in the bottom electrolyte to the hydrogen-evolution catalysts (that are the sites of proton consumption during current flow). Figures 4.5a and 4.5b, respectively show the ohmic loss calculated using system parameters that correspond to Figures 4.4a (iii) and 4.4b (iii), respectively. To produce low ohmic losses in the trough design, the electrode width cannot exceed 2 mm, and the electrode height cannot exceed 40 μm (Figure 4.5a). The corresponding low ohmic loss criterion for the bubble-wrap design was satisfied when the electrode diameter did not exceed 3 mm and the electrode height did not exceed 50 μm (Figure 4.5b). Compared to the trough design, the same electrode dimensions in the bubble-wrap design resulted in less resistive loss due to improved radial transport of ionic species in the electrolyte. Interestingly, a very small Nafion coverage (0.2%) could produce an ohmic resistive loss of <100 mV in a bubble-wrap cell with an electrode diameter as large as 2 mm.

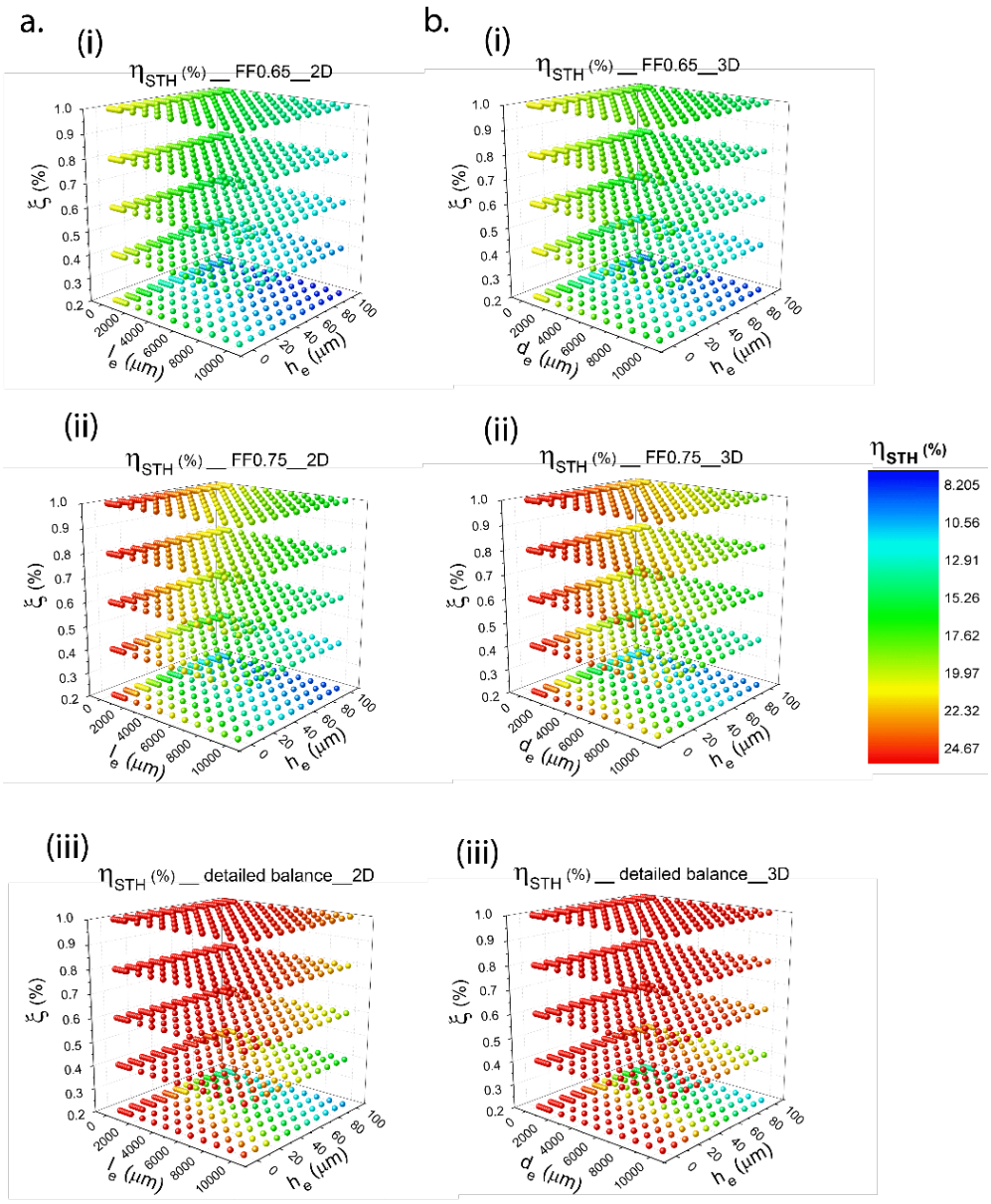

Figure 4.4. η_{STH} calculated for the "trough" design (a) and for the "bubble wrap" design (b) as a function of the electrode width/diameter, l_e/d_e, the electrode height, h_e, and the Nafion coverage, for the tandem photoabsorbers at 350 K with a fill factor of 0.65 (i), 0.75 (ii) and at the detailed-balance limit (iii). The electrode width/diameter, l_e/d_e, was varied from 10 μm to 1mm, with an interval of 150 μm, as well as from 1 mm to 1 cm, with an interval of 1 mm. The electrode height, h_e, was set from 1 μm to 100 μm, with an interval of 10 μm. The Nafion coverage, was set from 0.2% to 1%, with an interval of 0.2.

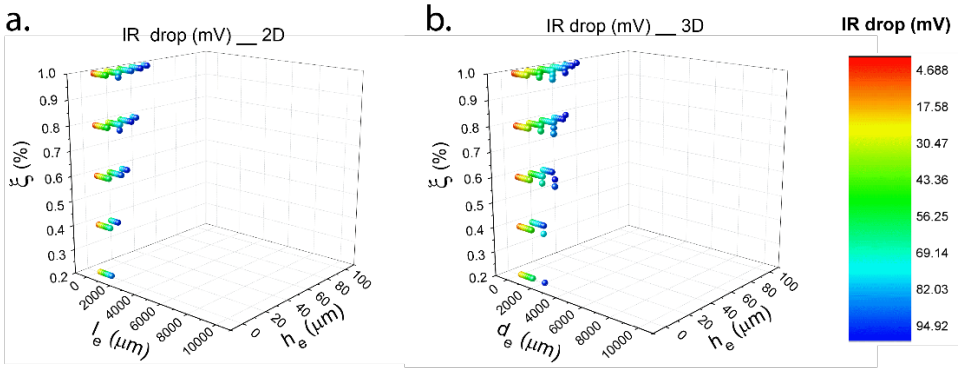

Figure 4.5. The geometric regions (electrode width, height and Nafion coverage) that maintained a low resistive loss (< 100 mV) in the "trough" design (a) and the "bubble wrap" design (b).

4.3.4 Effect of catalysts

The 10× concentrator design will operate at a higher current density (~ 10× higher on average) than an unconcentrated system, so the kinetic overpotentials for HER and OER may be more critical to the overall η_{STH} in concentrated designs than in systems that do not utilize solar concentration. Figure 4.6 compares η_{STH} for both pairs of catalysts under detailed-balance conditions at 300 K. For small electrode sizes (electrode width < 600 μm and electrode height < 10 μm for the trough design or electrode diameter < 1 mm and electrode height < 20 μm for the bubble-wrap design) η_{STH} was essentially unchanged (< 3 percentage-point difference) when the different electrocatalysts were used, because the water-splitting polarization and photodiode behavior crossed at the plateau of the current density versus voltage curve, where the operating current density remained nearly constant. As the electrode width increased, η_{STH} exhibited a stronger geometric dependence on the properties of the electrocatalysts. For instance, for the large electrode (l_e = 1 cm, h_e = 1 μm) in the trough design, η_{STH} decreased from 22.1% to 7.3% when the "No. 1" catalyst pair was exchanged for the "No. 2" catalyst pair. The 0-dimensional analysis in Figure 4.2

illustrated the situation in which η_{STH} was strongly dependent on the catalyst activities at large electrode dimensions.

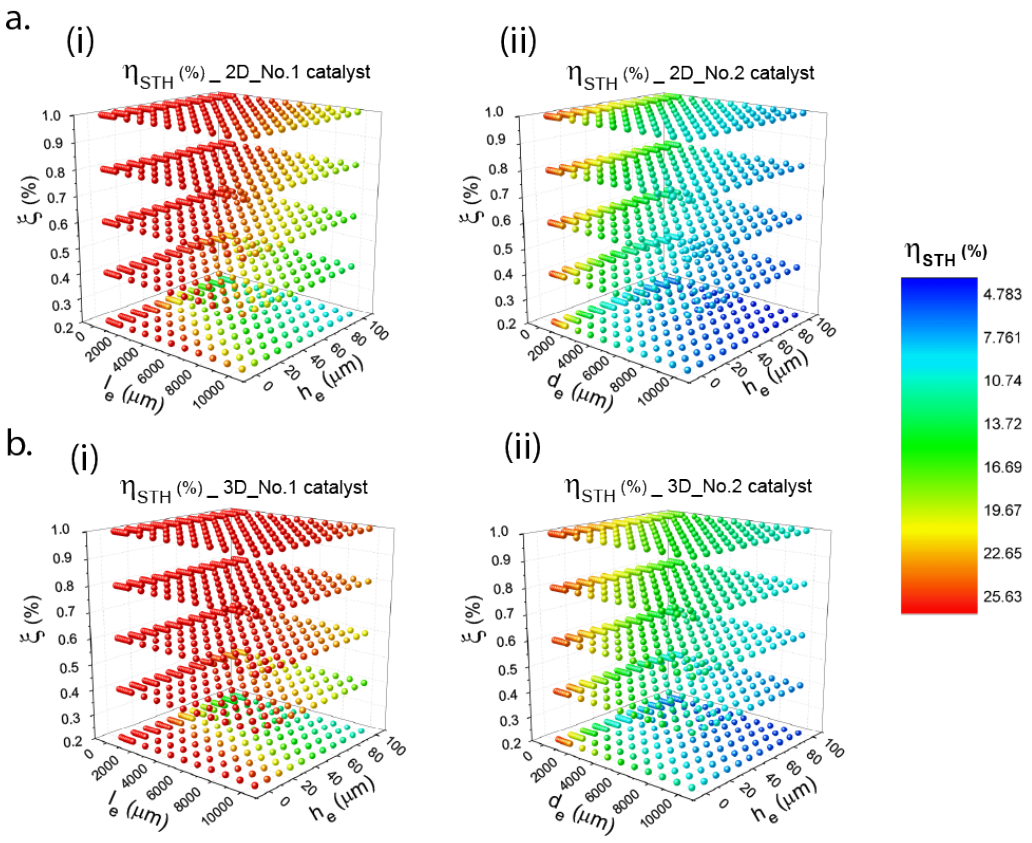

Figure 4.6. η_{STH} for the trough (a) and bubble-wrap (b) designs with the "No. 1" catalyst system (i) and the "No. 2" catalyst system (ii).

4.3.5 Effect of operating temperature

Figure 4.7 shows η_{STH} for the systems at operating temperatures of 300 K and 350 K, respectively, with various combinations of the geometric parameters and with the photoabsorbers assumed to operate at the Shockley-Queisser detailed-balance limit. Two geometric regions, that exhibited opposite dependences of η_{STH} vs *T*, were observed in the simulations. Figures 4.7a(iii) and 4.7b(iii) show, for both designs, the difference between η_{STH} at 350 K and η_{STH} at 300 K. When the solution transport and kinetic overpotential losses were small (i.e. at small electrode dimensions, and with a large Nafion coverage),

η_{STH} decreased with increased operating temperature. For example, η_{STH} decreased from 26.7% to 25.5% for an electrode that was 10 µm wide and 1 µm thick when the Nafion coverage was 1% in the trough design (and from 26.7% to 25.5% for an electrode with a

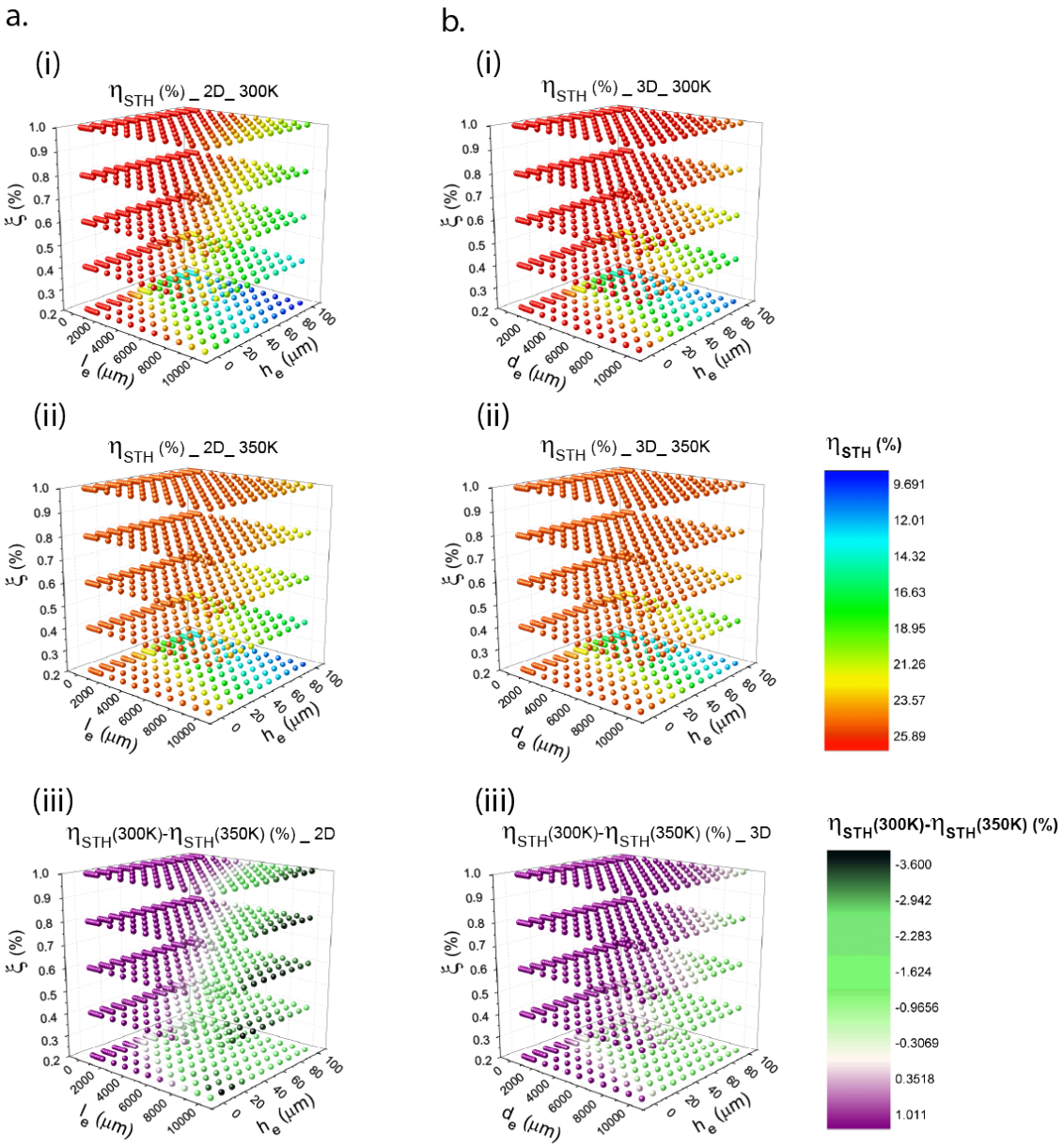

Figure 4.7. η_{STH} at 300 K (i) and 350 K (ii) and the STH conversion-efficiency difference in percentage points (iii) for the trough (a) and the bubble-wrap (b) designs.

diameter of 10 μm and 1 μm thick when the Nafion coverage was 1% in the bubble-wrap design). In this geometric region, the decrease of η_{STH} with increasing *T* was dominated by the degradation of the performance of the light absorbers as *T* increased. In contrast, when the solution-transport loss and the kinetic overpotential losses were large (i.e. at large electrode dimensions and with a small Nafion coverage), η_{STH} increased as *T* increased. For example, η_{STH} increased from 8.9% to 10.2% with a 1 cm electrode width, 100 μm electrode height and 0.2% Nafion coverage for the trough design (and from 10.6% to 11.7% with 1 cm electrode diameter, 100 μm electrode height and 0.2% Nafion coverage for the bubble-wrap design). In this geometric region, the increase of the η_{STH} as dominated by enhanced rate of electrocatalysis as well as by enhanced solution transport as the temperature was increased.

4.3.6 Comparison to a solar-hydrogen generator without a solar concentrator

While significant reduction of materials usage in solar concentrator coupled photoelectrochemical cells is advantageous comparing to cells without solar concentration, higher operating current densities in the concentrator design would result in higher catalytic overpotential and higher transport loss higher and thus would lower the STH conversion efficiency of the cell. Figure 4.8 shows η_{STH} of an un-concentrated cell system and the 10x "trough" design with identical cell geometries for the tandem photoabsorbers at different band gap combinations. With the optimized cell geometry and active catalysts ("No. 1" catalyst system), η_{STH} exhibited little change between the 10x concentrated and un-concentrated systems. However, when the cell geometry was not optimized, a significant decrease in η_{STH} and a significant difference in the band gap combination dependence of the cell efficiency were observed. A similar change in η_{STH} as a function of the band gap combination was also observed in the "bubble-wrap" design. When the state-of-the-art catalyst system was used and the cell geometry was optimized, η_{STH} in both concentrated and un-concentrated systems were not limited by the electrocatalysis or the solution resistive loss. As a result, no significant difference in η_{STH} was found between the two systems. However, when the resistive loss or electrocatalysis became the limiting factor

in the system, a notable change in η_{STH} was calculated between the two systems. From the simulation, the concentrated system exhibited a stronger dependence on the cell geometry than the unconcentrated system.

4.3.7 Comparison to a standalone PV + electrolyzer design

Figure 4.8 shows η_{STH} of a stand-alone PV+electrolyzer system (e) and of the integrated 10x "trough" design with an optimal geometry (b) as a function of different band gap combinations at 350 K. In both systems, state-of-the-art catalysts ("No. 1" catalyst system) were assumed. The highest value of η_{STH} for the PV+electrolyzer system was 25.9%, when the top material had a 1.6 eV band gap and the bottom material had a band gap of 0.9 eV. For comparison, when the cell geometry was optimized, the integrated "trough" design exhibited $\eta_{STH} = 29.8\%$ at the same band gap combination. A similar enhancement of η_{STH} was also observed in the "bubble-wrap" design relative to the PV+electrolyzer system. Of course, the efficiency values for the stand-alone PV+electrolyzer system are directly proportional to the values assumed for the dynamic DC-DC converter (85%) as well as the efficiency of the electrolyzer (73%), with changes in these subsystem efficiencies simply linearly affecting the overall efficiency values presented for the different band gap combinations in Figure 4.8.

4.4. Discussion

The higher currents in the 10× concentrator system increased the ohmic loss and also stressed the catalyst performance. However, the modeling described herein revealed that optimized cell designs, with the critical dimension of the photoelectrodes being less than a few millimeters, can result in very high STH conversion efficiencies, with η_{STH} =29.8% (Fig. 4.8b). These η_{STH} values are almost identical to the optimized instantaneous η_{STH} values for an integrated PEC system at 1 Sun (Fig. 4.8a). These 10× concentrator designs should therefore be considered as viable alternatives to "flat plate" designs that have been evaluated previously which utilize unconcentrated sunlight.

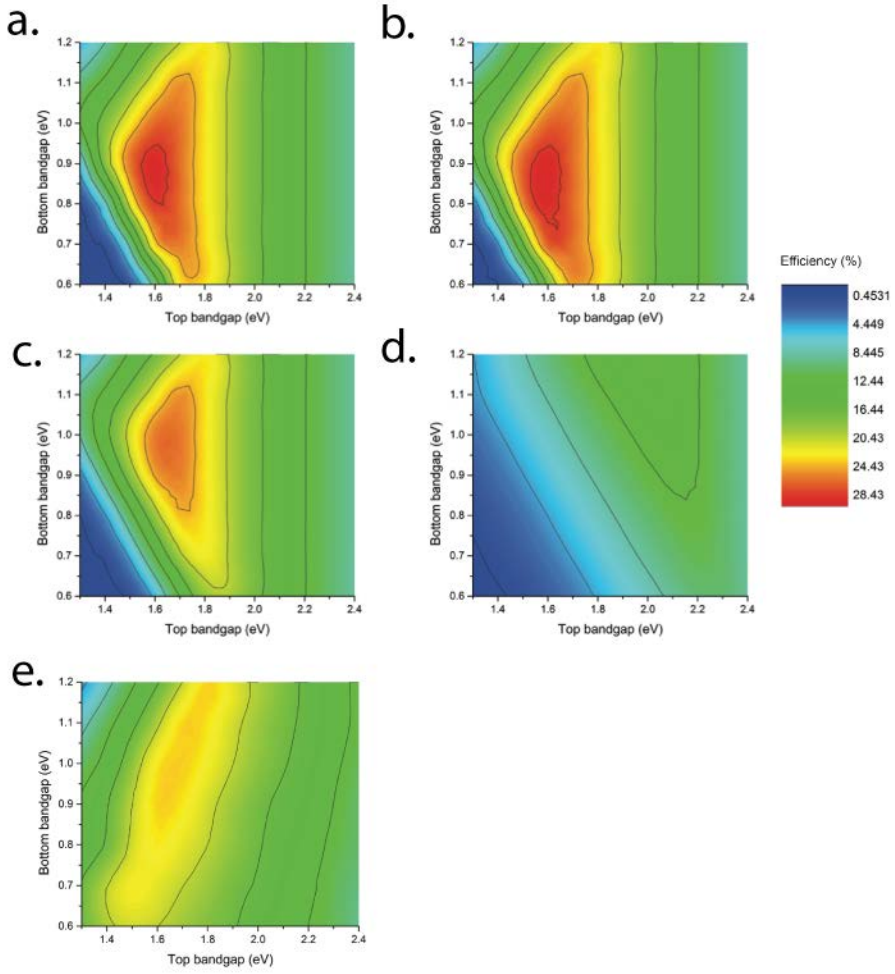

Figure 4.8. η_{STH} as a function of different band gap combinations for an un-concentrated system with optimized cell geometry (a), the 10x "trough" design with optimized cell geometry (b), an un-concentrated system with non-optimized cell geometry (l_e= 10 μm, h_e=1 μm) (c) and the 10x "trough" design with non-optimized cell geometry (l_e= 1 cm, h_e=100 μm) (d) at 350 K. η_{STH} as a function of different band gap combinations for a stand-alone PV+electrolyzer system (e) at 350 K. The "No. 1 catalyst system" was employed in all calculations.

The millimeter electrode length scale indicated by the modeling and simulation to be required for optimum η_{STH} with 10× solar concentration could be readily implemented in a practical electrode manufacturing and cell assembly process. Moreover, the reduction of the materials usage for the photoelectrode (10% of the system area) and the Nafion (< 1% of the system area) would significantly reduce the cost of these potentially expensive components of a whole, scalable, solar fuels generation system. Large areas of insulating plastic (~90% of the system area) and the absence of a diurnal solar and system temperature regulating system would reduce the maintenance of the system and additionally would likely reduce the cost of the balance of systems in the solar fuels generator.

In operation, the system will likely be tilted at some angle relative to the surface normal. However, the light absorption, carrier transport, electrocatalysis and solution transport analyzed herein within the constraints of the present model are not expected to be sensitive to the tilt angle of the system itself. Gas evolution and thermal lift would be expected to enhance the convective mass transport in the solution, but a through evaluation of these features of an operating system will require development of operational prototypes and comparison with a more complete model of such a system. Moreover, the choice of different levels of the tracking system (truly stationary, occasional tilt adjustment tracking or active diurnal tracking) is likely to be determined by the trade-off between the balance of systems cost and the efficiency of the solar concentrator, which is beyond the scope of this work.

The temperature profile of an actual operating system is highly dependent on the detailed construction of the cell, such as the particular encapsulation materials. Preliminary modeling results have suggested that a solar fuels generator system could operate at an elevated temperature (~330–350 K) without using an active cooling system.(13) However, the 10× concentrator designs exhibit a stronger temperature dependence of η_{STH} than systems that do not use solar concentration.(22) The trade-offs between the degradation of the PV performance and the enhancement of the solution transport and electrocatalysis as the temperature is increased depend strongly on the dimensions of the electrodes in the system. Specifically, for small electrode dimensions, at elevated temperatures the degradation of the PV materials dominates the entire cell performance (Figure 4.7).

However, for large electrode dimensions, under 10× concentration, the reduction of the ohmic loss and catalytic overpotentials improves η_{STH} for the designs evaluated herein (Figure 4.7).

In both of the simulated designs, a 500 nm thick TCO layer was applied on the top and the bottom of the photoabsorbers. This laterally conductive TCO layer facilitated a redistribution of current along the electrode width and reduced the ohimc loss in the system (Figure 4.3). In optimized cell designs, in which the electrode dimension is less than a few millimeters, η_{STH} was relatively insensitive to the presence or absence of the TCO layer. However, η_{STH} would be lowered by 1.0 percentage points for a large "trough" design (l_e = 1 cm, h_e = 100 μm) operating at 350 K under detailed balance conditions.

From an equivalent circuit viewpoint, the efficiency of the integrated system would be identical to that of a stand-alone PV+electrolyzer system, if both systems utilized light absorbers, catalysts, and electrolyzers that exhibited mutually identical current vs voltage relationships. In the specific case considered herein, the low resistive loss and low operating current density of the spatially distributed, "internal" electrolyzer in the integrated cell designs yielded a higher electricity-to-fuel conversion efficiency than a traditional electrolyzer, which often operates > 1 A cm^{-2}, due to the need to minimize the area-related balance of systems costs in stand-alone commercial electrolyzers. Therefore, the two optimized 10× concentrator designs, the "trough" design and the "bubble wrap" design, both outperformed the stand-alone PV+electrolyzer system on an efficiency basis when the same tandem photoabsorbers were utilized in each case. A full comparison between the two different system types would also clearly require an extensive cost analysi, but such is premature at this early stage of development of the type of integrated solar fuels generators evaluated herein.

A stand-alone PV+electrolyzer unit could in principle utilize a high-efficiency triple junction photovoltaic device, which can theoretically produce > 40% energy-conversion efficiency. The optimal band gaps, and operating voltages, of such triple junctions are

significantly larger than the optimal values for use in an integrated solar-driven water splitting system, which is more well-suited to use of tandem structures. An optimally performing triple-junction stand-alone PV+electrolyzer system would therefore clearly outperform the optically performing tandem-based integrated solar fuels generators considered herein. For comparison of both types of tandem-based systems, η_{STH} for the PV+electrolyzer is obviously dependent on the efficiency of the DC-to-DC converter as well as the efficiency of the stand-alone electrolyzer unit. For optimal performance, the stand-alone system would require a DC-DC converter that dynamically tracks the maximum power point of the PV array, and that also dynamically adjusts its output voltage and current to maintain optimal performance of the electrolyzer unit. Comparison of the data of Figures 4.4, 4.6 and 4.8, along with a linear increase of the efficiencies depicted in Figure 4.8 by higher assumed efficiencies for the electrolyzer and for the DC-DC converter in the stand-alone PV+electrolyzer combination, indicates that the optimized integrated system can in fact, with the physical electrode dimensions, membranes, electrolytes and system geometry described herein, provide comparable efficiency to that of an optimized, stand-alone PV+electrolyzer combination. The optimized 10× concentrator designs with smaller electrode dimensions described herein also permit the use of a semiconductor/liquid junction, in which no “buried” junction or lateral conductive TCO layer is required. The ability to utilize a stable semiconductor/liquid junction in the integrated design, e.g., a metal oxide/OER junction, would significantly broaden the materials choices relative to that available at present for a discrete PV unit, in which a solid-state “buried” junction is required.

4.5. Conclusions

In an integrated photoelectrolysis system that does not utilize solar concentration, maintaining low ohmic losses requires a maximum electrode width less than a few centimeters. In contrast, to maintain comparable ohmic losses, the integrated 10× concentrated devices modeled in this study, require that the maximum length of the electrode width or diameter must remain on the order of a few millimeters. The distribution of current density along the electrode width was observed to be nonuniform for the 10×

concentrator designs, particularly for large cell dimensions. The overall η_{STH} of systems with smaller electrode dimensions showed a weaker dependence on the performance of the photoabsorbers and the catalysts than cells with larger dimensions. Minimal coverage of Nafion (< 1% of the cell area) was needed to maintain an ohmic loss of < 100 mV in the bubble-wrap cell at the operating temperature of 350 K, with an electrode diameter and height as large as 2 mm and 1 μm, respectively. With the same Nafion coverage and electrode height, when the electrode width in the trough design equaled the electrode diameter in the bubble-wrap design, the bubble-wrap design exhibited higher η_{STH} due to enhanced radial solution transport. At elevated operating temperatures, η_{STH} of cells with smaller dimensions decreased due to degradation of the performance of the photoabsorber materials, while η_{STH} of cells with larger dimensions increased with temperature due to enhanced transport in the solution and enhanced catalytic activity. The simulations also indicated that both optimized 10× concentrator designs (having small electrode dimensions) yielded comparable performance to an optimized PV + electrolyzer system, validating the merit of considering such integrated designs for implementation of a solar fuels generator that minimizes the materials utilization of the light absorbers and ionically conductive membranes in the system.

REFERENCES:

1. Basic research needs for solar energy utilization, in, U.S. Department of Energy (DOE) , Office of Basic Energy Sciences,, Washington, D.C. (2005).

2. N. S. Lewis, *Science*, **315**, 798 (2007).

3. M. G. Walter, E. L. Warren, J. R. McKone, S. W. Boettcher, Q. X. Mi, E. A. Santori and N. S. Lewis, *Chem Rev*, **110**, 6446 (2010).

4. A. J. Bard and M. A. Fox, *Accts. Chem. Res.*, **28**, 141 (1995).

5. B. A. Pinaud, J. D. Benck, L. C. Seitz, A. J. Forman, Z. B. Chen, T. G. Deutsch, B. D. James, K. N. Baum, G. N. Baum, S. Ardo, H. L. Wang, E. Miller and T. F. Jaramillo, *Energ Environ Sci*, **6**, 1983 (2013).

6. B. D. James, G. N. Baum, J. Perez and K. N. Baum, Technoeconomic Analysis of Photoelectrochemical (PEC) Hydrogen Production, in, Directed Technologies (2009).

7. G. Peharz, F. Dimroth and U. Wittstadt, *Int. J. Hydrogen Energy*, **32**, 3248 (2007).

8. D. J. Friedman, R. R. King, R. M. Swanson, J. McJannet and D. Gwinner, *IEEE J Photovolt*, **3**, 1460 (2013).

9. D. C. Miller and S. R. Kurtz, *Sol. Energ. Mat. Sol. C*, **95**, 2037 (2011).

10. A. Luque, *J Appl Phys*, **110** (2011).

11. R. Winston, J. C. Miñano and P. G. Benitez, *Nonimaging optics*, Academic Press (2005).

12. J. J. O'Gallagher, *Synthesis Lectures on Energy and the Environment: Technology, Science, and Society*, **2**, 1 (2008).

13. J. C. Stevens and A. Weber, *Manuscript in preparation* (2014).

14. J. Turner, *Nat. Mater.*, **7**, 770 (2008).

15. B. Parkinson, *Sol. Cells*, **6**, 177 (1982).

16. S. Haussener, S. Hu, C. X. Xiang, A. Z. Weber and N. S. Lewis, *Energ. Environ. Sci.*, **6**, 3605 (2013).

17. S. Haussener, C. X. Xiang, J. M. Spurgeon, S. Ardo, N. S. Lewis and A. Z. Weber, *Energ. Environ. Sci.*, **5**, 9922 (2012).

18. S. Hu, C. X. Xiang, S. Haussener, A. D. Berger and N. S. Lewis, *Energ. Environ. Sci.*, **6**, 2984 (2013).

19. J. M. Gregoire, C. X. Xiang, X. N. Liu, M. Marcin and J. Jin, *Rev. Sci. Instrum.*, **84** (2013).

20. S. M. Sze, *Physics of Semiconductor Devices*, John Wiley and Sons, New York (1981).

21. A. J. Bard and L. R. Faulkner, *Electrochemical Methods, Fundamentals and Applications*, Wiley (2000).

22. S. Haussener, C. X. Xiang, J. M. Spurgeon, S. Ardo, N. S. Lewis and A. Z. Weber, *Energ. Environ. Sci.*, **5**, 9922 (2012).

23. A. Rabl, *Sol. Energy*, **18**, 93 (1975).

24. W. Shockley and H. J. Queisser, *J. Appl. Phys.*, **32**, 510 (1961).

25. C. H. Henry, *J. Appl. Phys.*, **51**, 4494 (1980).

26. H. E. Darling, *Journal of Chemical & Engineering Data*, **9**, 421 (1964).

27. H. Ito, T. Maeda, A. Nakano and H. Takenaka, *Int. J. Hydrogen Energy*, **36**, 10527 (2011).

28. Y. Sone, P. Ekdunge and D. Simonsson, *J. Electrochem. Soc.*, **143**, 1254 (1996).

29. J. George and C. Menon, *Surface and Coatings Technology*, **132**, 45 (2000).

30. K. Kinoshita, *Electrochemical Oxygen Technology. 1992*, New York: Wiley.

31. N. Markovic, B. Grgur and P. Ross, *J. Phys. Chem. B*, **101**, 5405 (1997).

32. W. Sheng, H. A. Gasteiger and Y. Shao-Horn, *J. Electrochem. Soc.*, **157**, B1529 (2010).

33. S. Siracusano, V. Baglio, A. Di Blasi, N. Briguglio, A. Stassi, R. Ornelas, E. Trifoni, V. Antonucci and A. Arico, *Int. J. Hydrogen Energy*, **35**, 5558 (2010).

34. A. T. Marshall, S. Sunde, M. Tsypkin and R. Tunold, *Int. J. Hydrogen Energy*, **32**, 2320 (2007).

35. F. Barbir, *Sol. Energy*, **78**, 661 (2005).

36. J. Ivy, *Summary of Electrolytic Hydrogen Production: Milestone Completion Report*, p. Medium: ED; Size: 28 pp. pages (2004).

37. J. Newman, P. G. Hoertz, C. A. Bonino and J. A. Trainham, *J. Electrochem. Soc.*, **159**, A1722 (2012).

Chapter V

NUMERICAL SIMULATION OF HYDROGEN GAS EVOLUTION ON PLANAR ELECTRODES AND MICROWIRE ARRAYS

5.1 Introduction

In an integrated photoelectrochemical water-splitting system, hydrogen and oxygen are continuously being produced in the cathodic and anodic chamber, respectively. Initially, gases are in a dissolved state within the electrolyte's liquid phase. However, due to the constant production of these gases by the electrochemical reactions,

$2H^+ + 2e^- \rightarrow H_2$

$2H_2O \rightarrow O_2 + 4H^+ + 4e^-$

the liquid electrolyte becomes supersaturated and bubble nucleation naturally occurs at the cavities on the electrode surface. When the bubbles grow larger, they will be released from the electrode and the system is then modeled as a two-phase flow. Although the existence of the rising bubbles promotes flow circulation inside the anodic or cathodic chamber, it has unwanted effects such as hindering the mass transport in the bulk electrolyte and causing optical losses at gas evolving photoelectrodes.[1] Nevertheless, bubbles will also affect effective contact between the liquid electrolyte and electrode surface.[2,3] From its birth to eventual bursting, the bubbles have experienced nucleation, growth, detachment from the electrode surface, ascending through the electrolyte phase and finally reaching the electrolyte free surface where they undergo bursting, each phase of the life cycle can be influenced by the design of the photoelectrochemical system regarding electrode surface wettability, roughness, electrode structure as well as catalytic activity. While chemical reactions by the electrode current kinetics, dissolved and disperse gas production, species transport within the bulk solution and two-phase fluid have been studied separately, their interactions demand a multi-physics framework in order to comprehensively understand the electrochemically gas-evolving system. Various mathematical models as well as experimental measurements have

been established for this purpose. Liu has studied how the bubble grows and releases at an electrode surface with volume of fluid (VOF) approach.[4] Physics of electrolytic gas evolution[5] including mass transfer and its effect on the electrical conductivity of bubble containing electrolytes has also been studied, which points out the relationship between the bubble vol. fraction within the solution and the electrolyte conductance decrease. El-Askary et al.[6] has employed numerical simulation for the hydrodynamics characteristics analysis of hydrogen evolution process through electrolysis and confirms the validity of the Euler-Euler model in the two-phase bubbly flow simulations. Paul has explored the bubble coverage and its effects on the electrochemical behavior of Si microwire arrays based on the experimental data. Under unconcentrated sunlight, the photocurrent density for hydrogen evolution turns out to be 24 mA cm^{-2} with the optimal dual-junction tandem light absorber[7]. Under this circumstance, the impact of the gas evolution on the system resistance is limited. However, under concentrated sunlight, the photocurrent densities can reach hundreds, even thousands of mA cm^{-2},[8] and gas bubbles take up a large part of the bulk electrolyte volume. In this case, accurately accounting for gas bubbles in the design of the photoelectrochemical devices helps to increase the energy conversion efficiency through reducing the cell voltage drop, increasing the two-phase mass transfer rate and protecting the effective electrode surface. A comprehensive understanding of the existing bubbles on the total potential drop within the photoelectrochemical system as well as their relationship with the nominal current density, electrode surface and electrode configuration have not been adapted.

In this work we report the impact of the hydrogen bubbles in the cathodic chamber with the electrolysis solution of 1.0 M sulfuric acid on the local reversible hydrogen electrode potential, the hyperpolarization, the electrolyte solution resistance, and compare the sum of all these bubble associated potential drop increases with the cathodic overpotential calculated for a planar Pt surface with a Tafel slope of 29 mV dec^{-1} under different nominal current densities with two different electrode surface roughness. Bubble break-off radius has been determined through the current density and the electrode surface cavity size. The size of bubble releasing from the electrode surface is crucial to calculate the two-phase mass transfer rates, the dissolved gas concentration at the electrode-electrolyte interface, and therefore the

local reversible hydrogen electrode potential shift, which is a main contribution for the total bubble associated potential drop increase in the system. Besides, electrolyte solution with various initial concentrations have been explored in order to understand how initial pH value will affect the bubble related ohmic drop increase of the bulk solution and its importance in terms of the total potential drop. Furthermore, two micro electrode array configurations, 6 μm diameter and 14 μm center-to-center pitch, μW 6 | 14 and 3μm diameter and 11 μm pitch, μW 3 | 11, have been applied for the purpose of enhancing the electrolyte conductance by reducing the local current density and therefore lowering the bubble vol. fraction in the bulk solution. The dissolved gas concentration at the electrode-electrolyte interface has been simulated and the local reversible hydrogen electrode potential shift has been evaluated and compared to those with the planar electrode configuration with the same nominal current density and electrode surface roughness.

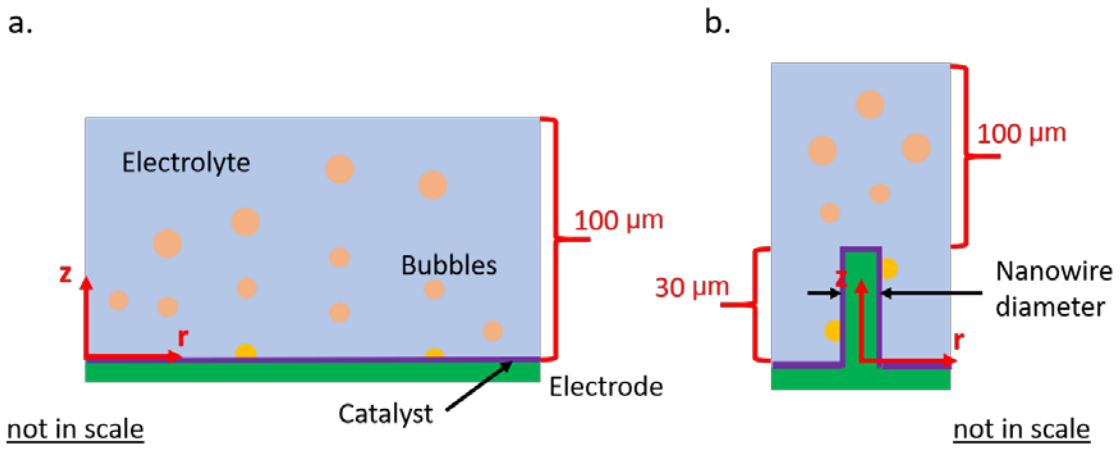

Figure 5.1 Schematic illustration of a cathodic gas evolving chamber with (a) planar photoelectrode configuration and (b) microwire photoelectrode configuration.

5.2 Modeling

5.2.1 Governing equations

A bulk liquid-electrolyte domain with hydrogen gas evolution were modeled (Figure 5.1). The green region in the illustration is the electrode, with Pt catalyst (in purple) on top. The orange circles represent the gaseous phase (H_2), which are released from the electrode surface, rising in the liquid electrolyte (in light blue) and going across the boundary layer. Before huge amounts of bubbles are generated and released from the electrode surface, this boundary layer can be considered as a stagnant layer, where all species transport is governed by diffusion and migration. Beyond this boundary layer, solution is assumed to be so well stirred that the concentration of all species is uniform throughout. In this work, a value of 100 μm was chosen for the thickness of this boundary layer, which can be calculated through rotating disk electrode (RDE) analogously and is estimated to depict low to moderate stirring.[16] Our hydrogen evolution process through electrolysis model is basically a two-phase fluid (gas and liquid) flow in the presence of mass transport between the phases and chemical reaction within the solution. Simulation of the two phases of bubble columns can be carried out either by using the Eulerian-Eulerian (E-E) model, Eulerian-Lagrangian (E-L) model or Direct Numerical Simulation (DNS) model. DNS model is without doubt the most accurate model of the three. But since the cost of DNS models is very expensive and it can only be performed for a very limited number of bubbles, this model is generally performed to obtain micro-scale data. In this work we adapted Eulerian-Eulerian model to treat the two-phase fluid flow. The E-E model is a general, macroscopic model for two-phase fluid flow, which considers both phases interoperating liquids and employs a continuum approach to both gas bubble and liquid phases. One velocity field is associated with each phase. A momentum balance equation and a continuity equation describe the dynamics of each of the phases. Although it cannot track bubbles' movement like the E-L model, which tracks each bubble individually using Newton's second law, due to the following three reasons,

1) the E-E model has been well applied for gas-evolution electrodes. For example, Liu et al. used it to simulate the electrochemical oxidation of *p*-methoxyphenol while El-Askary et al. modeled hydrogen production in an electrochemical cell with it.

2) the E-E model is economic and does not consume an extra-ordinary amount of computation time.
3) specific particle tracing is not the purpose of this work,

the Eulerian-Eulerian model is believed the most suitable model for the considered bubbly flow. Moreover, since 1) the product gas in this work is hydrogen, the density of which is negligible compared to that of the liquid. 2) The motion of the gas bubbles relative to the liquid is determined by a balance between viscous drag and pressure forces.[9] 3) Gas phase and liquid phase share the same pressure field, in this work, the E-E Model can further be slightly simplified, which means momentum and continuity equations for the two phases can be combined and a gas phase transport equation is kept in order to track the volume fraction of the bubbles. The momentum equation is

$$\emptyset_l \rho_l \frac{\partial u_l}{\partial t} + \emptyset_l \rho_l u_l \cdot \nabla u_l = -\nabla p + \nabla \cdot \left[\emptyset_l \mu_l \left(\nabla u_l + \nabla u_l^T - \frac{2}{3}(\nabla \cdot u_l) I\right)\right] + \emptyset_l \rho_l g, \quad \text{(Eq. 5.1)}$$

where u represents the velocity vector, p, ρ stands for the pressure and the density, respectively. $\emptyset$ is the phase volume fraction. μ_l is the dynamic viscosity of the liquid, the flows in this work has been considered as laminar flow due to low Reynold numbers. The subscripts 'l' and 'g' denote quantities related to the liquid phase and gas phase, correspondingly.

The continuity equation is

$$\frac{\partial}{\partial t}\left(\rho_l \phi_l + \rho_g \phi_g\right) + \nabla \cdot \left(\rho_l \phi_l u_l + \rho_g \phi_g u_g\right) = 0, \quad \text{(Eq. 5.2)}$$

while the gas phase transport equation is

$$\frac{\partial \rho_g \phi_g}{\partial t} + \nabla \cdot \left(\rho_g \phi_g u_g\right) = -m_{gl}, \quad \text{(Eq. 5.3)}$$

where m_{gl} represents the mass transfer rate from the gas to the liquid. The gas velocity u_g is calculated as the sum of the liquid phase velocity, u_l, the relative velocity between the phases, u_{slip}.

$$u_g = u_l + u_{slip}. \quad \text{(Eq. 5.4)}$$

In the bulk electrolyte, the sum of forces on bubbles is composed of gravity, buoyancy, viscous drag force, shear-induced lift force, and virtual mass force. The virtual mass force

should account for the contribution of changing volume of the bubbles, as described by Magnaudet and Eames. But comparing size of different terms, it can be argued that the pressure forces on a bubble are balanced by the viscous drag force, f_D, which is called the pressure-drag balance model, and has been employed in this work,

$$\emptyset_l \nabla p = f_D, \quad \text{(Eq. 5.5)}$$

$$f_D = -C_d \frac{3}{4} \frac{\rho_l}{d_b} |u_{slip}| u_{slip}, \quad \text{(Eq. 5.6)}$$

where d_b represents the bubble diameter and C_d stands for the viscous drag coefficient. Hadamard and Rybczynski have proposed an appropriate model to calculate the drag coefficient for small spherical bubbles with diameter less than 2 mm and bubble Reynolds number much less than one, this model has been applied in this work,

$$C_d = \frac{16}{Re_b}, \quad \text{(Eq. 5.7)}$$

$$Re_b = \frac{d_b \rho_l |u_{slip}|}{\mu_l}. \quad \text{(Eq. 5.8)}$$

The gas density ρ_g is achieved through the ideal gas law,

$$\rho_g = \frac{(p + p_{ref})M}{RT}, \quad \text{(Eq. 5.9)}$$

where *M* is the molecular weight of the gas, *R* is the ideal gas constant, which is 8.314 J $mol^{-1}K^{-1}$, p_{ref} is a reference pressure, which in our work is 1 atm, and *T* is temperature. Since we are working with a two-phase flow, it is obvious that

$$\emptyset_l = 1 - \emptyset_g. \quad \text{(Eq. 5.10)}$$

The mass transport rate from gas phase to the liquid phase m_{gl} can also be specified through two film theory,

$$m_{gl} = k(c^* - c)Ma, \quad \text{(Eq. 5.11)}$$

where *k* represents the mass transfer coefficient, *a* is defined as the interfacial area per volume, *c* is the local dissolved gas concentration, while c^* is the equilibrium concentration of the gas dissolved in liquid and given by

$$c^* = \frac{p + p_{ref}}{H}, \quad \text{(Eq. 5.12)}$$

H stands for the Henry's constant here. The interfacial area per volume is calculated through the number density, *n*, and the volume fraction of gas, $\emptyset_g$,

$a = (4n\pi)^{1/3}(3\emptyset_g)^{2/3}$. (Eq. 5.13)

The mass transfer coefficient k is calculated through the Sherwood number, *Sh*,

$Sh = \frac{kd_b}{D_{H_2}}$. (Eq. 5.14)

Since pure diffusion and micro-convective mass transfer act simultaneously. The Sherwood number must take into account the joint action of both mechanisms. As Ibl proposed,

$Sh = 1.38Re_{H_2}^{0.5}Sc^{0.5}(1-\Theta)^{0.5}$, (Eq. 5.15)

In Eq. 5.15, a value of 0.5 was chosen for the exponent of the Schmidt number, which can be justified because pure diffusion substantially predominates convection.[17] And the Schmidt number is defined as

$Sc = \frac{\nu}{D_{H_2}}$,

where ν is the kinematic viscosity of the electrolyte, which is set to 0.01 $cm^2\ s^{-1}$ in this work.

Simulation of the transport of dissolved hydrogen can be carried out by Nernst-Plank equation,

$\frac{\partial c_{H_2}}{\partial t} + \nabla \cdot (-D_{H_2}\nabla c_{H_2}) + u_l \cdot \nabla c_{H_2} = R_{H_2}$, (Eq. 5.16)

where D_{H_2} and c_{H_2} are the diffusion coefficient and concentration, respectively, of dissolved hydrogen within the electrolyte, R_{H_2} is associated with the mass transfer rate between two species, m_{gl},

$R_g = -m_{gl}/M$. (Eq. 5.17)

5.2.2 Initial conditions and other employed parameters

The electrolysis solution in this work varies from 0.1 M to 1.0 M sulfuric acid with saturated dissolved hydrogen. The initial pressure within the solution is set as $\rho_l gh + p_{ref}$, h stands for the distance from the outer boundary layer. The other parameters used here are the same as those in Glas and Westwater,[4] as shown in Table 5.1.

Diffusion coefficient of H_2, D_{H_2}	7.38 x 10^{-9} m^2 s^{-1}
Diffusion coefficient of H^+, D_{H^+}	9.31 x 10^{-9} m^2 s^{-1}
Diffusion coefficient of OH^-, D_{OH^-}	5.26 x 10^{-9} m^2 s^{-1}
Surface tension, σ	0.075 N m^{-1}
Solution density, ρ_l	1000 kg m^{-3}
Hydrogen gas density, ρ_g	0.09 kg m^{-3}
Saturation concentration of H_2 in solution, $c_{H_2}^0$	0.78 mM
Operating temperature, T	298.15 K
Operating pressure, p	1 atm

Table 5.1 Kinematic and operating parameters used in the modeling.

5.2.3 Boundary conditions

a) Two-phase fluid model

Boundary conditions for the two-phase fluid model has been set as follows. At the electrolyte-electrode interface, slip condition was assumed for the liquid phase, while gas mass flux and number density flux are fixed,

$$u_l \cdot n = 0. \quad \text{(Eq. 5.18)}$$

At the other end of the bulk electrolyte layer, no slip condition was assumed for the liquid phase, while for the gaseous phase it is considered as outlet. As for the vertical wall, no slip condition was assumed for the liquid phase, while no flux was set for the dispersed phase.

The break-off diameters of the bubbles R_r are required for the purpose of acquiring the gas mass flux and number density flux. During the electrolysis process they are determined by many aspects. For instance, the electrolysis solution, surface roughness and wettability, applied current density, operation temperature and pressure, gas and liquid density, dissolved gas diffusion coefficient in the solution, saturation concentration of dissolved gas in the solution, surface tension between gas and electrode surface as well as gas and solution, etc. In the same time, it would also be largely affected by the neighbor bubbles disturbance, which

can result in a premature departure from the electrode surface. Experimentally people have observed that for gas evolving electrodes, under the same operation temperature and pressure, the break-off bubble radius is mainly influenced by the applied nominal current densities and the roughness of the electrodes. Data and analysis have been presented by Vogt[10] showing how the break-off bubble radius decreases with increasing nominal current density for different electrode roughness. In our work, this relationship has been adapted and shown in Figure 5.2.

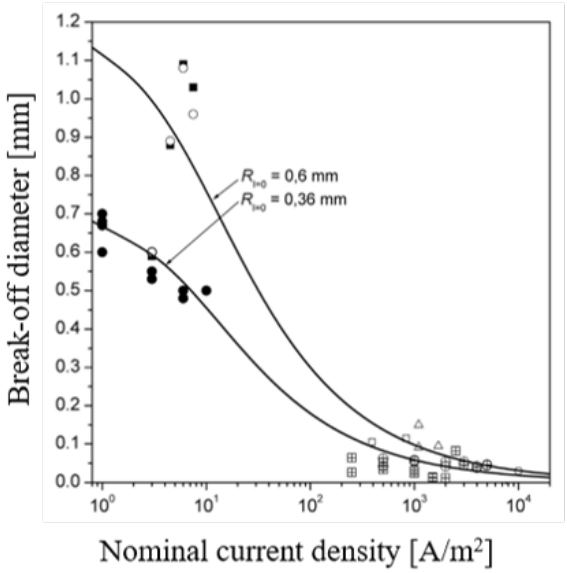

Figure 5.2 Bubble break-off diameter with increasing nominal current density from different electrode surface cavity sizes based on experimental investigations.

The bubble break-off radius on the other hand can also be interrelated to the fractional bubble coverage on the electrode surface,

$$\frac{R_r}{R_f} = (1 + 1200\Theta)^{-0.5}, \qquad \text{(Eq. 5.19)}$$

where R_f denotes the bubble radius as zero current as calculated in the Fritz equation,

$$R_f = \left(\frac{3}{2}\frac{\sigma R_{site}}{(\rho_l - \rho_g)g}\right)^{1/3}, \qquad \text{(Eq. 5.20)}$$

under the following two assumptions:

1) bubble nucleation as gas pocket in the cone cavities on the electrode, R_{site} denotes the radius of the flat surface of the cone. Noted that it is well established that scratches and pits on the electrode surface are the active nucleation sites for oxygen/hydrogen bubbles during the electrolysis process.[11]
2) force balance between buoyancy and surface tension is achieved when bubbles on the electrode reaches break-off radius.

It is well understood that the total amount of product gas transferred into the gaseous phase adhering to the electrode surface, f_G, is determined by the fractional bubble coverage, Θ, of the electrode. At very small values of the current density (< 1 mA cm^{-2}) with nearly no bubbles adhering to the electrode surface, $\Theta \rightarrow 0$, all the generated product gas crosses the electrolyte-electrode interface as dissolved gas, $f_G \rightarrow 0$. On the other hand, when the electrode surface is overcrowded by adhering bubbles, $\Theta \rightarrow 1$, almost 100% of the dissolved gas is transferred into the gaseous phase, $f_G \rightarrow 1$. This relationship has been studied using various mathematical models, the outcomes of which do not differ substantially[12,13] and can approximately be described by[14],

$$f_G = 0.55\Theta^{0.1} + 0.45\Theta^{8}. \quad \text{(Eq. 5.21)}$$

The gas mass flux and number density flux are then given through f_G,

$$m_{gas,in} = \frac{|J| f_G M}{zF}, \quad \text{(Eq. 5.22)}$$

where J represents the nominal cathodic current density.

b) Transport of electrolyte species model

At the outer bulk electrolyte layer, constant concentrations of all electrolyte species at the initial conditions were assumed, due to the high convective fluxes beyond the boundary layer. At the electrode-electrolyte interface, inward flux of H^+ as well as dissolved hydrogen across the boundary have been specified,

$$n_{dissolved,in} = \frac{|J|(1-f_G)}{zF}. \quad \text{(Eq. 5.23)}$$

On the vertical wall, no flux for each species is applied for simulation.

The standard FEM solver in the COMSOL multi-physics package was used to obtain the modeled two-phase flow and electrochemical behavior. The maximum element size, the maximum element growth rate and curvature factor for this 2-D axisymmetric model were 1.3 μm, 1.08 and 0.25, respectively. A relative tolerance of the corresponding variable of 0.001 was applied as the convergence criterion for all simulations.

5.3 Results and Discussion

In the absence of mass transport limitations, the ideal current vs. overpotential behavior predicted for a planar Pt surface with a Tafel slope of 29 mV dec^{-1} can be expressed by

$$\eta_{Tafel} = a + b\ log_{10}|J|, \qquad \text{(Eq. 5.24)}$$

where a and b here are the empirical Tafel parameters and fitted as 89 mV and 29 mV, respectively, from the experimental data curve, which is shown in Figure 5.3. *J* is the nominal cathodic current density in the unit of A cm^{-2}.

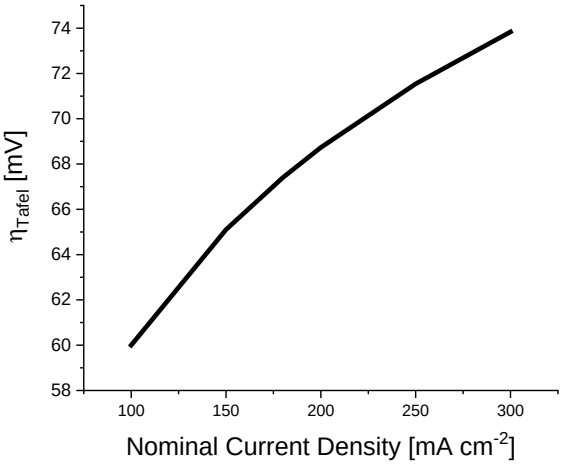

Figure 5.3 Ideal current density vs. overpotential behavior predicted for a planar Pt surface with a Tafel slope of 29 mV dec^{-1}.

5.3.1 Impact on electrolyte resistance from gas evolution

Figure 5.4(a) shows that for planar electrode with surface cavity radius equal to 20 μm, the generating bubble vol. fraction within the 100 μm boundary layer varies from 0.74% to 12.7% with respect to the nominal current density. When the surface cavity radius decreases, based on the information from Figure 5.2 the break-off bubble radius decreases accordingly, which results in an increase in the bubble vol. fraction in the bulk electrolyte domain. Under the current density of 100 mA cm^{-2}, the H_2 gas vol. fraction is 1.9%, it goes up to 57.8% when the current density increases to 300 mA cm^{-2}. Meanwhile, since hydrogen bubbles blocks part of the pathways of ion transport within the solution, the conductivity of the bulk electrolyte decreases accordingly. Maxwell's equation, which is a fundamental result in the theory of heterogeneous conductivity, describes the relationship between ratio of the conductance with dispersed phase present to the conductance in the absence of the dispersed phase, K_m, and the void fraction, f_{void},[5]

$$K_m = (1 - f_{void})/(1 + \frac{f_{void}}{2}). \quad \text{(Eq. 5.25)}$$

Oscar and Robert[15] have shown that Maxwell's equation fits the experimental data remarkably well when the volumetric fraction of gas in the adhering to the electrode surface bubble monolayer is less than 50%. Through calculation it is noted that for planar electrode with surface cavity radius equal to 20 μm, K_m decreases from 0.99 to 0.82 due to the increase of nominal current density. Bubbles don't have a huge impact on the electrolyte conductance in these cases. On the other hand, if the cavity radius on the electrode surface is down to 4 μm, under the current density of 100 mA cm^{-2}, K_m can reach as high as 0.97, but it goes down to 0.33 when the nominal current density increases to 300 mA cm^{-2} due to the high vol. fraction of the hydrogen gas bubble existing in the solution. Based on the calculated K_m, Eq. 5.25 can then be applied to evaluate the additional ohmic drop during gas evolution ΔE_{ohm},[3]

$$\Delta E_{ohm} = \Delta E'_{ohm} + \frac{|J|L}{\kappa}, \quad \text{(Eq. 5.26)}$$

$$\Delta E'_{ohm} = \frac{|J|L(1-K_m)}{\kappa K_m}, \quad \text{(Eq. 5.27)}$$

where the second term on the right-hand side of Eq. 5.26 stands for the ohmic drop present in the absence of gas bubbles, while $\Delta E'_{ohm}$ represents the remaining ohmic drop after removal of this term, κ in the equation is the solution conductivity, which can be defined as[16]

$$\kappa = F \sum_i |z_i| u_{m,i} c_i. \qquad \text{(Eq. 5.28)}$$

a.

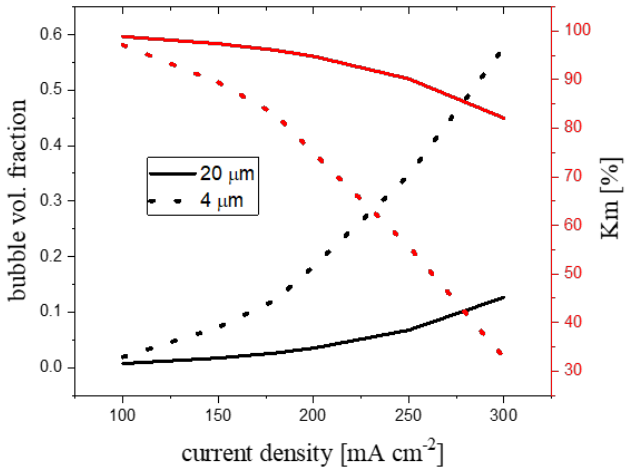

b.

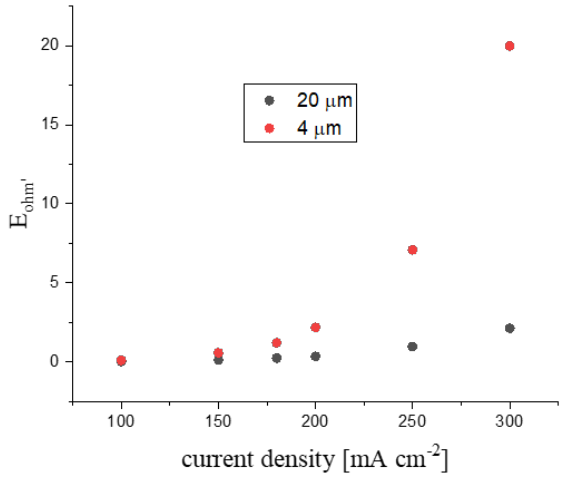

Figure 5.4 **(**a) Hydrogen gas bubble vol. fraction in the bulk electrolyte and its impact on the solution conductivity as well as (b) the resulting ohmic drop under various current densities on a planar cathode with different electrode surface roughness.

Figure 5.4(b) shows that for planar electrode with surface cavity radius equal to 20 μm, $\Delta E'_{ohm}$ is 0.036 mV under the nominal current density of 100 mA cm^{-2}, and increases to 2.12 mV with the current density of 300 mA cm^{-2}. On the other hand, when the surface cavity radius is reduced to 4 μm, under 100 mA cm^{-2}, $\Delta E'_{ohm}$ is 0.095 mV, but it goes up to 19.99 mV with the current density of 300 mA cm^{-2}, mostly due to the huge reduction in the solution conductance.

5.3.2 Impact on local reversible hydrogen electrode potential from gas evolution

The accumulations of dissolved H_2 at the electrode-electrolyte interface can shift the local reversible hydrogen electrode potential, it is predicted by a Nernstian relationship:

$$\eta_C = \frac{2.3RT}{zF} log_{10} \frac{c_{H_2|\ at\ the\ interface}}{c^0_{H_2}}. \quad \text{(Eq. 5.29)}$$

Based on the calculated dissolved H_2 concentration at the electrode-electrolyte interface, η_C is achieved and shown in Figure 5.5. With surface cavity radius equal to 4 μm, η_C decreases from 48.35 mV to 31.38 mV with respect to the increasing nominal current density. When the surface cavity radius increases to 20 μm, η_C reaches 49.68 mV under the current density of 100 mA cm^{-2}, it goes up with the nominal current density to 55.35 mV at 250 mA cm^{-2} and then decreases if the applied current density keeps increasing. It is noted that η_C and η_{Tafel} have the same order of magnitude and therefore η_C is a non-negligible term with regard to the total overpotential in system.

Figure 5.5 shows that for planar electrode system with the boundary layer of 100 μm, with surface cavity radius equal to 4 μm, the dissolved H_2 concentration at the electrode-electrolyte interface decreases from 33.76 mM to 9 mM under the nominal current density increasing from 100 mA cm^{-2} to 300 mA cm^{-2}. Since there is huge amount of dissolved H_2

gas in the bulk converting into the gaseous H_2 bubbles under higher current densities, although with the increasing current densities more and more dissolved hydrogen flows into the bulk solution, the dissolved H_2 concentration at the electrode-electrolyte interface decreases accordingly. On the other hand, with surface cavity radius equal to 20 μm, the dissolved H_2 concentration at the electrode-electrolyte interface increases with the nominal current density at first then deceases if the current density keeps increasing. It is obvious that under lower current densities, the increased amount of dissolved H_2 in the electrolyte solution transferring into the gaseous phase is not large enough to compensate for the increasing dissolved H_2 flow from the electrode.

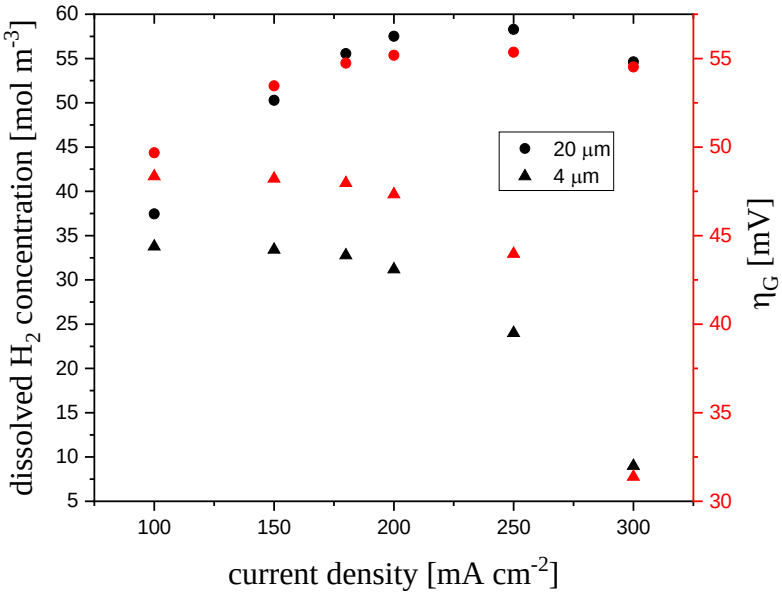

Figure 5.5 Dissolved H_2 concentration at the cathode electrolyte interface and its resulting local reversible hydrogen electrode potential shift under various current densities on a planar cathode with different electrode surface roughness.

5.3.3 Impact on hyperpolarization from gas evolution

When electrode surfaces are covered with adhering hydrogen bubbles with the same nominal current density, an additional overpotential is required due to an increase in effective current density at sites not covered by bubbles. This additional overpotential is given by

$$\eta_h = b\ log_{10}\frac{A}{A'}, \quad \text{(Eq. 5.30)}$$

where η_h represents the hyperpolarization, which is determined by its Tafel behavior as well as the ratio of the surface area A to the remaining active area A'. A/A' is interrelated to fractional bubble coverage on the electrode surface, Θ, which is shown in Figure 5.6. Θ increases with the increasing nominal current density. When the surface cavity radius equals to 20 μm, Θ reaches 12.93% under the nominal current density of 100 mA cm^{-2} and goes up to 36.85% under the current density of 300 mA cm^{-2}. The fractional bubble coverage doesn't change a lot in terms of the electrode surface cavity radius, since the bubble departure radius and Fritz radius decrease monotonously. Therefore, the electrode surface roughness doesn't make a significant impact on the hyperpolarization. Besides η_h varies from 1.4 mV to 5.9 mV under nominal current densities range from 100 mA cm^{-2} to 300 mA cm^{-2}. Since η_h is one order of magnitude less than η_{Tafel}, it doesn't make a huge contribution in terms of the total overpotential in the cathodic side.

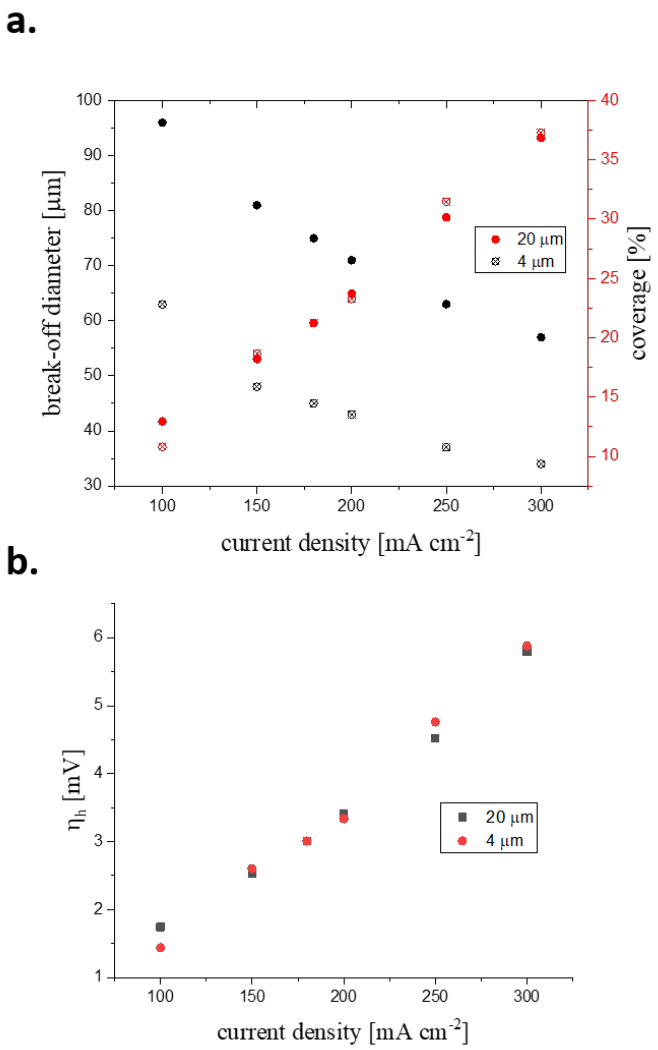

Figure 5.6 (a) Hydrogen gas bubble coverage and (b) its resulting hyperpolarization under various current densities on a planar cathode with different electrode surface roughness.

5.3.4 Total bubble related potential drop between the cathode and reference electrode

The total potential drop between the cathode and reference electrode, following correction for the cell resistance, can be expressed in Eq. 5.31:

$$\eta_T = \eta_{Tafel} + \eta_C + \eta_h + \Delta E'_{ohm}. \quad \text{(Eq. 5.31)}$$

Figure 5.7 shows that for planar electrode with surface cavity radius equal to 20 µm, under the nominal current density of 100 mA cm^{-2}, the gas bubble related overpotential increase reaches 51.46 mV and contributes to 46.17% of the total potential drop between the cathode and reference electrode. This overpotential increase goes up with the increasing nominal

current density and reaches 62.43 mV under 300 mA cm^{-2}, but it contributes slightly less and turns out to take up 45.82% of the total potential drop since η_{Tafel} grows logarithmically with the current density. The total impact of the hydrogen bubbles in the bulk on the total potential drop, η_T, doesn't show a big difference when the surface cavity radius decreases to 4 μm. Although with smaller cavities, bubbles have a larger influence on the solution conductance, especially under current densities > 200 mA cm^{-2}, its impact on the local reversible hydrogen electrode potential is weaker due to the lower dissolved H_2 concentration at the electrode-electrolyte interface.

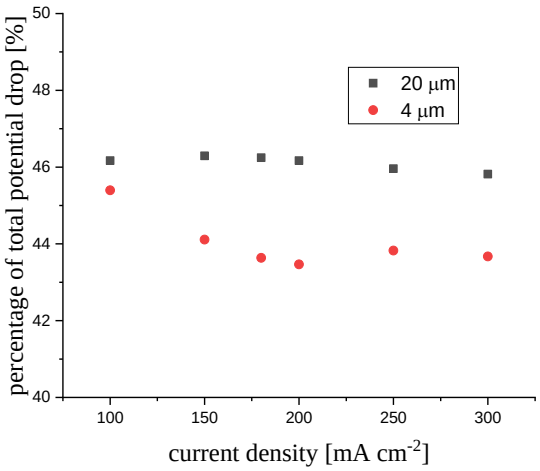

Figure 5.7 Percentage of total potential drop between the cathode and reference electrode, following correction for cell resistance, under various current densities on a planar cathode with different electrode surface roughness.

5.3.5 Gas evolution in the microwire electrode array configuration

The computation above indicates that the main impact of the hydrogen gas on the system resistance comes from the accumulations of dissolved H_2 at the electrode-electrolyte interface. In this section microwire arrays have been applied and η_C under the same nominal current densities have been studied. Pt catalyst has been coated all over the electrode surface, as shown in Figure 5.1(b). 6 μm diameter and 14 μm center-to-center pitch, μW 6 | 14 and 3μm diameter and 11 μm pitch, μW 3 | 11 have been investigated in this work. If the surface

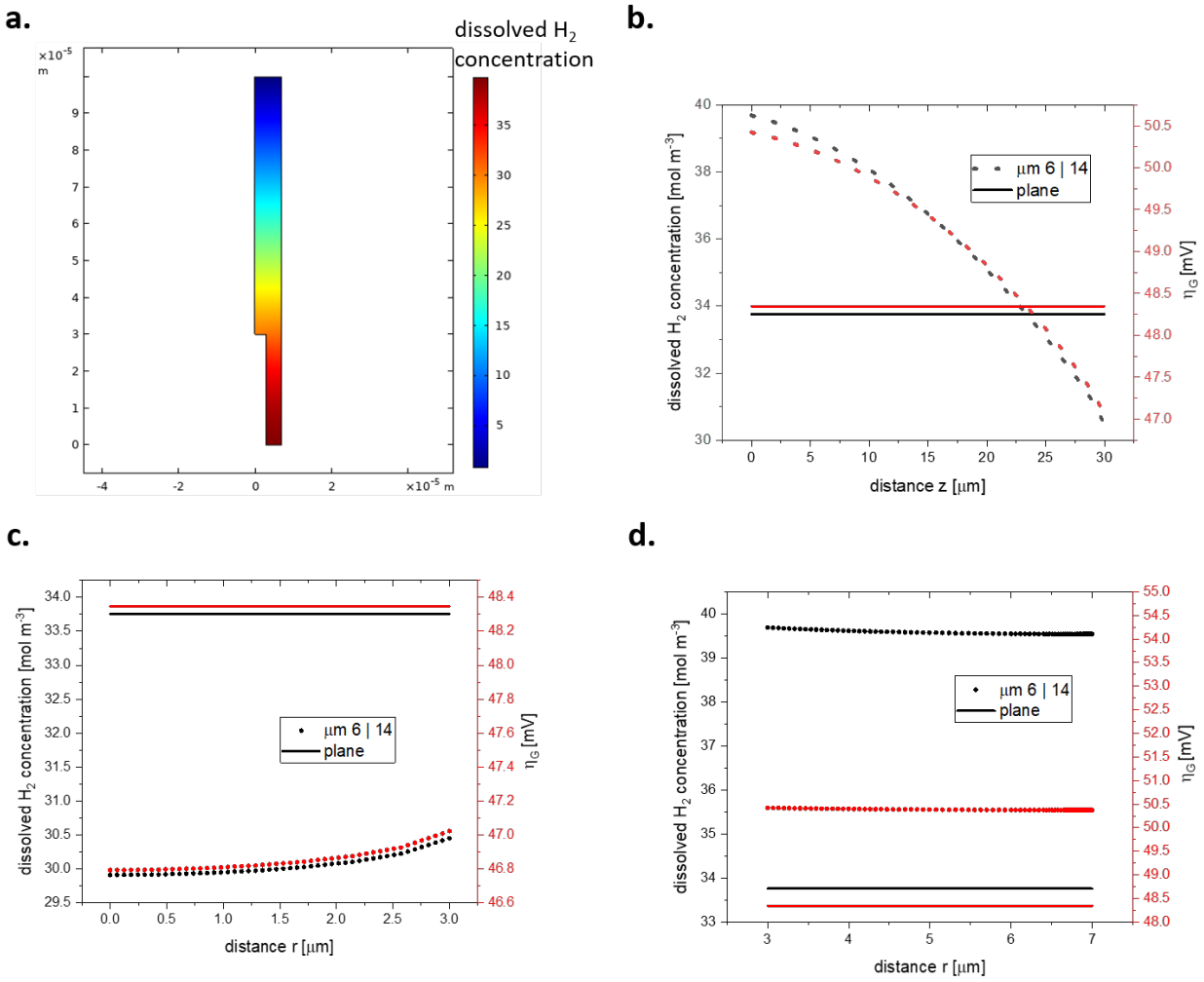

Figure 5.8 Dissolved hydrogen concentration (a) in the bulk electrolyte, (b) on the top end of the microwires, (c) on the surface of the microwire sides, and (d) on the rest of the electrode surface as well as its resulting local reversible hydrogen electrode potential shift for a microwire array with 6 μm diameter and 14 μm center-to-center pitch under the nominal current density of 100 mA cm^{-2} and with electrode surface cavity radius of 4 μm. (Solid lines indicates the corresponding values with a planar electrode under the same conditions.)

cavity radius has been set as 4 μm, under the nominal current density of 100 mA cm^{-2}, the H_2 gas vol. fraction in the solution is 1.9% for the planar electrode while it is only 0.33% for μW 6 | 14. The main reason for that is microwire array structure increases the electrode

surface area, therefore under the same nominal current density, the local current density is lower than it is for the planar electrode, which results in smaller break-off bubble diameters and less dissolved hydrogen gas transferring into bubbles. Similarly, the H_2 gas vol. fraction in the solution is only 0.3% for μW 3 | 11. Figure 5.8(a) indicates that dissolved H_2 concentration on the microwire array surface varies in terms of different locations. On the top end of the microwires, the dissolved H_2 concentration is lower than that is on the planar electrode, which leads to lower local reversible hydrogen electrode potential shift, η_C. On the surface of the microwire sides, the dissolved H_2 concentration decreases from 39.69 mM near the bottom to 30.45 mM near the top and the calculated η_C decreases from 50.42 mV to 47.02 mV accordingly. On the other hand, under the same initial conditions for the planar electrode, the dissolved H_2 concentration at electrode-electrolyte interface is 33.76 mM and η_C turns out to be 48.35 mV. On the rest of the electrode surface of μW 6 | 14, the dissolved H_2 concentration is approximately 6 mM higher than it is for the planar configuration, which causes a higher η_C of 2 mV. Figure 5.9 indicates that the dissolved H_2 at electrode-electrolyte interface for μW 3 | 11 shows a great similarity as that for μW 6 | 14. It is noted that although applying the microwire array instead of the planar electrode will help increasing the solution conductance due to lower bubble vol. fraction, it is not necessarily useful in terms of reducing the local reversible hydrogen electrode potential shift.

With the μW 6 | 14 configuration, when the nominal current density increases to 150 mA cm^{-2}, the bubble vol. fraction in the electrolyte solution increases to 0.82% correspondingly.

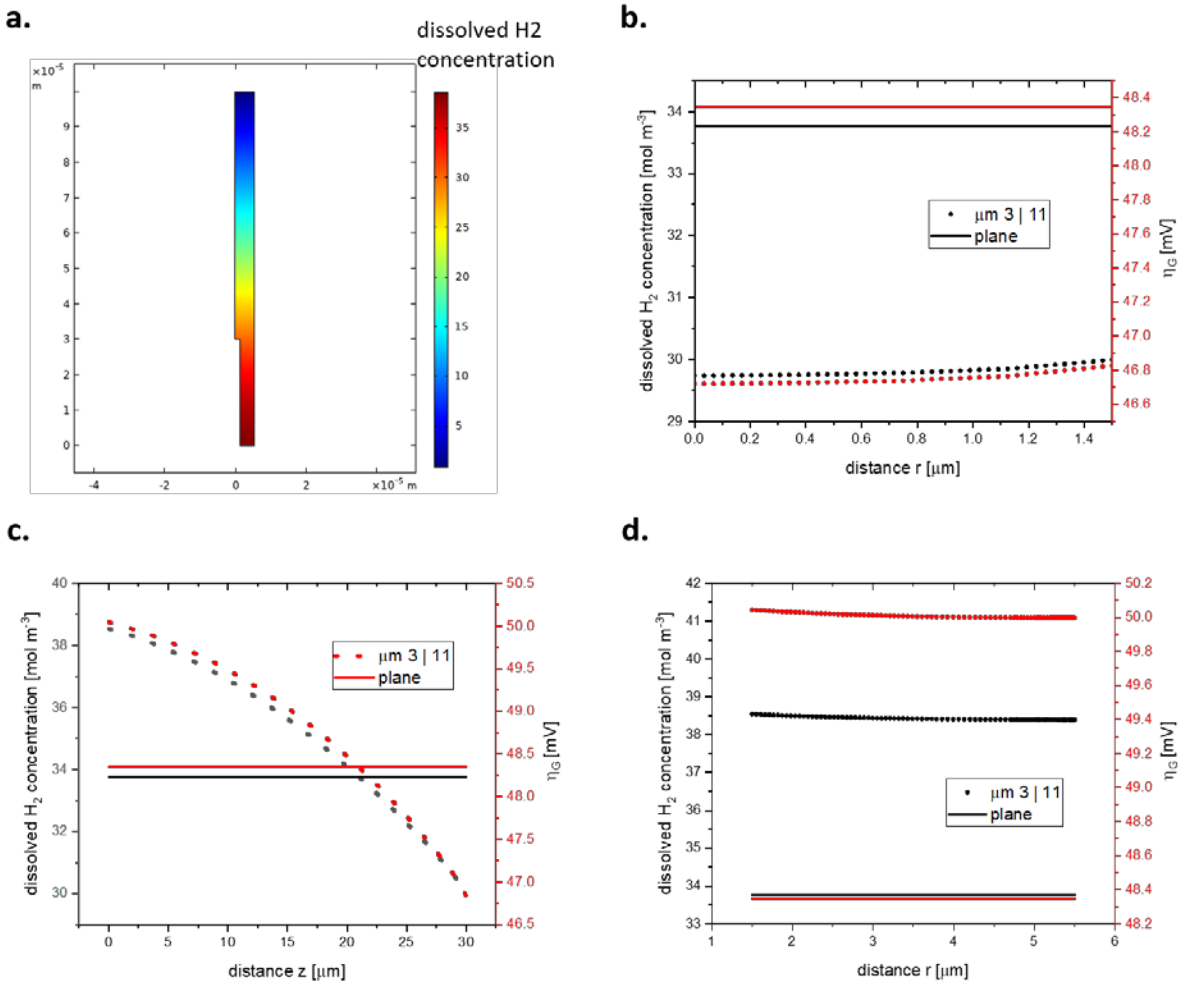

Figure 5.9 Dissolved hydrogen concentration (a) in the bulk electrolyte, (b) on the top end of the microwires, (c) on the surface of the microwire sides, and (d) on the rest of the electrode surface as well as its resulting local reversible hydrogen electrode potential shift for a microwire array with 3 µm diameter and 11 µm center-to-center pitch under the nominal current density of 100 mA cm^{-2} and with electrode surface cavity radius of 4 µm. (Solid lines indicates the corresponding values with a planar electrode under the same conditions.)

Compared to the bubble vol. fraction with the planar electrode configuration under the same nominal current density, which reaches 7.2%, microwire array configuration reduces the bubble vol. fraction by 9 times, while under 100 mA cm^{-2}, it helps to reduce the bubble vol. fraction by 5.7 times. It is noted that the microwire array configuration can contribute more

in terms of increasing solution conductance with higher nominal current densities. When the nominal current density increases from 100 mA cm^{-2} to 150 mA cm^{-2}, the dissolved H_2 concentration on the top end of the microwires increases by 12 mM accordingly, which results in 3 mV of η_C increase. On the other hand, with the planar electrode, the dissolved H_2 concentration at the electrode-electrolyte interface reduces from 33.76 mM to 33.42 mM. The dissolved H_2 accumulates even more rest part of the microwire electrodes. The reason for this great accumulation is that with surface cavity radius of 4 μm and under the nominal current density of 150 mA cm^{-2}, for the μW 6 | 14 configuration, the bubble break-off diameter is 102 μm, while for the planar electrode, the bubble break-off diameter is only 48 μm, which leads to a much higher mass transfer rate of hydrogen from the liquid phase to the gas phase and much less accumulation of dissolved hydrogen at the electrode-electrolyte interface.

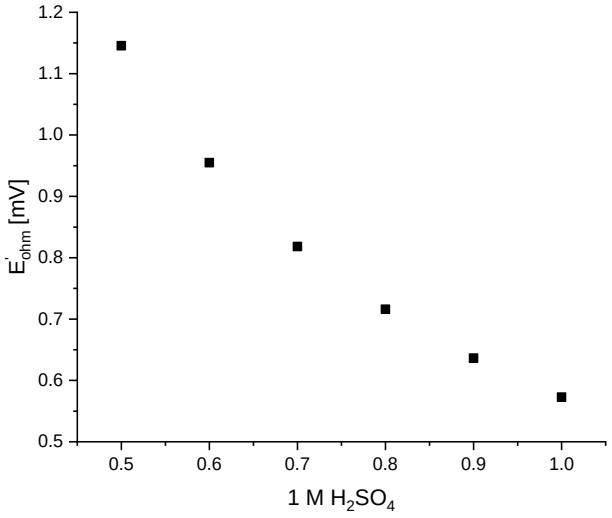

Figure 5.10 For the planar electrode system with the same nominal current density, the bubble related ohmic drop linearly decreases with the increasing initial sulfuric acid concentration.

5.3.6 Impact of the electrolyte initial pH values

The initial sulfuric acid concentration for all the simulation above is 1 M. Based on Eq. 5.28, the solution conductivity will linearly decrease with lower sulfuric acid concentration.

Therefore, under the same current density, the ohmic drop in the solution turns out to be higher with lower initial sulfuric acid concentration. As Figure 5.10 shows, for the planar electrode system with the same nominal current density, the bubble related ohmic drop linearly decreases with the increasing initial sulfuric acid concentration. Besides, with the same boundary layer thickness, the limiting current density will also linearly decrease with the reducing sulfuric acid concentration. For example, with the boundary layer thickness of 100 μm, the limiting current density is 159 mA cm^{-2} for 0.5 M sulfuric acid, while 318 mA cm^{-2} for 1 M sulfuric acid.

5.4 Conclusions

The bubble related ohmic drop within the solution increase with the nominal current density and flatness of the electrode surface. With the surface cavity radius of 20 μm, even the nominal current density reaches 300 mA cm^{-2}, the bubble associated ohmic drop, $\Delta E'_{ohm}$, is not playing an important role in terms of the total bubble related potential drop increase in the cathodic chamber. But when the surface cavity radius is reduced to 4 μm, under nominal current density larger than 200 mA cm^{-2}, $\Delta E'_{ohm}$ is equivalent to at least 10% of η_{Tafel} due to the increased bubble vol. fraction and reduced conductance within the solution. The decrease of initial sulfuric acid concentration would cause an increase in $\Delta E'_{ohm}$ and the solution conductance is proportional to the initial electrolyte concentration. The local reversible hydrogen electrode potential can be shifted by accumulations of dissolved H_2 at the electrode-electrolyte interface, which contributes the most in terms of the bubble associated potential drop between the cathode and reference electrode. When the electrode surface is relatively flat with the cavity radius equal to 4 μm, the local reversible hydrogen electrode potential shift due to existing bubbles, η_C, decreases with the nominal current density due to the decreasing dissolved H_2 concentration at the electrode-electrolyte interface. On the other hand, when the electrode surface is relatively rough with the cavity radius equal to 20 μm, the change of η_C doesn't behave monotonously with the nominal current density. Under lower current densities, it goes up with the current density and reaches the peak at 250 mA cm^{-2} for a planar electrode configuration then gradually decreases. It is

worth pointing out that with this kind of electrode surface roughness, the local reversible hydrogen electrode potential shift contributes at least 85% of the total bubble associated potential drop increase in the cathodic chamber. Bubbles adhering to the electrode surface will cause an additional overpotential increase, η_h. But based on the calculation, it is known that η_h contributes less than 10% of the total bubble related potential drop increase in the cathodic chamber when the nominal current density is not greater than 300 mA cm^{-2}. $\Delta E'_{ohm}$, η_C and η_h makes up the total additional potential drop between the cathode and reference electrode due to existing bubbles. For a planar electrode configuration, the sum of these terms is comparable to the ideal overpotential, η_{Tafel}, predicted for a planar Pt surface under the same current density, it equals to larger than 75% of η_{Tafel}.

Although microwire array structure will help to increase the solution conductance by decreased ion transfer pathway blockage within the electrolyte due to lower the bubble vol. fraction, it can cause an increase of dissolved H_2 accumulation on some part of the electrode surface compared to the planar electrode under the same nominal current density and therefore lead to an increase in the local reversible hydrogen electrode potential shift.

REFERENCES:

1. Holmes-Gentle, I., et al., *Optical Losses at Gas Evolving Photoelectrodes: Implications for Photoelectrochemical Water Splitting.* The Journal of Physical Chemistry C, 2019. **123**(1): p. 17-28.

2. Coridan, R.H., et al., *Inhibition of Tafel Kinetics for Electrolytic Hydrogen Evolution on Isolated Micron Scale Electrocatalysts on Semiconductor Interfaces.* ACS Appl Mater Interfaces, 2016. **8**(37): p. 24612-20.

3. Leistra, J.A. and P.J. Sides, *Voltage Components at Gas Evolving Electrodes.* Journal of The Electrochemical Society, 1987. **134**(10): p. 2442-2446.

4. Liu, H., L.-m. Pan, and J. Wen, *Numerical simulation of hydrogen bubble growth at an electrode surface.* The Canadian Journal of Chemical Engineering, 2015. **94**: p. n/a-n/a.

5. Sequeira, C.A.C., et al., *Physics of Electrolytic Gas Evolution.* Brazilian Journal of Physics, 2013. **43**(3): p. 199-208.

6. El-Askary, W.A., et al., *Hydrodynamics characteristics of hydrogen evolution process through electrolysis: Numerical and experimental studies.* Energy, 2015. **90**: p. 722-737.

7. Hu, S., et al., *An analysis of the optimal band gaps of light absorbers in integrated tandem photoelectrochemical water-splitting systems.* Energy & Environmental Science, 2013. **6**(10): p. 2984-2993.

8. Tembhurne, S., F. Nandjou, and S. Haussener, *A thermally synergistic photo-electrochemical hydrogen generator operating under concentrated solar irradiation.* Nature Energy, 2019. **4**(5): p. 399-407.

9. Darmana, D., N.G. Deen, and J.A.M. Kuipers, *Detailed modeling of hydrodynamics, mass transfer and chemical reactions in a bubble column using a discrete bubble model.* Chemical Engineering Science, 2005. **60**(12): p. 3383-3404.

10. Vogt, H., *The Quantities Affecting the Bubble Coverage of Gas-Evolving Electrodes.* Electrochimica Acta, 2017. **235**: p. 495-499.

11. Westerheide, D.E. and J.W. Westwater, *Isothermal growth of hydrogen bubbles during electrolysis.* AIChE Journal, 1961. **7**(3): p. 357-362.

12. Vogt, H., *On the gas-evolution efficiency of electrodes I – Theoretical.* Electrochimica Acta, 2011. **56**(3): p. 1409-1416.

13. Vogt, H., *On the gas-evolution efficiency of electrodes. II – Numerical analysis.* Electrochimica Acta, 2011. **56**(5): p. 2404-2410.

14. Vogt, H., *On the various types of uncontrolled potential increase in electrochemical reactors—The anode effect.* Electrochimica Acta, 2013. **87**: p. 611-618.

15. Lanzi, O. and R.F. Savinell, *A Modified Constriction Model for the Resistivity of a Bubble Curtain on a Gas Evolving Electrode.* Journal of The Electrochemical Society, 1983. **130**(4): p. 799-802.

16. *Allen J. Bard and Larry R. Faulkner, Electrochemical Methods: Fundamentals and Applications, New York: Wiley, 2001, 2nd ed.* Russian Journal of Electrochemistry, 2002. **38**(12): p. 1364-1365.

17. Vogt, H., *Local microprocesses at gas-evolving electrodes and their influence on mass transfer.* Electrochimica Acta, 2015. **155**: p. 348-356.

Chapter VI

OPERATIONAL CONSTRAINTS AND STRATEGIES FOR SYSTEMS TO EFFECT THE SUSTAINABLE, SOLAR-DRIVEN REDUCTION OF ATMOSPHERIC CO_2

6.1 Introduction

A solar-fuels generation system designed to effect the sustainable reduction of CO_2 includes components for light absorption and charge separation, electrocatalysis of both the CO_2-reduction reaction (CO_2RR) and the oxygen-evolution reaction (OER), and a mechanism to transport ions between the two reaction chambers while maintaining robust product separation for both efficiency and safety reasons. Efficient electrochemical or photoelectrochemical conversion of CO_2 into usable fuels under mild pressure and temperature conditions entails greater physical and chemical constraints than efficient solar-driven water-splitting systems that can generate renewable H_2(g).

At the laboratory scale, no currently known catalyst can perform the multi-electron, multi-proton, electrochemical or photoelectrochemical CO_2RR efficiently and selectively. Polycrystalline metal electrodes are among the most studied class of materials for electrocatalysis of the CO_2RR, and most metals have been classified as being selective for CO, $HCOO^-$, or H_2.[1] Copper and copper-containing metal alloys have shown promise for forming hydrocarbons and C-C coupled products with a wide array of major and minor products, albeit at high overpotentials and with limited stability under operating

---

This chapter is based on results in: Yikai Chen, Nathan S Lewis and Chengxiang Xiang, Energy Environ. Sci., 2015, 8, 3663-3674 – Published by The Royal Society of Chemistry.

conditions.[2] Recent work on single-crystal,[3] nanostructured Au substrates[4] or oxide-derived Cu substrates[5] has shown the preferred formation of certain products with limited selectivity and activity. The low activity for the hydrogen-evolution reaction (HER) of semiconductor surfaces may provide opportunities to improve the electrocatalytic performance of GaAs,[6-8] GaP,[9, 10] InP,[6, 11] and of other semiconductors for CO_2RR.

Assuming the discovery of a suitable catalyst, robust and efficient couplings between the CO_2RR, the oxygen-evolution reaction (OER), and the necessary ionic transport processes between two potentially different electrolytes or solvent environments will be required for operation of a full, efficient, sustainable CO_2RR system. Traditional three-electrode, two-compartment electrochemical cells are typically employed to study the catalytic and energy-conversion performance of electrocatalysts and semiconductor/catalyst assemblies.[12] However, the transport of ions between the working electrode compartment (cathode chamber) and the counter electrode compartment (anode chamber) is often far from ideal, and the resistive losses and concentration overpotentials are typically compensated for by the additional external bias applied by the potentiostat.[13] The efficient and sustainable coupling of the CO_2RR and OER, with low potential losses and minimal product crossover between the two chambers, has been investigated only to a very limited degree. Moreover, in the absence of perfectly selective catalysts for both the CO_2RR and OER, a robust and efficient separator needs to be developed to prevent product crossover and thus provide efficient and safe operation of a CO_2RR system. While traditional membrane separators such as Nafion™ [14-19] are highly conductive and effective for preventing gas crossover in water-splitting systems, Nafion membranes yield high crossover losses in direct methanol fuel cells and would not be suitable for solar-driven CO_2RR devices that produce alcohols as products. Development of membranes with the desired permeability and ionic conductivity in the presence of a variety of solution species thus constitutes a significant research opportunity for CO_2RR systems.

Regardless of the performance of the full electrochemical cell at the laboratory scale, the sustainable reduction of CO_2 at global scale will additionally require effective mass

transport and uptake of atmospheric CO_2 on large areas of the Earth's surface. The large-scale, sustainable reduction of CO_2 requires a robust and cost-effective method for the delivery of CO_2 to the cathode surface of the device. Whereas liquid water or water vapor is readily able to produce sufficient reactant flux to allow for construction of an efficient solar-driven water-splitting system,[20] the low concentration of CO_2 in the atmosphere (~400 ppm), and the low solubility of CO_2 in aqueous solutions (~34 mM at standard temperature and pressure), present significant physical limitations to obtaining sufficient reactant transport to achieve technologically relevant efficiencies for the operation of a solar-driven CO_2RR system with atmospheric CO_2. To produce a reasonable partial pressure of CO_2 by direct air capture, the surface area for the CO_2 collection and concentration is likely to be many orders of magnitude larger than the surface area for the solar photon collection and conversion part of the system. Use of separate CO_2 concentration and reduction systems would present additional challenges for integration and coupling of the two technologies. While active research and development has been pursued to achieve efficient capture of CO_2 from air,[21-25] significant advances are still needed to make such technologies cost effective and functional in the presence of humidity and temperature variations in the atmosphere.

In this work, we have evaluated analytically the transport limitations of CO_2 from the tropopause down to a cathode surface, through five different regions with five different length scales (from tens of nanometers to tens of kilometers) (Figure 6.1a) that are coupled in series from a mass transport perspective. In each case, an effective mass transfer coefficient, σ_i, has been obtained. The mass transfer coefficients will add reciprocally to produce the reciprocal of the overall CO_2 mass transfer coefficient of the system, σ_{system}:

$$\frac{1}{\sigma_{system}} = \sum_i \frac{1}{\sigma_i} \qquad \text{(Eq. 6.1)}$$

The approach allows estimates of the concentration overpotentials and achievable solar-to-fuels efficiency for a hypothetical CO_2 reduction reactor fed by air that contains the same concentration of CO_2 as the surrounding atmosphere. We describe and model

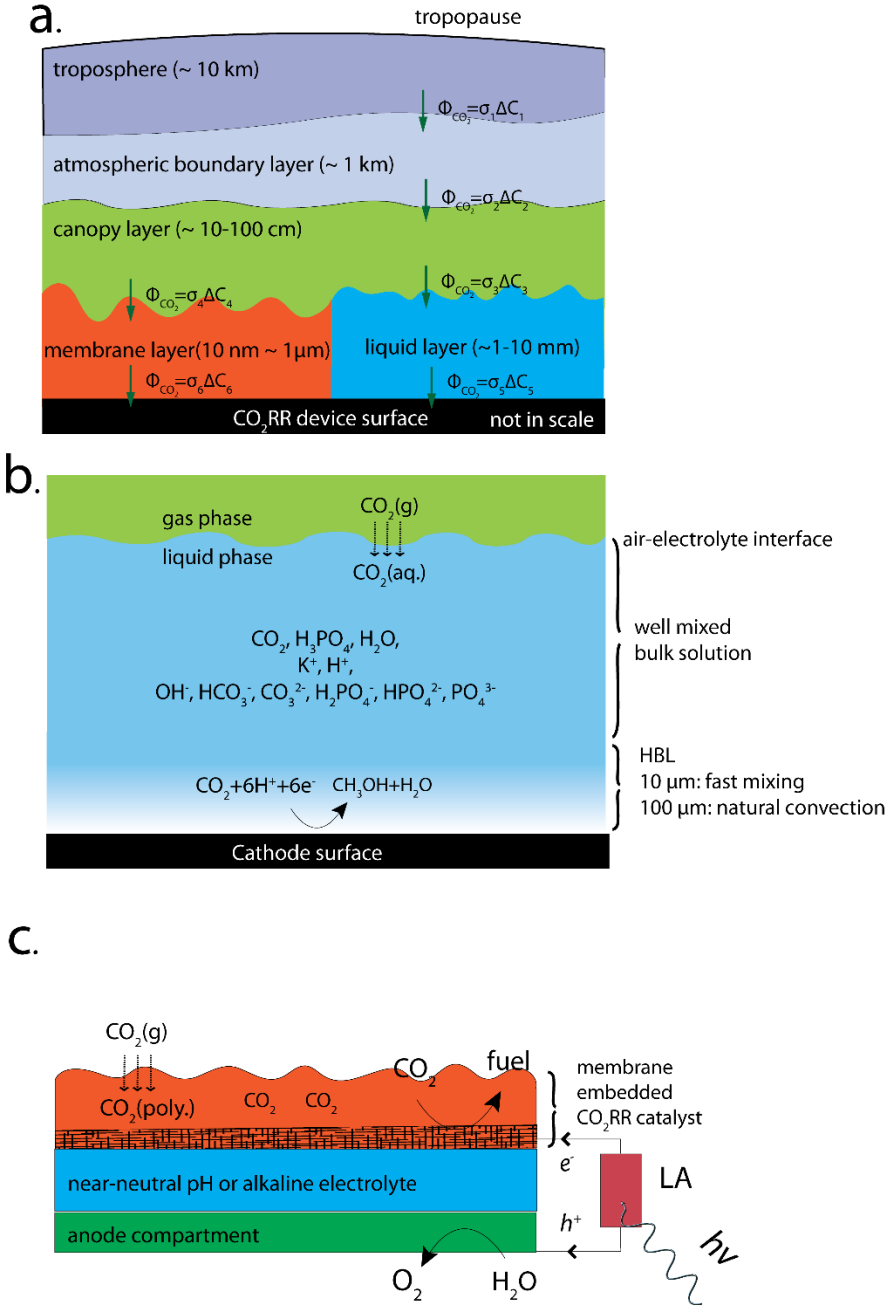

Figure 6.1. (a) Schematic illustration of CO_2 transport in five different regions with five different length scales. (b) Schematic illustration of the model used for CO_2 transport near the cathode surface that contains an aqueous layer with a variety of solution species. (c) Schematic illustration of the CO_2RR reactor that incorporates a light absorber (LA), a catalyst-embedded, thin-layer membrane assembly (orange), an anode compartment for OER (green) and a proton-transport electrolyte (blue).

quantitatively the effects of two strategies to improve the feasibility of producing efficient and sustainable CO_2 transport to a cathode surface at p_{CO_2} = 400 ppm: development of new catalysts analogous to metalloenzymes such as carbonic anhydrase, to dramatically enhance the kinetics of the interconversion of bicarbonate ions and CO_2 in the bicarbonate buffer system and thus improve the ability to maintain the concentration of CO_2 in the aqueous solution at p_{CO_2}= 400 ppm; and the use of a thin-layer cell architecture that minimizes the required CO_2 transport in an aqueous or polymeric electrolyte. These two strategies could, in principle, yield significant increases in the air/electrolyte CO_2 conductance relative to the natural transport at global scale of CO_2 across the atmosphere/ocean interface. The atmospheric transport of CO_2 between the troposphere and atmospheric boundary layer (ABL), and the corresponding constraints for the transport of CO_2 to the reactor at regional scale, have also been evaluated to complete the expression for the overall system CO_2 conductance and in turn to establish the ultimate limit on the efficiency of a sustainable solar-driven CO_2RR system deployed at global scale.

6.2 Modeling

6.2.1 CO_2 transport

Figure 6.1a shows a schematic illustration of the CO_2 transport from tropopause towards the surface of a CO_2RR device. Five different layers with different characteristic length scales are coupled in series with the same CO_2 flux. Three distinctive types of phase boundaries: gas/gas (troposphere/atmospheric boundary layer (ABL), ABL/canopy layer), gas/electrolyte (canopy layer/membrane layer, or canopy layer/liquid layer) and electrolyte/electrode interface (liquid layer/cathode surface, or membrane layer/cathode surface) were included in the transport schematics. The CO_2 concentrations within the troposphere, the ABL, and the canopy layer were assumed to separately be constant due to rapid turbulent mixing within each layer, while the net CO_2 flux across the troposphere/ABL interface and across the ABL/canopy interface results in CO_2 concentration differentials between the different gas-phase layers. The equilibrium CO_2 concentrations at the various gas/electrolyte interfaces were assumed to follow Henry's

law. At the electrolyte/electrode interfaces, and a 4-electron/4-proton OER was assumed and a 6-electron/6-proton CO_2RR was assumed, to represent a favorable situation for the ratio of CO_2 molecules to electrons in the electrochemical cell.

At the phase boundaries, the CO_2 flux across the interface, Φ_{CO2} [mol cm^{-2} s^{-1}] was expressed as $\Phi_{CO2}= \sigma \Delta C$, where σ is an effective mass transfer coefficient [cm s^{-1}] and ΔC is the concentration differential of CO_2 [mM] between the two neighboring layers. Two transport pathways, one containing the membrane layer (σ_1, σ_2, σ_4 and σ_6) and the other containing the liquid layer (σ_1, σ_2, σ_3 and σ_5), were modeled and evaluated in this study. The CO_2 flux across all of the interfaces, $\Phi_{CO2,}$ can be expressed as $\Phi_{CO2}= \sigma_{system}$ ($C_{troposphere}$-$C_{cathode}$), where σ_{system} is the overall effective mass transfer coefficient of the system, which can be expressed as $\frac{1}{\sigma_{system}} = \frac{1}{\sigma_1} + \frac{1}{\sigma_2} + \frac{1}{\sigma_3} + \frac{1}{\sigma_5}$ for the system that contains the liquid layer and as $\frac{1}{\sigma_{system}} = \frac{1}{\sigma_1} + \frac{1}{\sigma_2} + \frac{1}{\sigma_4} + \frac{1}{\sigma_6}$ for the system that contains the membrane layer. As a result of the reciprocal summation relation, the overall effective mass transfer coefficient of the system, σ_{system}, is smaller than any individual mass transfer coefficient, and is dominated by the process with the smallest mass transfer coefficient in the system.

6.2.2 One-dimensional traditional cell design

Figure 6.1b illustrates the one-dimensional (1-D) model used in this work to evaluate the CO_2 transport near a cathode performing a 6-electron/6-proton CO_2RR. The electrode was assumed to have a sufficiently high catalytic activity that under operating conditions the CO_2 concentration was driven to zero at the electrode surface. A well-mixed bulk solution was assumed, and two hydrodynamic boundary layers (HBL), that accounted for forced convective mixing (l_{HBL} = 10 μm) and natural convection (l_{HBL} = 100 μm), respectively, were introduced near the cathode surface. Rapid equilibration of CO_2 was assumed at the air-electrolyte interface, and the acid-base equilibria for the carbonate buffer and for the phosphate buffer, as well as the equilibria for the corresponding chemical reactions, were included in the model for the liquid regions. The same configuration,

representing a well-mixed bulk solution layer and two HBLs, was assumed for the OER at the anode.

Figure 6.1 summarizes the diffusion coefficients of species in water, as well as the forward and reverse rate constants for the bicarbonate buffer solution, that were used in the simulation.[26, 27] Note that the total CO_2 concentration in Figure 6.1 has been defined as the sum of the dissolved CO_2 in aqueous solution, $CO_2(aq)$, and the carbonic acid concentration, H_2CO_3. The forward and reverse reaction rates, k_{1+} and k_{1-}, respectively, fully describe the acid-base equilibrium between $CO_2(aq)$, H_2CO_3 and HCO_3^- in the buffer system.[26, 27] The transport loss in the system was assumed to be independent of the detailed electrocatalytic parameters for the cathode and anode, and was assumed to be a function only of the operating current density at the electrode surfaces. In some situations, an interconversion enhancement factor was introduced to increase both the forward and reverse reactions for reaction (1-4) in Figure 6.1, to represent the behavior of a hypothetical catalyst for these reactions with the catalyst having a reactivity analogous to that exhibited by the enzyme carbonic anhydrase.

6.2.3 Catalyst-embedded, thin-layer membrane assembly for rapid transport of CO_2

Figure 6.1c illustrates a conceptually distinct system that consists of a CO_2-reduction reactor based on a catalyst-embedded, thin-layer membrane device architecture. The cell consists of a solar-driven CO_2RR reactor that incorporates a light absorber (LA), a catalyst-embedded thin-layer membrane assembly, an anode compartment, and an electrolyte that is either buffered at near-neutral pH or is maintained under alkaline conditions. The LA (red) captures the solar photons and converts them into energetic electrons and holes for the fuel-forming reactions. The device has been designed to achieve large mass transport fluxes of CO_2 to the electrode surface, based purely on diffusional transport of CO_2 in the ultrathin electrolyte, because the catalyst-embedded, thin-layer membrane assembly (orange) reduces the length of the pathways for the CO_2 transport within the polymer electrolyte.

In this device, the equilibrium CO_2 concentration at the gas/polymer electrolyte interface was assumed to follow Henry's law. Three different permeabilities for CO_2 transport in the polymer electrolyte were assumed. The buffered near-neutral pH or alkaline electrolytes (blue) were chosen so that the small proton concentration at the cathode surface would suppress the rate of the hydrogen-evolution reaction (HER) relative to the rate of the CO_2RR. The anode compartment (green) performed the OER and provided the necessary proton source for the cathode. The anode compartment also contained an anion-exchange membrane for the alkaline operation or a bi-polar membrane for CO_2RR and OER at two different pHs, to facilitate the ionic transport and reduce the product crossover in the system.

6.2.4 Governing equations

Ionic species and neutral species in the electrolyte solution were modeled using the Nernst-Planck equation,[12] in which the diffusion, migration and bulk reactions of water and buffer dissociation were explicitly included. Forced convection was approximated by the use of the hydrodynamic boundary layers.

The total voltage requirement $\left(\Delta\phi_{\text{cell}}\right)$ for the electrochemical cell was calculated as the sum of the equilibrium potential $\left(E_0\right)$, kinetic overpotentials $\left(\eta\right)$, solution potential drop losses $\left(\Delta\phi_{\text{solution}}\right)$, and the Nernstian potential losses associated with pH gradients, $\left(\Delta\phi_{\text{pH gradients}}\right)$, as well as the potential drops associated with CO_2 concentration gradients, $\left(\Delta\phi_{CO_2\text{ gradients}}\right)$ at the surface of the electrodes:

$$\Delta\phi_{\text{cell}} = E_0 + \eta_{\text{OER}} - \eta_{\text{HER}} + \Delta\phi_{\text{solution}} + \Delta\phi_{\text{pH gradient}} + \Delta\phi_{CO_2\text{ gradient}} \qquad \text{(Eq. 6.2)}$$

The solution losses, $(\Delta\phi_{\text{solution}})$, were calculated as the sum of the ohmic resistive loss (first term) and the electrodialysis loss (second term). These losses can be expressed as:

$$\Delta\phi_{\text{solution}} = \int \frac{J}{\kappa} dx + \sum_i \int \frac{F z_i D_i \nabla c_i}{\kappa} dx \qquad \text{(Eq. 6.3)}$$

where ϕ is the electric potential, κ is the conductivity of the electrolyte, J is the current density, x is distance along the axis of the 1-D model, F is Faraday's constant, z is the charge number, D_i is the diffusion coefficient and c_i is the molar concentration of the i^{th} species, R is the gas constant, and T is the absolute temperature. The distribution of the ionic conductivity, $\kappa(x)$, and of the species concentrations, $c_i(x)$, obtained from COMSOL Multiphysics software were used in the above equations to calculate the ohmic and electrodialysis losses of the system.

The Nernstian potential losses associated with the pH gradients $\left(\Delta\phi_{\text{pH gradients}}\right)$ and CO_2 concentration gradients $\left(\Delta\phi_{CO_2 \text{ gradients}}\right)$ at the surface of the electrodes can be expressed as:

$$\Delta\phi_{\text{pH gradient}} = 2.303\frac{RT}{F}\left(\text{pH}_{\text{cathode}} - \text{pH}_{\text{anode}}\right) = 59(mV)\left(\text{pH}_{\text{cathode}} - \text{pH}_{\text{anode}}\right)$$

$$\Delta\phi_{CO_2 \text{ gradients}} = \frac{RT}{nF}\ln\left(\frac{p_{CO_2,cathode}}{p_{CO_2,bulk}}\right) = \frac{59(mV)}{n} Log\left(\frac{p_{CO_2,cathode}}{p_{CO_2,bulk}}\right) \qquad \text{(Eq. 6.4)}$$

where n is number of electrons transferred in the CO_2 reduction process, with $n = 6$ assumed as a as favorable case for the purposes of this study. $p_{CO_2,cathode}$ and $p_{CO_2,bulk}$ are the partial pressures of CO_2 at the cathode surface and in the bulk solution, respectively.

$CO_2 + H_2O \underset{k_{1-}}{\overset{k_{1+}}{\rightleftharpoons}} H^+ + HCO_3^-$	k_{1+}=0.037 s^{-1} k_{1-}=7.83x10^4 M^{-1} s^{-1}
$CO_2 + OH^- \underset{k_{2-}}{\overset{k_{2+}}{\rightleftharpoons}} HCO_3^-$	k_{2+}=2.23x10^3 M^{-1} s^{-1} k_{2-}=4.85x10^{-5} s^{-1}
$HCO_3^- \underset{k_{3-}}{\overset{k_{3+}}{\rightleftharpoons}} H^+ + CO_3^{2-}$	k_{3+}=2.5 s^{-1} k_{3-}=5x10^{-10} M^{-1} s^{-1}
$HCO_3^- + OH^- \underset{k_{4-}}{\overset{k_{4+}}{\rightleftharpoons}} H_2O + CO_3^{2-}$	k_{4+}=6x10^9 M^{-1} s^{-1} k_{4-}=1.2 s^{-1}

Table 6.1. The forward and the backward rate constants the bicarbonate buffer solution and used in the simulation.

6.3. Results

6.3.1 Limiting performance of cells operated using a 400 ppm CO_2 feedstock

At 400 ppm of CO_2 in the reactant atmosphere, CO_2 transport at the electrolyte/electrode interface, specifically, $\Phi_{CO2}=\sigma_5\ \Delta C_5$ in Fig. 6.1a, produced significant concentration polarization and limited the device efficiency. Figure 6.2a shows the steady-state limiting current density as a function of the electrolyte pH for a 6-electron/6-proton CO_2 reduction process. Two HBL thicknesses, 100 μm (red) and 10 μm (blue) were used to account for natural convection and forced convection, respectively. In addition to the bicarbonate buffer system, in which the dissolved CO_2 concentration was set to the solubility limit, the electrolyte solution was buffered at different pHs with a 1.0 M phosphate buffer. The steady-state limiting current density was < 0.2 mA cm^{-2} for all cases, which is ~2 orders of magnitude smaller than the current density required to produce a CO_2RR reactor with a 10% solar-to-fuels efficiency. In the higher pH solutions (pH > 10.2), a slight increase in

the obtainable steady-state limiting current densities was observed. The higher concentration of bicarbonate in higher pH electrolytes at p_{CO_2}=400 ppm resulted in an enhanced conversion from bicarbonate species to CO_2.

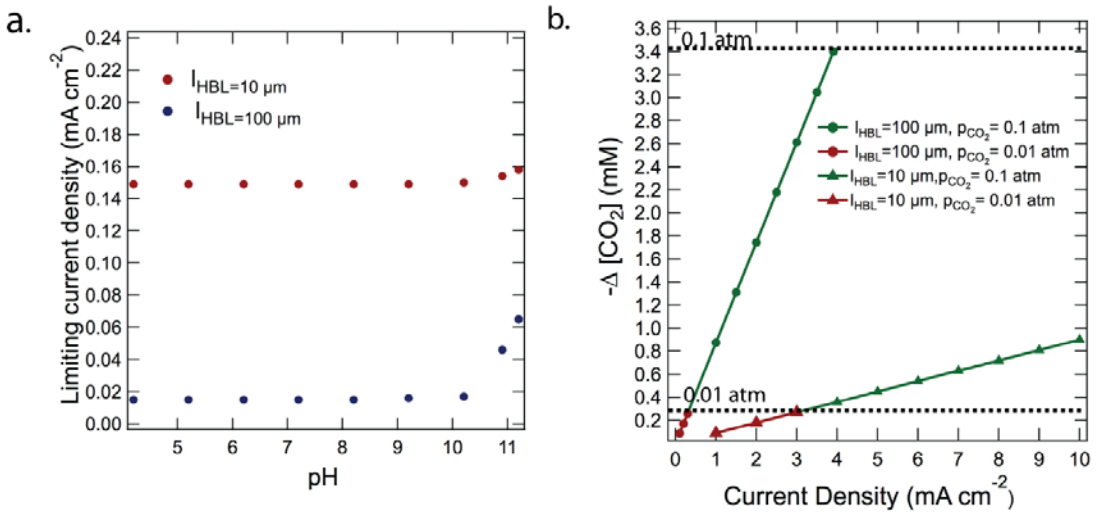

Figure 6.2. a) Steady-state limiting current densities as a function of solution pH for a 6-electron/6-proton CO_2 reduction process fed by air containing CO_2 at p_{CO_2}=400 ppm for l_{HBL}=100 μm (red) and l_{HBL}=10 μm (blue). b) The change of CO_2 concentration at the electrode surface from the bulk equilibrium values as a function of the operating current density for a 6-electron/6-proton CO_2 reduction process at the p_{CO_2}= 0.1 atm (green) and p_{CO_2}= 0.01 atm (red) and for l_{HBL}=100 μm (circle) and l_{HBL}=10 μm (triangle). The concentration of CO_2 at the solubility limit in aqueous solutions at p_{CO_2}= 0.01 atm and p_{CO_2}= 0.1 atm were indicated by the black dotted lines.

Figure 6.2b shows the change of the CO_2 concentration at the cathode surface relative to the bulk equilibrium value, $\Delta[CO_2]$, as a function of the operating current density for a 6-electron/6-proton CO_2 reduction process at two different partial pressures of CO_2. A linear relationship between $\Delta[CO_2]$ and the operating current density was observed for two

different partial pressures of CO_2. At a given HBL thickness, a constant slope was observed at different partial pressures of CO_2. When $\Delta[CO_2]$ approached the solubility limit for CO_2, a steady-state limiting current density was reached. For a cell fed by a 25-fold higher CO_2 partial pressure than found in air, i.e., p_{co_2} = 0.01 atm, the limiting current densities were 0.3 mA cm^{-2} and 3 mA cm^{-2} for l_{HBL}=100 μm and l_{HBL}=10 μm, respectively. Although numerous solution species and chemical reactions in the liquid layer are associated with the inter-conversion of CO_2 species, a linear relation, $\Phi_{CO2}=\sigma_5 \Delta C_5$, was sufficient to describe the CO_2 transport process at the gas/electrolyte interface. Effective mass transfer coefficients, σ_5= 0.002 cm s^{-1} and 0.018 cm s^{-1}, were obtained for l_{HBL}=100 μm and l_{HBL}=10 μm, respectively. Note that the value of the effective mass transfer coefficient reflected both the pure diffusive transport of the neutral CO_2 species and the chemically enhanced transport due to the interconversion of CO_2 and the bicarbonate ion.

6.3.2 Effect of enhancing the rates of interconversion for the bicarbonate buffer system

The low mass transfer coefficient, σ_5, at the electrolyte/electrode interface significantly limited the attainable operating current density in the system. One approach to in principle accelerate the rate of chemically enhanced transport in the system involves the development of catalysts that can rapidly interconvert dissolved CO_2, carbonic acid, and bicarbonate.

Figures 6.3a and 6.3b show the steady-state limiting current density as a function of a hypothetical interconversion-enhancement factor for the bicarbonate buffer system for l_{HBL}=100 μm and l_{HBL}=10 μm, respectively. The bulk CO_2 concentration was equilibrated with p_{CO_2}= 400 ppm and was set to 14 μM. The situation for four different pH values, 9.2, 10.2, 10.9 and 11.2, which correspond to bicarbonate concentrations of 0.01 M, 0.1 M, 0.5 M and 1.0 M, respectively, were evaluated. A significant increase in the steady-state limiting current density required an increase of 6 orders of magnitude in the rates for the interconversion of carbon dioxide and bicarbonate (or vice versa) relative to the natural

interconversion rate. In particular, in higher pH solutions, where the bicarbonate concentration was higher, the reverse reactions, $H^+ + HCO_3^- \rightarrow CO_2 + H_2O$ and $HCO_3^- \rightarrow CO_2 + OH^-$, were significantly increased at higher interconversion-enhancement factors. For instance, for l_{HBL}=10 μm, the steady-state limiting current density exceeded 20 mA cm^{-2} for pH=10.9 and 11.2 in the presence of this hypothetical million-fold increase in equilibration rate relative to the natural situation.

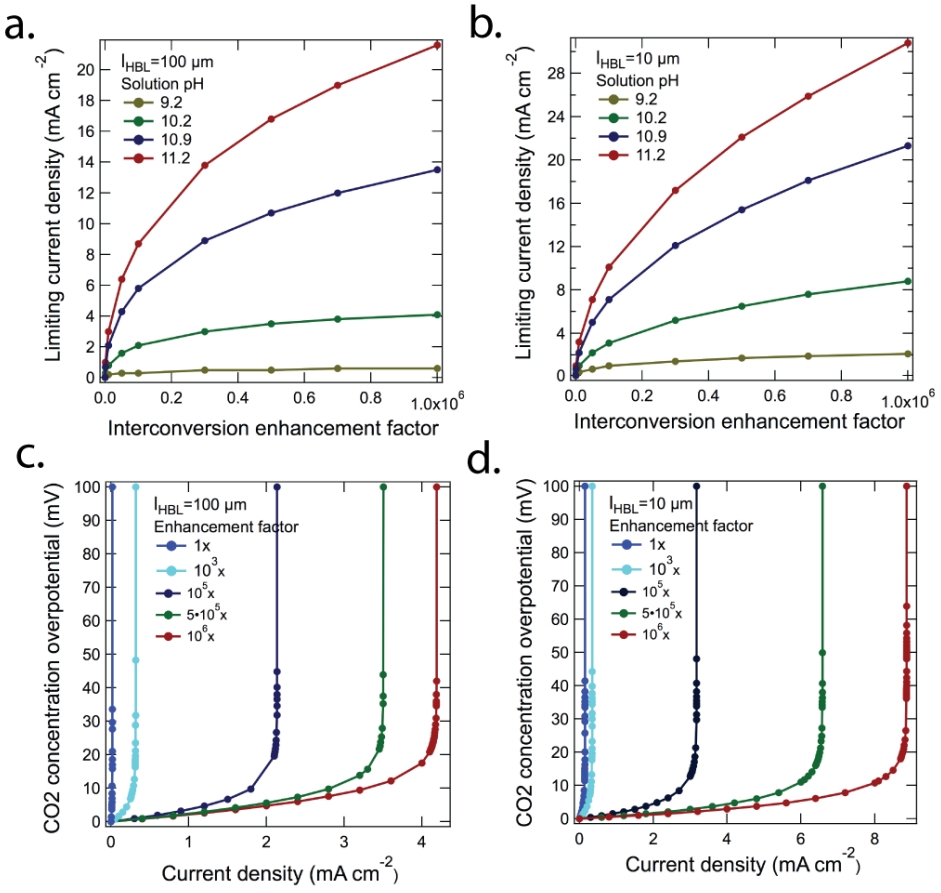

Figure 6.3. The limiting current density of a 6-electron/6-proton CO_2 reduction process as a function of the interconversion-enhancement factor in four solutions with different pH values and fed by air with p_{CO_2}=400 ppm for (a) l_{HBL}=100 μm and (b) l_{HBL}=10 μm, respectively. The Nernstian potential loss resulting from the CO_2 concentration gradient which develops near the surface of a cathode in contact with an electrolyte with pH = 10.2, as a function of the operating current density for (c) l_{HBL}=100 μm and (d) l_{HBL}=10 μm, respectively. The concentration of the dissolved CO_2 in at the HBL was assumed to follow Henry's law and was set to 14 μM for p_{CO_2}=400 ppm.

Figures 6.3c and 6.3d show the Nernstian potential losses associated with the development of CO_2 gradients near the surface of a cathode in contact with an electrolyte with pH = 10.2, as a function of the operational current density, for five different interconversion-enhancement factors with l_{HBL}=100 μm and l_{HBL}=10 μm, respectively. The CO_2 concentration overpotential increased exponentially when the operating current density approached the steady-state limiting current density according to the Nernst equation. Minimization of the potential losses (< 100 mV) due to concentration overpotentials requires that the operating current densities remain below the values at which the concentration-overpotential curves rise nearly vertically in Fig. 6.3c and 6.3d. The solution loss and the Nernstian potential losses associated with pH gradients at the electrode surfaces were small (< 50 mV) in the assumed cell design, and were additionally minimized by the use of a phosphate buffer and a convected electrolyte. Similar results were also reported recently in an analytical assessment of solar water-splitting systems at near-neutral pH.[28]

Figure 6.4 shows the spatially resolved concentration profile of the ionic and neutral species between the cathode surface and the hydrodynamic boundary layer (HBL) at an operational current density of 1 mA cm^{-2}. At the bulk-solution edge of the HBL, the concentration of the dissolved CO_2 was set to 14 μM. In a cell fed by air with p_{CO_2}=400 ppm, and containing a pH=10.2 solution and 1.0 M phosphate buffer, minimal pH gradients were observed (Fig 6.4a). Figure 6.4b shows the steady-state CO_2 generation/consumption rate within the HBL. As the enhancement factor increased, a rapid increase of the CO_2 generation rate near the cathode surface, and a rapid increase of uptake of CO_2 at the edge of the HBL, were observed. In the middle region, an acid-base equilibrium with near-zero CO_2 generation/consumption was observed. The increased CO_2 generation rate near the cathode surface increased the steady-state limiting current density of the system at higher enhancement factors. Fig. 6.4c and 6.4d also depict the corresponding CO_2 concentration and the bicarbonate concentration profile.

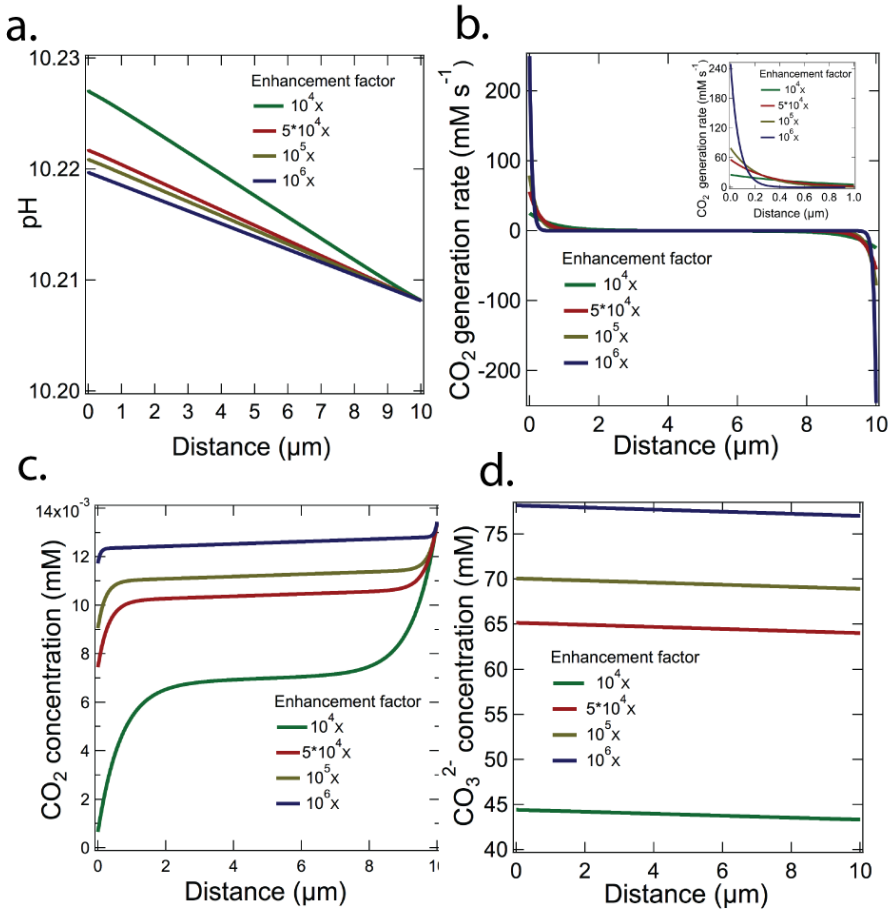

Figure 6.4. (a) The pH profile, (b) CO_2 generation/consumption rate in the HBL and close to the electrodes (b, insert), (c) CO_2 concentration and (d) bicarbonate concentration within the HBL as a function of distance from the cathode for a cell operating at a current density of 1 mA cm^{-2} and for four different interconversion enhancement factors.

6.3.3 Performance of the catalyst-embedded, thin-layer membrane assembly for rapid transport of CO_2

Instead of dramatically accelerating the chemically enhanced transport in aqueous solutions, an alternative strategy to significantly improve the purely diffusive transport would involve the use of a thin-layer electrochemical cell design (Fig. 6.1c). The CO_2 transport at the polymer-electrolyte/electrode interface, specifically, $\Phi_{CO2}=\sigma_6\ \Delta C_6$ in Fig.

6.1c, and the resulting limiting current density, can in principle be significantly enhanced by use of a thin-layer membrane electrolyte, and consequently relying on purely diffusive fluxes to achieve the desired current density at sufficiently small membrane thicknesses.

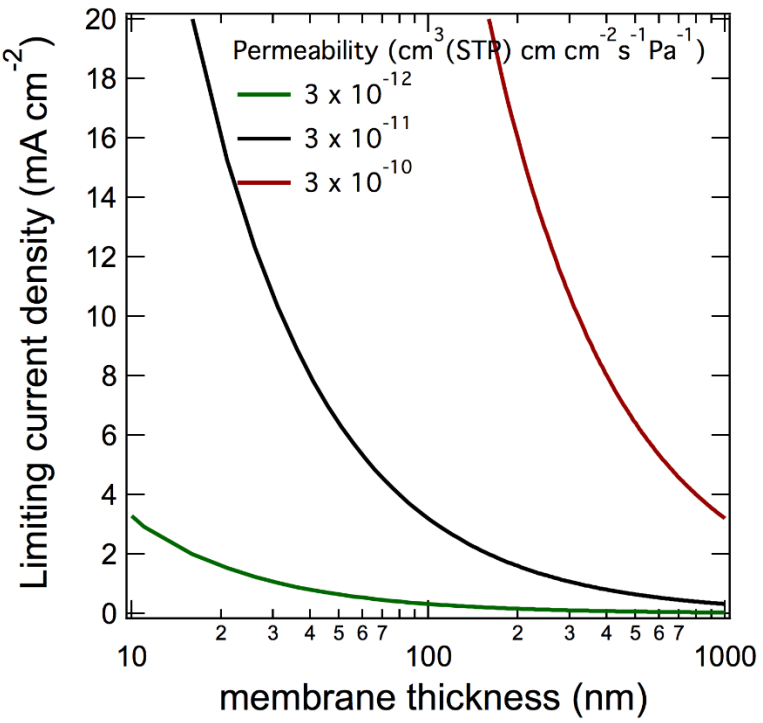

Figure 6.5. The calculated limiting current density as a function of the membrane thickness for three different permeabilities of CO_2 in the membrane.

Figure 6.5 shows the limiting current density as a function of the membrane thickness for three different permeabilities of CO_2 in the polymer electrolytes of the catalyst-embedded thin-layer membrane-assembly design (Fig. 6.1c). The solubility and the diffusion coefficient of CO_2 in the polymer electrolytes, i.e., Nafion, are highly dependent on the polymer morphology, the polymer segmental dynamics, the hydration conditions, and the operating temperature.[29-32] The permeability of CO_2 and other gases for Nafion

membranes is the product of the diffusion coefficient and the solubility. The permeability is the key figure of merit for CO_2 transport in membrane-based systems, and has been measured experimentally by others under various conditions. The black curve used a typical value, $3x10^{-11}$ [cm^3(STP) cm cm^{-2} s^{-1} Pa^{-1}], for the permeability of CO_2 in Nafion near room temperature.[31, 32] The red and green curves represent results for permeability values of $3x10^{-10}$ and $3x10^{-12}$ [cm^3(STP) cm cm^{-2} s^{-1} Pa^{-1}], respectively, and represent the upper and lower bounds for the calculation. The attainable current density in the membrane-based system was independent of the pH conditions and was determined by the solubility and the diffusion coefficient of CO_2 in the membrane, as well as by the thickness of the membrane. The effective mass transfer coefficient at the polymer-electrolyte/electrode interface, σ_6, at a membrane thickness of 100 nm was 0.038 cm s^{-1} and 3.8 cm s^{-1} for the upper and lower limit of the membrane permeability values, respectively. The thin layer of the catalyst-embedded membrane minimized the CO_2 transport in the aqueous solution or polymeric media, and enabled the direct electrochemical reduction of CO_2 from air at current densities in excess of 10 mA cm^{-2} without mass transport limitations in the liquid layer.

6.4. Discussion

Assumptions and Limitations of the Treatment of CO_2RR Systems

The limiting electrochemical current densities and concentration polarization losses obtained in this study pertain solely to the cathode and electrolyte region near the cathode, in a fashion analogous to evaluating the flux-limited current densities at the working electrode in a traditional 3-electrode electrochemical experiment. In an actual two-electrode photoelectrosynthetic system comprised of catalysts that effect the CO_2RR and OER, the current density at the cathode is likely to be nonuniform,[33] resulting in even higher local CO_2 flux demands by a factor of 10 or more than those assumed herein for an isopotential electrode surface. The cathodic reduction products and CO_2RR intermediates were assumed to have negligible reactivity with O_2(g) in the atmosphere, and despite the

much higher concentration of O_2 relative to CO_2 in ambient air, O_2(g) was assumed to be electroinactive at the cathode at potentials required to effect the CO_2RR, despite the >1 V driving force for O_2(g) reduction to H_2O and the ease of reducing O_2(g) to H_2O_2 at these potentials. No CO_2 catalysts or electrode systems known to date meet any of these criteria. The CO_2RR products and intermediates at the cathode were assumed to be separated from the anode, which was assumed to have 100% faradaic efficiency for O_2(g) evolution. The ohmic resistive loss, pH gradients, and electrodialysis due to the incorporation of an cation exchange membrane or an anion exchange membrane in the near-neutral pH system,[28] such as the bicarbonate buffer system, which can individually or collectively produce significant and in some cases overwhelming voltage losses in the operating cell, have not been considered in the present assessment.

Standard temperature conditions 273.15 K were assumed for the operational temperature of the CO_2RR systems in the simulations performed herein. Solar-driven CO_2RR systems may operate at elevated temperatures. The solubility of CO_2 in water is strongly temperature dependent, and the Henry's law constant for CO_2 decreases from 34 mM atm^{-1} to 13 mM atm^{-1} when the operational temperature is increased from 273 K to 333 K.[34] Hence, at elevated temperatures, the decreased solubility of CO_2 in water would lead to a further reduction the mass-transport-limited current density in the cell. One approach to increase the solubility of CO_2 in the electrolyte is to use ionic liquids. For instance, the solubility of CO_2 in imidazolium-based ionic liquids can be ~40 x larger than the CO_2 solubility in aqueous bicarbonate solutions at standard temperature.[35] However, the ~10-20 fold lower low diffusion coefficient of CO_2[36, 37] in ionic liquids as compared to in aqueous solutions, combined with the lack of chemically enhanced CO_2 transport in the ionic liquids, will produce mass-transport limited current densities in such media that are on the same order of magnitude as those in aqueous solutions (Fig. 6.2).

Conductance at the Atmosphere/Aqueous Electrolyte Interface

Regardless of the ideal activity, selectivity and coupling between OER and CO_2RR in the full electrochemical cells, the CO_2 flux at the atmosphere/aqueous electrolyte interface imposes constraints on the mass transfer and thus on the efficiency for the system. For aqueous electrolytes that have thicknesses larger than the width of the hydrodynamic boundary layer, the low solubility of CO_2 in water, combined with the relatively small diffusion coefficient of CO_2 in liquid water compared to in the gas phase, produces very low CO_2 fluxes and conductances. Hence, over large areas, either with natural convection or with forced convection sufficient to thin the hydrodynamic boundary layer in the aqueous phase to 10 μm, a value comparable to that obtained according to the Levich equation with a rotating disk electrode at a rotation velocity of 10^6 rpm,[12] the steady-state limiting CO_2 flux even with a 6-electron reduction of each CO_2 molecule is 100-1000 fold lower than the 10 mA cm^{-2} current density produced by the solar photon flux in an efficient single or tandem photoelectrode system.[38, 39] Hence regardless of the activity of an electrocatalyst for CO_2 reduction, the solar-to-fuels conversion efficiency of such a system will be limited to < 0.1% based on the active area of the solar collection component. Additionally, the concentration overpotential will require higher voltages for a complete CO_2 reduction system than are expected based on the potential differences between the CO_2RR half-reaction and the OER half-reaction alone, including their associated kinetic overpotentials at each electrode surface.

This conclusion is in accord with the CO_2 uptake fluxes that have been established previously for the air/ocean boundary for use in assessing the global carbon cycle in coupled air/ocean general circulation models. Specifically, extensive studies of CO_2 exchange at the air-sea interface have shown that the effective mass transfer coefficient of CO_2 across the air-liquid interface, specifically, σ_3, in Fig. 6.1c, is on the order of 10^{-3} - 10^{-2} cm s^{-1}, corresponding to a current density of ~ 10-100 μA cm^{-2} for a 6-electron/6-proton CO_2RR, over a large range of temperatures, wind velocities, salinities and pH conditions.[40-42] In situations where the effective mass transfer coefficient, σ_3 or σ_4, presents a transport limitation, the air/electrolyte interface equilibrium according to Henry's law may not be

achieved. In this case, the device efficiency would be yet lower and would ultimately be limited by the rate of CO_2 transport across the air/electrolyte interface. Hence, without strategies to circumvent the inherently low CO_2 conductance at the air/water interface, very low solar-to-fuel conversion efficiencies will be obtained and/or the CO_2 capture and collection area will have to greatly exceed, by a factor of 100-1000, the active solar photon collection area of a sustainable solar-driven, aqueous-based, CO_2RR system.

Enhancement of interconversion rates for the bicarbonate buffer system

One strategy to circumvent the conductance limit imposed by liquid-phase transport, specifically by, $\Phi_{CO2}=\sigma_5\ \Delta C_5$, involves chemically enhancing the rate of CO_2 uptake by equilibrating the dissolved CO_2 with the bicarbonate and carbonic acid reservoirs in aqueous solutions buffered to pH values >7. Carbonic anhydrases are among the most well-known metalloenzymes that catalyze the rapid interconversion of carbon dioxide and water to bicarbonate and protons.[43] In the absence of a catalyst, the reversible reaction occurs relatively slowly, as reflected in the rate constants tabulated in Figure 6.1. At a CO_2 concentration of 14 μM, the catalyzed rate for the buffer interconversion reaction, as described using Michaelis–Menten kinetics for carbonic anhydrases, is ~ 200 s^{-1} (assuming a maximum rate of conversion of 4 x 10^5 s^{-1} and a Michaelis constant of 26 mM).[44, 45] As a result, a carbonic anhydrase concentration of ~2.5 mM would be required to achieve an interconversion enhancement factor of 10^6 relative to the uncatalyzed case. The concentration of carbonic anhydrase in sea water is estimated to be < ~ 100 nM,[46] so a 10^6 enhancement of the interconversion rate using such enzymes would require an enzyme concentration ~ 25,000-fold higher than the peak value in sea water systems.[46]

A hypothetical catalyst that had analogous catalytic activity to carbonic anhydrase, and that extremely rapidly replenished dissolved CO_2 near the cathode surface due to enhanced rates for the reverse reactions, reaction $H^+ + HCO_3^- \rightarrow CO_2 + H_2O$ and reaction $HCO_3^- \rightarrow CO_2 + OH^-$, could in principle produce significant increases in the limiting current density for a CO_2RR reactor, even when l_{HBL}=100 μm, i.e., for the natural

convection case. As shown in Figure 6.3, an interconversion-enhancement factor of at least 10^5 would however be needed before a CO_2RR cell with 10% solar-to-fuels conversion efficiency could be constructed, other transport limitations notwithstanding (vide infra). The heretofore unknown interconversion catalyst must of course itself be robust, electrochemically inert at both of the electrodes in the system, and operate under conditions with which the other components of the CO_2RR device are compatible.

Implemenation of thin –layer membrane assembly.

The required CO_2 flux to the cathode could in principle alternatively be obtained by use of a thin-layer membrane-based system (Figure 6.5). The efficient transport in a thin-layer (tens of nanometers thick) membrane (Fig. 6.5) exploits the very small distance between the gas phase CO_2 and the catalyst at the cathode surface. Due to the required short length of the pathways, the implementation of this strategy in the CO_2RR cell constrains the reduction products to be highly volatile/gaseous species such as methane or ethylene. Liquid fuel products, such as methanol or ethanol, which will form a liquid layer of the product at the electrocatalyst surface, will impede the CO_2 reactant transport towards the catalyst, and hence will result in unacceptably low CO_2 fluxes to the electrode surface, as in the case when the electrode is coated with a layer of liquid water (vide supra).

Transport between the canopy layer and the electrolyte.

The gas-phase transport of CO_2 near the electrode surface, specifically, at the canopy layer/membrane layer interface, $\Phi_{CO2}=\sigma_4\ \Delta C_4$, or the canopy layer/liquid layer interface, $\Phi_{CO2}=\sigma_3\ \Delta C_3$, does not impose significant limitations on the ability to deliver CO_2 to the CO_2RR reactor. According to the kinetic theory of gases, the rate of surface bombardment of CO_2 molecules at p_{CO_2}= 400 ppm is ~10^{20} molecules cm^2 s^{-1}, which could produce a mass-transport-limited current density many orders of magnitude higher than the photon flux in unconcentrated solar illumination. Another more practical estimation of the CO_2 flux at the air/membrane or air/liquid interfaces can be obtained by using Fick's first law:

$$\Phi_{CO2} = D\,\frac{[CO_2]_{atmosphere} - [CO_2]_{ground}}{l}, \qquad \text{(Eq. 6.5)}$$

where D is the diffusion coefficient of CO_2 in the atmosphere and l is the characteristic length for the diffusion gradient. Assuming laminar flow near the electrode surface of the CO_2RR reactor at a modest wind velocity, 5 m s^{-1}, the characteristic diffusion length, l, is given by $l \sim L/(U\,L/D)^{1/2}$,[47, 48] where L is the characteristic length scale of the device, U is the velocity magnitude, and D is the characteristic diffusion coefficient. Assuming $[CO_2]_{ground} = 0$ yields a mass transport limited equivalent current density of ~5 mA cm^{-2} (~5 x10^{15} molecules cm^2 s^{-1}) for a 6-electron/6-proton CO_2 reduction process. A more turbulent, convective mixing in the canopy layer would produce a higher CO_2 flux to the electrolyte. Hence, from these estimations, rapid gas-phase transport near the electrode surface would be able to produce an equilibrium CO_2 concentration that follows Henry's law and would not serve as the ultimate practical constraint on the system efficiency.

The rapid transport between the canopy layer and the electrolyte is a result of the relatively high gas-phase diffusion coefficient of CO_2. In the natural photosynthetic system, the terrestrial plant-based CO_2 fixation rate is significantly higher than the CO_2 flux across the air/ocean interface. Terrestrial plant-based photosynthesis thus takes advantage of the rapid CO_2 transport in the gas-phase as well as the 3-dimensional structure of the plants and trees on an ~1 m height scale, which leads to a significant increase in the contact area per unit of geometric area on the earth's surface and results in a more optimal "contactor" design than can be achieved at a planar air/water boundary over large horizontal length scales.

Gas-phase transport of CO_2 between the troposphere and the ABL and between the ABL and the canopy layer for regional-scale deployment of CO_2-reduction reactors

The fluxes of CO_2 between the troposphere and the atmospheric boundary layer (ABL), and between the ABL and the canopy layer, specifically, $\Phi_{CO2}=\sigma_1\,\Delta C_1$ and $\Phi_{CO2}=\sigma_2\,\Delta C_2$, in Fig. 6.1c, also impose a constraint on the CO_2 conductance of CO_2RR systems deployed

at regional-scale, for which the length-scale of the CO_2RR system is larger than the scale height of the atmosphere, broadly defined in the range between 10^4 and 10^6 km^2 (i.e. when vertical transport in the atmospheric column is more important than advection in determining the CO_2 concentration in the column), regardless of strategies used to enhance the conductance at the air/water or air/polymer interfaces. An estimate of the CO_2 mass transport limitation on scale lengths comparable to or larger than the scale height of the atmosphere can also be obtained by eqn. 5, where now D is the turbulent diffusion coefficient of the atmosphere and l is the vertical gradient scale height. The minimal value for l is set by the scale height of the atmosphere, which is ~ 100 km. In conjunction with an approximate value for the atmospheric diffusivity, D, of 10^6 cm^2 s^{-1}, the maximum CO_2 flux is thus ~10^{15} molecules cm^{-2} s^{-1}, which for a 6-electron/6-proton CO_2RR corresponds to a CO_2-transport-limited current density of ~1 mA cm^{-2}.

Another estimation of the mass-transport-limited CO_2 flux can be obtained by reference to the net ecosystem-exchange (NEE) rate for CO_2, which has been directly measured and monitored by various techniques, including eddy covariance methods, over long periods (months or years) in different regions worldwide.[49-52] Satellite retrieval methods that allow extraction of the vertical profile of CO_2 in an atmospheric column in turn allow formulation of a flux relationship between the CO_2 concentration differential "i.e. draw-down" in the ABL relative to the CO_2 concentration in the troposphere, as a function of the local NEE rate. A quasi-linear relationship at regional spatial scales between the net CO_2 flux and the CO_2 draw-down between the troposphere and the ABL has been observed, as expected.[49, 53] On average, an ~ 2 μmol m^{-2} s^{-1} net CO_2 flux between the troposphere and the ABL results in ~10 ppm reduction in the CO_2 concentration in the ABL[49], which corresponds to an effective mass transfer coefficient of 0.44 cm s^{-1}. If a sustained 10% solar-to-fuel (STF) conversion efficiency were achieved for a 6-electron/6-proton CO_2 reduction process and the cell level, and such a system were deployed on a regional scale, extrapolation of this linear relationship indicates that a daily average CO_2 draw-down of ~ 130 ppm would be produced between the troposphere and the entire (well-mixed) ABL, 2-2.5 km in height (assuming a 20% capacity factor for the CO_2RR reactor), by the sustained mass flux, and

consumption, of CO_2 at the electrode surface. During the peak operation of a solar-driven CO_2RR system deployed on a regional scale, a significantly larger (5×) drawdown of CO_2 in the ABL, and a large temporal variation of the CO_2 concentration in the ABL, would be expected. The decreased CO_2 levels in the ABL would in turn require even more active catalysts (because the concentration is lower at the electrode surface if it is driven to near zero) and also will involve, at least transiently, a depletion of essentially all of the CO_2 in a column of the atmosphere that is ~2.5 km height, depriving local plant life of CO_2 for use in photosynthesis. Moreover, the height of ABL and the concentration of CO_2 in the ABL are also highly dependent on storms, and weather conditions in the atmosphere, etc. The flux into the ABL can even under some conditions invert in sign. Hence, the significant alteration of the CO_2 concentration in the ABL, and concomitant spatial and temporal variations in the attainable CO_2 uptake at the surface of the Earth, present significant practical and engineering impediments to the deployment of regional-scale systems that would involve rapid CO_2 consumption rates at the electrode surface, assuming that such a system can be achieved through unprecedented catalyst development, along with aggressive strategies to increase the CO_2 uptake flux into the reactor (i.e., new CO_2 reservoir interconversion catalysts and/or for gaseous products implementing an ultra-thin polymeric cathode electrolyte) to significantly enhance the diffusive CO_2 flux relative to the value observed for natural air/ocean boundaries. It is reasonable to surmise that the peak net primary productivity of plant-based photosynthesis is constrained, in part due to down-regulation of photosynthesis at high light intensities, to minimize the sensitivity of the system to atmospheric CO_2 concentration and transport fluctuations, because otherwise these fluctuations that occur as a function of changes in the physical state of the atmosphere due to weather, storms, and other processes would significantly affect the CO_2 concentration in the ABL and thus the performance of the CO_2RR system at the Earth's surface.

The CO_2 flux between the ABL and the canopy layer has an effective mass transfer coefficient, $\sigma_2 = 0.44$ cm s^{-1} that is comparable to the mass transfer coefficient, σ_1, at the troposphere/ABL interface. Hence, at the CO_2 flux required to sustain a 10% efficient

CO_2RR cell at the electrode surface, a daily average CO_2 concentration differential of 260 ppm would be produced between the canopy layer and the troposphere. Furthermore, the troposphere/ABL CO_2 flux would limit the system efficiency to <5% at tropospheric CO_2 concentrations of 400-500 ppm, because at peak CO_2RR periods, the canopy/troposphere CO_2 draw-down would either be over 1000 ppm, or for a 400 ppm CO_2 concentration in the troposphere, would be limited yet further by transport between the troposphere and the ABL. 1000 ppm of CO_2 represents a larger CO_2 concentration than has been present in the troposphere for at least the past million years, and significantly exceeds the atmospheric CO_2 concentration projected under the most aggressive scenarios for growth in anthropogenic CO_2 emissions for the next century.[54] The lower CO_2 concentration (< 400 ppm) in the canopy layer, to which the dissolved CO_2 concentration in electrolytes is equilibrated, would further increase the CO_2 concentration overpotential by ~100-200 mV in the system for a 5% efficient cell operation, but at peak depletion would produce a much larger overpotential, because the entire ABL would be depleted of CO_2 and thus would result in a near-zero concentration of CO_2 at the electrode surface under such conditions.

6.5. Conclusions

The limited CO_2 transport in the presence of bulk electrolyte layers (> 10 μm) at a cathode surface serves as a physical limitation to the construction of a sustainable, scalable solar-driven CO_2RR cell with a technologically relevant efficiency that operates at p_{CO_2}= 400 ppm. Rapid replenishment of CO_2(aq) near a cathode surface using catalysts with activities and reactivities analogous to the carbonic anhydrase enzymes, that enhance the interconversion between the bicarbonate and CO_2, could hypothetically significantly increase the achievable steady-state limiting current density and concomitantly reduce the CO_2 concentration overpotential for such a system. For instance, an interconversion enhancement factor of 10^6 could in principle increase the steady-state limiting current density to > 20 mA cm^{-2} in a pH=11.2 aqueous solution. Alternatively, a catalyst-embedded, thin-layer architecture that minimizes the CO_2 transport pathways in electrolyte

layers could in principle also produce large and sustainable CO_2 reduction current densities at p_{CO_2}=400 ppm, for gas-phase products and reactants. The CO_2 flux at the troposphere/ABL interface and at the ABL/canopy layer interface imposes significant physical constraints on the realization of an efficient, sustainable, and globally scalable CO_2RR solar-fuels system. Large-scale implementation of CO_2RR cells with a 10% solar-to-fuel (STF) conversion efficiency for a 6-electron/6-proton CO_2 reduction process would entail a 130 ppm steady-state drawdown of the CO_2 concentration over the entire 2.5 km high ABL, much higher depletion of the CO_2 concentration during periods of high solar insolation onto the reactors. This level of CO_2 depletion would have profound environmental impacts in the region, and would produce a system performance that was subject to large variability in response to the weather conditions as well as to the presence and intensity of storms, etc. and other conditions that affect the CO_2 transport at the troposphere/ABL boundary as well as in the ABL.

REFERENCES:

1. Y. Hori, *Electrochemical CO2 Reduction on Metal Electrodes. In Modern Aspects of Electrochemistry,* Springers, 2008.
2. K. P. Kuhl, E. R. Cave, D. N. Abram and T. F. Jaramillo, *Energ Environ Sci*, 2012, **5**, 7050-7059.
3. K. J. P. Schouten, Z. S. Qin, E. P. Gallent and M. T. M. Koper, *J Am Chem Soc,* 2012, **134**, 9864-9867.
4. Y. H. Chen, C. W. Li and M. W. Kanan, *J Am Chem Soc*, 2012, **134**, 19969-19972.
5. C. W. Li and M. W. Kanan, *J Am Chem Soc*, 2012, **134**, 7231-7234.
6. K. Hirota, D. A. Tryk, T. Yamamoto, K. Hashimoto, M. Okawa and A. Fujishima, *J Phys Chem B,* 1998, **102**, 9834-9843.
7. K. W. Frese and D. Canfield, *J Electrochem Soc*, 1984, **131**, 2518-2522.
8. B. Aurianblajeni, M. Halmann and J. Manassen, *Sol Energ Mater*, 1983, **8**, 425-440.

9. S. Ikeda, A. Yamamoto, H. Noda, M. Maeda and K. Ito, *B Chem Soc Jpn*, 1993, **66**, 2473-2477.
10. H. Noda, A. Yamamoto, S. Ikeda, M. Maeda and K. Ito, *Chem Lett*, 1990, DOI: Doi 10.1246/Cl.1990.1757, 1757-1760.
11. H. Yoneyama, K. Sugimura and S. Kuwabata, *J Electroanal Chem*, 1988, **249**, 143-153.
12. A. J. Bard and L. R. Faulkner, *Electrochemical Methods, Fundamentals and Applications*, Wiley, 2nd edition edn., 2000.
13. B. A. Rosen, A. Salehi-Khojin, M. R. Thorson, W. Zhu, D. T. Whipple, P. J. A. Kenis and R. I. Masel, *Science*, 2011, **334**, 643-644.
14. M. S. Dresselhaus, G. W. Crabtree and M. V. Buchanan, *MRS Bulletin*, 2005, **30**, 518-524.
15. S. J. Hamrock and M. A. Yandrasits, *Polymer Reviews*, 2006, **46**, 219-244.
16. M. A. Hickner and B. S. Pivovar, *Fuel Cells*, 2005, **5**, 213-229.
17. J. M. Spurgeon, M. G. Walter, J. F. Zhou, P. A. Kohl and N. S. Lewis, *Energ Environ Sci*, 2011, **4**, 1772-1780.
18. A. Z. Weber, M. M. Mench, J. P. Meyers, P. N. Ross, J. T. Gostick and Q. H. Liu, *J. Appl. Electrochem.*, 2011, **41**, 1137-1164.
19. http://www.sc.doe.gov/bes/hydrogen.pdf.).
20. C. Xiang, Y. Chen and N. S. Lewis, *Energ Environ Sci*, 2013, **6**, 3713-3721.
21. S. Choi, J. H. Drese, P. M. Eisenberger and C. W. Jones, *Environ Sci Technol*, 2011, **45**, 2420-2427.
22. D. W. Keith, *Science*, 2009, **325**, 1654-1655.
23. S. Stucki, A. Schuler and M. Constantinescu, *Int J Hydrogen Energ*, 1995, **20**, 653-663.
24. R. Baciocchi, G. Storti and M. Mazzotti, *Chem Eng Process*, 2006, **45**, 1047-1058.
25. F. Zeman, *Environ Sci Technol*, 2007, **41**, 7558-7563.
26. K. S. Johnson, *Limnol Oceanogr*, 1982, **27**, 849-855.
27. K. G. Schulz, U. Riebesell, B. Rost, S. Thoms and R. E. Zeebe, *Mar Chem*, 2006, **100**, 53-65.

28. M. R. Singh, K. Papadantonakis, C. X. Xiang and N. S. Lewis, *Energ Environ Sci*, 2015, **8**, 2760-2767.
29. K. Broka and P. Ekdunge, *J Appl Electrochem*, 1997, **27**, 117-123.
30. J. S. Chiou and D. R. Paul, *Ind Eng Chem Res*, 1988, **27**, 2161-2164.
31. V. A. Sethuraman, S. Khan, J. S. Jur, A. T. Haug and J. W. Weidner, *Electrochim Acta*, 2009, **54**, 6850-6860.
32. S. Ma and E. Skou, *Solid State Ionics*, 2007, **178**, 615-619.
33. S. Haussener, C. X. Xiang, J. M. Spurgeon, S. Ardo, N. S. Lewis and A. Z. Weber, *Energ Environ Sci*, 2012, **5**, 9922-9935.
34. *CRC Handbook of Chemistry and Physics*, 96th edn., 2015.
35. C. Cadena, J. L. Anthony, J. K. Shah, T. I. Morrow, J. F. Brennecke and E. J. Maginn, *J Am Chem Soc*, 2004, **126**, 5300-5308.
36. Y. Hou and R. E. Baltus, *Ind Eng Chem Res*, 2007, **46**, 8166-8175.
37. S. S. Moganty and R. E. Baltus, *Ind Eng Chem Res*, 2010, **49**, 9370-9376.
38. L. C. Seitz, Z. B. Chen, A. J. Forman, B. A. Pinaud, J. D. Benck and T. F. Jaramillo, *Chemsuschem*, 2014, **7**, 1372-1385.
39. S. Hu, C. X. Xiang, S. Haussener, A. D. Berger and N. S. Lewis, *Energ Environ Sci*, 2013, **6**, 2984-2993.
40. B. J. H. Matthews, Ph. D Thesis, University of East Anglia, Norwich, 1999.
41. M. Frankignoulle, *Limnol Oceanogr*, 1988, **33**, 313-322.
42. R. H. Wanninkhof and L. F. Bliven, *J Geophys Res-Oceans*, 1991, **96**, 2785-2796.
43. M. R. Badger and G. D. Price, *Annu Rev Plant Phys*, 1994, **45**, 369-392.
44. J. M. Berg, J. L. Tymoczko and L. Stryer, *Biochemistry*, W. H. Freeman, 5 edn., 2002.
45. C. K. Mathews, K. E. Van Holde and K. G. Ahern, *Biochemistry*, Prentice Hall, 4th edn., 1999.
46. J. T. Hardy, *The Sea Surface and Global Change*, Cambridge UP, 1997.
47. J. Newman and K. Thomas-Alyea, *Electrochemical Systems*, Wiley & Sons, 2004.
48. S. V. Patankar, *Numerical Heat Transfer and Fluid Flow*, New York: McGraw-Hill, 1980.

49. B. R. Helliker, J. A. Berry, A. K. Betts, P. S. Bakwin, K. J. Davis, A. S. Denning, J. R. Ehleringer, J. B. Miller, M. P. Butler and D. M. Ricciuto, *J Geophys Res-Atmos*, 2004, **109**.

50. S. C. Wofsy, M. L. Goulden, J. W. Munger, S. M. Fan, P. S. Bakwin, B. C. Daube, S. L. Bassow and F. A. Bazzaz, *Science*, 1993, **260**, 1314-1317.

51. J. Grace, J. Lloyd, J. Mcintyre, A. C. Miranda, P. Meir, H. S. Miranda, C. Nobre, J. Moncrieff, J. Massheder, Y. Malhi, I. Wright and J. Gash, *Science*, 1995, **270**, 778-780.

52. M. L. Goulden, J. W. Munger, S. M. Fan, B. C. Daube and S. C. Wofsy, *Science*, 1996, **271**, 1576-1578.

53. C. T. Lai, A. J. Schauer, C. Owensby, J. M. Ham, B. Helliker, P. P. Tans and J. R. Ehleringer, *Tellus B*, 2006, **58**, 523-536.

54. Carbon Dioxide: Projected emissions and concentrations, Intergovernmental Panel on Climate Change, http://www.ipcc-data.org/observ/ddc_co2.html).

Chapter VII

MODELING AND SIMULATION OF THE SPATIAL AND LIGHT-INTENSITY DEPENDENCE OF PRODUCT DISTRITIONS IN AN INTEGRATED PHOTOELECTROCHEMICAL CO_2 REDUCTION SYSTEM

7.1 Introduction

An efficient solar-driven CO_2 reduction system[1-5] requires effective delivery of CO_2 to the electrode surface, selective reduction of CO_2 by an active electrocatalyst at the cathode, adequate ionic transport between the anolyte and catholyte chambers, and robust and cost-effective methods for separating the products. Electrocatalysts including metals,[6, 7] metal alloys,[8] metal oxides[9] and semiconductors[10-12 13, 14 10, 15] have been investigated for electrocatalytic CO_2 reduction (CO_2R). For most electrocatalysts operated in contact with aqueous electrolytes, the branching ratio between water reduction (i.e., the hydrogen-evolution reaction, HER) and CO_2R depends on the applied potential.[9] For instance, in a three-electrode potentiostatic configuration, the Faradaic efficiency for the production of formate, HCO_3^- at the surface of an oxidized Cu foil changes from 5.5% to 32.9% when the potential of the working electrode is changed by ~20 mV.[9] In contrast to experiments performed using three-electrode potentiostatic configurations, the potential at the cathode of a full photoelectrosynthetic cell depends on the reaction kinetics at the anode surface as well as transport losses associated with solution resistance, electrodialysis, pH gradients, and CO_2 concentration gradients near the surface of the cathode. Modeling and simulation

---

This chapter is based on results in: Yikai Chen, Nathan S Lewis and Chengxiang Xiang, ACS Energy Lett. 2016, 1, 1, 273-280 – Published by American Chemical Society.

has shown that many test-bed configurations for water-splitting devices produce spatially dependent potential distributions, with variations of > 100 mV across the electrode surface even under constant illumination intensity.[16-19] Moreover, variation in the illumination intensity during operation additionally affects the solar-to-fuel (STF) conversion efficiency for such systems.

Herein, a 2-dimensional numerical model has been developed using COMSOL Multiphysics to evaluate the spatial and temporal variation of the product distribution in an integrated photoelectrochemical CO_2 reduction cell driven by triple-junction light absorbers operating at the Shockley-Queisser (S-Q) limit. The current-voltage behaviors and the Faradaic efficiencies of metallic Cu and Ag catalysts, respectively, for CO_2R in 0.10M bicarbonate solution (pH=6.8) [8, 20] were used to describe the reactions at the cathode. Due to the lack of experimental data for OER catalysts at pH=6.8 or in contact with bicarbonate solutions, the current-voltage behavior of a phosphate-containing CoO_x, Co-Pi, in 0.10 M K-Pi (aq) solution at pH=7.2[21] was used to describe the reactions at the anode. No membrane was included in the model, and any transport loss produced by a membrane separator was neglected. The model also assumed robust separation of products, by neglecting reactions such as oxidation of the reduced products at the anode, reduction of O_2 at the cathode, or recombination of product s in the solution.

7.2 Modeling

The coupled equations under the corresponding boundary conditions for the 1-dimensional and 2-dimensional cell architectures were solved using a commercial finite-element program, COMSOL Multiphysics. In the 1-dimensional cell architecture, the cathode and anode were arranged face-to-face and were separated by 4 mm. In the 2-dimensional cell architecture (Figure 7.2a), the ratio between the width of the photoelectrodes and the width of the entire unit cell was set to 0.9. The electrolyte height above the cathode surface and below the anode surface was set to 5 mm. A hydrodynamic boundary layer with a thickness of 100 μm was used to account for moderate convection near the photoelectrode. To account for the convective forces in the cell, effective diffusion

coefficients for solution species were used beyond the hydrodynamic boundary layer in the bulk solution.

The current-voltage behavior of the triple-junction light absorber device was obtained from the Shockley-Queisser model and was subsequently fitted using the ideal diode relationship:

$$J = J_{ph} - J_0[\exp\left(\frac{eV}{\gamma kT}\right) - 1] \quad \text{(Eq. 7.1)}$$

The transport of electrons and holes within the TCO layer was described using Ohm's Law:

$$j_s = -\sigma_s \nabla \phi_s \quad \text{(Eq. 7.2)}$$

where j_s represents the current density, σ_s is the electrical conductivity of the TCO layer, and $\nabla\phi_s$ is the electric potential gradient within the TCO layer.

The current density versus potential characteristics and the Faradaic efficiency of the metallic Cu and Ag catalysts for CO_2R were based on experimental data [8, 21] and were fitted into piecewise functions, in which the sub-functions were described by the Butler-Volmer relation:

$$J_{OER/CO2\,RR} = J_{0,OER/CO2\,RR}[\exp(\frac{\alpha_{a,OER/CO2\,RR} F\eta}{RT}) - \exp(-\frac{\alpha_{c,OER/CO2\,RR} F\eta}{RT})] \quad \text{(Eq. 7.3)}$$

where $J_{0,OER/CO2RR}$ is the exchange-current density for the OER or CO_2RR, respectively, and $\alpha_{a,OER/CO2\,RR}$ and $\alpha_{c,OER/CO2\,RR}$ are the anodic and cathodic transfer coefficients, respectively, for the OER or the CO_2RR. The overpotential, η, is defined as,

$$\eta = \phi_s - \phi_l - \phi_0, \quad \text{(Eq. 7.4)}$$

where ϕ_s and ϕ_l are the corresponding electric and electrolyte potential at the electrode-electrolyte interface, and ϕ_0 is the equilibrium potential. The solution transport that

includes diffusion, migration, convection and bulk reactions of water or buffer dissociation was given by the Nernst-Plank equation. Ionic species, including protons, hydroxide, bicarbonate, carbonate, and potassium ions, as well as neutral species including water, dissolved CO_2 and carbonic acid, were included in the model. The transport loss, $\Delta\phi_{\text{transport}}$, in the system includes the solution losses, $\Delta\phi_{\text{solution}}$, the voltage losses associated with pH gradients, $\Delta\phi_{\text{pH gradient}}$, and CO_2 concentration gradients at the electrode surface, $\Delta\phi_{co_2\ \text{gradient}}$. The transport loss was given by:

$$\Delta\phi_{\text{transport}} = \Delta\phi_{\text{solution}} + \Delta\phi_{\text{pH gradient}} + \Delta\phi_{co_2\ \text{gradient}} \quad \text{(Eq. 7.5)}$$

The solution losses, $\Delta\phi_{\text{solution}}$, were calculated as the sum of the ohmic resistive loss (first term) and the electrodialysis loss (second term). These losses can be expressed as:

$$\Delta\phi_{\text{solution}} = \int \frac{J}{\kappa} dx + \sum_i \int \frac{F z_i D_i \nabla c_i}{\kappa} dx \quad \text{(Eq. 7.6)}$$

where ϕ is the electric potential, κ is the conductivity of the electrolyte, J is the current density, x is distance along the axis of the 1-D model, F is Faraday's constant, z is the charge number, D_i is the diffusion coefficient and c_i is the molar concentration of the i^{th} species, R is the gas constant, and T is the absolute temperature.

The Nernstian potential losses associated with the pH gradients, $\Delta\phi_{\text{pH gradient}}$, and CO_2 concentration gradients, $\Delta\phi_{co_2\ \text{gradient}}$, at the surface of the electrodes can be expressed as:

$$\Delta\phi_{\text{pH gradient}} = 2.303\frac{RT}{F}\left(\text{pH}_{\text{cathode}} - \text{pH}_{\text{anode}}\right)$$

$$\Delta\phi_{co_2\ \text{gradient}} = \frac{59(mV)}{n} Log\left(\frac{p_{co_2,cathode})}{p_{co_2,bulk}}\right) \quad \text{(Eq. 7.7)}$$

where n is number of electrons transferred in the CO_2 reduction process, with $n = 6$ assumed as a as favorable case for the purposes of this study. $p_{CO_2,cathode}$ and $p_{CO_2,bulk}$ are the partial pressures of CO_2 at the cathode surface and in the bulk solution, respectively.

The chemical reactions included in the simulation were:

$$CO_2 + H_2O \underset{k_{1-}}{\overset{k_{1+}}{\rightleftharpoons}} H^+ + HCO_3^-$$

$$CO_2 + OH^- \underset{k_{2-}}{\overset{k_{2+}}{\rightleftharpoons}} HCO_3^-$$

$$HCO_3^- \underset{k_{3-}}{\overset{k_{3+}}{\rightleftharpoons}} H^+ + CO_3^{2-}$$

$$HCO_3^- + OH^- \underset{k_{4-}}{\overset{k_{4+}}{\rightleftharpoons}} H_2O + CO_3^{2-}$$

$$H_2O \underset{k_{5-}}{\overset{k_{5+}}{\rightleftharpoons}} H^+ + OH^-$$

with k_f and k_b representing the forward and backward rate constant, respectively, for each reaction.

7.3 Results and Discussion

Figure 7.1a shows the current-voltage characteristics of three triple-junction light-absorber devices that are operating at the Shockley Queisser (S-Q) limit, as well as the overall load curve for Ag performing the CO_2R reaction (CO_2RR) and Co-Pi performing the OER in a 1-dimensional, face-to-face cell design. The operational current density of the overall reaction, J_{total}, was determined by the crossing point between the load curve (black) and the power curve (green, blue or red) of the light absorber device. The optimal J_{total} of 11.9 mA cm^{-2} was obtained at the maximum power point of the red curve (point A), which corresponded to a band gap combination of 2.1 eV, 1.6 eV and 1.2 eV for the top band gap, middle band gap and bottom band gap, respectively of the light-absorber

structure (Device 1). However, the cathode overpotential at the optimal J_{total} was 1.4 V, which led to a Faradaic efficiency of 36% for all CO_2R products (CO and HCO_3^-) and a Faradaic efficiency of 64% for H_2. The partial current density that corresponded to CO_2R, J_{CO_2}, was thus low (4.3 mA cm^{-2}).

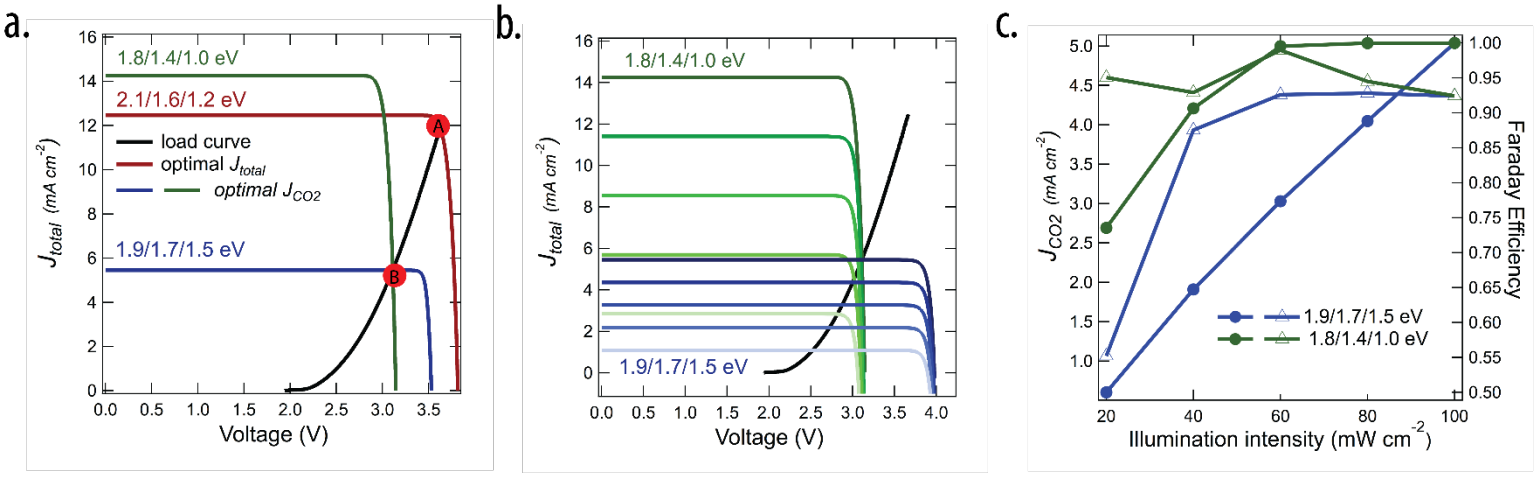

Figure 7.1. (a) The calculation of the optimal J_{total} (point A) from the crossing point determined by the overall load-curve (black) and the power curve (red) from a triple-junction light absorber device with an optimal band-gap combination of 2.1 eV/1.6 eV/1.2 eV (Device 1), and the calculation of the optimal J_{CO_2} (point B) from the crossing point determined by the overall load-curve and two power curves from triple junction light absorber devices having optimal band gap combinations of 1.9 eV/1.7 eV/1.5 eV (blue, Device 2), and 1.8 eV/1.4 eV/1.0 eV (green, Device 3), in a 1-dimensional cell configuration. (b) The overall load curve for CO_2R and OER and the current-voltage characteristics of two ideal triple-junction light absorbers (Devices 2 and 3) under different illumination intensities. (c) The J_{CO_2} (solid circle, left axis) and the Faradaic efficiency of CO_2R (hollow triangle, right axis) as a function of the illumination intensity for two different triple-junction light absorbers (Devices 2 and 3) that produced the same J_{CO_2} and J_{total} at a simulated light intensity of 100 mW cm^{-2} of Air Mass (AM) 1.5 Global Illumination.

In contrast, the blue and the green power curves, which correspond to band-gap combinations of 1.9 eV/1.7 eV/ 1.5 eV (Device 2) and 1.8 eV/1.4 eV/1.0 eV (Device 3), respectively, yielded an optimal J_{CO_2} of 5.0 mA cm^{-2}, even though J_{total} (point B) (5.5 mA cm^{-2}) was lower than its value at point A (11.9 mA cm^{-2}). A series of band-gap combinations that produced the crossing point at point B would thus yield the optimal J_{CO_2} for this specific catalyst system and cell architecture.

Figure 7.1b depicts the dependence of the current-voltage characteristics of Device 2 and Device 3 on the light intensity. The two light-absorber structures yielded identical J_{total} and J_{CO_2} values under 100 mW cm^{-2} of simulated Air Mass (AM) 1.5G illumination. However, when the illumination intensity was decreased from 100 mW cm^{-2} to 20 mW cm^{-2}, Device 2 exhibited a larger shift in the total operational voltage, from 3.1 V to 2.5 V, than Device 3. Figure 7.1c shows the light-intensity dependence for Devices 2 and 3 of the Faradaic efficiency for CO_2R. The Faradaic efficiency for CO_2R for Device 2 (blue triangles, right axis) varied from 93% to 55% as the light intensity varied from 100 mW cm^{-2} to 20 mW cm^{-2}, whereas the Faradaic efficiency for CO_2R for Device 3 (green triangles, right axis) remained nearly constant (93% to 95%) over the same range of illumination intensities. The J_{CO_2} of Device 2 (blue circles, left axis) exhibited a linear dependence on the illumination intensity, because the crossing points between the load curve and the photodiode characteristic occurred in the plateau region of the photodiode curve. In contrast, J_{CO_2} of Device 3 (green circles, left axis) exhibited a weaker dependence on the illumination intensity, because the crossing points occurred at the rising portion of the photodiode curve. Hence, even in a 1-dimensional cell architecture, the rate of formation of CO_2R products, as well as the ratio of CO_2R products to hydrogen, varied as the illumination intensity changed and were dependent on the choice of the light absorbers. The different product branching ratio under varying illumination conditions that result from the diurnal cycle as well as siting of a deployed system will thus have an impact on product mixtures as well as on requirements for product separation and collection processes in solar-driven CO_2R devices.

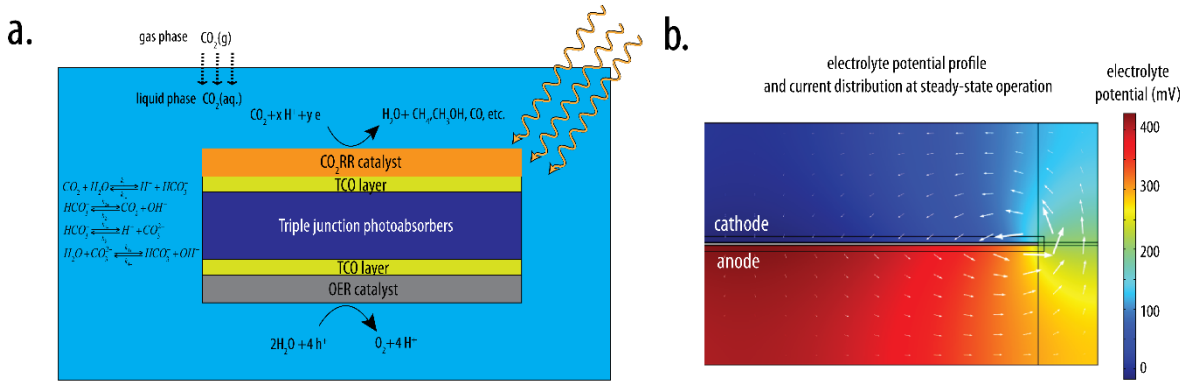

Figure 7.2. (a) A schematic illustration of an integrated PEC CO_2 reduction cell. (b) A snapshot of the electrolyte potential profile and current distribution (white arrows) of an integrated photoelectrochemical CO_2 reduction cell under steady-state operation. [Katie, add the reference potential] The size of the arrow indicates the magnitude of the ionic current density.

Figure 7.2a shows a schematic illustration of an integrated, 2-dimensional photoelectrosynthetic CO_2 reduction cell, in which the triple-junction light-absorber (blue) is coated on the top by a transparent conductive oxide (TCO) layer and a CO_2RR catalyst, and on the bottom by a TCO layer and an OER catalyst. In this cell, a bicarbonate solution that contained 0.1 M $NaHCO_3$(aq) was equilibrated with 1 atm pressure of CO_2(g). The concentration of CO_2 in the aqueous solution was set to 34 mM, according to Henry's law. The detailed cell dimensions are summarized in the Modeling section. Figure 7.2b shows a snapshot of the electrolyte potential profile and the associated current distribution in the PEC cell. The electrolyte potential profile was determined by iteratively solving the equations that describe in a two-dimensional simulation domain the current-voltage relationship of the light absorber, transport losses in the electrolyte, and the electrocatalytic performance of the catalysts. Generally, a larger transport loss would result in a larger electrolyte potential difference between the cathode and anode region and would result in a smaller kinetic overpotential as well as a smaller operational current density at the

electrode surface. As shown in Fig. 7.2b, the operating current densities for the OER and CO_2R were concentrated at the edge of the device, due to the short ionic path length and the low solution resistive losses at such positions relative to other positions on the device. The CO_2R current density at the edge of the electrode was ~4.5 times larger than the CO_2R current density at the middle of the electrode. Moreover, when the electrode width was 1.0 cm, the potential at the cathode varied spatially by > 400 mV.

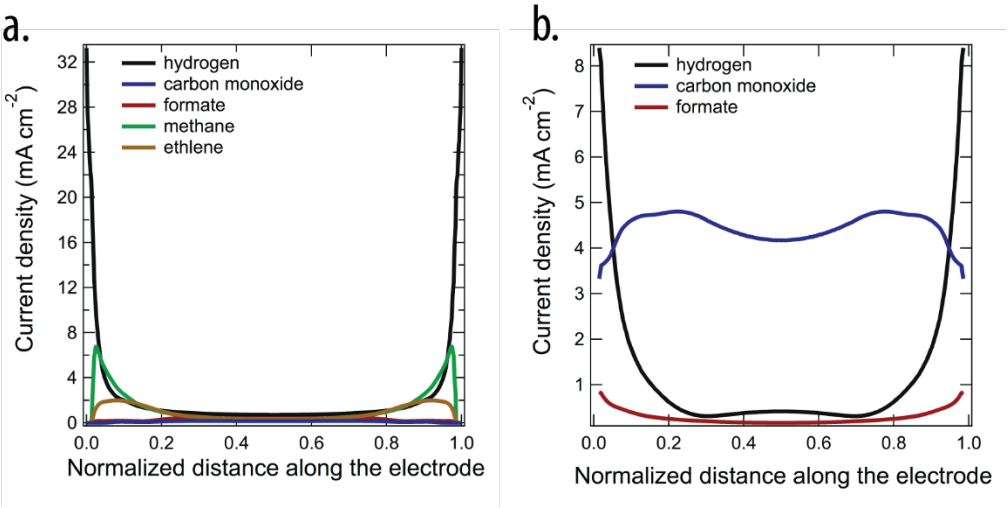

Figure 7.3. The CO_2RR product distribution as a function of the normalized distance along 1 cm electrodes for the Cu catalyst (a) and the Ag catalyst (b) in an integrated photoelectrochemical CO_2 reduction cell that incorporates the optimal-triple junction (2.1 eV/ 1.6 eV/1.2 eV) light-absorber structure under 100 mW cm^{-2} of simulated AM 1.5G illumination.

Figure 7.3 shows the distribution of products from water reduction and CO_2R, as well as the partial current density for each of the major products, as a function of the normalized distance along the electrode, for the Cu catalyst (Fig. 7.3a) and for the Ag catalyst (Fig. 7.3b) in an integrated PEC CO_2 reduction cell under 100 mW cm^{-2} of simulated AM (Air Mass) 1.5G illumination. Because a series of band-gap combinations would yield the same J_{CO_2}, the single, optimal band-gap combinations that produced the optimum J_{total} were used for the Cu catalyst (2.1 eV/1.6 eV/1.1 eV) and the Ag catalyst (2.1 eV/1.6 eV/1.2eV) to

permit evaluation of the resulting spatial distribution of the reduction products under such conditions. The mathematical forms of the transport losses modeled for the 2-dimensional PEC cell are described in the modeling section, and include the resistive loss and electrodialysis of the electrolyte, as well as the concentration overpotentials associated with pH gradients and CO_2 concentration gradients at the electrode surface. Moderate agitation and convection of the electrolyte was assumed by taking the thickness of the hydrodynamic boundary layer to be 100 μm. Consequently, under 100 mW cm^{-2} illumination, the voltages losses due to pH gradients, CO_2 concentration gradients, and electrodialysis of the electrolyte were < 100 mV for the largest electrode width. The resistive loss in the bicarbonate solution comprised the largest component of the transport loss in the system.

For the Cu catalyst, H_2 was the dominant (nearly 100 mol% of the total) product near the edge of the electrode, because of the small solution transport losses, high overpotential for the CO_2RR, and high Faradaic efficiency for hydrogen evolution at such potentials. In contrast, at the mid-point of the electrode, ~52% of the current led to $H_2(g)$. Similar variations of the product distributions were observed when Ag was the CO_2R electrocatalyst. Thus, the spatial variation of the product distributions as shown in Fig. 7.3, and the resulting overall product branching ratio in full electrochemical devices, could be very different from the Faradaic efficiency for production of various products determined by three-electrode measurements under well-controlled potentials with equipotential electrode surfaces. Numerical modeling of photo-reactors that have realistic dimensions, under realistic operating conditions, therefore is needed to obtain a firm prediction of the performance of the whole cell by using the intrinsic materials properties of the system in conjunction with the transport properties of the reactant, product and reaction media.

Figure 7.4a shows the integrated current densities over the electrode width for H_2 (black), CO (blue) and formate (red), as a function of the width of the electrode, in a cell with Ag as the CO_2R catalyst. As the electrode width increased from 1.0 mm to 1.0 cm, the integrated partial current density for H_2 (black) decreased from 8 mA cm^{-2} to 1.4 mA cm^{-}

^{2}, and the integrated partial current density for CO (blue) increased slightly, from 3.5 mA cm^{-2} to 4.4 mA cm^{-2}. The reduction in transport losses as the electrode width decreased resulted in the change in the integrated current densities as well as in the spatial variation of the product distribution.

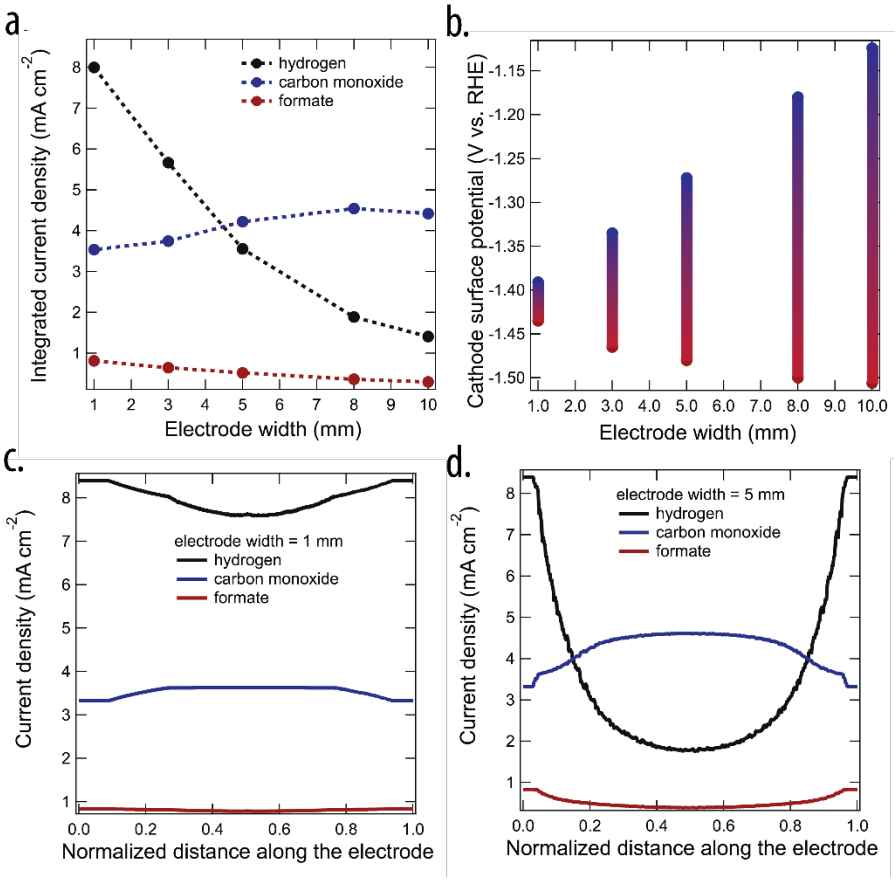

Figure 7.4. (a) The integrated CO_2R product distribution as a function of the electrode width for the Ag catalyst in the integrated PEC CO_2 reduction cell that incorporates the optimal triple- junction light absorber structure (Device 1, 2.1 eV/ 1.6 eV/1.2 eV) under simulated 100 mW cm^{-2} of AM1.5G illumination. (b) The cathode surface potential and its variation as a function of the electrode width under 100 mW cm^{-2} of simulated AM1.5G illumination. (c) The partial current density for hydrogen, carbon monoxide and formate as a function of the normalized distance along the electrode when the electrode width of the cell was set to (c) 1.0 mm and (d) 5.0 mm.

Figure 7.4b shows the dependence of the potential at the surface of the cathode on the width of the electrode, under 100 mW cm^{-2} of simulated AM1.5G illumination. The surface potential at any particular location on the cathode was determined by the overall transport losses (solution resistive loss, electrodialysis of electrolyte, voltage losses associated with pH gradients and CO_2 concentration gradients), the current-voltage characteristics of the light absorbers, the behavior of the OER catalyst behavior, and the lateral conduction properties of the TCO layers. The spatial variation in the potential of the cathode produced a variable product distribution along the width of the electrode. Figure 7.4c and 4d show the partial current density as a function of the normalized distance along the electrode when the electrode width was set to 1.0 mm and 5.0 mm, respectively. Under constant illumination (100 mW cm^{-2}), the cathode surface potential varied by > 400 mV when the electrode width was 1.0 cm, but varied by < 50 mV when the electrode width was decreased to 1.0 mm. The greater variation in surface potential for the larger electrode resulted in a greater variation in the product distribution along the surface of the larger electrode than the smaller electrode, and thus the two electrodes would yield different product distributions: the 1 mm electrode yields 65% H2, 28% CO, and 7% formate with a total STF efficiency of 14.8 %, while the 5 mm electrode yields 43% H2, 51% CO, and 6% formate with a total STF efficiency of 9.9 %. To achieve the same level of selectivity as in a potentiostatically controlled, “half-cell” configuration, nearly constant Faradaic efficiencies for the products are required across the operating voltage windows (indicated by the gradient bars in Figure 7.4b). As the electrode dimension increased, the voltage window of required constant Faradaic efficiency also increased.

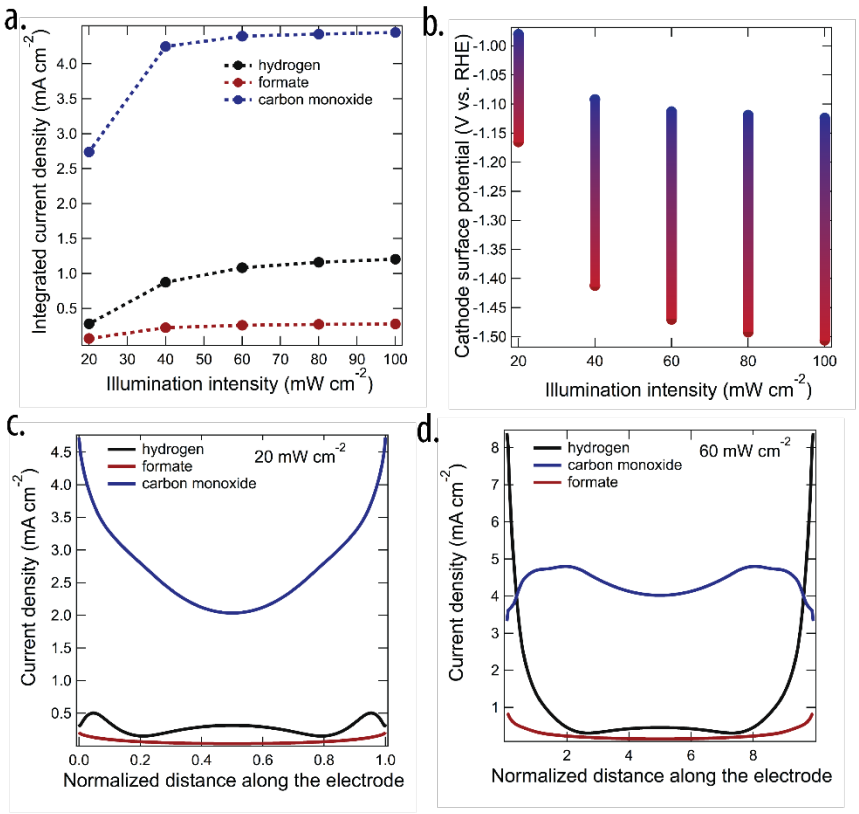

Figure 7.5. (a) The integrated CO_2RR product distribution as a function of the illumination intensity for the Ag catalyst in the integrated PEC CO_2 reduction cell that incorporates the optimal triple junction light absorber structure (2.1 eV/ 1.6 eV/1.2 eV). The width of the electrode was set to 1.0 cm. (b) The cathode surface potential and its variation as a function of the illumination intensity when the electrode width was set to 1.0 cm. (c) The partial current density for hydrogen, carbon monoxide and formate as a function of the normalized distance along the electrode under (c) 20 mW cm^{-2} illumination and (d) 60 mW cm^{-2} of simulated AM1.5G illumination when the electrode width was set to 1.0 cm.

Figure 7.5a shows the integrated current densities over the electrode width for H_2 (black), CO (blue) and formate (red) as a function of the illumination intensity, with Ag as the CO_2RR catalyst. The integrated partial current density for all of the products increased as the illumination intensity increased. However the partial current density did not scale

linearly with the illumination intensity. The product distribution also varied due to the non-monotonic product distribution produced by the Ag catalyst as a function of potential. Figure 7.5b shows the cathode surface potential and its variation as a function of the illumination intensity, when the electrode width was set to 1.0 cm. Furthermore, Figure 7.5c and 5d show the detailed partial current density of H_2 (black), CO (blue) and formate (red) as a function of the normalized distance along the electrode under 20 mW cm^{-2} and 60 mW cm^{-2}, respectively, of simulated AM 1.5G illumination. For an integrated PEC cell having this specific design, with an electrode width of 1.0 cm under varying illumination intensities, achieving the same product selectivity as in a potentiostatically controlled three-electrode, "half-cell" configuration would require a constant CO_2R Faradaic efficiency for potentials in the range between 0.98 V and 1.50 V vs. the reversible hydrogen electrode (RHE). Note that the selectivity of the CO_2R catalyst in this study was defined as maintaining the ratios of Faradaic efficiencies among all of the various reduced products in the system. Depending on the end-use of the reduced products, a mixture of carbon-containing products, including products in liquid or gaseous phases or both, could be valuable. The model described herein can be used to design the cell geometry to produce the desired product branching ratios in a realistic PEC cell under various illumination conditions.

7.4 Conclusions

In summary, integrated photoelectrosynthetic CO_2R cells will require a different triple-junction light absorber to optimize J_{CO_2} than the light-absorber structure that optimizes J_{total}. The partial current densities for each of the reduction products will depend on the electrode dimensions and on the illumination intensity. The surface potential variation in a realistic cell under varying light intensities, relative to a potentiostaticallly controlled, "half-cell" configuration, would require catalysts with a substantial voltage window within which the Faradaic efficiency for each product remains unchanged. For example, a cathode voltage window of ~ 400 mV with constant Faradaic efficiency for each product is required for an integrated PEC architecture with an electrode width of 1.0 cm under varying illumination conditions.

REFERENCES:

1. S. Sato, T. Arai and T. Morikawa, *Inorg Chem*, 2015, **54**, 5105-5113.
2. M. Schreier, L. Curvat, F. Giordano, L. Steier, A. Abate, S. M. Zakeeruddin, J. S. Luo, M. T. Mayer and M. Gratzel, *Nat Commun*, 2015, **6**.
3. H. S. Jeon, J. H. Koh, S. J. Park, M. S. Jee, D. H. Ko, Y. J. Hwang and B. K. Min, *Journal of Materials Chemistry A*, 2015, **3**, 5835-5842.
4. B. Kumar, M. Llorente, J. Froehlich, T. Dang, A. Sathrum and C. P. Kubiak, *Annu Rev Phys Chem*, 2012, **63**, 541-+.
5. J. P. Jones, G. K. S. Prakash and G. A. Olah, *Isr J Chem*, 2014, **54**, 1451-1466.
6. Y. Hori, *Electrochemical CO_2 Reduction on Metal Electrodes. In Modern Aspects of Electrochemistry*, Springers, 2008.
7. Y. H. Chen, C. W. Li and M. W. Kanan, *J Am Chem Soc*, 2012, **134**, 19969-19972.
8. K. P. Kuhl, E. R. Cave, D. N. Abram and T. F. Jaramillo, *Energy & Environmental Science*, 2012, **5**, 7050-7059.
9. C. W. Li and M. W. Kanan, *Journal of the American Chemical Society*, 2012, **134**, 7231-7234.
10. K. Hirota, D. A. Tryk, T. Yamamoto, K. Hashimoto, M. Okawa and A. Fujishima, *J Phys Chem B*, 1998, **102**, 9834-9843.
11. K. W. Frese and D. Canfield, *Journal of the Electrochemical Society*, 1984, **131**, 2518-2522.
12. B. Aurianblajeni, M. Halmann and J. Manassen, *Sol Energ Mater*, 1983, **8**, 425-440.
13. S. Ikeda, A. Yamamoto, H. Noda, M. Maeda and K. Ito, *B Chem Soc Jpn*, 1993, **66**, 2473-2477.
14. H. Noda, A. Yamamoto, S. Ikeda, M. Maeda and K. Ito, *Chem Lett*, 1990, 1757-1760.
15. H. Yoneyama, K. Sugimura and S. Kuwabata, *J Electroanal Chem*, 1988, **249**, 143-153.

16. D. A. Torelli, S. A. Francis, J. C. Crompton, A. Javier, J. R. Thompson, B. S. Brunschwig, M. P. Soriaga and N. S. Lewis, *ACS Catalysis*, 2016, **6**, 2100-2104.

17. S. Haussener, S. Hu, C. X. Xiang, A. Z. Weber and N. S. Lewis, *Energy Environ. Sci.*, 2013, **6**, 3605-3618.

18. S. Haussener, C. X. Xiang, J. M. Spurgeon, S. Ardo, N. S. Lewis and A. Z. Weber, *Energy & Environmental Science*, 2012, **5**, 9922-9935.

19. C. Xiang, Y. Chen and N. S. Lewis, *Energ Environ Sci*, 2013, **6**, 3713-3721.

20. Y. K. Chen, C. X. Xiang, S. Hu and N. S. Lewis, *Journal of the Electrochemical Society, In Press*, 2014.

21. T. Hatsukade, K. P. Kuhl, E. R. Cave, D. N. Abram and T. F. Jaramillo, *Phys Chem Chem Phys*, 2014, **16**, 13814-13819.

22. K. Sun, F. H. Saadi, M. F. Lichterman, W. G. Hale, H. P. Wang, X. H. Zhou, N. T. Plymale, S. T. Omelchenko, J. H. He, K. M. Papadantonakis, B. S. Brunschwig and N. S. Lewis, *P Natl Acad Sci USA*, 2015, **112**, 3612-3617.

21. K. Sun, F. H. Saadi, M. F. Lichterman, W. G. Hale, H. P. Wang, X. H. Zhou, N. T. Plymale, S. T. Omelchenko, J. H. He, K. M. Papadantonakis, B. S. Brunschwig and N. S. Lewis, *P Natl Acad Sci USA*, 2015, **112**, 3612-3617.

Chapter VIII

MODELING THE PERFORMANCE OF A FLOW-THROUGH GAS DIFFUSION ELECTRODE FOR ELECTROCHEMICAL REDUCTION OF CO OR CO_2

8.1 Introduction

Electrochemical CO_2 or CO reduction is often performed in aqueous electrolytes, such as bicarbonate or carbonate solutions. The low solubility of CO_2 and CO in aqueous solutions, in conjunction with the values of the liquid-phase diffusion coefficients of CO_2 and CO, consequently constrains the attainable current densities for CO_2 or CO reduction. For example, at various nanostructured electrodes in aqueous solutions, the geometric current densities for CO reduction are limited to < 1 mA cm^{-2}.[1-4] The low mass-transport-limited current density in aqueous systems is consistent with Fick's law of diffusion, with a mass-transport-limited current density for CO reduction (COR) of ~ 0.81 mA cm^{-2} at a boundary layer thickness of ~100 μm.

One approach to increasing the operating current density of the electrode is to substantially reduce the thickness of the boundary layer.[5] Gas-diffusion electrodes (GDEs) provide an opportunity to effectively reduce the boundary-layer thickness to hundreds of nanometers. Two general types of GDE configurations have been constructed and studied.

This chapter is based on results in: Yikai Chen *et al* 2020 J. Electrochem. Soc. 167 114503 – Published by The Electrochemical Society.

In one configuration, no gas flow-through occurs at the GDE/electrolyte interface, and the pressure differential is regulated between the gaseous compartment and the liquid compartment.[6-9] A similar flow-by pattern can also be achieved by the use of a membrane electrolyte that is directly bonded to GDEs, e.g., a membrane-electrode-assembly (MEA).[10, 11] Alternative configurations involve flow-through of gaseous reactants from the GDE/electrolyte interface into the bulk liquid electrolytes.[12-16] The flow-by configurations have been modeled, simulated[17, 18] and are analogous physically to oxygen reduction electrodes in fuel cells, whereas the behavior of the flow-through configuration has not been evaluated or modeled quantitatively. The major focus of this study was to understand the local reaction rates and pH profiles for COR and to reveal challenges for CO_2 utilization due to the highly alkaline local environments within GDEs. The concept of a gas/vapor-fed cell for electrochemical reactions, such as N_2 or CO_2 fixation, and COR, has been considered extensively. Various configurations of GDEs have been designed and tested for CO_2R or COR over a range of operating pHs and electrolytes.[6-9, 11, 14, 19-21] For example, highly active and stable Sn-based GDEs have been reported for selective formate generation,[22] and Cu-based GDEs have shown enhanced selectivity and activity for CO_2R at abrupt junctions.[6] Recently, Cu-nanoparticle-based GDEs in a flow-through configuration exhibited a partial current density of 50.8 mA cm^{-2} for C_2H_4 generation using CO as the feedstock.[13] Two general types of GDE configurations have been constructed and studied. In one configuration, no gas flow-through occurs at the GDE/electrolyte interface, and the pressure differential between the gaseous compartment and the liquid compartment is regulated.[6-9] A similar flow-by pattern can also be achieved by the use of a membrane electrolyte that is directly bonded to GDEs, e.g., a membrane-electrode-assembly (MEA).[10, 11] Alternative configurations involve flow-through of gaseous reactants from GDE/electrolyte interface into the bulk liquid electrolytes.[12-16] The flow-by configurations have been modeled, simulated[17, 18] and are analogous physically to oxygen reduction electrodes in fuel cells, whereas the behavior of the flow-through configuration has not been evaluated or modeled quantitatively. Herein the geometric partial current densities and Faradaic efficiencies (FEs) for COR and CO_2R in a flow-through gas diffusion electrode (GDE) were simulated and compared to aqueous planar electrodes.

Substantial increases in electrochemical reaction rates and Faradaic efficiencies were observed when such flow-through GDE's were used as compared to aqueous solutions, especially for COR. For CO_2R, the chemical reaction between CO_2 and the locally alkaline electrolyte within GDEs contributed to substantial CO_2 loss at high overpotentials.

8.2 Modeling

A catalyst-layer domain (100 μm) and a bulk liquid-electrolyte domain (100 μm) were modeled for the flow-through GDE (Figure 8.1). The yellow region and the bubble was a proper illustration of the flow-through GDEs evaluated because in the experimental demonstration[23], the GDE was facing down and gaseous CO_2 or CO was forced through the electrodes.

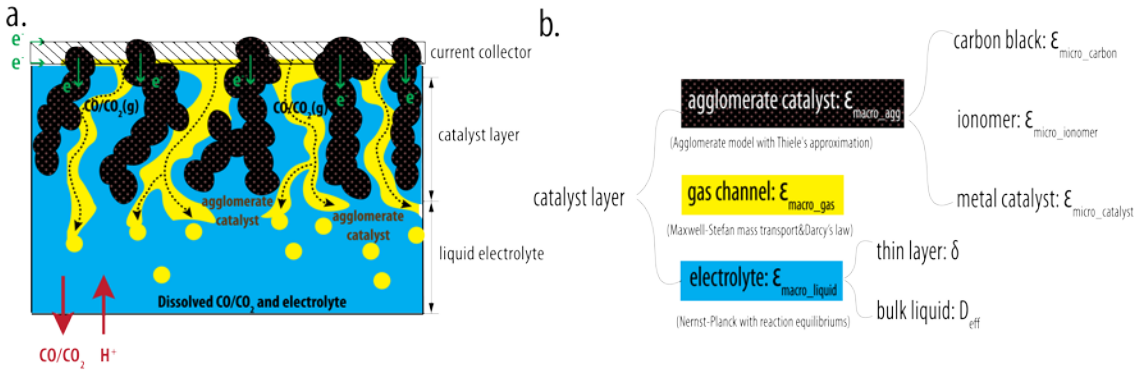

Figure 8.1 (a) A schematic illustration of a flow through gas diffusion electrode (GDE). (b) A schematic illustration of the catalyst layer containing an agglomerate catalyst, gas channel, and aqueous electrolyte.

The bulk liquid-electrolyte layer was modeled as a stagnant liquid layer with a thickness of 100 μm, in which transport of electrolyte species was controlled by the diffusion and migration terms in the Nernst-Plank equation:

$$\frac{\partial c_i}{\partial t} + \nabla \cdot (-D_i \nabla c_i - z_i u_{m,i} F c_i \nabla V) = R_i, \qquad \text{(Eq. 8.1)}$$

where D_i, c_i, z_i and $u_{m,i}$ are the diffusion coefficient, concentration, charge number, and mobility, respectively, of species i within the electrolyte, and R_i is chemical/electrochemical

reaction rate of the corresponding species. For an electrolyte at pH=14, the only chemical reaction considered was water dissociation:

$$H_2O \underset{k_{1b}}{\overset{k_{1f}}{\rightleftarrows}} H^+ + OH^- .$$

For an electrolyte at pH=8, three additional reactions were included in the model for the phosphate buffer solution:

$$H_3PO_4 \underset{k_{2b}}{\overset{k_{2f}}{\rightleftarrows}} H_2PO_4^- + H^+ ,$$

$$H_2PO_4^- \underset{k_{3b}}{\overset{k_{3f}}{\rightleftarrows}} HPO_4^{2-} + H^+ ,$$

$$HPO_4^{2-} \underset{k_{4b}}{\overset{k_{4f}}{\rightleftarrows}} PO_4^{3-} + H^+ .$$

In this Eq 8.1, the second and third term on the left side represents diffusion and migration, respectively. These two, along with the electrochemical/chemical reaction (R_i) would affect the species transport throughout the GDE catalyst layer and the bulk liquid solution layer. We did not model the double layer structure at the electrode/electrolyte interface in this study, consequently, no discontinuity is present in the electric potential throughput the modeling domain. The migration term was considered throughout the study. For example, different operating conditions (pH 8 vs pH 14, COR vs CO_2R) were studied under different applied voltage and, a) H^+ is non-negligible, b) even when H^+ barely exists, OH^- is non-negligible, along with other co-cations. The migration term was therefore always included in the simulation. The continuity equation and mass conservation were assumed for all electrolyte species at the catalyst layer/bulk electrolyte interface. The dissolved CO concentration at the catalyst layer/bulk electrolyte interface was determined by the CO pressure at the interface. At the outer bulk electrolyte layer, constant concentrations of all electrolyte species at the initial conditions were assumed, due to the high convective fluxes beyond the stagnant liquid layer. The current collector was assumed to be an insulator for all electrolyte species.

The catalyst layer consisted of three components (Figure 8.1b): the gas channel domain (gas phase), the electrolyte domain (liquid phase) and the agglomerate catalyst domain (mixed

phase). In the gas channel domain, Darcy's law was used to describe the gas flow in the porous gas channel:

$$q = -\frac{\kappa}{\mu}\nabla p, \quad \text{(Eq. 8.2)}$$

where q is the flux and κ and μ are the intrinsic permeability and viscosity, respectively, of the medium. ∇p represents the pressure gradient along the gas channel. The inlet gas pressure in the GDE catalyst layer was set to 1 atm. Before exiting into the bulk electrolyte domain, under operation, CO supplied through the gas channel can be electrochemically reduced at the agglomerate catalyst domain.

In the electrolyte domain within the catalyst layer, two types of liquid layers were modeled: a thin liquid layer with a thickness of 200 nm that surrounds the agglomerate, and a "bulk" liquid layer which was 10 vol. % of the catalyst layer during steady-state operation. The liquid layer was responsible for the reactant transport to the agglomerate catalyst, while the "bulk" liquid electrolyte was responsible for the ionic transport to the bulk electrolyte during the operation. At the thin liquid layer/gas channel interface, Henry's law was used to determine the concentration of the dissolved CO, the majority of which was supplied to the agglomerate catalysts:

$$C = kP_{gas}, \quad \text{(Eq. 8.3)}$$

where C is the solubility of the gas at a fixed temperature (taken to be room temperature in this work) in a particular solvent, k is the Henry's law constant and P_{gas} is the partial pressure of the gas.

In the agglomerate catalyst domain, three microscopic components were modeled to describe the catalyst: the carbon black domain was used as the current collector to supply electrons into the GDE, the ionomer domain with a micro-porosity of 0.2 was used as the transport medium for dissolved CO and electrolyte species, and a metal catalyst was bonded to the carbon black as the active site for CO reduction. Effective diffusion coefficients were used in the agglomerate catalyst for CO and for all electrolyte species within the ionomer domain. The effects of CO dissolution and transport limitations in the porous catalyst

agglomerates were approximated by an efficiency factor, *E*, using Thiele's modulus, *mL*.[24] For a first-order irreversible reaction with a spherical interior surface in the agglomerate model, the efficiency factor was given by:[25]

$$E = \frac{\frac{1}{\tanh(3mL)} - \frac{1}{3mL}}{mL}, \text{ in which } mL = L\sqrt{\frac{k}{C_{CO}^{0} D_{eff}}} \quad . \qquad \text{(Eq. 8.4 and Eq. 8.5)}$$

Here, *L* represented the characteristic length of the agglomerates, and for the sphere geometry was given by:

$$L = \frac{R}{3}, \qquad \text{(Eq. 8.6)}$$

where *R* is the radius of the agglomerate particle, C_{CO}^{0} is the dissolved CO concentration at the gas channel and thin liquid-layer interface, and D_{eff} is the effective CO diffusion coefficient within the ionomer domain. The reaction rate for a specific electrochemical reaction, *k*, was described as:

$$k = \frac{A i_{O,COR}}{nF} \exp\left(-\frac{\alpha_{O,COR} F}{RT}\eta_{COR}\right), \qquad \text{(Eq. 8.7)}$$

where *A* is the specific active surface area for the agglomerate model, which is defined as the total agglomerate particle surface area divided by the volume of the gas diffusion electrode. *F* is Faraday's constant, *R* is the universal gas constant, *T* is the absolute temperature, *n* is the number of electrons in each reaction, and η_{COR} is the overpotential of each reaction, which is the difference between an electrochemical reaction's thermodynamically determined reduction potential and the potential at which the redox process is observed experimentally. For COR, two reaction pathways, CO reduction to CH_4 and CO reduction to C_2H_4, were considered within the catalyst layer. The pH-dependent kinetics for both reactions were measured experimentally and fitted to a Butler-Volmer relation:[1]

$$i(C_2H_4) = J_e exp\left[-\frac{\alpha_e F(E-E^0)}{RT}\right], \qquad \text{(Eq. 8.8)}$$

$$i(CH_4) = J_m[H^+] exp\left[-\frac{\alpha_m F(E-E^0)}{RT}\right], \qquad \text{(Eq. 8.9)}$$

where *i* is the current density in mA cm^{-2}. The parameters α_e and α_m are the transfer coefficients for C_2H_4 and CH_4 formation, respectively, and were estimated as 0.35 and 1.33 from Figure 8.2(a). The constants J_e and J_m were 1.18 x 10^{-8} mA cm^{-2} and 3.47 x 10^{-18} mA cm^{-2}, as calculated from the presented linear correlations.

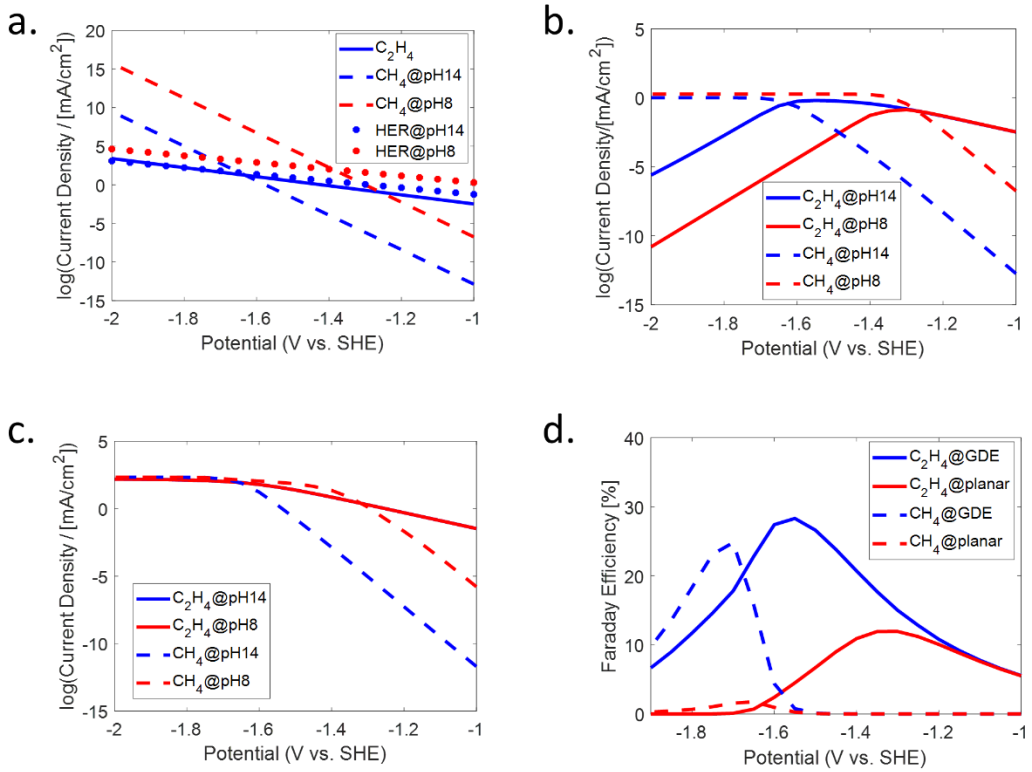

Figure 8.2 (a) The intrinsic kinetics used in the agglomerate model for COR and the HER. (b) The geometric partial current densities for CH_4 and C_2H_4 generation in an aqueous planar electrode at two pH values. (c) Geometric partial current densities for CH_4 and C_2H_4 generation in the flow-through GDE at two pHs. (d) Faradaic efficiencies for CH_4 and C_2H_4 generation using an aqueous planar electrode or a flow-through GDE.

When the attainable current densities were plotted versus the potential of the standard hydrogen electrode (SHE), the intrinsic kinetics assumed in the model for CO reduction to CH_4 were pH-dependent whereas the intrinsic kinetics vs SHE for CO reduction to C_2H_4 were independent of pH. This behavior occurs because the rate-determining step for CH_4 generation is a proton-coupled electron transfer reaction, whereas the rate-determining step for C_2H_4 is independent of the pH of the electrolyte. The volumetric current density of COR in the catalyst layer, j_{COR}, was generated from the two electrochemical reductions listed above: CO to C_2H_4 and CO to CH_4. The volumetric current density of each reaction was described as:

$$j_{COR} = nF\left(\frac{1}{\frac{\delta}{AC^0_{CO}D_{eff}}+\frac{1}{kE}}\right), \quad \text{(Eq. 8.10)}$$

where δ is the thickness of the thin liquid layer that surrounded the sphere. And A is the specific area. Two parallel paths for CO/CO2 to diffuse to the active catalyst are assumed: a) diffusion through the thin liquid layer around the agglomerate particle, so that the thickness of the thin liquid layer is important; b) diffusion into the agglomerate particles, in which case the radius of the agglomerate sphere is important.

In addition to CO reduction, the hydrogen-evolution reaction (HER) also can occur within the catalyst layer domain. Previous experimental data (Figure 8.2a) were used to model the partial volumetric current density generated due to the HER, and representative values of the exchange current density for the HER of 0.010 mA cm^{-2} and a transfer coefficient of 0.258 were taken from the literature.[25] The data were fitted using the Butler-Volmer equation:[25]

$$i(HER) = i_{0\_HER}\exp\left(\alpha_{HER}\eta_{HER}\right), \quad \text{(Eq. 8.11)}$$

where i_{0_HER} is the exchange-current density for HER, α_{HER} is the transfer coefficient, and η_{HER} represents the overpotential for this electrochemical reaction. The corresponding volumetric current density, j_{HER}, is then obtained by multiplication of the specific active surface area for the agglomerate model.

Potential has been applied to drive the electrochemical reaction within the GDE catalyst layer. No extra electric potential has been applied to influence migration in the device. The equilibrium potential represents an interplay between the partial volumetric current densities that determine the rest potential when several electrochemical processes are proceeding simultaneously. The thermodynamic potentials for the reduction of CO to C_2H_4 and CH_4 are -0.34 V and -0.25 V, correspondingly, vs NHE at pH 7, and the equilibrium potential of the HER is 0 V vs RHE. When a specific potential is been applied, these three electrochemical reactions proceed simultaneously but have different overpotentials due to their different thermodynamic potentials.

The total volumetric current density generated from electrochemical reactions in the catalyst layer was expressed as:

$$j_{total} = j_{CO\rightarrow CH_4} + j_{CO\rightarrow C_2H_4} + j_{HER}. \quad \text{(Eq. 8.12)}$$

This total volumetric current density contributes to the electrochemical reaction rate for OH^- within the ionomer domain in the catalyst layer:

$$R_{OH^-\_electrochem} = j_{total}/F, \quad \text{(Eq. 8.13)}$$

$$R_{OH^-} = R_{OH^-\_electrochem} + R_{OH^-\_chem}. \quad \text{(Eq. 8.14)}$$

For other species in the ionomer domain, the $R_{i\_electrochem}$ term is absent, thus:

$$R_i = R_{i\_chem}. \quad \text{(Eq. 8.15)}$$

When CO_2 is used as the supply gas instead of CO, a CO_2 acid/base equilibrium in aqueous electrolytes is also present. In this work, initial conditions were set to 1 M HCO_3^- and therefore the initial pH was 7.8. The CO_2 concentration at equilibrium was calculated as 33.6 mM based on Henry's law. Other than water dissociation, the following chemical reactions were also considered:

$$CO_2 + H_2O \underset{k_{5b}}{\overset{k_{5f}}{\rightleftharpoons}} H^+ + HCO_3^-$$

$$CO_2 + OH^- \underset{k_{6b}}{\overset{k_{6f}}{\rightleftharpoons}} HCO_3^-$$

$$HCO_3^- \underset{k_{7b}}{\overset{k_{7f}}{\rightleftharpoons}} H^+ + CO_3^{2-}$$

$$HCO_3^- + OH^- \underset{k_{8b}}{\overset{k_{8f}}{\rightleftharpoons}} H_2O + CO_3^{2-}$$

The CO_2 to CO reaction is not the rate-limiting step in CO_2 reduction reactions;[27-30], consistently, almost identical reduction products have been observed experimentally for CO_2 reduction and CO reduction[31]. Due to the lack of systematic experimental data for CO_2 reduction kinetics at various local pH values at the electrode surface, the kinetic parameters for CO_2 reduction were obtained by replacing the concentration of CO with CO_2. For CO_2 reduction, the simulation did not take into account the generation of formate as an intermediate, in accordance with observations for many Cu based catalysts[27-29]. The chemical reaction rates for CO_2 within the highly alkaline GDE structures should be independent of

the product branching ratios for CO_2 reduction and should only be affected by the total operating current density, which determines, the rate of hydroxide generation in the GDE. The standard FEM solver in the COMSOL multi-physics package was used to obtain the modeled electrochemical behavior. The maximum element size and the maximum element growth rate for this 1-D model were 10 nm and 1.4, respectively. A relative tolerance of the corresponding variable of 0.001 was applied as the convergence criterion for all simulations.

$H_2O \underset{k_{1b}}{\overset{k_{1f}}{\rightleftharpoons}} H^+ + OH^-$	$k_{1f} = 10^8\ s^{-1}$ $k_{1b} = 10^{19}\ M^{-1}\ s^{-1}$
$H_3PO_4 \underset{k_{2b}}{\overset{k_{2f}}{\rightleftharpoons}} H_2PO_4^- + H^+$	$k_{2f} = 10^7\ s^{-1}$ $k_{2b} = 1.32\text{x}10^9\ M^{-1}\ s^{-1}$
$H_2PO_4^- \underset{k_{3b}}{\overset{k_{3f}}{\rightleftharpoons}} HPO_4^{2-} + H^+$	$k_{3f} = 10^7\ s^{-1}$ $k_{3b} = 1.62\text{x}10^{14}\ M^{-1}\ s^{-1}$
$HPO_4^{2-} \underset{k_{4b}}{\overset{k_{4f}}{\rightleftharpoons}} PO_4^{3-} + H^+$	$k_{4f} = 10^7\ s^{-1}$ $k_{4b} = 4.68\text{x}10^{19}\ M^{-1}\ s^{-1}$
$CO_2 + H_2O \underset{k_{5f}}{\overset{k_{5b}}{\rightleftharpoons}} H^+ + HCO_3^-$	$k_{5f} = 0.036\ s^{-1}$ $k_{5b} = 7.83\text{x}10^4\ M^{-1}\ s^{-1}$
$CO_2 + OH^- \underset{k_{6b}}{\overset{k_{6f}}{\rightleftharpoons}} HCO_3^-$	$k_{6f} = 2.23\text{x}10^3\ M^{-1}\ s^{-1}$ $k_{6b} = 4.85\text{x}10^{-5}\ s^{-1}$
$HCO_3^- \underset{k_{7b}}{\overset{k_{7f}}{\rightleftharpoons}} H^+ + CO_3^{2-}$	$k_{7f} = 2.5\ s^{-1}$ $k_{7b} = 5\text{x}10^{10}\ M^{-1}\ s^{-1}$
$HCO_3^- + OH^- \underset{k_{8b}}{\overset{k_{8f}}{\rightleftharpoons}} H_2O + CO_3^{2-}$	$k_{8f} = 6\text{x}10^9\ M^{-1}\ s^{-1}$ $k_{8b} = 1.2\ s^{-1}$

Table 8.1 Forward and backward rate constants used in the modeling.

D_{H^+}	9.31 x 10^{-5} $cm^2\ s^{-1}$	Diffusion coefficient of H^+
D_{OH^+}	5.26 x 10^{-5} $cm^2\ s^{-1}$	Diffusion coefficient of OH^+

D_{CO}	1.02 x 10^{-5} cm^2 s^{-1}	Diffusion coefficient of CO
D_{CO_2}	1.92 x 10^{-5} cm^2 s^{-1}	Diffusion coefficient of CO_2
$D_{HCO_3^-}$	1.185 x 10^{-5} cm^2 s^{-1}	Diffusion coefficient of HCO_3^-
$D_{H_2PO_4^-}$	0.879 x 10^{-5} cm^2 s^{-1}	Diffusion coefficient of $H_2PO_4^-$
$D_{HPO_4^{2-}}$	0.439 x 10^{-5} cm^2 s^{-1}	Diffusion coefficient of HPO_4^{2-}
$D_{PO_4^{3-}}$	0.612 x 10^{-5} cm^2 s^{-1}	Diffusion coefficient of PO_4^{3-}
$D_{H_3PO_4}$	0.879 x 10^{-5} cm^2 s^{-1}	Diffusion coefficient of H_3PO_4
A	1 x 10^5 m^{-1}	Specific active surface area
α_e	0.35	transfer coefficient for C_2H_4 formation
α_m	1.33	transfer coefficient for CH_4 formation
α_{HER}	0.258	transfer coefficient for HER
J_e	1.18 x 10^{-8} mA cm^{-2}	Constant present in Eq (8.8) for C_2H_4 formation
J_m	3.47 x 10^{-18} mA cm^{-2}	Constant present in Eq (8.9) for CH_4 formation
i_{0_HER}	0.01 mA cm^{-2}	Exchange current density for HER

Table 8.2 Kinematic parameters used in the simulations.

8.3 Results and Discussion

Figure 8.2a shows the intrinsic kinetics used in the model at two different pHs for COR and the HER, for both the planar electrode and the GDE. As described by Eq. 8.8 and Eq. 8.9, the partial current density for C_2H_4 generation was independent of the operating pH, while the partial current density for CH_4 generation shifted by ~360 mV vs SHE, according to the Nernst equation. Figure 8.2b shows the simulated partial current densities for CH_4 generation and C_2H_4 generation as a function of the applied potential at a planar electrode in an aqueous electrolyte with moderate stirring, with the hydrodynamic boundary layer at the planar electrode set to 100 μm. The limiting current density for COR was 1 mA cm^{-2} for an initial pH value of 14 and was 1.9 mA cm^{-2} for an initial pH of 8. At high overpotentials, the partial current density associated with COR to C_2H_4 was nearly zero at both pH values, due to the competing reactions for CH_4 generation and limited CO supply from the bulk solution. Furthermore, Figure 8.2b and Figure 8.2c indicate that beyond -1.8 V vs. SHE the partial current density for the planar electrode for CO reduction reached a plateau, and the plateau current density was ~1 mA cm^{-2}. In contrast, for the GDE configuration, the partial current density associated with COR reached the same value at -1.25 V vs. SHE. For the planar electrode, this partial current density is dominated by CH_4 generation, but for the GDE configuration the partial current density is dominated by C_2H_4 generation.

Figure 8.2d shows the Faradaic efficiencies for the planar electrode and the flow-through GDE, respectively, in the pH=14 electrolyte. In the flow-through GDE configuration, the Faradaic efficiency for C_2H_4 generation exhibited a maximum of 28.3% at an electrode potential of -1.55 V vs. SHE, whereas the maximum Faradaic efficiency for CH_4 was 24.8% at -1.7 V vs. SHE. With a planar electrode under the same initial conditions, the maximum Faradaic efficiencies for C_2H_4 and CH_4 were 11.9% at -1.3 V vs. SHE and 1.8% at -1.65 V vs. SHE, respectively. In both the GDE and planar electrode configurations, the maximum Faradaic efficiencies for methane and ethylene occurred at mutually different overpotentials. The maximum FEs for COR occurred at more positive potentials for the planar electrode configuration than for the GDE configuration. At large negative potentials (<-1.6 V vs. SHE), the current densities at the planar electrode approached the mass- transport-limited

current densities for COR and consequently a large enhancement of the FEs for C_2H_4 generation (from 1.8% to 24.8%) were observed in the flow-through GDE configurations relative to the planar configurations. In general, with the GDE configuration, the Faradaic efficiencies for production of both ethylene and methane were larger than on than the planar electrode, attesting to the strong dependence of the Faradaic efficiency on mass transport.

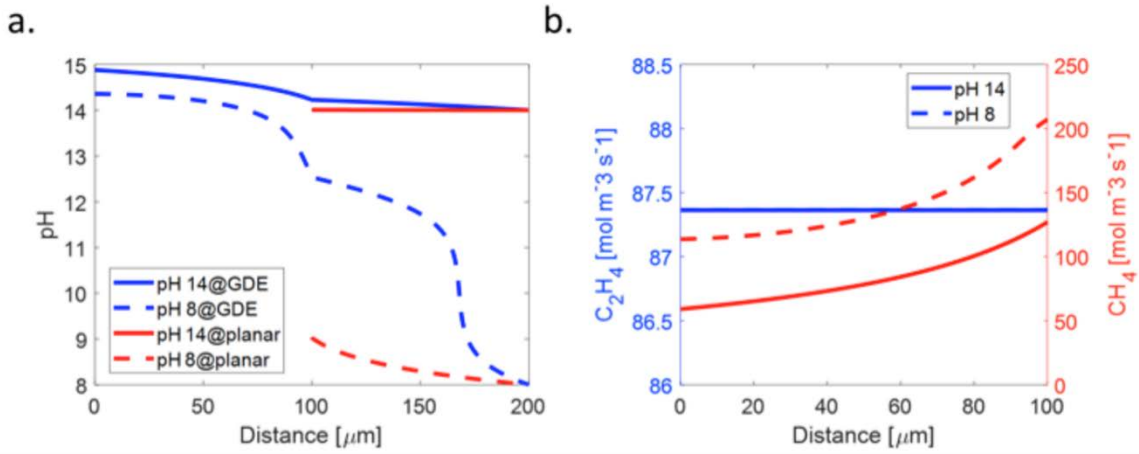

Figure 8.3 (a) Spatially resolved pH profile for a planar electrode and a GDE, at two pH values. (b) Volumetric generation rates in a GDE of CH_4 and C_2H_4 during COR at two pH values.

The spatially resolved pH profiles and volumetric generation rates for COR were modeled and simulated at two different pHs under moderate overpotential (-1.65 V vs. SHE) and the assumption of a high CO coverage. In the flow-through GDE at pH=8, due to the high operating current density of the GDE, a large pH differential of 4.5 was observed within the bulk electrolyte layer relative to the planar electrode (Fig. 8.3a). Within the catalyst layer in the flow-through GDE, the pH increased by 1.8, from 12.5 to 14.3. Although the GDE nominally operated under near-neutral pH conditions (bulk pH=8), during operation and under moderate overpotentials, the local pH within the catalyst layer was highly alkaline, even with 1.0 M buffer in the electrolyte. When the initial pH was set to 14, the pH increased

by 0.9 in the flow-through GDE configuration, compared to 0.01 in the planar electrode. Figure 8.3b indicates that the volumetric generation rate of C_2H_4 along the catalyst layer in the flow-through GDE configuration was independent of pH and was also not dependent on location in the catalyst layer, due to the intrinsic kinetics (Eq. 8.8). In contrast, the volumetric generation rate of CH_4 was substantially lower as the distance towards the current collector decreased, where the local pH was high and the solution was locally highly alkaline. Moreover, the volumetric generation rate of CH_4 also increased when the initial pH of the electrolyte was set to pH = 8.

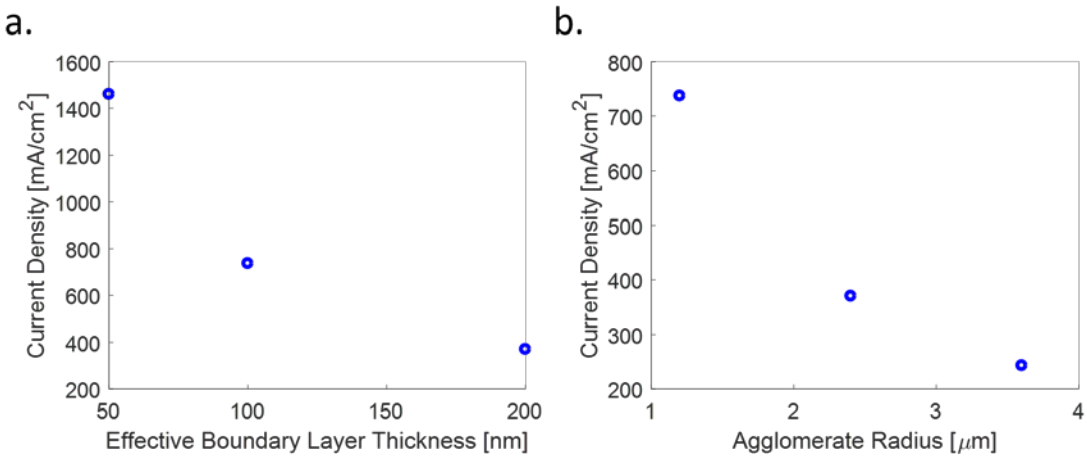

Figure 8.4 Current density for CO reduction as a function of different (a) effective boundary layer thicknesses and (b) agglomerate radii.

In the flow-through GDE configuration, the limiting current density for COR, with an initial pH value of 14, reached 370 mA cm^{-2}, 737 mA cm^{-2} and 1460 mA cm^{-2} with an effective boundary layer thickness of 200 nm, 100 nm and 50 nm, respectively (Figure 8.4a). Decreasing the boundary layer thickness resulted in an increased CO reduction current density because the effective diffusion length of CO was reduced accordingly. At high overpotentials, the limiting partial current density was inversely proportional to the thickness of the boundary layer, because in those cases, CO diffusion was the dominant factor in the rate of CO reduction. As shown in Figure 8.4b, decreasing the agglomerate radius had a similar effect on the CO reduction rate as decreasing the effective boundary layer thickness.

Low CO_2 utilization efficiencies have been observed for aqueous-based electrochemical CO_2 reduction, due to bicarbonate crossover in cells that utilize ion-selective membranes.[32] The flow-through GDE configuration presents additional constraints that impede effective utilization of CO_2. Figure 8.5a shows the spatially resolved pH profile for CO_2R at three different potentials in 1 M bicarbonate electrolyte at pH=7.8. At the electrode/electrolyte interface, the pH values increased to 8.06, 11.92 and 13.52, corresponding to the different applied potentials, whereas at the current collector site, the pH values further increased to 8.6, 12.63 and 14.13, respectively.

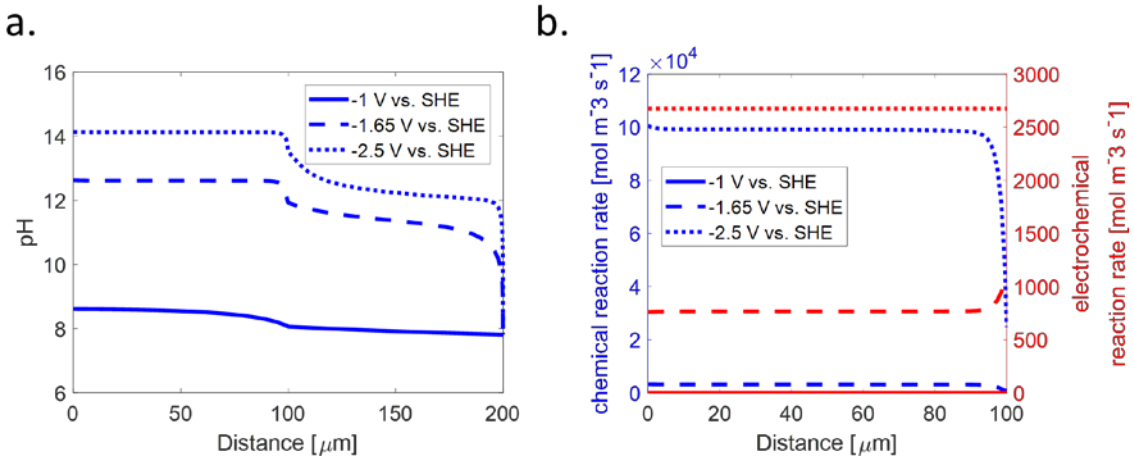

Figure 8.5 (a) Spatially revolved pH profile at three different potentials for CO_2R. (b) Volumetric reaction rates at three different potentials for electrochemical CO_2R and for chemical reaction with alkaline electrolytes.

The highly alkaline conditions at the catalyst layer caused locally substantial CO_2 consumption due to the acid/base equilibrium within the GDE. Figure 8.5b shows the chemical and electrochemical volumetric CO_2 consumption rates at three different overpotentials. At a potential of -1.65 V vs. SHE, the chemical CO_2 consumption rate increased from to 631 mol m^{-3} s^{-1} at the electrode/electrolyte interface to 3156 mol m^{-3} s^{-1} at the current collector site, whereas the electrochemical rate decreased from 1079 mol m^{-3} s^{-1} to 758 mol m^{-3} s^{-1}. When the applied potential was -2.5 V vs. SHE, the chemical volumetric CO_2 consumption rates along the catalyst layer were at least an order of magnitude higher

than the corresponding electrochemical rates. At very low overpotentials (-1 V vs. SHE) that resulted in the pH within the flow-through GDEs being close to the bulk pH due to the low operating current density, the chemical consumption of CO_2 was negligible. In contrast, at large overpotentials, substantial CO_2 loss within the flow-through GDEs was observed due to the chemical consumption of CO_2 in the highly alkaline environment.

For a flow-through configuration, the gas supply was assumed to be sufficient to maintain a stable ~ 1 atm gas pressure within the catalyst layer.

8.4 Conclusions

Flow-through GDEs provide an effective approach to increase the limiting current density for COR or CO_2R relative to planar or nanostructured electrodes, with the internal structure within the GDE playing an important role in the electrochemical behavior. Limiting partial current densities for both C_2H_4 and CH_4 generation were essentially constant as the initial electrolyte conditions were varied. Substantial increases in Faradaic efficiencies for COR or CO_2R are also expected in the flow-through GDEs relative to traditional planar electrodes, especially at large overpotentials. The local CO or CO_2 concentration, the local pH at the reaction site, the pH-dependent kinetics of the catalysts, and the detailed agglomerate catalyst morphology all played important roles in determining the volumetric reaction rates for COR or CO_2R. For CO_2R at relatively large overpotentials, the pH within the flow-through GDEs is highly alkaline even with buffered electrolytes, with the highly alkaline local pH contributing to substantial CO_2 loss due to the acid/base equilibrium within the GDE.

REFERENCES:

1. Y. Hori, R. Takahashi, Y. Yoshinami and A. Murata, *J Phys Chem B*, 1997, **101**, 7075-7081.

2. X. F. Feng, K. L. Jiang, S. S. Fan and M. W. Kanan, *Acs Central Sci*, 2016, **2**, 169-174.

3. C. W. Li, J. Ciston and M. W. Kanan, *Nature*, 2014, **508**, 504-+.

4. A. Verdaguer-Casadevall, C. W. Li, T. P. Johansson, S. B. Scott, J. T. McKeown, M. Kumar, I. E. L. Stephens, M. W. Kanan and I. Chorkendorff, *J Am Chem Soc*, 2015, **137**, 9808-9811.

5. A. J. Bard and L. R. Faulkner, *Electrochemical Methods: Fundamentals and Applications, 2nd Edition*, 2000.

6. C. T. Dinh, T. Burdyny, M. G. Kibria, A. Seifitokaldani, C. M. Gabardo, F. P. G. de Arquer, A. Kiani, J. P. Edwards, P. De Luna, O. S. Bushuyev, C. Q. Zou, R. Quintero-Bermudez, Y. J. Pang, D. Sinton and E. H. Sargent, *Science*, 2018, **360**, 783-787.

7. M. Jouny, W. Luc and F. Jiao, *Nat Catal*, 2018, **1**, 748-755.

8. S. C. Ma, M. Sadakiyo, R. Luo, M. Heima, M. Yamauchi and P. J. A. Kenis, *J Power Sources*, 2016, **301**, 219-228.

9. T. T. H. Hoang, S. Verma, S. C. Ma, T. T. Fister, J. Timoshenko, A. I. Frenkel, P. J. A. Kenis and A. A. Gewirth, *J Am Chem Soc*, 2018, **140**, 5791-5797.

10. G. K. S. Prakash, F. A. Viva and G. A. Olah, *J Power Sources*, 2013, **223**, 68-73.

11. D. S. Ripatti, T. R. Veltman and M. W. Kanan, *Joule*, 2019, **3**, 240-256.

12. R. L. Cook, R. C. Macduff and A. F. Sammells, *Journal of the Electrochemical Society*, 1990, **137**, 607-608.

13. L. H. Han, W. Zhou and C. X. Xiang, *Acs Energy Lett*, 2018, **3**, 855-860.

14. T. T. Zhuang, Z. Q. Liang, A. Seifitokaldani, Y. Li, P. De Luna, T. Burdyny, F. L. Che, F. Meng, Y. M. Min, R. Quintero-Bermudez, C. T. Dinh, Y. J. Pang, M. Zhong, B. Zhang, J. Li, P. N. Chen, H. Y. Liang, W. N. Ge, B. J. Ye, D. Sinton, S. H. Yu and E. H. Sargent, *Nat Catal*, 2018, **1**, 421-428.

15. K. Ogura, R. Oohara and Y. Kudo, *Journal of The Electrochemical Society*, 2005, **152**, D213-D219.

16. H. Yano, F. Shirai, M. Nakayama and K. Ogura, *J Electroanal Chem*, 2002, **519**, 93-100.

17. L. C. Weng, A. T. Bell and A. Z. Weber, *Phys Chem Chem Phys*, 2018, **20**, 16973-16984.

18. L. C. Weng, A. T. Bell and A. Z. Weber, *Energ Environ Sci*, 2019, **12**, 1950-1968.

19. B. Kim, F. Hillman, M. Ariyoshi, S. Fujikawa and P. J. A. Kenis, *J Power Sources*, 2016, **312**, 192-198.

20. D. T. Whipple, E. C. Finke and P. J. A. Kenis, *Electrochem Solid St*, 2010, **13**, D109-D111.

21. P. De Luna, R. Quintero-Bermudez, C. T. Dinh, M. B. Ross, O. S. Bushuyev, P. Todorovic, T. Regier, S. O. Kelley, P. D. Yang and E. H. Sargent, *Nat Catal*, 2018, **1**, 103-110.

22. D. Kopljar, A. Inan, P. Vindayer, N. Wagner and E. Klemm, *J Appl Electrochem*, 2014, **44**, 1107-1116.

23. L. Han, W. Zhou and C. Xiang, *ACS Energy Letters*, 2018, **3**, 855-860.

24. E. W. Thiele, *Ind Eng Chem*, 1939, **31**, 916-920.

25. L. J. J. Janssen, *Mass transfer at gas-evolving vertical electrodes*, 1987.

26. K. P. Kuhl, E. R. Cave, D. N. Abram and T. F. Jaramillo, *Energ Environ Sci*, 2012, **5**, 7050-7059.

27. Y. Hori, in *Modern Aspects of Electrochemistry*, eds. C. G. Vayenas, R. E. White and M. E. Gamboa-Aldeco, Springer New York, New York, NY, 2008, pp. 89-189.

28. S. Nitopi, E. Bertheussen, S. B. Scott, X. Liu, A. K. Engstfeld, S. Horch, B. Seger, I. E. L. Stephens, K. Chan, C. Hahn, J. K. Nørskov, T. F. Jaramillo and I. Chorkendorff, *Chemical Reviews*, 2019, **119**, 7610-7672.

29. K. Kuhl, E. Cave, D. Abram and T. Jaramillo, *Energy & Environmental Science*, 2012.

30. R. Kortlever, J. Shen, K. J. P. Schouten, F. Calle-Vallejo and M. T. M. Koper, *The Journal of Physical Chemistry Letters*, 2015, **6**, 4073-4082.

31. L. Wang and C. Morales-Guio, *ACS Catalysis*, 2018, **8**.

32. M. Lin, L. H. Han, M. R. Singh and C. X. Xiang, *ACS Appl Energ Mater*, 2019, **2**, 5843-5850.

Appendix A

SUPPLEMENTARY FIGURES AND DISCUSSION

A.1 The schematic illustration of a nanostructured electrode

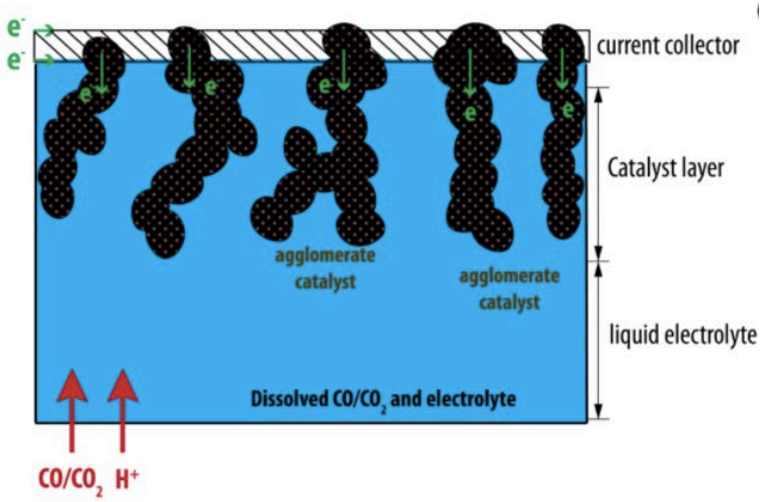

Figure A1 A schematic illustration of a nanostructured electrode

A.2 Comparison of the simulation results between nanostructured- and planar electrode

An aqueous based, nanostructured electrode, illustrated in Figure A1, was modeled and simulated, and very similar limiting current density values for COR were observed relative to planar electrodes. The low limiting current density for COR at aqueous planar and nanostructured electrodes is consistent with many previous observations, in which the partial current density for COR is limited to ~1 mA cm^{-2}.[1-4] The pH dependent kinetics for COR and the local CO concentration for the catalytic reaction were responsible for the different product branching ratios at large negative potentials. For example, the highly alkaline local environment for the nanostructured electrode (Fig. A2b) relative to the planar electrode

substantially reduced the rate of CH_4 generation as the electrode potential became more negative. As a result, in the nanostructured electrodes the partial current density for CH_4 generation was on the same order of magnitude as the partial current density for C_2H_4 generation (Fig. A2a). In contrast, in the flow-through GDE configuration, the limiting partial current densities for C_2H_4 generation and CH_4 generation were 158 mA cm^{-2} and 212 mA cm^{-2}, respectively, in electrolytes with two different pHs. The high electrochemically active surface area (ECSA) and the small effective boundary layer thickness within the catalyst layer were responsible for the substantial increase in the attainable current densities for COR relative to a planar electrode.

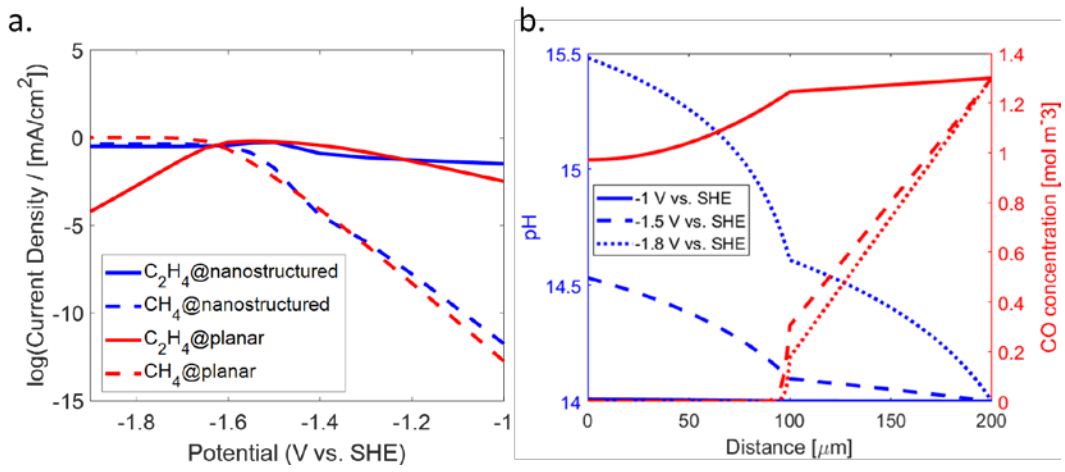

Figure A2 (a) The geometric partial current densities for CH_4 and C_2H_4 generation under the initial pH of 14 in both nanostructured- and planar electrode. (b) The spatially resolved pH and CO concentration for a nanostructured at different overpotentials.

A.3 Comparison of HER performance under low CO coverage and under high CO coverage for a GDE configuration

A low CO coverage within the catalyst layer has been assumed in the main text. To model the HER performance under high CO coverage, the transfer coefficient was decreased to 10% of its original (0.01) value. The CO coverage had little effect on the partial current densities (Figure A3(a)). For either low or high coverages of CO, the maximum Faradaic

efficiencies for methane and ethylene production occurred at mutually different overpotentials. With an electrolyte having an initial pH of 14, the difference in overpotential for maximum Faradaic efficiency between methane and ethylene became larger (by 19.2%) as the assumed CO coverage increased. Figure A3(b) shows that the Faradaic efficiency had a strong dependence on the CO gas coverage. At high CO coverage, the maximal methane and ethylene Faradaic efficiencies were ~50% and ~75%, respectively, but the Faradaic efficiencies were < 30% for low CO coverage.

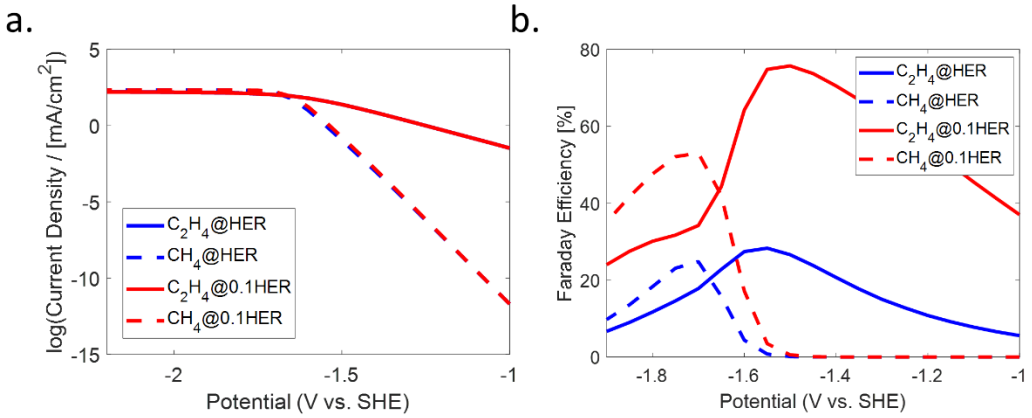

Figure A3 (a) The geometric partial current densities and (b) The Faraday efficiencies for CH_4 and C_2H_4 generation under different assumptions of CO coverage in the catalyst layer (@HER stands for low CO coverage and @0.1HER stands for high CO coverage)

A.4 Using bicarbonate to produce electrolyte with an initial pH=8 for a GDE configuration

In addition to using phosphate buffer, bicarbonate was also used to produce an electrolyte with an initial pH = 8. The partial current density for C_2H_4 generation was independent of the operating pH, and thus did not depend on the buffer species. Under low to moderate overpotentials, due to the higher buffer strength, the partial current density for CH_4 generation was higher with phosphate buffer than with bicarbonate buffer (Figure A4). In contrast, at high overpotentials, the GDEs reached the same plateau of current density, 212

mA cm^{-2}, in either buffered electrolyte because the current density was primarily determined by diffusion of CO(g) to the spherical surface.

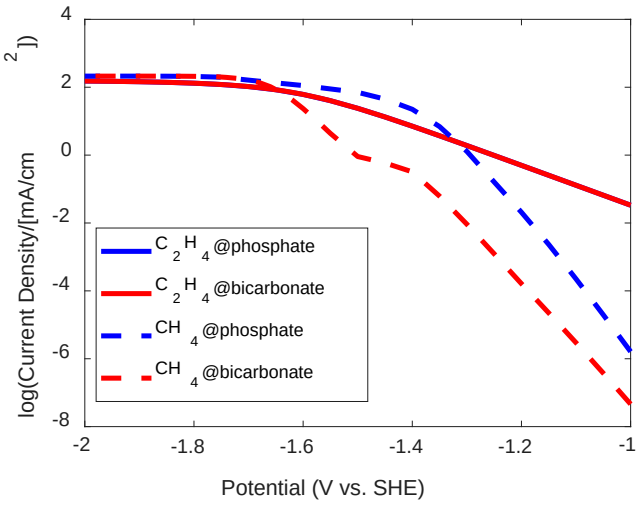

Figure A4 The geometric partial current densities for CH_4 and C_2H_4 generation with phosphate buffer and bicarbonate buffer, both under the initial pH value of 8.

A.5 The volumetric product generation rates from CO_2 reduction within GDE

As shown in Figure A5, at -1.65 V vs. SHE, the volumetric generation rate of C_2H_4 was independent of position and remained at 37 mol m^{-3} s^{-1} within the GDE, due to the lack of dependence of the rate on the local pH. In contrast, the volumetric generation rate of CH_4 increased from 697 mol m^{-3} s^{-1} to 1047 mol m^{-3} s^{-1} as the local pH at the electrode/electrolyte interface decreased from 12.6 to 11.9.

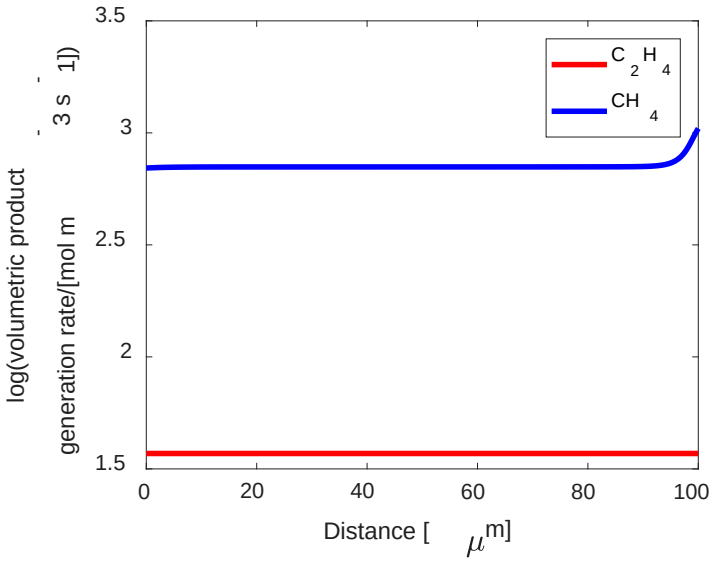

Figure A5 The volumetric product generation rates from CO_2 reduction as a function of position within GDE at -1.65 V vs. SHE.

A.6 Dependence on gas supply of GDE performance

When the gas supply is not large enough, the extreme case, i.e., the nanostructured electrode configuration, was simulated. At -1.4 V vs SHE, the partial current density for CO_2 reduction was 9.11 mA cm^{-2} for sufficient CO_2 gas supply; 8.41 mA cm^{-2} for a fixed gas supply of 1 mol cm^{-2} s^{-1}; and 7.36 mA cm^{-2} for the nanostructured electrode configuration. Thus, sufficient gas supply, moderate gas supply, and no gas supply cases, respectively, have been evaluated for an electrode potential of -1.4 V vs SHE. The resulting difference in terms of partial current density for CO2 reduction due to the different types of gas supply has been shown. The generation of gaseous products (CH_4, C_2H_4 or H_2) was assumed to have minimal effects on transport within the GDEs. The CO_2 concentration distribution was simulated for all of these cases (Fig. A6). The total current density generated at -1.65 V vs. SHE from CO_2R under 1 atm in the catalyst layer from the flow-through GDE was > 5000 mA cm^{-2}, whereas for a planar electrode configuration, the limiting current density for CO_2R was < 20 mA cm^{-2}.

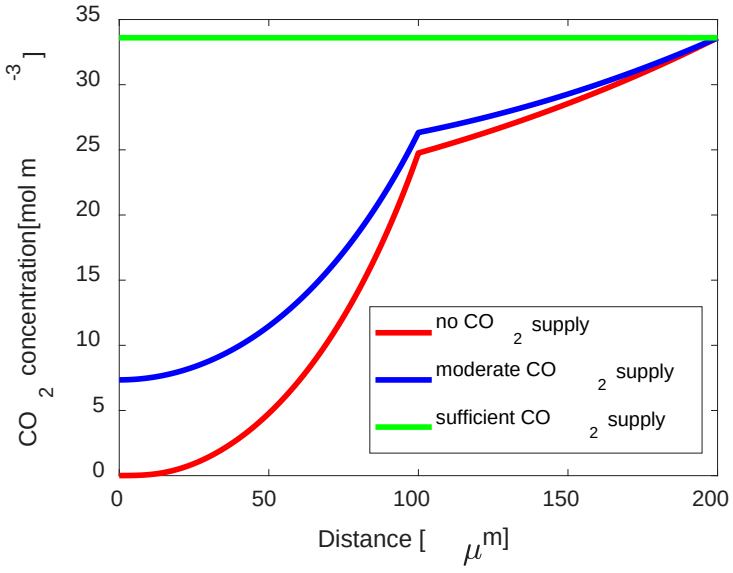

Figure A6 The CO_2 concentration as a function of position inside GDEs with different kinds of CO_2 supply at 1.4 V vs. SHE.

A.7 Dependence on water content and water displacement of GDE performance

The performance of GDEs was also dependent on the water content and water displacement within the structure. As the water content in the GDE layer changed from 10% to 5%, the C_2H_4 generation rate remained the same as previously analyzed due to its lack of dependence on the local pH, but the CH_4 generation rate decreased substantially. In contrast, the partial current density associated with the HER increased substantially. For example, at -1.4 V vs. SHE, the partial current density of CH_4 generation is 14.5 mA cm^{-2} with 10% water content, and decreased to 1.52 mA cm^{-2} with 5% water content, whereas the partial current density associated with the HER increased from 4.2 mA cm^{-2} to 177 mA cm^{-2}.

At this specific potential, Figure A7 shows the local OH^- concentration within the GDE under these assumptions of mutually differing two water content. As the water content decreased, the OH^- transferred with a smaller diffusion coefficient, which resulted in a higher OH^- concentration with the catalyst layer and eventually led to a lower partial current density for CH_4 generation and a higher partial current density related.to the HER.

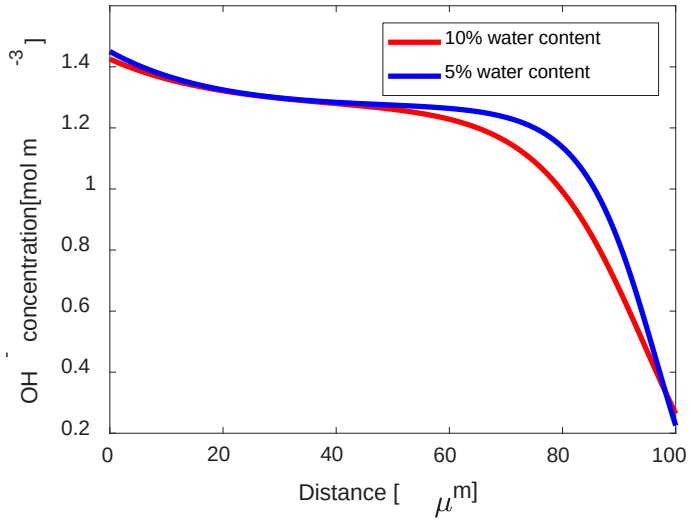

Figure A7 The OH^- concentration as a function of position inside GDEs with two different water content assumptions at -1.4 V vs. SHE.

REFERENCES:

1. Y. Hori, R. Takahashi, Y. Yoshinami and A. Murata, *J Phys Chem B*, 1997, **101**, 7075-7081.

2. X. F. Feng, K. L. Jiang, S. S. Fan and M. W. Kanan, *Acs Central Sci*, 2016, **2**, 169-174.

3. C. W. Li, J. Ciston and M. W. Kanan, *Nature*, 2014, **508**, 504-+.

4. A. Verdaguer-Casadevall, C. W. Li, T. P. Johansson, S. B. Scott, J. T. McKeown, M. Kumar, I. E. L. Stephens, M. W. Kanan and I. Chorkendorff, *J Am Chem Soc*, 2015, **137**, 9808-9811.

Appendix B

EQUATIONS IN CYLINDRICAL COORDINATES

B.1 Simplified Euler-Euler model (axisymmetric)

a. Momentum equation:

r-component:

$$\emptyset_l \rho_l \left(\frac{\partial u_{l,r}}{\partial t} + u_{l,r}\frac{\partial u_{l,r}}{\partial r} + u_{l,z}\frac{\partial u_{l,r}}{\partial z}\right) = -\frac{\partial p}{\partial r} - \frac{2}{3}\frac{\partial}{\partial r}\left[\emptyset_l \mu_l \left(\frac{u_{l,r}}{r} - 2\frac{\partial u_{l,r}}{\partial r} + \frac{\partial u_{l,z}}{\partial z}\right)\right] + \frac{\partial}{\partial z}\left[\emptyset_l \mu_l \left(\frac{1}{r}\frac{\partial u_{l,r}}{\partial z} + \frac{\partial u_{l,z}}{\partial r}\right)\right] + \frac{2\emptyset_l \mu_l}{r}\left(\frac{\partial u_{l,r}}{\partial r} + \frac{u_{l,r}}{r}\right)$$

z-component:

$$\emptyset_l \rho_l \left(\frac{\partial u_{l,z}}{\partial t} + u_{l,r}\frac{\partial u_{l,z}}{\partial r} + u_{l,z}\frac{\partial u_{l,z}}{\partial z}\right) = -\frac{\partial p}{\partial z} + \emptyset_l \rho_l g - \frac{2}{3}\frac{\partial}{\partial z}\left[\emptyset_l \mu_l \left(\frac{u_{l,r}}{r} + \frac{\partial u_{l,r}}{\partial r} - 2\frac{\partial u_{l,z}}{\partial z}\right)\right] + \frac{\partial}{\partial r}\left[\emptyset_l \mu_l \left(\frac{\partial u_{l,z}}{\partial r} + \frac{\partial u_{l,z}}{\partial z}\right)\right] + \frac{\emptyset_l \mu_l}{r}\left(\frac{\partial u_{l,r}}{\partial z} + \frac{\partial u_{l,z}}{\partial r}\right)$$

Here u represents the velocity vector, p, ρ stands for the pressure and the density, respectively. $\emptyset$ is the phase volume fraction. μ_l is the dynamic viscosity of the liquid. The subscripts 'l' and 'g' denote quantities related to the liquid phase and gas phase, correspondingly.

b. Continuity equation:

$$\frac{\partial}{\partial t}\left(\rho_l \phi_l + \rho_g \phi_g\right) + \frac{1}{r}\frac{\partial}{\partial r}\left[r\left(\rho_l \phi_l u_{l,r} + \rho_g \phi_g u_{g,r}\right] + \frac{\partial}{\partial z}\left(\rho_l \phi_l u_{l,z} + \rho_g \phi_g u_{g,z}\right) = 0\right.$$

c. Gas transport equation:

$$\frac{\partial}{\partial t}(\rho_g \phi_g) + \frac{1}{r}\frac{\partial}{\partial r}(r\rho_g \phi_g u_{g,r}) + \frac{\partial}{\partial z}(\rho_g \phi_g u_{g,z}) = -m_{gl}$$

B.2 Nernst-Planck equation (axisymmetric)

$$\frac{\partial c_{H_2}}{\partial t} - D_{H_2}\left(\frac{1}{r}\frac{\partial c_{H_2}}{\partial r} + \frac{\partial^2 c_{H_2}}{\partial r^2} + \frac{\partial^2 c_{H_2}}{\partial z^2}\right) + \left(u_{l,r}\frac{\partial c_{H_2}}{\partial r} + u_{l,z}\frac{\partial c_{H_2}}{\partial z}\right) = R_{H_2}$$

Here D_{H_2} and c_{H_2} are the diffusion coefficient and concentration, respectively, of H_2 within the electrolyte, R_{H_2} is associated with the mass transfer rate between two phases, $R_{H_2} = -m_{gl}/M$.

B.3 Boundary conditions for the two-phase flow (axisymmetric)

a. At the electrode-electrolyte interface:

$$u_l \cdot \hat{z} = 0,$$

which means the liquid velocity component normal to the electrode surface is zero.

$$m_{gas,in} = \frac{|J| f_G M}{zF},$$

where $m_{gas,in}$ represents the gas mass flux, J is the cathodic current density. M and z are the molecular weight and the charge number of the gas, respectively. f_G is the percentage of the product gas transferred into the gaseous phase adhering to the electrode surface.

b. On the vertical wall:

$$u_l = 0,$$

which means no slip condition for the liquid.

$$\frac{\partial}{\partial r}(\rho_g \phi_g) = 0,$$

Which means no gas flux towards the vertical wall.

c. At the top of the boundary layer:

$$u_l \cdot \hat{z} = 0,$$

which means the liquid velocity component normal to the electrode surface is zero.

$$u_g \rho_g \phi_g = (u_g \rho_g \phi_g \cdot \hat{z})\hat{z},$$

which means at the top of the interface layer is gas outlet.

B. 4 Boundary conditions for Nernst-Planck equation (axisymmetric)

a. At the electrode-electrolyte interface:

$n_{dissolved,in} = \frac{|J|(1-f_G)}{zF}$,

where $n_{dissolved,in}$ stands for the dissolved hydrogen influx.

b. On the vertical wall:

$\frac{\partial c_{H_2}}{\partial r} = 0$,

which means no flux condition for dissolved hydrogen.

c. At the outer bulk electrolyte layer:

Dissolved hydrogen concentration at the initial conditions were assumed, $c_{H_2,outer} = c_{H_2}^0$.